

Frictional behaviour of megathrust fault gouges under in-situ subduction zone conditions

Sabine A.M. den Hartog

UTRECHT STUDIES IN EARTH SCIENCES
No. 033

Members of the dissertation committee:

Prof.dr. M.R. Drury

Utrecht University
The Netherlands

Prof.dr. K. Kanagawa

Chiba University
Japan

Prof.dr. A.J. Kopf

University of Bremen
Germany

Prof.dr. D.M. Saffer

Pennsylvania State University
United States of America

Prof.dr. T. Shimamoto

State Key Laboratory of Earthquake Dynamics
Institute of Geology, China Earthquake Administration
China

This research was carried out at:

High Pressure and Temperature Laboratory
Faculty of Geosciences, Utrecht University
Budapestlaan 4, 3584 CD Utrecht
The Netherlands

Local editors: Prof.dr. Steven de Jong, Dr. Marjan Rossen, Prof.dr. Cor Langereis, Drs. Jan-Willem de Blok

ISBN/EAN: 978-90-6266-323-1

Copyright © 2013 Sabine den Hartog

All rights reserved. No part of this publication may be reproduced in any form, by print or photo print, microfilm or any other means, without written permission by the publishers.

Printed by: CPI Wöhrmann Print Service

Cover image: microstructure of sheared illite-quartz gouge, see also Fig. 2.7b.

Frictional behaviour of megathrust fault gouges under in-situ subduction zone conditions

Wrijvingsgedrag van breukmeel uit mega-opschuivingen
onder *in situ* subductiezone condities
(met een samenvatting in het Nederlands)

Proefschrift

ter verkrijging van de graad van doctor aan de Universiteit Utrecht op gezag van
de rector magnificus, prof.dr. G.J. van der Zwaan, ingevolge het besluit van het
college voor promoties in het openbaar te verdedigen op maandag 15 april 2013
des ochtends te 10.30 uur

door

Sabine Albertina Maria den Hartog

geboren op 8 oktober 1984
te Woerden

Promotor: **Prof.dr. C.J. Spiers**

Co-promotor: **Dr. A.R. Niemeijer**

Dit proefschrift werd (mede) mogelijk gemaakt met financiële steun van de Nederlandse Organisatie voor Wetenschappelijk Onderzoek (NWO) door middel van een Toptalent subsidie (Dossiernummer 021.002.025).

Contents

Summary	XI
----------------	-----------

Chapter 1 Introduction	1
-------------------------------	----------

1.1 General motivation and scope of this study	2
1.2 Controls on subduction megathrust slip and seismicity	2
1.2.1 The up-dip seismogenic limit	4
1.2.2 The down-dip seismogenic limit	4
1.2.3 Slow Slip Events	5
1.2.4 Role of fault rock friction	5
1.3 Experimental studies addressing the frictional behaviour of megathrust gouges	5
1.3.1 Low temperature studies	5
1.3.2 Experiments at in-situ P-T conditions	6
1.3.3 Fault gouge compositions used in previous lab studies	8
1.4 Modelling fault friction and seismogenesis	9
1.5 Aims of this thesis	12

Chapter 2 Frictional properties of megathrust fault gouges at low sliding velocities: new data on effects of normal stress and temperature	13
---	-----------

Abstract	14
2.1 Introduction	15
2.2 Methods	16
2.2.1 Starting material	16
2.2.2 Experimental apparatus and procedures	17
2.2.2.1 Biaxial experiments	17
2.2.2.2 Ring shear experiments	19
2.2.3 Data processing	20
2.2.4 Microstructural methods	21
2.3 Results	23
2.3.1 Mechanical data	23
2.3.1.1 Biaxial data on ODP material	23
2.3.1.2 Biaxial data on illite	24
2.3.1.3 Ring shear data on illite	27
2.3.2 Microstructural observations	28
2.3.2.1 Biaxial experiments	28
2.3.2.2 Ring shear experiments	28
2.4 Discussion	30
2.4.1 Comparison with previous data	30

2.4.2 Microscopic shear mechanisms	33
2.4.3 Implications for seismogenesis	34
2.4.4 Implications for modelling studies	35
2.5 Conclusions	38
Acknowledgements	38

Chapter 3 New constraints on megathrust slip stability under subduction zone *P-T* conditions **41**

Abstract	42
3.1 Introduction	43
3.2 Material and methods	44
3.2.1 Sample material	44
3.2.2 Experimental apparatus and procedure	44
3.2.3 Data processing	46
3.2.4 Microstructural methods	48
3.3 Results	48
3.3.1 Mechanical data	48
3.3.2 Microstructural observations	50
3.4 Discussion	54
3.4.1 Temperature-dependent frictional properties: present versus previous work	54
3.4.2 Microscopic shear mechanisms	55
3.4.3 Implications for seismogenesis	57
3.4.4 Implications for modelling studies	58
3.5 Conclusions	60
Acknowledgements	61
Appendix 3.A: Supplementary data	62

Chapter 4 Influence of subduction zone conditions and gouge composition on frictional slip stability of megathrust faults **63**

Abstract	64
4.1 Introduction	65
4.2 Material and methods	67
4.2.1 Sample material	67
4.2.2 Experimental apparatus and procedure	68
4.2.3 Data acquisition and processing	69
4.3 Results	72
4.3.1 Frictional strength	72
4.3.2 Velocity dependence of friction	75
4.4 Discussion	78
4.4.1 Microscopic shear mechanisms: microphysical model versus results	81

4.4.1.1 Predicted and observed effects of temperature	81
4.4.1.2 Predicted and observed effects of other variables on (a-b)	82
4.4.1.3 Predicted and observed trends in μ	83
4.4.2 Comparison with previous work on other gouge compositions	84
4.4.3 Implications for seismogenesis under in-situ megathrust conditions	85
4.4.3.1 Sensitivity of (a-b) to sliding velocity	86
4.4.3.2 Sensitivity of (a-b) to quartz content	86
4.4.3.3 Sensitivity of (a-b) to P_f and σ_n^{eff}	87
4.4.3.4 Extrapolation to in-situ conditions	87
4.4.3.5 Stiffness, strength and stability	88
4.5 Conclusions	89
Acknowledgements	90
 Chapter 5 Friction on subduction megathrust faults: beyond the illite-muscovite transition	 91
Abstract	92
5.1 Introduction	93
5.2 Material and methods	94
5.2.1 Sample material	94
5.2.2 Experimental apparatus and procedure	94
5.2.3 Data processing	96
5.2.4 Microstructural methods	98
5.3 Results: mechanical data	98
5.3.1 Muscovite-quartz samples	98
5.3.2 Pure muscovite samples	101
5.4 Results: microstructural observations	101
5.4.1 Sectioned samples	101
5.4.1.1 Starting microstructure muscovite-quartz samples	101
5.4.1.2 Sheared muscovite-quartz samples	103
5.4.1.3 Sheared pure muscovite samples	103
5.4.2 Fracture surfaces	103
5.4.2.1 Sheared muscovite-quartz samples	103
5.4.2.2 Sheared pure muscovite samples	104
5.5 Discussion	105
5.5.1 Role of muscovite versus quartz in controlling friction	105
5.5.2 Microphysical mechanisms	106
5.5.3 Present results versus data for illite-quartz gouge and implications for subduction zone seismogenesis	107
5.6 Conclusions	110
Acknowledgements	111
 Chapter 6 A microphysical model for fault gouge friction and slip stability applied to subduction megathrusts	 113

Abstract	114
6.1 Introduction	115
6.2 Microstructural model	117
6.2.1 Microstructural observations	117
6.2.2 Idealised microstructural model	119
6.2.3 Assumed deformation process	121
6.2.4 Microstructural state variables	124
6.3 Macroscopic shear stress balance and kinematic relations	125
6.3.1 Non-dilatant deformation	125
6.3.2 Dilatant deformation	125
6.4 Microscopic stress balance and shear resistance to deformation	126
6.4.1 Clast body zones	126
6.4.2 Clast overlap zones	126
6.4.3 Stress supported during dilatant deformation	126
6.5 Thermally activated deformation of quartz	127
6.6 Final model assembly and implementation	128
6.6.1 Determining shear strength as a function of slip velocity	128
6.6.1.1 Non-dilatant deformation	128
6.6.1.2 Dilatant deformation	128
6.6.2 Model input data	129
6.7 Model predictions and comparison with experimental results	130
6.7.1 Dependence of shear strength (μ) on deformation conditions and microstructural variables	130
6.7.1.1 Predicted effect of sliding velocity V	130
6.7.1.2 Predicted effect of T	131
6.7.1.3 Predicted effect of σ_n^{eff}	131
6.7.1.4 Predicted effect of f_{qtz}	132
6.7.1.5 Predicted effect of D	132
6.7.1.6 Effect of P_f	133
6.7.1.7 Comparison with experimental trends in μ	134
6.7.2 Trends in the RSF parameter (a-b)	135
6.7.2.1 Predicted effects of V and T	136
6.7.2.2 Predicted effects of σ_n^{eff} , f_{qtz} and D	137
6.7.2.3 Comparison with experimental trends	137
6.8 Implications for subduction megathrust seismogenesis	138
6.9 Conclusions	141
Acknowledgements	142
Appendix 6.A: Shear strain rate of clast bodies	143
Appendix 6.B: Shear strain rate of clast overlaps	144
Appendix 6.C: Compaction rate	145

Chapter 7 General conclusions and suggestions for future research 147

7.1 Main findings	148
-------------------	-----

7.1.1 Effect of temperature on the frictional properties of illite-quartz gouge	148
7.1.2 Effects of other variables on frictional properties	148
7.1.3 Effect of quartz-phyllosilicate composition on frictional properties	149
7.1.4 Microscale processes	150
7.2 Implications for subduction megathrust behaviour: a synthesis	151
7.3 Remaining problems and suggestions for further research	152
7.3.1 Unsolved issues and remaining data needs	152
7.3.2 Broader challenges for the future	154
References	159
Samenvatting	171
Acknowledgements	175
Curriculum vitae	178

Summary

Subduction megathrust faults generate the largest earthquakes and tsunamis known. Understanding and modelling seismogenesis on such faults requires an understanding of the frictional processes that control nucleation and propagation of both seismogenic slip and so-called Slow Slip Events (SSEs). However, experimental data on the frictional behaviour of megathrust fault rocks is limited and almost no experiments have been performed on compositionally realistic materials under relevant in-situ conditions. Data that do exist are usually described empirically, using the Rate and State Friction (RSF) theory, with no microphysical underpinning to constrain extrapolation to nature. In this thesis, I report the results of an experimental study aimed at determining the frictional behaviour of compositionally realistic megathrust fault rocks under near in-situ P - T conditions, addressing low sliding velocities relevant to earthquake nucleation and SSEs. In addition, an attempt is made to explain and quantify the underlying microscale processes in terms of a microphysical model.

In Chapter 1, the motivation and scope of the study are outlined and current knowledge on subduction zone seismogenesis is summarized. Previous experimental work is then discussed and key knowledge gaps identified. This is followed by the definition of the aims of the current thesis.

Chapter 2 investigates the influence of in-situ effective stress and temperature on the frictional properties of (simulated) fault gouges, prepared either from Nankai ODP megathrust samples or from illite-quartz mixtures. Double direct shear experiments were performed at room temperature, normal stresses of 5-30 MPa, and sliding velocities of 0.16-18 $\mu\text{m/s}$. Both materials thus tested exhibited velocity-strengthening slip and an increase in friction coefficient (μ) and slip hardening rate with increasing normal stress. Illite-rich gouge showed increased velocity-strengthening towards higher normal stresses. These results imply an enhanced tendency for earthquake nucleation and SSEs at low effective normal stresses. In addition, the first results of ring shear experiments on illite-rich gouge, at near in-situ seismogenic zone conditions are presented. These experiments, conducted at an effective normal stress (σ_n^{eff}) of 170 MPa, a pore fluid pressure (P_f) of 100 MPa and sliding velocities (V) of 1-100 $\mu\text{m/s}$, at 200-300°C, showed evidence for a transition, at ~250°C, from velocity-strengthening to velocity-weakening behaviour needed for seismogenic slip.

To explore this transition further, in Chapter 3, the ring shear friction experiments on illite-quartz gouge are extended to 150-500°C, under otherwise the same conditions employed in Chapter 2. The results show three temperature-dependent “slip stability” regimes, characterized by velocity-strengthening at 150-250°C, velocity-weakening at 250-400°C and velocity-strengthening at 400-500°C. The regimes are defined by a decrease in the RSF parameter ($a-b$) at 150-300°C followed by an increase at 300-500°C, alongside systematic changes in other RSF parameters and an increase in μ above 300°C. Using earlier microphysical models developed for friction in granular, clast-supported halite-phylllosilicate (analogue) gouges, the effects of increasing temperature are qualitatively explained in terms of a transition from (i) critical state granular flow (at 150-250°C), through (ii) granular flow whereby dilatation is balanced by compaction involving thermally activated deformation of quartz clasts by stress corrosion cracking (SCC) or perhaps pressure solution (at 250-400°C), to (iii) non-dilatant slip on the phyllosilicates with accommodation at quartz clasts

by the thermally activated process (at 400-500°C). Accounting for effects of sliding velocity, the observed velocity-weakening regime broadly explains the extent of the seismogenic zone on subduction megathrusts.

To assess the importance of other variables in determining the in-situ conditions of the seismogenic zone, Chapter 4 addresses the influence of effective normal stress, pore fluid pressure and quartz content on the three-regime behaviour seen in illite-quartz gouge. Ring shear friction experiments were performed at effective normal stresses of 25-200 MPa, P_f values of 50-200 MPa and sliding velocities of 1-100 $\mu\text{m/s}$, at 140-600°C, using gouge mixtures with an illite:quartz ratio varied between 65:35 and zero. The velocity-weakening regime identified in Chapter 3 was found to shift towards higher temperatures with a decrease in the effective normal stress, being located at ~ 350 -600°C at $\sigma_n^{\text{eff}} = 50$ MPa. Trends in (a - b) versus quartz fraction and sliding velocity suggested a shift of the velocity-weakening regime, towards lower temperatures, with an increase in the quartz content and a decrease in the velocity. An increase in the pore fluid pressure slightly increased (a - b) at all temperatures explored, narrowing the temperature extent of the velocity-weakening regime. The results are explained by the same microphysical mechanisms inferred in Chapter 3. They imply that the depth extent of velocity-weakening on subduction megathrusts will depend on all variables investigated and that to predict the location of the seismogenic zone on a given megathrust, it is essential to know how temperature, pore fluid pressure and effective normal stress depend on depth.

In Chapter 5, additional effects on megathrust fault rock friction are determined by considering the illite-muscovite transition. To this end, ring shear friction experiments were performed again at $\sigma_n^{\text{eff}} = 170$ MPa, $P_f = 100$ MPa, $V = 1$ -100 $\mu\text{m/s}$, but on simulated muscovite-quartz (65:35) gouge, at 100-600°C. The effects of quartz versus muscovite were discriminated by shearing pure muscovite gouge at 200-600°C, under otherwise identical conditions. Like the illite-quartz gouge, both the mixed and pure muscovite gouges showed an increase in friction coefficient with temperature. In addition, similar three-regime behaviour of velocity-dependence was observed for the muscovite-quartz gouge, characterised by velocity-strengthening or neutral behaviour at 100-350°C, velocity-weakening at 350-500°C and velocity-strengthening at 500-600°C. By contrast, the pure muscovite gouges showed predominantly velocity-strengthening, demonstrating that quartz plays an essential role in producing velocity-weakening of phyllosilicate-quartz mixtures. Interestingly, the velocity-weakening regime in the mixed gouge overlaps in temperature with that for illite-quartz gouge, but extends to higher temperatures. Taken together with the data on illite-quartz gouge, the results offer an explanation for the seismogenic zone on subduction megathrusts. Comparison with the microphysical model qualitatively applied in Chapters 3 and 4 again suggests that the underlying mechanisms controlling friction of muscovite-quartz gouge involve an interplay between slip on the phyllosilicates, dilatation at quartz clasts, compaction due to clast deformation by a thermally activated process (like pressure solution or SCC), and shear deformation of the clasts by this process.

In Chapter 6, a new microphysical model is developed properly to capture the microstructural characteristics of the illite-quartz gouge studied. The new model assumes a phyllosilicate-rich, matrix-supported microstructure in which rate-independent frictional slip on aligned

phyllosilicates and thermally activated deformation of the intervening quartz clasts occurs. At low slip rates or high temperatures, thermally activated deformation of the clasts is easy, accommodating slip on the phyllosilicate foliation. With increasing velocity (decreasing temperature), shear of the quartz clasts by the thermally activated mechanism becomes more difficult, increasing the shear stress, until slip is activated on phyllosilicates anastomosing around the clasts. Slip on this curved foliation leads to dilation, balanced at steady state by compaction through thermally activated clast deformation. Model predictions, taking pressure solution as the thermally activated mechanism, show broad agreement with the experiments on illite-quartz gouge reported in Chapters 3 and 4. Both show three regimes of velocity dependence, with velocity-weakening occurring at intermediate temperatures. Changing the slip rate, effective normal stress and quartz fraction in the model shifts the three regimes in temperature, as seen experimentally (Chapter 4). Extrapolation of the model to earthquake nucleation slip rates successfully predicts the onset of velocity-weakening behaviour at the temperatures associated with the up-dip seismogenic limit. The results suggest that the location of the seismogenic zone on subduction megathrusts is controlled by fault rock compaction through pressure solution of quartz clasts, operating in competition with dilatation due to slip on anastomosing phyllosilicates.

Finally, in Chapter 7, the main findings are summarized, along with the main implications for subduction megathrust behaviour. Issues that remain unsolved are reported and suggestions for future research are given. A major overall conclusion drawn concerns the agreement obtained in the main trends of frictional behaviour versus T , V , σ_n^{eff} and quartz content, between model predictions, experimental data, and the location of the up-dip seismogenic limit on subduction megathrusts. This implies that seismogenesis is caused by a key brittle-ductile transitional process, namely competition between dilation, due to slip on an anastomosing phyllosilicate foliation, and thermally activated compaction, most likely involving pressure solution of quartz clasts.

Chapter 1

Introduction

1.1 General motivation and scope of this study

Subduction zone megathrusts generate the Earth's largest earthquakes and most destructive tsunamis (National Geophysical Data Center, 2012). The impact of such events was tragically demonstrated most recently by the M_w 9.0 Tohoku-Oki earthquake and subsequent tsunami that struck NE Japan on 11 March 2011 (e.g. Koketsu et al., 2011; Ozawa et al., 2011; Simons et al., 2011). Other examples of major megathrust earthquakes include the Chile 1960 M_w 9.5 event (e.g. Bilek, 2010; Plafker and Savage, 1970), the Alaska 1964 M_w 9.2 event (e.g. Plafker, 1965; Suito and Freymueller, 2009), and the Sumatra M_w 9.1 earthquake plus associated Indian-Ocean-wide tsunami of December 2004 (e.g. Lay et al., 2005). Besides the devastating effects that these phenomena have on human life and environment, they also cause major regional economic damage (Guha-Sapir et al., 2012). In the event of key international centres being hit, such as Tokyo, Los Angeles or Shanghai, the economic impact can even attain global proportions.

The risks posed by megathrust earthquakes, and the impact they have had in the last decade, have raised both regional and global awareness of the need to improve seismic and tsunami hazard evaluation capability. Such improvements depend in part on understanding how unstable, seismogenic slip is nucleated and propagates on subduction zone megathrusts – i.e. on understanding the mechanics of subduction zone seismogenesis. This, in turn, requires a quantitative understanding and description of the rheological behaviour, specifically the frictional strength and potential for allowing stable versus unstable (seismogenic) slip, of the fault rocks or gouges present in subduction zone megathrusts. Such questions can be addressed by experimental studies, modelling studies or scientific drilling initiatives, such as the Nankai Trough Seismogenic Zone Experiment (NanTroSEIZE), one of the most ambitious Ocean Drilling Programs (ODP) to date, which aims to drill, sample and instrument the shallow (≤ 6 km) Nankai subduction megathrust (e.g. Kimura et al., 2007).

In this thesis, I report the results of an experimental study designed to determine the frictional behaviour of compositionally realistic megathrust fault gouges at near in-situ P - T conditions, and at low sliding velocities relevant for earthquake nucleation, in one of the first studies to address large displacement deformation under such conditions. A microphysical model is subsequently developed and compared with the experimental results, providing an explanation of the main trends observed and offering improved scope for modelling the frictional behaviour of megathrust fault rocks at the low slip rates characteristic of seismogenesis.

1.2 Controls on subduction megathrust slip and seismicity

Subduction megathrust earthquakes occur when unstable or accelerating slip is nucleated on a subduction décollement fault, in the so-called seismogenic zone (Fig. 1.1). Nucleation occurs when the fault weakens with accelerating slip, i.e. when the fault shows velocity-weakening behaviour as opposed to velocity-strengthening behaviour, which yields stable, aseismic behaviour. Besides velocity-weakening properties, earthquake nucleation requires the elastic stiffness of the rock occupying the elastically deformed region surrounding the seismogenic zone to be less than a critical value, defined in terms of the spring stiffness in an equivalent spring-slider model for the fault (e.g. Beeler, 2007; Scholz, 1998). When these conditions are met, a rupture can initiate, and when sufficient elastic energy is present to

drive motion, it will propagate in the fault plane to produce a megathrust earthquake (e.g. Beeler, 2007).

Focal depth data show that the seismogenic zone on subduction megathrusts is limited to the region that is located between the $\sim 100\text{--}150^\circ\text{C}$ isotherms, at $\sim 5\text{--}15$ km depth, and the $\sim 350^\circ\text{C}$ isotherm, typically at ~ 40 km depth (e.g. Hyndman, 2007; Hyndman et al., 1997; Oleskevich et al., 1999). The zone is bound at its up-dip and down-dip limits by aseismic zones (e.g. Hyndman et al., 1997; Marone and Saffer, 2007; Schwartz and Rokosky, 2007; Fig. 1.1). Although these aseismic zones do not host the foci of large megathrust earthquakes, they can host coseismic rupture if perturbed by a large enough increase in velocity. They are then said to exhibit “conditional stability” (e.g. Paterson and Wong, 2005; Scholz, 1998; Schwartz and Rokosky, 2007). Coseismic slip, at depths shallower than the seismogenic zone, is of particular importance because of its high potential for causing tsunamis (Faulkner et al., 2011; Oleskevich et al., 1999).

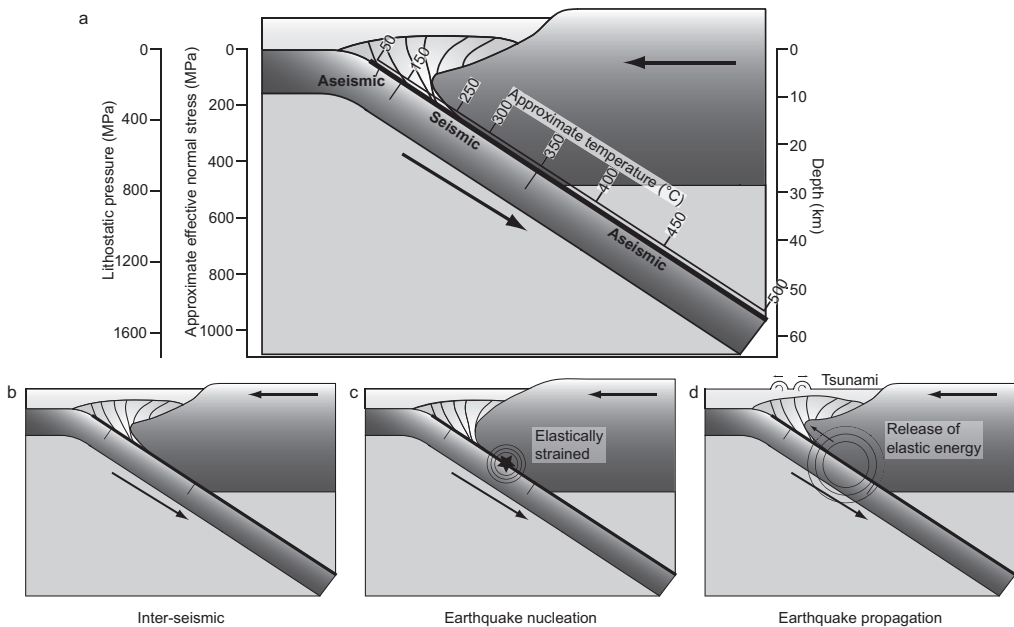


Figure 1.1 Schematic cross sections of a subduction zone illustrating the location of the seismogenic zone and the seismic cycle on subduction megathrust faults. (a) Section showing the temperature dependence of seismic behaviour (i.e. the seismogenic zone). Temperature is generally believed to be the primary control on seismicity. The corresponding depth, lithostatic pressure and effective normal stress axes displayed here are scaled using the geotherm for the Japan subduction zone at Shikoku, given by Peacock (2009). The effective normal stress is scaled assuming a hydrostatic pore fluid pressure, and a constant density of water. Compaction and mineral dehydration effects generally imply that this will be the minimum pore fluid pressure. The effective normal stress displayed therefore represents the likely maximum value (see also Section 1.3.2). (b–d) Schematic representation of the seismic cycle characterizing subduction megathrusts. During the inter-seismic period (b), no motion occurs along the megathrust, whereas plate convergence continues, resulting in a build-up of (elastic) stresses. When these overcome the frictional resistance on the fault, then provided the fault rocks and surrounding material possess the necessary frictional and elastic properties, an earthquake rupture nucleates (c). This subsequently propagates (d), in some cases initiating a tsunami.

1.2.1 The up-dip seismogenic limit

Several hypotheses have been put forward to explain the onset of seismogenesis on megathrusts at ~100-150°C. One of the most widely cited hypotheses is that it is the diagenetic transformation of the weak, hydrous, clay mineral (phyllosilicate) smectite, to the stronger, non-hydrous clay mineral illite, that is responsible for the onset of seismic behaviour (e.g. Hyndman et al., 1997; Oleskevich et al., 1999). This idea originates in the work of Vrolijk (1990). He estimated the depth of the smectite-to-illite transition beneath the Barbados accretionary prism, using reported sediment burial and heating rates and assuming a mineral transition temperature of 100-110°C. Based on the apparent correspondence of this depth with the depth inferred for the up-dip seismogenic limit within the Barbados subduction zone, Vrolijk (1990) suggested that the increase in frictional strength accompanying the smectite-to-illite transition results in the onset of unstable behaviour. Qualitative support for the smectite-to-illite hypothesis has been provided by a more general correspondence of the temperature of the smectite-to-illite transition (~120-150°C; Pytte and Reynolds, 1988) with that of the up-dip seismogenic limit observed in a variety of subduction zones (Oleskevich et al., 1999). The concept relies on the notion that the higher strength of illite leads to an increase in stored elastic energy such that a sufficiently large stress drop can occur to drive dynamic growth of a rupture (cf. Marone and Saffer, 2007; Moore et al., 2007). However, to a first order approximation, slip instability is independent of fault strength (e.g. Tullis, 1988). Moreover, any model that attributes the onset of seismogenesis to the smectite-illite transition, implicitly assumes that illite-rich fault rock exhibits velocity-weakening behaviour, as opposed to velocity-strengthening in smectite.

An alternative hypothesis put forward to explain the up-dip seismogenic limit, is that potentially unstable (“velocity-weakening”) shear localization is brought about by temperature- and depth-dependent lithification (porosity reduction, consolidation and cementation) of megathrust fault rocks occurring alongside the smectite-illite transition (Byrne et al., 1988; Marone and Scholz, 1988; Moore et al., 2007; Moore and Saffer, 2001; Saffer and Marone, 2003). It has further been proposed that megathrusts are destabilized by diminishing pore fluid overpressures, and hence higher effective normal stresses, resulting from a decrease in internal fluid production at temperatures beyond 150°C where smectite is fully dehydrated (Marone and Saffer, 2007; Moore and Saffer, 2001). Again, however, this presupposes velocity-weakening properties of the fault zone material.

1.2.2 The down-dip seismogenic limit

In contrast to the up-dip limit, the down-dip seismogenic limit at ~350°C is widely believed to be determined by the transition from brittle to ductile behaviour with increasing temperature (Hyndman and Wang, 1993; Hyndman et al., 1997; Marone and Saffer, 2007; Peacock and Hyndman, 1999; Scholz, 1998). This view is based on friction experiments performed on wet granite gouge, which show velocity-weakening behaviour at ~100-350°C but velocity-strengthening above this temperature (Blanpied et al., 1991; 1995; 1998). However, in some subduction zones, namely those that are relatively cold or are located beneath a thin oceanic crust, the fore-arc mantle wedge is reached at shallower depths than the 350°C isotherm and nucleation of earthquakes ceases at correspondingly shallower levels. This has been explained by the presence of weak, aseismically deforming, serpentinite in the mantle wedge (e.g. Hyndman and Peacock, 2003; Hyndman et al., 1997;

Peacock and Hyndman, 1999). In such situations, silica metasomatism may also lead to the formation of talc from serpentinite (antigorite), further weakening and stabilizing the plate boundary (Hirauchi et al., 2012; Moore and Lockner, 2011).

1.2.3 Slow Slip Events

Although earthquake nucleation is confined to the seismogenic zone of subduction megathrusts, it has been discovered in the last ~10 years that non-destructive, so-called Slow Slip Events (SSEs; e.g. Peng and Gomberg, 2010; Schwartz and Rokosky, 2007), sometimes accompanied by low-frequency tremor (Episodic Tremor and Slip, ETS; Rogers and Dragert, 2003), can nucleate in the aseismic regions of subduction zone megathrusts. Such SSEs mainly occur at or just beyond the lower limit of the seismogenic zone (~30 km depth; Mitsui and Hirahara, 2006), as seen for example in the Cascadia (northwestern US; Dragert et al., 2001; Miller et al., 2002) and southwestern Japan subduction zones (e.g. Obara et al., 2004). However, SSEs have also been observed within the up-dip aseismic zone (e.g. Ito and Obara, 2006). Like earthquakes, SSEs are a demonstration of velocity-weakening slip, but at subseismic velocities ($\sim 10^{-9}$ - 10^{-7} m/s; Iio et al., 2002; Liu and Rice, 2005), just approaching the criterion for instability (e.g. Ader et al., 2012; Liu and Rice, 2005). In SSEs, the duration of slip is much longer and the radiated seismic energy is much less than for earthquakes, rendering these events aseismic (Ide et al., 2007). A growing body of evidence suggests that SSEs are possible precursors to major subduction zone earthquakes (Kanamori and Cipar, 1974; Kato et al., 2012; Linde and Sacks, 2002; Linde et al., 1988; Mogi, 1984). Understanding the mechanism behind these events is therefore of fundamental importance for megathrust hazard evaluation (e.g. Kato et al., 2012). An important observation in this respect is that available seismological data suggest that SSEs correlate with regions characterized by overpressurized pore fluids (e.g. Kato et al., 2010; Kodaira et al., 2004). These high pore pressures will result in low effective normal stresses, yielding conditionally stable behaviour (Kodaira et al., 2004; see also Section 1.4).

1.2.4 Role of fault rock friction

In the case of both conventional subduction zone earthquakes and SSEs, it is clear that the mechanical properties of the fault rocks hosting slip must play a key role. Early ideas that earthquakes are caused by brittle failure of strong rocks have been replaced in recent decades by the view that these events occur by frictional movement along the pre-existing, presumably more or less cohesionless fault or plate interface (Scholz, 1998). Accordingly, the frictional properties of the materials present at the interface, and especially the velocity dependence thereof, are believed to be the main controls on seismic versus aseismic and SSE behaviour (e.g. Ader et al., 2012; Scholz, 1998). No theory yet exists that enables such properties to be predicted from first principles. Presently, data on these properties can, therefore, only be derived from friction experiments.

1.3 Experimental studies addressing the frictional behaviour of megathrust gouges

1.3.1 Low temperature studies

The need for rock friction data for understanding seismogenesis has led to numerous studies of the frictional behaviour of (simulated) subduction megathrust fault gouges at sub-seismic velocities (e.g. Ikari and Saffer, 2011; Ikari et al., 2009b; Kopf and Brown, 2003; Saffer and Marone, 2003). Mainly because of the difficulty of conducting large-strain

shear experiments at high P - T , these have focused on shallow megathrust behaviour, using either natural gouges obtained from (Integrated) Ocean Drilling Programs (e.g. IODP NanTroSEIZE; Ikari and Saffer, 2011; Ikari et al., 2009a; ODP Legs 110, 131, 156 and 190 Kopf and Brown, 2003) or simulated smectite and/or illite-rich gouges. A prime objective of studies performed at low sliding velocities, i.e. those most relevant for earthquake nucleation, has been to test the smectite-to-illite hypothesis for the onset of unstable behaviour at the up-dip seismogenic limit. In line with the original hypothesis, as put forward by Vrolijk (1990), smectite-rich gouges have been shown to be weaker than illite-rich gouges (e.g. Brown et al., 2003; Ikari et al., 2009b; Kopf and Brown, 2003; Saffer and Marone, 2003). As already indicated, however, unstable behaviour is not dictated by the absolute strength of a fault, but rather depends on changes in strength as a function of velocity (e.g. Marone and Saffer, 2007; Scholz, 1998), though these may be related (Ikari et al., 2011). Specifically, nucleation of earthquakes, and SSEs, requires velocity-weakening or, in the case of SSEs, at least velocity-neutral slip behaviour (e.g. Ader et al., 2012). For the transformation of smectite to illite to explain the onset of seismic behaviour, smectite and illite-rich gouges must show velocity-strengthening and velocity-weakening behaviour, respectively, under in-situ conditions (cf. Marone and Saffer, 2007).

Natural, smectite-rich subduction megathrust fault gouges have been found to be generally velocity-strengthening (e.g. Ikari and Saffer, 2011; Ikari et al., 2009a; Kopf and Brown, 2003) when deformed experimentally, under water-saturated conditions, at low (effective) normal stresses (several tens of MPa) and room temperature. Similarly, simulated smectite-rich fault gouges have been found to be velocity-strengthening when water-saturated or in equilibrium with room humidity (e.g. Ikari et al., 2009b; Logan and Rauenzahn, 1987; Tembe et al., 2010), except at low (effective) normal stresses (< 40 MPa) and sliding velocities (< 20 $\mu\text{m/s}$), under which conditions velocity-weakening behaviour has been observed (Ikari et al., 2007; Saffer et al., 2001; Saffer and Marone, 2003). Dry simulated smectite gouges also show velocity-weakening (Ikari et al., 2007). By contrast, previous studies addressing illite-rich gouges report only velocity-strengthening behaviour for the room temperature conditions investigated (Brown et al., 2003; Ikari et al., 2009b; Morrow et al., 1992; Saffer and Marone, 2003; Tembe et al., 2010). Moreover, Saffer et al. (2012) recently found that intact gouge wafers sampled from Nankai Trough core material, and representing different stages of the smectite-to-illite transition, consistently showed velocity-strengthening behaviour. This suggests that neither illitization nor accompanying lithification or fabric development can explain the onset of seismogenesis at the up-dip seismogenic limit (Saffer et al., 2012). Taken together, these results for illite-rich gouge suggest that the smectite-to-illite hypothesis should be rejected as an explanation for the onset of seismogenesis on subduction megathrusts. On the other hand, very few data exist pertaining to the in-situ pressure and temperature conditions that actually exist at the up-dip seismogenic limit (100-200°C, ~ 0 -260 MPa effective normal stress, ~ 50 -400 MPa pore fluid pressure).

1.3.2 Experiments at in-situ P - T conditions

The effects of varying experimental conditions on the frictional properties of (simulated) subduction megathrust gouges have been investigated only to a limited extent and have only partly explored the P - T conditions expected along the seismogenic portions of subduction megathrusts. Strikingly, experimental studies have not yet systematically

addressed the effect of temperature on the frictional properties of megathrust-derived or megathrust composition fault rocks, despite the importance of temperature suggested by the temperature-dependent location of the seismogenic zone inferred for natural subduction zones (e.g. Hyndman et al., 1997; Fig. 1.1). An effect of temperature on the frictional behaviour of megathrust fault gouges is, nonetheless, suggested by the temperature dependence of frictional behaviour observed for other gouges. Notably, for illite-smectite-quartz gouge sampled from the San Andreas Fault, Tembe et al. (2009) reported velocity-weakening behaviour at temperatures between 266°C and 283°C, versus velocity strengthening above and below this range. Though the separate effects of smectite and illite on the frictional stability were not determined, the results do suggest an important influence of temperature on the slip stability of megathrust gouges. Similar, temperature-dependent slip stability regimes have been reported for wet quartz (Chester and Higgs, 1992; cf. Kanagawa et al., 2000; cf. Niemeijer et al., 2008), granite (Blanpied et al., 1991; 1995; 1998), and gabbro gouges (He et al., 2007). These materials are characterized by velocity-weakening behaviour at 300°C, 100-350°C and 170°C-310°C respectively, with velocity-strengthening occurring at lower and higher temperatures. In addition, Moore et al. (1986a; 1986b; 1989) reported the occurrence of stick-slip events in saw-cut experiments performed at constant velocity on simulated illite-rich gouge at temperatures of 400°C and 600°C, but not at 200°C, suggesting the potential for velocity-weakening behaviour at elevated temperatures. Similar effects of temperature on stick-slip have been reported by Van Diggelen et al. (2010) and Mariani et al. (2006) in experiments on muscovite. However, to properly test the smectite-to-illite hypothesis for the onset of seismogenesis at the up-dip seismogenic limit, a more systematic approach is needed, involving friction experiments on illite-rich gouge in which the velocity dependence is quantitatively determined at realistic pressures and temperatures.

Alongside temperature, the effective normal stress, a crucial factor controlling fault friction, also varies along megathrusts with depth. This is due to the depth-dependent increase in lithostatic overburden (Fig. 1.1a) as well as variations in pore fluid pressure controlled by fault zone dehydration, compaction, damage evolution and permeability. Lithostatic pressure is easily estimated. However, the manner in which the pore fluid pressure and hence effective normal stress vary and evolve along a megathrust is largely unknown at present (Saffer and Tobin, 2011). Fluid pressures must increase with depth in shallow accretionary prisms due to compaction processes and dehydration reactions (Moore and Vrolijk, 1992; Saffer and Tobin, 2011), similar to those occurring in pelitic sedimentary basins. Comparison with the high pore fluid pressure measured in such basins (e.g. Hart et al., 1995) implies significant overpressuring (beyond hydrostatic values) in accretionary prism settings, where loading rates are generally much faster (Moore and Vrolijk, 1992; Saffer and Tobin, 2011). Indeed, measurements in shallow ODP boreholes do point to fluid overpressuring at only 400-500 m depth below sea floor (Becker et al., 1997; Bekins and Screatton, 2007; Foucher et al., 1997). In addition, the observation of ultra-slow shear wave velocities, an anomalously high Poisson's ratio and a high ratio of compressional to shear wave velocity above and below the seismogenic portion of subduction megathrusts (namely in regions hosting SSEs and tremor) are also believed to indicate the presence of highly overpressurized pore fluids (Audet et al., 2009; Kato et al., 2010; Kodaira et al., 2004; Shelly et al., 2006; Song et al., 2009). On the basis of such geophysical observations, Saffer

and Tobin (2011) suggested near-lithostatic pore fluid pressures in the transition zones at the limits of the seismogenic zone. Fluid pressure in the seismogenic zone itself is believed to lie between hydrostatic and lithostatic values (Saffer and Tobin, 2011), due to drainage of the active fault system, or reflecting pore pressure cycling tied to the seismic cycle (cf. Sibson, 1981).

The above all suggests a complicated depth profile for the pore fluid pressure and effective normal stress along subduction megathrusts, with rapid changes around the limits of the seismogenic zone. Several experimental studies directed at understanding megathrust friction and seismogenesis have addressed a range of pore fluid pressures and/or effective normal stresses approaching the relevant in-situ ranges (e.g. Moore et al., 1986a; 1986b; 1989; Morrow et al., 1992; Saffer and Marone, 2003). To date, only Moore et al. (1986a; 1986b; 1989) have addressed the relevant temperatures simultaneously. However, the velocity dependence of friction was not determined. In addition, almost nothing is known about the effects of (very) low effective normal stresses – currently believed to be associated with SSE generation – on the frictional properties of megathrust gouges at in-situ temperatures.

Finally, it is important to consider the slip velocities associated with motion on megathrust faults. These range from (plate) velocities of around 10^{-9} m/s to 10^{-7} m/s during earthquake and SSE nucleation (Iio et al., 2002; Liu and Rice, 2005), to values as high as 1 to 3 m/s associated with coseismic slip (e.g. Cowan, 1999; Di Toro et al., 2006). The experimental studies discussed above have used sliding velocities mainly in the range of 0.01–300 $\mu\text{m/s}$, thus approaching velocities relevant for nucleation to within an order of magnitude. Such displacement rates are typical of the range accessible using high *P-T* rock deformation equipment. Recently, spectacular developments in rotary shear machine design, notably in Japan by Shimamoto and co-workers, have made it possible to address coseismic slip velocities as well (e.g. Di Toro et al., 2010; Tanikawa et al., 2012; Tsutsumi et al., 2011; Ujiie and Tsutsumi, 2010), though attaining normal stresses >5 MPa and controlling pore fluid pressure remain problematic in such machines. Nonetheless, these developments are crucial for quantifying co-seismic frictional behaviour and for modelling rupture propagation.

1.3.3 Fault gouge compositions used in previous lab studies

Equally important to the use of in-situ or near in-situ temperatures, pore fluid pressures, effective normal stresses and slip velocities in lab friction experiments, is the use of materials with similar compositions to those inferred for the gouges present within subduction zone megathrusts. Implicit to the use of (meta)pelitic (phyllosilicate-quartz) fault gouges in the experimental studies discussed so far is the assumption that megathrust behaviour is localized in the subducted, (meta)pelitic sediments (e.g. Marone and Saffer, 2007; Shipboard Scientific Party, 2001; Underwood et al., 1993) at the interface between the subducting and overlying plate (e.g. Marone and Saffer, 2007; Moore, 1989; Saffer et al., 2012). This is frequently the case, though quartz-rich sandstones and cherts are commonly present (Kameda et al., 2012; Underwood, 2007). Seamount-borne carbonates are also sometimes present in the subducted sediment supply (e.g. at Costa Rica; Spinelli and Underwood, 2004).

Focusing on typical quartz-phyllosilicate dominated metapelites, with increasing depth/

temperature, these sediments undergo progressive diagenesis (e.g. Kameda et al., 2011), whereby smectite transforms into illite at ~120-150°C (Pytte and Reynolds, 1988). This is followed by the replacement of illite by muscovite at ~200-300°C (Hunziker, 1986; Merriman and Frey, 1999; Van de Kamp, 2008), as low grade metamorphism sets in approximately midway within the seismogenic zone. While smectite and illite, often mixed with quartz, have been the subject of many frictional studies addressing subduction megathrust behaviour at room temperature, the frictional properties of muscovite-quartz mixtures, in particular the velocity dependence of friction, have not been investigated in relation to subduction zone seismogenesis (though some work has been done on muscovite in relation to continental fault zones; Mariani et al., 2006; Van Diggelen et al., 2010). Such data have clear relevance to megathrust behaviour not only in the deeper portions of the seismogenic zone but also beyond the down-dip limit, where SSEs are important.

In addition, experimental studies have not yet isolated the roles of the phyllosilicate and quartz components in determining the frictional behaviour of (meta)pelitic fault gouges. An understanding of the separate effects of the phyllosilicate and quartz phases could yield valuable insight into the mechanisms controlling the deformation of gouge mixtures. Moreover, it is highly likely that the phyllosilicate/quartz ratio plays a major role in controlling the frictional response, leading perhaps even to velocity-weakening in certain compositional ranges while the pure end member minerals, or other compositional ratios, show velocity-strengthening. Evidence for such effects has been clearly demonstrated in earlier rock-analogue experiments on phyllosilicate-halite gouges (Bos et al., 2000; Niemeijer and Spiers, 2006), but the effects of phyllosilicate/quartz ratio have not yet been investigated for megathrust fault gouges. As the sediment input into subduction zones often varies laterally due to the regional source difference, data on the effects of gouge composition on frictional behaviour may also prove relevant for assessing regional variability in seismic hazard (e.g. Underwood, 2007).

As indicated above, some megathrust faults may contain major amounts of other minerals besides phyllosilicates and quartz. Chalks entering the Costa Rica subduction zone are a good example (e.g. Spinelli and Underwood, 2004). An improved understanding of subduction zone seismogenesis, in general, therefore requires determination of the frictional properties of carbonate-rich sediments under (approximate) in-situ subduction zone conditions too. A recent preliminary study by Ikari et al. (pers. comm.) suggests a greater potential for unstable slip when carbonate is present (see also Verberne et al., 2010). Furthermore, field observations suggest that basaltic slices, derived from the top of the subducting plate, may be involved in megathrust faulting (e.g. Ikesawa et al., 2005; Kimura and Ludden, 1995; Meneghini and Moore, 2007). This suggests that under certain conditions the frictional strength of oceanic basalts is less than that of the overlying sediments, resulting in a stepdown of the décollement into the basaltic material at the top of the subducting slab. Clearly, then, data on the frictional properties and stability of basalt(-rich) fault gouges under in-situ megathrust conditions are required to complement those on accretionary (metapelitic or carbonate-rich) sediments.

1.4 Modelling fault friction and seismogenesis

Alongside experimental work on fault rock friction behaviour, essential to the improvement

of subduction zone earthquake and tsunami hazard assessment is the development of numerical models that allow simulation and ideally the prediction of megathrust earthquake and SSE rupture nucleation and propagation. Simulations of this type have already been accomplished in many modelling studies (e.g. Hori et al., 2004; Kato and Yoshida, 2011; Liu and Rice, 2005; 2007; 2009; Matsuzawa et al., 2010; Perfettini and Ampuero, 2008; Shibazaki et al., 2010; Shibazaki and Iio, 2003; Shibazaki et al., 2011; Shibazaki and Shimamoto, 2007). The models employed rely on input describing the depth-dependent frictional properties of the fault zone/rock. In the absence of data on metapelitic gouges under in-situ conditions, the frictional properties of dry halite (Shimamoto, 1986), wet granite (Blanpied et al., 1991; 1995; 1998) and gabbro gouges (He et al., 2007) gouges have been widely used for this. Clearly, these materials are likely to be poorly representative of the metapelitic fault rocks expected in subduction megathrusts, highlighting once again the importance of obtaining data on the frictional properties of realistic subduction zone gouges under realistic conditions.

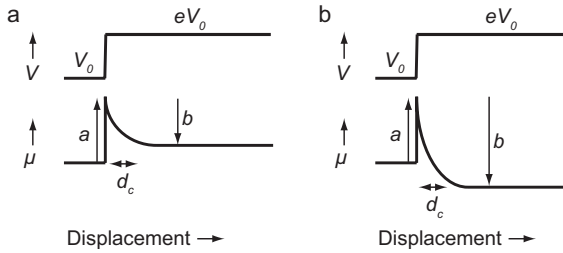


Figure 1.2 Schematic representation of the frictional response to an imposed step in the sliding velocity and interpretation in terms of the RSF framework, for velocity-strengthening friction (a) and velocity-weakening friction (b). Drawn for a velocity step from V_0 to $V = eV_0$.

Following up on the slip stability concepts introduced in Section 1.2, the principal frictional property required in modelling studies of subduction zone seismogenesis is the velocity dependence of friction. This is widely described and interpreted within the framework of the rate and state friction (RSF) model, originally proposed by Dieterich (1978; 1979) and Ruina (1983). In the RSF approach to modelling fault slip, the coefficient of friction is written as a function of slip velocity using the relation

$$\mu = \mu_0 + a \ln\left(\frac{V}{V_0}\right) + b \ln\left(\frac{V_0 \theta}{d_c}\right) \quad (1.1)$$

where μ is the instantaneous coefficient of friction (the ratio of the shear stress τ to the effective normal stress σ_n^{eff}), μ_0 is a reference coefficient of friction at a reference velocity V_0 , V is the instantaneous sliding velocity, θ is an internal state variable, a determines the absolute magnitude of the instantaneous change in μ upon a given step change in sliding velocity from a reference value V_0 to a new value V and where b reflects the magnitude of the change in μ during the subsequent evolution to a new steady state value over a critical sliding distance d_c (Fig. 1.2). For changes in steady state friction coefficient ($\Delta\mu_{ss}$) resulting from a stepwise change in slip velocity, Eq. (1.1) yields:

$$(a - b) = \frac{\Delta\mu_{ss}}{\Delta \ln V} \quad (1.2)$$

(e.g. Marone, 1998; Paterson and Wong, 2005; Scholz, 2002). A positive ($a-b$) value indicates an increase in friction coefficient with increasing velocity or velocity strengthening slip behaviour, which is inherently stable (e.g. Scholz, 1998). A negative ($a-b$) value means that the behaviour is velocity weakening, which is potentially unstable (e.g. Scholz, 1998).

Whether the behaviour is unstable or not in the velocity-weakening field, depends on the elastic stiffness of the material surrounding the slipping portion of a fault, compared to a critical stiffness value. This critical value is defined in terms of the spring stiffness in an equivalent spring-slider model for the fault (Ruina, 1983), and is given:

$$K_c = \frac{-(a-b)\sigma_n^{eff}}{d_c} \quad (1.3)$$

Earthquake nucleation requires the elastic stiffness (K) of the material surrounding the slip zone to be less than this critical value, alongside a negative value for ($a-b$). The material stiffness K is inversely proportional to the length of the slip zone, so that dynamically unstable slip ($K < K_c$) is favoured for large slip zones (e.g. Segall et al., 2010; Thomas et al., 2012). When ($a-b$) < 0 and $K > K_c$, slip is conditionally stable, becoming unstable only for a large enough increase in driving velocity. Non-destructive SSEs observed up- and down-dip of the seismogenic zone are believed to be an expression of conditional stability, with K being close to (just larger than) K_c (e.g. Liu and Rice, 2005; Ruina, 1983; Scholz, 1998; Segall et al., 2010), resulting in self-sustaining oscillatory motion. A higher pore fluid pressure and hence lower effective normal stress will promote such behaviour, as the slip zones involved in SSEs are typically large (several tens of km; e.g. Segall et al., 2010). Aside from the explanation of SSEs in this framework, another way to generate these events would be by slip weakening in a material that exhibits nearly velocity-neutral frictional behaviour. However, experimental data to underpin these possible mechanisms of SSE nucleation are very scarce, especially at the very low effective normal stresses believed to be relevant.

Despite the wide application of RSF laws, they are empirical, phenomenological equations without a microphysical basis, although physical interpretations of the RSF friction parameters have been suggested (Baumberger et al., 1999; Dieterich, 1978; Dieterich, 1979; Nakatani, 2001; Rice et al., 2001). In order to more reliably apply experimental results to natural fault zones, and notably to extrapolate lab data beyond laboratory P , T , pore fluid pressure and velocity conditions, an understanding of the microphysical mechanisms governing the frictional behaviour is required.

A step towards a microphysical basis for fault rock frictional and frictional-viscous behaviour was provided by Bos et al. (2000) and Bos and Spiers (2001; 2002) and later by Niemeijer and Spiers (2005; 2006; 2007), who formulated a microphysical model to explain the velocity dependence of friction of phyllosilicate-halite mixtures (simulated fault gouge) undergoing shear deformation under conditions favouring thermally activated deformation of the halite clasts by pressure solution plus intergranular slip on the intervening phyllosilicates. As opposed to employing an RSF description of frictional strength, Bos and Spiers (2001) and Niemeijer and Spiers (2005; 2007) formulated a model allowing gouge shear strength to be expressed as a function of effective normal stress, shear strain rate, temperature

and microstructural parameters. The basic idea of this model is that changes in friction coefficient and (a - b) with velocity and temperature are brought about by changes in the relative importance of deformation of the clast phase, by a thermally activated mechanism (pressure solution), versus athermal granular flow of the mixture accompanied by dilatation. Although the fit of this model to the experiments on analogue (halite-phylllosilicate) gouges was found to be good, the correspondence of some elements of the model with natural (megathrust) fault gouges may be questioned. Specifically, the phylllosilicate phase was assumed to be only a minor gouge-constituent exhibiting velocity-neutral behaviour, while natural fault gouges are usually dominated by phylllosilicates, which often show velocity-strengthening behaviour at least at room temperature (Ikari et al., 2011). In addition, quartz clasts expected to be present in megathrust gouges may not deform by pressure solution as readily as halite, so that other thermally activated mechanisms should be considered as well.

1.5 Aims of this thesis

From the above considerations, it is clear that improved modelling of subduction zone seismogenesis, and application of such work to advance seismic hazard assessment, requires (i) data on the rheological behaviour, in particular the velocity dependence of the frictional strength, of realistic (smectite, illite or muscovite plus quartz) megathrust fault gouges, under realistic megathrust P - T conditions spanning the seismogenic zone, and (ii) an understanding of the underlying microphysical processes and governing constitutive equations. Against this background, the aims of the current study are as follows:

1. To explore the potentially destabilising effects of effective normal stress (cf. effective pressure) on the frictional behaviour and velocity dependence of frictional strength exhibited by shallow megathrust fault gouges, where smectites are the main phylllosilicate phase, and by simulated illite-rich gouges, representing greater depths.
2. To determine experimentally the effect of temperature on the frictional properties of simulated illite-rich subduction megathrust gouges, at fixed effective normal stresses and pore fluid pressures, lying in the range thought to characterise the illite-bearing portions of the megathrust seismogenic zone (e.g. normal stresses of 130-800MPa, pore fluid pressures of 50-800MPa).
3. To investigate systematically the effects of effective normal stress, pore fluid pressure, sliding velocity and quartz content, at in-situ temperatures, on the frictional properties and velocity dependence of friction of illite-dominated megathrust gouges.
4. To investigate experimentally the effect of phylllosilicate type and the role of quartz in determining the frictional properties of quartz-phylllosilicate megathrust fault gouges, focusing on muscovite-quartz compositions expected in the deeper portions of megathrust seismogenic zones and at depths exhibiting SSEs.
5. To develop a microphysical model for the frictional behaviour of fault gouges consisting of quartz clasts embedded in a phylllosilicate matrix, to test the model against experimentally derived results for simulated megathrust fault gouges, and to apply it to predict the frictional behaviour of megathrust gouges at natural slip nucleation rates.

These topics are tackled sequentially in Chapters 2-6. Finally, in Chapter 7, general conclusions are drawn and suggestions made for future work.

Chapter 2

Frictional properties of megathrust fault gouges at low sliding velocities: new data on effects of normal stress and temperature

Sabine A.M. den Hartog, Colin J. Peach, D.A. Matthijs de Winter^a, Christopher J. Spiers and Toshihiko Shimamoto^b

Journal of Structural Geology 38, 156-171, 2012

^aBiomolecular Imaging, Department of Biology, Faculty of Science, Utrecht University, Utrecht, The Netherlands.

^bDepartment of Earth and Planetary Systems Science, Graduate School of Science, Hiroshima University, Higashi-Hiroshima 739-8526, Japan; present address: State Key Laboratory of Earthquake Dynamics, Institute of Geology, China Earthquake Administration, Beijing 100029, China.

Abstract

Friction data used in modelling studies of subduction zone seismogenesis are often poorly representative of in-situ conditions. We investigated the influence of in-situ effective stresses and temperatures on the frictional properties of (simulated) fault gouges, prepared either from Nankai ODP material or illite shale, at sliding velocities approaching those relevant for earthquake nucleation and SSEs. Biaxial (double direct shear) experiments were performed at room temperature, normal stresses of 5-30 MPa, and sliding velocities of 0.16-18 $\mu\text{m/s}$. All materials exhibited velocity strengthening under these conditions, along with an increase in the friction coefficient and slip hardening rate with increasing normal stress. Illite gouge showed increased velocity strengthening towards higher normal stresses. The effect of temperature was investigated by means of ring shear experiments on illite gouge at 200-300°C, an effective normal stress of 170 MPa, a pore fluid pressure of 100 MPa and sliding velocities of 1-100 $\mu\text{m/s}$. These experiments showed a transition from velocity strengthening to velocity weakening at $\sim 250^\circ\text{C}$. Our results provide a possible explanation for the updip seismogenic limit within subduction zone megathrusts and imply an enhanced tendency for earthquake nucleation and SSEs at low effective normal stresses.

2.1 Introduction

Subduction megathrust earthquakes and associated tsunamis present some of the most destructive natural hazards on the planet. This has most recently been demonstrated by the M_w 9.0 Tohoku earthquake (Japan) and the related tsunami of 11 March 2011 (e.g. Ide et al., 2011; Ozawa et al., 2011; Simons et al., 2011). Other examples of major megathrust earthquakes include the Chile 1960 M_w 9.5 event (e.g. Bilek, 2010; Plafker and Savage, 1970), the Alaska 1964 M_w 9.2 event (e.g. Plafker, 1965; Suito and Freymueller, 2009), and the Sumatra 2004 M_w 9.1 event (e.g. Lay et al., 2005). Besides megathrust earthquakes, it is now recognized that many subduction zones around the world also release strain energy by non-destructive slow slip events (SSEs; e.g. Peng and Gomberg, 2010; Schwartz and Rokosky, 2007), sometimes accompanied by tremor (episodic tremor and slip, ETS; Rogers and Dragert, 2003). Examples of subduction zones in which SSEs have been observed include those of southwestern Japan (Hirose et al., 1999; Obara et al., 2004), Cascadia (northwestern US; Dragert et al., 2001; Miller et al., 2002), southern Alaska (Ohta et al., 2006), Mexico (Lowry et al., 2001), Chile (Pritchard and Simons, 2006), New Zealand (Douglas et al., 2005) and Costa Rica (Davis et al., 2011). In the hope of improving seismic and tsunami hazard evaluation, there is presently intense interest (i) in megathrust earthquake nucleation processes (e.g. Faulkner et al., 2011; Kaneko and Lapusta, 2008) and (ii) in SSEs as possible precursors to major subduction zone earthquakes (Dragert et al., 2001; Houston and Vidale, 2007; Linde and Sacks, 2002; Mazzotti and Adams, 2004; Rogers and Dragert, 2003; Shibazaki et al., 2010).

In subduction zone megathrust systems, the transition from aseismic slip at shallow depths to unstable, seismogenic slip typically occurs at depths of 5–15 km (Hyndman et al., 1997). The onset of seismogenesis at 5–15 km has often been attributed to the dehydration of the hydrous clay mineral smectite, present at shallow levels in accretionary sediments, to form anhydrous illite at temperatures above 120–150°C (Hyndman et al., 1997; Marone and Saffer, 2007; Vrolijk, 1990). However, experimental studies of simulated illite-rich fault gouges show only stable (“velocity strengthening”) sliding behaviour, at least under the room temperature and room humidity conditions investigated to date (Saffer and Marone, 2003). No experiments have yet been published that address the velocity dependent behaviour, at in-situ megathrust conditions, of the illite- or muscovite-rich (smectite-free) gouges expected to dominate in (meta)pelitic material at seismogenic depths and temperatures (Merriman and Frey, 1999), i.e. at ~150 to 350°C (Hyndman et al., 1997). Modelling studies (Hori et al., 2004; Liu and Rice, 2005; Matsuzawa et al., 2010; Shibazaki and Shimamoto, 2007) so far performed on earthquake nucleation within subduction zone megathrusts have therefore been forced to assume velocity-dependent frictional properties similar to those seen in other (analogue) materials, namely dry halite (Shimamoto, 1986) or wet granite (Blanpied et al., 1998).

In contrast to conventional earthquakes, SSEs on subduction megathrusts mainly occur at or just beyond the lower limit of the seismogenic zone (~30 km depth; Mitsui and Hirahara, 2006), but have also been observed at shallower depths (~15–20 km; McCaffrey et al., 2008; Outerbridge et al., 2010; Sagiya, 2004). Regardless of depth range, SSEs are a demonstration of unstable slip at subseismic velocities ($\sim 10^{-9}$ – 10^{-7} m/s; Iio et al., 2002; Liu and Rice, 2005). Available seismological data suggest that SSEs correlate with regions characterized by

overpressurized pore fluids (e.g. Kato et al., 2010; Kodaira et al., 2004), resulting in low effective normal stresses, which may promote unstable slip (Peng and Gomberg, 2010). However, as in the case of conventional earthquakes, the frictional data on dry halite (Shimamoto, 1986), wet granite (Blanpied et al., 1998) and wet gabbro gouges (He et al., 2007) used for modelling SSEs to date (e.g. Liu and Rice, 2009; Shibazaki et al., 2010), are poorly representative of the fault rocks expected in-situ, and of the conditions.

In this paper, we report experiments designed to provide additional data on the frictional behaviour of (simulated) megathrust fault gouges under water-wet or saturated conditions relevant to nucleation of conventional megathrust earthquakes in particular, but also to some extent to SSEs. We performed two sets of experiments:

- (i) Biaxial experiments at low (effective) normal stresses (5-30 MPa) and room temperature. For these experiments, we used natural smectite-rich samples, obtained from the Nankai Trough during Ocean Drilling Program (ODP) Leg 190, which are expected to control frictional behaviour at relatively low temperatures (shallow depths). For comparison, we also used simulated illite-rich gouge material prepared from crushed Rochester Shale (Folk, 1962), since this material is more appropriate for deeper levels and has been used in previous room temperature experiments aimed at addressing the seismogenic zone (e.g. Brown et al., 2003; Saffer and Marone, 2003).
- (ii) Ring shear experiments at elevated temperatures (200-300°C) and in-situ pressures corresponding to ~10 km depth (i.e. an effective normal stress of 170 MPa and pore fluid pressure of 100 MPa). We used the illite gouge for these experiments. This is considered representative for subducted accretionary sediments at temperatures of ~120-200°C (Merriman and Frey, 1999) and probably up to ~300°C, where illite, sometimes viewed as a proto or K-deficient muscovite (Rieder et al., 1998), slowly transforms to muscovite proper (Merriman and Frey, 1999).

In both sets of experiments, our focus is on low sliding velocities, approaching the upper end of the range relevant for earthquake nucleation (and SSEs) in subduction zones ($\sim 10^{-7}$ m/s). The use of widely different temperatures and (effective) normal stresses accessible in the two types of experiment provides a means of assessing the influence of these variables on frictional behaviour, notably of illite gouge. We compare our results with previous data and with the frictional properties used in modelling studies of subduction zone seismogenesis, and we assess the implications.

2.2 Methods

2.2.1 Starting material

We used material from two sources: clays derived from the Muroto Transect across the Nankai Trough, cored during ODP Leg 190 (Shipboard Scientific Party, 2001a, b) plus simulated illite-rich gouge consisting of crushed Rochester Shale (Folk, 1962). The ODP material was recovered from Site 1174, Hole B (Fig. 2.1), which cuts the megathrust décollement in Cores 070R-073R (see Shipboard Scientific Party, 2001a; b for exact locations in the core and lithological sequence). Three batches were used, of which two were derived from within the décollement zone (ODP-IN-A and ODP-IN-B) and one from ~2.6 m above the décollement zone (ODP-OUT). ODP-IN-A was taken from a depth position of 17-31 cm in Core 073R, Section 01W (i.e. 831.97-832.11 meter below seafloor, mbsf), and ODP-IN-B from 39-50 cm depth in the same core section (832.19-832.30 mbsf). ODP-OUT was derived

from Core 070R, Section 02W, at 9-18 cm depth (804.89-804.98 mbsf). To prepare simulated gouges for our experiments, these materials were crushed in a mortar with ethanol, then dried at 40°C for several days, followed by dry crushing and sieved at $< 125 \mu\text{m}$. X-Ray Diffraction (XRD) analysis on the ODP material showed the presence of smectite, illite, chlorite, quartz, albite and minor kaolinite in all three batches. The clay content was estimated to be $> 90 \text{ wt}\%$ with the highest clay content being in the batch from above the décollement zone (ODP-OUT material). These results were in good agreement with those of Steurer and Underwood (2003), which revealed smectite ($\sim 46\%$), Illite ($\sim 31\%$), chlorite/kaolinite ($\sim 17\%$) and quartz ($\sim 6\%$).

The illite gouge was kindly provided by Chris Marone and Brett Carpenter of Penn State University, who crushed Rochester Shale and sieved it to a grain size of $< 106 \mu\text{m}$ (Ikari et al., 2009b). XRD analysis that we performed on the illite gouge showed it was composed of illite, quartz and chlorite. Saffer and Marone (2003) reported a similar composition for this material (59% illite, 23% quartz, 9% kaolinite/dickite and 4% plagioclase), but inferred the presence of plagioclase and of kaolinite/dickite instead of chlorite.

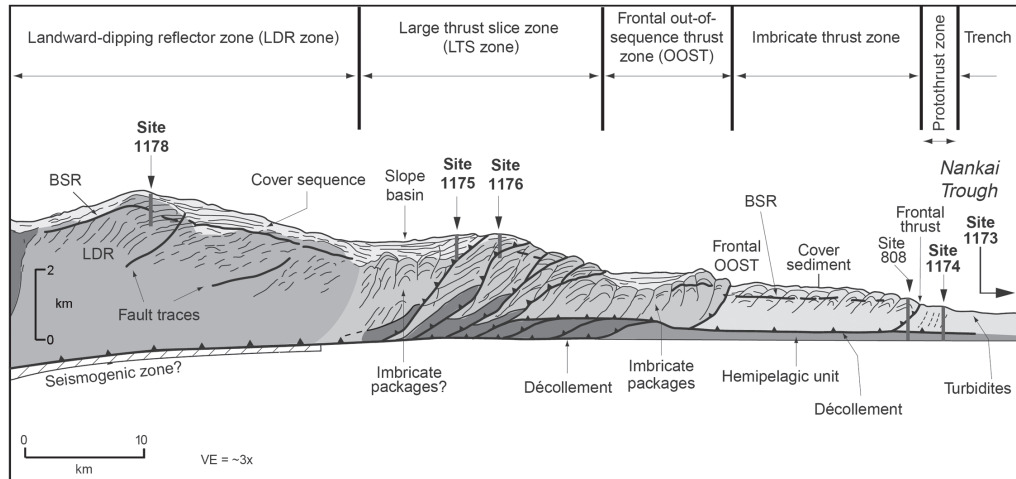


Figure 2.1 Schematic cross-section of the ODP Muroto Transect across the Nankai Trough, showing the locations of the Leg 190 drill sites. Our ODP samples are from Site 1174, which is located in the protothrust zone. Figure modified from Leg 190 Preliminary Report (Shipboard Scientific Party, 2000).

2.2.2 Experimental apparatus and procedures

Two types of experiment were performed, namely biaxial (double direct shear) and ring shear experiments. These allowed us to explore the effects of a low (effective) normal stress and high temperature, respectively, on the frictional properties of wet subduction zone fault gouges.

2.2.2.1 Biaxial experiments

Our biaxial experiments were performed using the double direct shear frictional testing machine located at Hiroshima University, using the same set-up and following similar procedures as Kawamoto and Shimamoto (1997, 1998) and Noda and Shimamoto (2009).

The sample assembly used involved two layers of gouge sandwiched between three gabbro forcing blocks (Fig. 2.2a), having dimensions of 40x40x70 mm and 20x40x50 mm (WxDxH) for the central and side blocks, respectively. This assembly allowed a maximum shear displacement of about 20 mm (Fig. 2.2a). The side blocks were always in full contact with the moving central block, resulting in a constant gouge surface area of $\sim 2000 \text{ mm}^2$. To inhibit slip localization at the gabbro-gouge boundary, the relevant surfaces of the gabbro blocks were roughened with #80 grade silicon carbide powder.

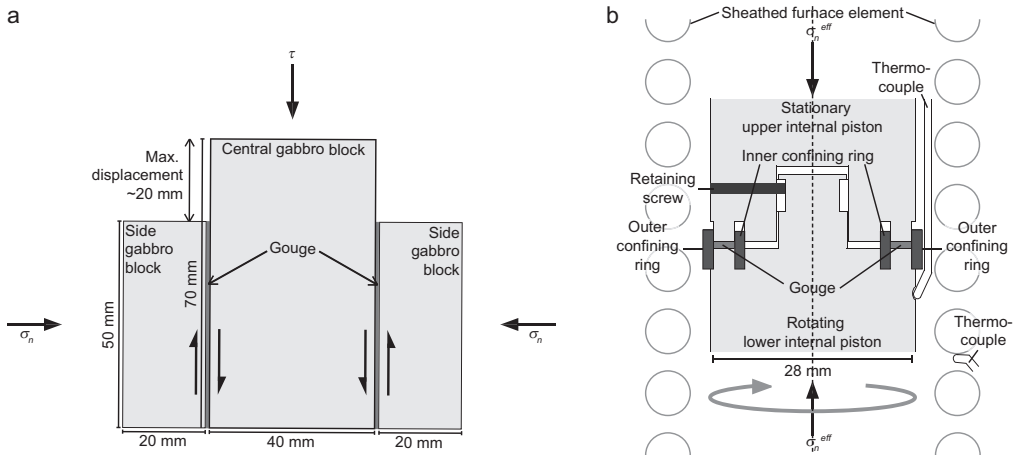


Figure 2.2 Schematic diagrams of samples assemblies used. $\sigma_n^{(eff)}$ = (effective) normal stress, τ = shear stress. (a) Sample assembly used in the biaxial testing machine at Hiroshima University. (b) Central portion of sample assembly and furnace used in the hydrothermal ring shear machine at Utrecht University (after Niemeijer et al., 2008). Note that the pore fluid surrounding the piston-sample assembly within the apparatus has access to the sample via the unsealed confining rings, retaining screw bore and a conduit to the centre of the annulus (not shown in the figure).

Gouge layers were prepared by evenly distributing 1.5 grams of lab-dry sample material onto the upturned side blocks. The forcing block plus gouge assembly was then taped together and pre-compacted in the biaxial loading frame in the horizontal direction for 30 minutes at $\sim 20 \text{ MPa}$ or $\sim 30 \text{ MPa}$ (BRS13) normal stress. This produced coherent gouge layers with a reproducible starting porosity. After pre-compaction, the assembly was removed from the loading frame, fixed in a G-clamp and placed in a tray containing $\sim 1\text{-}2 \text{ cm}$ of distilled water to wet the gouge by capillary action. After $\sim 5\text{-}24$ hours, the gouge was completely wet and the assembly was returned to the loading frame and subjected to a second phase of pre-compaction at $\sim 20 \text{ MPa}$ or $\sim 30 \text{ MPa}$ (BRS13) normal stress for 2 hours, yielding a gouge layer thickness of nominally $250 \mu\text{m}$. During this stage and subsequent friction testing, the gouge layers were kept wet by wrapping with loose, wet wadding.

The biaxial machine at Hiroshima is described in detail by Noda and Shimamoto (2009). In this machine, normal force and shear force are measured with accuracies of 0.05% of 200 kN and 500 kN, respectively. Vertical (shear) displacement is measured using an eddy current sensor with an absolute accuracy better than 0.1 mm.

The biaxial experiments were conducted at room temperature (14-16°C) and at applied (effective) normal stresses of 5, 10, 15 or 30 MPa. The pore fluid pressure could not be controlled and is assumed to be atmospheric, neglecting minor capillary pressure or dilation/compaction effects. The normal stress applied in these experiments is therefore by implication assumed equal to the effective normal stress. We will refer to it as such, or, simply 'normal stress' to avoid repetition. Both velocity stepping and constant velocity tests were performed. In the stepping tests, the sliding velocity was stepped between either 0.16, 1.6 and 16 $\mu\text{m/s}$ or 0.18, 1.8 and 18 $\mu\text{m/s}$. The constant velocity experiments were conducted at 1.8, 10 or 18 $\mu\text{m/s}$. The conditions during individual experiments are given in Table 2.1. Normal force, shear force and displacement data were logged using a 16 bit AD converter operating at a 1 Hz conversion rate.

2.2.2.2 Ring shear experiments

These were conducted using the hydrothermal ring shear apparatus at Utrecht University (Niemeijer et al., 2008; Van Diggelen et al., 2010). In this machine, a ring-shaped gouge sample with an inner diameter of 22 mm, an outer diameter of 28 mm, a width of 3 mm and a thickness of ~ 1 mm is used (Fig. 2.2b). To reduce loss of sample material during shearing, and to obtain a reproducible, relatively dense starting microstructure, we used a ring-shaped steel die to press 0.52 grams of evenly distributed illite gouge mixed with 0.04 grams of distilled water into a pre-formed ring, before emplacement into the machine. Pre-pressing was done using a 40 ton hydraulic press, loading for ~ 20 minutes at ~ 170 MPa normal stress. The cohesive sample of ~ 1 mm thickness obtained was then dried overnight at 50°C and the starting porosity (typically about 15%) determined. This was done using the final sample weight, dimensions and mineral composition and densities.

In the ring shear machine, gouge samples are sandwiched between the tips of two roughened René® 41 pistons (Fig. 2.2b). Inner and outer confining rings (Fig. 2.2b) of hardened Remanit® 1.4122 or René® 41 alloys keep the gouge sample in place. Before assembly, these rings were coated with either a graphite powder suspension or Molykote® spray to reduce wall friction and dried to remove volatiles at 50-175°C for 10-30 minutes. Runs with and without confining rings and using samples of known friction coefficient showed that the confining rings did not contribute significantly to the measured torque. To complete the sample assembly, we wrapped Teflon® tape around the outer confining ring and piston ends to inhibit infiltration of pore fluid from the water-filled apparatus into the sample before application of normal load, thus preventing sample liquefaction and loss by extrusion.

In the ring shear machine, the sample-piston assembly is located inside a pressure compensated, water-cooled, 300 MPa pressure vessel, which in turn is positioned in a servo-controlled Instron 1362 loading frame. The pressure vessel is filled with the pore fluid (distilled water), which can be pressurized up to ~ 300 MPa using a syringe pump. The fluid pressure is measured with a resolution of 0.005 MPa. In this pressure compensated vessel, effective normal stress is applied and held constant to within 0.2 MPa, independently of the pore pressure, using the Instron loading ram, and is measured externally by means of a 100 kN Instron load cell. The sample is heated using an internally mounted, 3 kW Inconel-sheathed furnace element and external Eurotherm controller. Temperatures up to

700°C are measured to within 1°C using two K-type thermocouples, located on the furnace element near the sample and just below the sample (Fig. 2.2b). The temperature gradient between the thermocouples indicates that the gradient over the sample is $\ll 2^\circ\text{C}$. Vertical displacement is measured externally with a resolution of 0.005 mm using a linear variable differential transformer (LVDT). A servo-controlled motor and gearbox system rotates the vessel and lower piston while the upper piston is prevented from rotating with respect to the Instron frame. This produces constant sliding velocities at the sample of $\sim 10\text{ nm/s}$ to 0.3 mm/s . The shear stress generated is measured externally, using a torque-gauge mounted in line with the upper piston (accuracy of 0.2 MPa). Shear displacements are measured with an accuracy of 0.001 mm using an external potentiometer, connected to the drive of the rotating pressure vessel.

In preparing each experiment, the sample-piston assembly was loaded into the pore-fluid-filled vessel, and the chosen effective normal stress was applied. The pore fluid pressure was then increased to $\sim 5\text{ MPa}$ and the furnace switched on, heating up the sample to the desired temperature in approximately 20 minutes and causing the pore fluid pressure to rise to a value of 90-100 MPa. The system was subsequently equilibrated for about 2 hours, the pore pressure trimmed and rotation initiated. Experiments were terminated by removing the torque and axial load, then switching off the furnace. Pore fluid pressure was maintained during cooling so as to prevent steam formation, and finally removed by venting.

The ring shear experiments were performed at an effective normal stress of 170 MPa, a pore fluid pressure of 100 MPa, sliding velocities stepped between 1, 10 and $100\text{ }\mu\text{m/s}$ and at temperatures of 200°C , 250°C and 300°C (Table 2.1). Shear and axial displacement, normal force, torque, pore fluid pressure and temperature were logged at either 1 or 4 Hz, using a 16 bit A/D converter.

2.2.3 Data processing

In both the biaxial and ring shear experiments, machine distortion effects were small compared to the large displacements imposed, so no corrections were applied for this. External torque measured in the ring shear tests was corrected for seal friction by performing friction calibration experiments on a Remanit® 1.4122 dummy piston set sandwiching either a single sheet of Teflon® or two layers of PEEK coated with graphite powder, at true experimental conditions.

For all experiments, the coefficient of friction μ was calculated as the ratio of the shear stress τ to the effective normal stress σ_n^{eff} . Cumulative error analysis showed μ -values to be accurate to within 0.07% and 3.8% for the biaxial and ring shear experiments, respectively. The maximum error in the ring shear results would be systematic and is caused by uncertainties in the seal friction correction.

In the biaxial experiments, only the final shear strain could be estimated and was calculated as the ratio of the shear displacement to the final sample thickness. For the ring shear experiments, the evolution of sample thickness and shear strain with displacement was calculated from the final piston-sample assembly length and the vertical displacement measured during each experiment. Because of uncertainties caused by seal friction, the

error in sample thickness measured was relatively large (~5-10%), so we used these data only to estimate the evolution of shear strain.

The velocity dependence of μ was quantified in terms of the parameter $(a - b)$, defined in rate and state dependent friction (RSF) theory (Dieterich, 1978, 1979; Ruina, 1983) as:

$$(a - b) = \frac{\Delta \mu_{ss}}{\Delta \ln V} \quad (2.1)$$

(e.g. Marone, 1998; Paterson and Wong, 2005; Scholz, 2002). Here, μ_{ss} is the steady state friction coefficient, V is the sliding velocity and Δ indicates changes in these quantities following a step change in sliding velocity. The parameter a represents the magnitude of the instantaneous change in μ upon a change in sliding velocity, while b reflects the magnitude of the drop in μ during the evolution to a new steady state value. A positive $(a - b)$ value indicates an increase in friction coefficient with increasing velocity or “velocity strengthening” slip behaviour, which is inherently stable (e.g. Scholz, 1998). A negative $(a - b)$ value means that the behaviour is “velocity weakening”, which is potentially unstable (e.g. Scholz, 1998).

Values of $(a - b)$ can be calculated using Eq. (2.1) applied for consecutive velocity steps in a plot of μ versus displacement obtained from a velocity stepping experiment. However, the step-related changes in μ are often superimposed onto a gradual increase or decrease of the friction coefficient with displacement (x), i.e. a slip hardening or softening trend ($\delta\mu/\delta x$). Following standard practice for experiments in which (modest) slip hardening or softening is observed (e.g. Tembe et al., 2010), the μ versus displacement curve was detrended for slip hardening based on the hardening rates measured in each consecutive step. This yielded equivalent steady state friction coefficients, which were used to calculate $(a - b)$. Errors in $(a - b)$ were determined from the cumulative errors in friction measurement, sliding velocity and the correction for the slip hardening/softening.

Mean slip hardening rates at a given velocity were determined by fitting a linear envelope to the relevant portions of the μ versus displacement curve. They were characterized by errors of $<0.0008 \text{ mm}^{-1}$.

2.2.4 Microstructural methods

After each biaxial test, the sample assembly was taped together, removed from the apparatus and dried at 40°C for ≥ 24 hours. The assembly was then impregnated with low viscosity resin, which penetrated the gouge surfaces to a depth of ~1-5 mm. An oil-lubricated diamond wafering saw was used to section the shear zones parallel to the shear direction and perpendicular to the shear plane. The disturbed surface of the resulting section was then removed with adhesive tape, exposing undisturbed material for microstructural analysis.

After completion of the ring shear experiments, the sample assembly was dried at 50°C for 12-24 hours. Upon dismantling, the sample generally disintegrated into platy fragments, along Riedel-type fractures. The larger fragments were set in resin and wafer sawn parallel

Table 2.1 List of experiments, conditions and key data. σ_n^{eff} = effective normal stress, T = temperature, P_f = pore fluid pressure, V = sliding velocity, γ = shear strain, μ = coefficient of friction. Biaxial experiment codes start with B, ring shear with RS. Quantities for which only estimates could be made are in grey. The externally applied pore fluid pressure was atmospheric in the biaxial experiments and thus is indicated as “atm.”. The sequence of sliding velocities is indicated for velocity stepping experiments. The initial gouge thickness is the thickness after pre-compaction, but before shearing. See text for the method of calculating γ and for the motivation to use $\gamma = 20$ in addition to 10 mm displacement to report friction values at.

Experiment	Material	σ_n^{eff} (MPa)	T (°C)	P_f (MPa)	V ($\mu\text{m/s}$)	Initial gouge thickness (mm)	Final gouge thickness (mm)	Final displacement (mm)	Final γ μ at 10 mm displacement (or $\gamma = 20$)
BODP-IN-A01	BODP-IN-A	15	14.4	atm.	18-1.8-0.18-1.8-18-1.8-0.18-1.8	0.22	0.14	18.20	130 0.38
BODP-IN-A02	BODP-IN-A	10	14.7	atm.	18-1.8-0.18-1.8-18-1.8-0.18-1.8	0.22	0.19	19.17	101 0.35
BODP-IN-B01	BODP-IN-B	15	14.1	atm.	18-1.8-0.18-1.8-18-1.8-0.18-1.8	0.23	0.18	19.15	106 0.41
BODP-IN-B02	BODP-IN-B	15	n.d.	atm.	1.8	0.13	0.09	20.31	226 0.39
BODP-OUT01	BODP-OUT	15	15.7	atm.	18-1.8-0.18-1.8-18-1.8-0.18-1.8	0.19	0.10	19.54	195 0.41
BODP-OUT02	BODP-OUT	10	15.1	atm.	18-1.8-0.18-1.8-18-1.8-0.18-1.8	0.18	0.09	19.18	213 0.33
BR506	Illite	5	16.0	atm.	10	0.45	0.39	9.98	26 0.37
BR507	Illite	5	13.5	atm.	16-1.6-0.16-1.6	0.22	0.25	10.16	41 0.31
BR509	Illite	10	13.5	atm.	16-1.6-0.16-1.6-16-1.6	0.34	0.24	16.67	71 0.33
BR511	Illite	15	14.5	atm.	18-1.8-0.18-1.8-18-1.8-0.18-1.8	0.32	0.14	18.19	135 0.38
BR512	Illite	15	15.3	atm.	18	0.31	0.11	20.00	182 0.42
BR513	Illite	30	15.4	atm.	18-1.8-0.18-1.8-18-1.8-0.18-1.8	0.35	0.22	19.16	87 0.43
BR514	Illite	10	14.5	atm.	18-1.8-0.18-1.8-18-1.8-0.18-1.8	0.19	0.18	19.17	106 0.34
BR515	Illite	15	15.7	atm.	18-1.8-0.18-1.8-18-1.8-0.18-1.8	0.36	0.23	19.17	83 0.35
BR516	Illite	15	15.6	atm.	1.8	0.25	0.17	19.54	115 0.39
BR517	Illite	10	15.8	atm.	18	0.22	0.13	19.91	159 0.35
BR518	Illite	5	15.5	atm.	1.8	0.27	0.15	19.61	131 0.30
RSRS07	Illite	170	200	100	10-100-10-1-10-100-10	0.61	0.46	49.95	109 0.47 (0.47)
RSRS09	Illite	170	300	100	10-100-10-1-10	0.32	0.23	25.39	110 0.57 (0.51)
RSRS16	Illite	170	250	100	10-100-10-1-10-100-10	0.75	0.59	40.65	69 0.42 (0.43)

to the shear plane.

Microstructures were examined using either a field emission Scanning Electron Microscope (FEG-SEM) or a Focused Ion Beam (FIB) – SEM. We used the FIB-SEM to ion-mill our ring shear samples, producing sections oriented parallel (tangential) to the shear direction and perpendicular to the shear plane. Both instruments used were equipped with an Energy-Dispersive X-ray detector.

2.3 Results

All experiments and key data including the coefficient of friction measured at 10 mm displacement are listed in Table 2.1. A displacement of 10 mm (or equivalent shear strain of ~ 20) was selected to report friction values because this was the maximum displacement attained in some of the biaxial runs (Table 2.1).

2.3.1 Mechanical data

2.3.1.1 Biaxial data on ODP material

The evolution of the coefficient of friction as a function of displacement as obtained for ODP material in the biaxial machine is shown in Fig. 2.3a for representative experiments. We found very similar behaviour for all three ODP materials tested. The friction curves obtained for samples BODP-IN-A02 and BODP-OUT02, at an effective normal stress of 10 MPa, exemplify this. These curves show an apparent yield point at a coefficient of friction of 0.21-0.23 and a displacement of 0.5-1 mm, followed by slip weakening, giving way after a further displacement of ~ 1 mm to slip hardening until a coefficient of friction of 0.33-0.35 is attained at a displacement of 10 mm (Fig 3a). At an applied normal stress of 15 MPa (BODP-IN-A01), similar yield behaviour occurs, but μ subsequently increases more rapidly to 0.38 at 10 mm displacement and to 0.47 at 20 mm displacement. A further experiment (BODP-IN-B02) conducted at 15 MPa but at a constant velocity of $1.8 \mu\text{m/s}$, shows that the apparent yield point increases to a μ -value of ~ 0.3 at this lower initial slip velocity.

The shear stress measured at a displacement of 10 mm during the biaxial experiments on ODP material is plotted versus the effective normal stress in Fig. 2.3b. Though the data are few, the results show a roughly linear to slightly concave upward relation, confirming an increase in friction coefficient from around 0.34 at 10 MPa effective normal stress to ~ 0.40 at 15 MPa.

Referring to Fig. 2.3a, the first velocity step, (from 18 to $1.8 \mu\text{m/s}$) in these three velocity stepping tests depicted, shows a considerable increase in friction coefficient. This velocity weakening behaviour is not seen in subsequent velocity steps. Once a steady hardening rate is achieved at displacements beyond ~ 5 mm, the ODP materials consistently show velocity strengthening behaviour (Fig. 2.3a). This is illustrated by the positive $(a - b)$ values plotted for these materials in Fig. 2.3c. The $(a - b)$ values obtained for ODP materials from within and above the décollement zone are all very similar. No correlation between $(a - b)$ and effective normal stress or sliding velocity is visible.

Finally, mean slip hardening rates for the ODP materials are plotted as a function of effective normal stress in Fig. 2.3d, for different sliding velocities. The highest slip hardening rates

occur at 18 $\mu\text{m/s}$. Although the data are limited, a positive correlation seems to exist between slip hardening rate and effective normal stress.

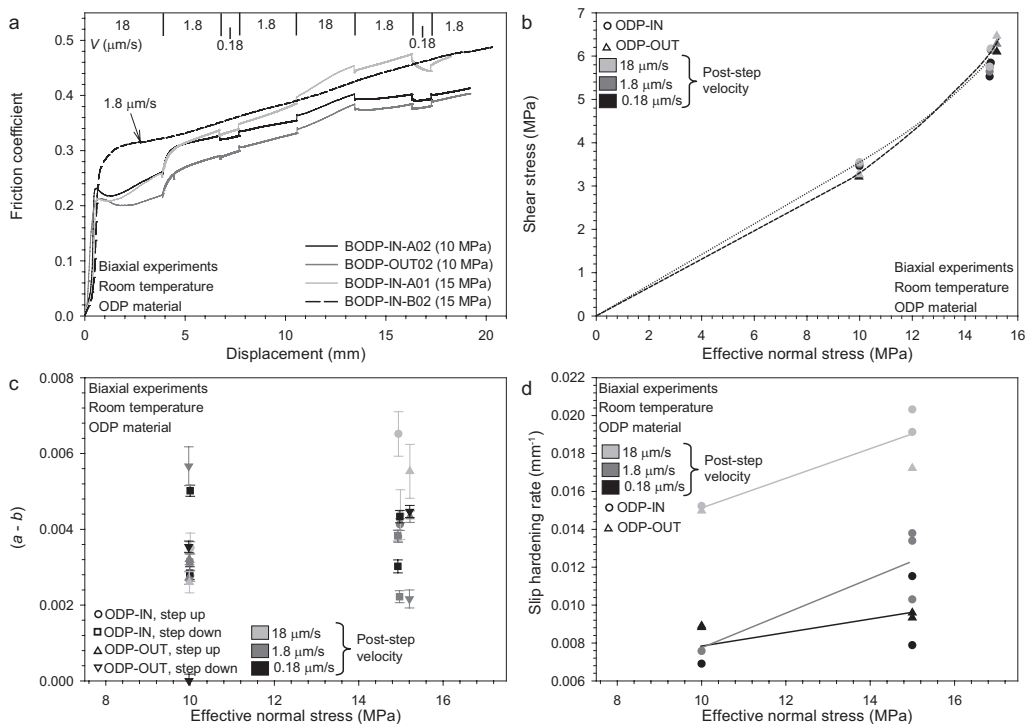


Figure 2.3 Frictional characteristics of ODP material obtained from the present biaxial experiments conducted at room temperature. (a) Friction coefficient versus displacement for experiments on all ODP sample types, performed at the effective normal stresses shown, using the velocity steps indicated at the top of the figure. BODP-IN-B02 was conducted at a constant slip velocity of 1.8 $\mu\text{m/s}$. (b) Shear stress at 10 mm displacement versus effective normal stress for all ODP samples. The shear stress was either determined directly or interpolated between velocity steps at the indicated velocities. The errors are $\leq 0.07\%$ and smaller than the symbol size. (c) Values of $(a - b)$ versus effective normal stress. (d) Slip hardening rate versus effective normal stress. The hardening rates are estimated to be accurate to within 0.0008 mm^{-1} . Lines highlighting the main trends are added to (b), using dotted and dashed lines for ODP-IN and ODP-OUT respectively. Trend lines are added to (d) for the different post-step velocities used.

2.3.1.2 Biaxial data on illite

A representative selection of friction coefficient versus displacement curves obtained in the velocity stepping experiments performed on illite gouge using the biaxial machine at different effective normal stresses is shown in Fig. 2.4a. In all experiments, the friction coefficient increased rapidly until an apparent yield point was reached at a friction coefficient of about 0.30–0.36 and a displacement of ~ 0.5 –1.5 mm. This was usually followed by minor hardening reaching near steady state friction values at a displacement of 4–5 mm. Subsequent velocity steps show small but clear effects of sliding velocity on friction coefficient. The coefficient of friction increased with normal stress and varied between 0.30 and 0.43 at 10 mm displacement (Fig. 2.4a, Table 2.1), with the lowest values being

obtained at 5 MPa (Table 2.1) and the highest values at 30 MPa effective normal stress. A single experiment (BRS16) performed at a constant sliding velocity of $1.8 \mu\text{m/s}$ and 15 MPa effective normal stress shows a very similar coefficient of friction to that obtained at $1.8 \mu\text{m/s}$ in stepping test BRS11, performed at the same applied normal stress.

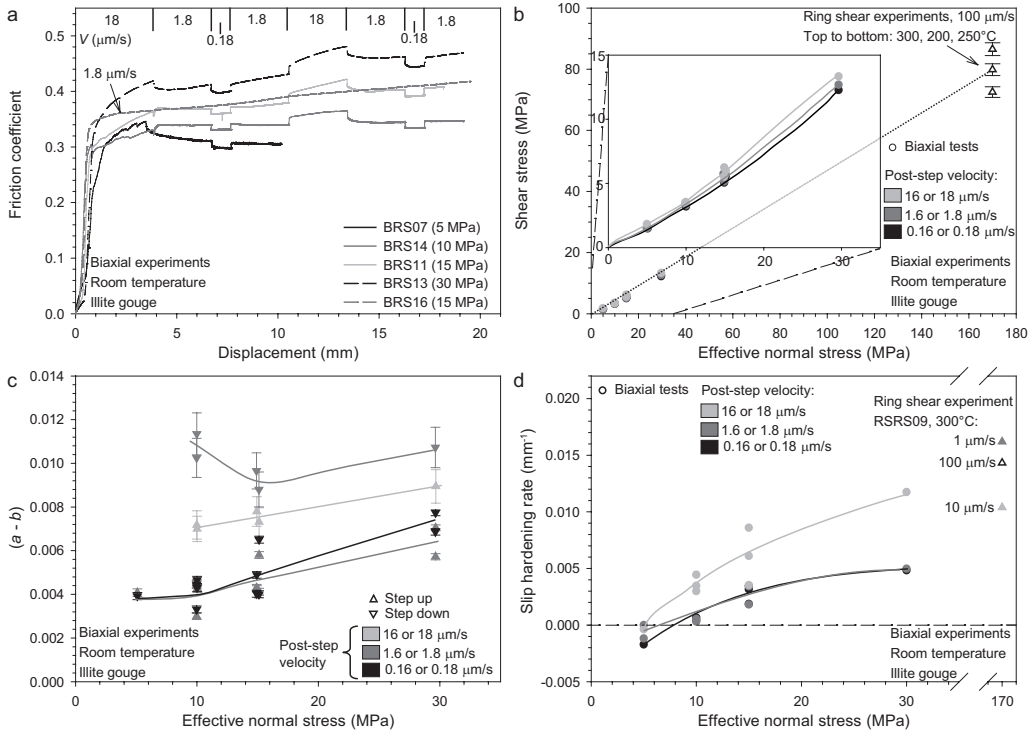


Figure 2.4 Frictional characteristics of illite gouge obtained from the present biaxial experiments executed at room temperature. Data obtained from ring shear experiments are added to (b) and (d) for comparison. (a) Friction coefficient versus displacement for experiments performed at different effective normal stresses, using the velocity steps indicated at the top of the figure. BRS07 was performed at slightly different sliding velocities of 0.16, 1.6 and 16 $\mu\text{m/s}$ and BRS16 was conducted at a constant velocity of $1.8 \mu\text{m/s}$. (b) Inset: shear stress supported in the biaxial tests at 10 mm displacement versus effective normal stress. Shear stress values were interpolated between velocity steps where necessary. Errors are smaller than the symbol size. In the full figure, ring shear data are plotted for comparison at an equivalent shear strain of 20. (c) Values of $(a - b)$ versus effective normal stress. (d) Slip hardening rate versus effective normal stress. Errors in hardening rate are estimated to be $< 0.0008 \text{ mm}^{-1}$. For comparison, ring shear data are added for RRS09, conducted at 300°C , which had a similar final thickness as the samples deformed in the biaxial machine. Lines highlighting the main trends seen at the different velocities are added to (b), (c) and (d) for clarity.

The shear stress supported by the illite samples in the biaxial tests at 10 mm displacement is plotted against effective normal stress in the inset in Fig. 2.4b for the various velocity steps applied. These results show a slightly concave upward increase of the shear strength with the normal stress, demonstrating an increase in friction coefficient μ with effective normal stress. The data also shows a small increase in shear strength with increasing velocity.

Returning to the velocity dependence seen in Fig. 2.4a, the steady state friction coefficient clearly increases with increasing sliding velocity, demonstrating that illite gouge exhibits velocity strengthening behaviour at the conditions investigated with the biaxial machine. Values of $(a - b)$ are plotted versus effective normal stress for various post-step velocities in Fig. 2.4c. The values vary between 0.003 and 0.11, show an overall increase with increasing normal stress and are higher for velocity steps to 16 or 18 $\mu\text{m/s}$ than those involving lower velocities. By contrast, $(a - b)$ values obtained for velocity steps down from 16 or 18 $\mu\text{m/s}$ to 1.6 or 1.8 $\mu\text{m/s}$ are the highest obtained and, instead of the near-linear increase in $(a - b)$ with σ_n observed for other steps, show a minimum at an applied normal stress of 15 MPa.

Again referring to Fig. 2.4a, whereas most samples showed slip hardening, slip weakening occurred at the lowest applied normal stress of 5 MPa. In individual experiments, the slip hardening rate also changed with sliding velocity. These trends are illustrated in Fig. 2.4d. This demonstrates that the slip hardening rate increases with applied normal stress at fixed velocity. At the same time, the slip hardening rate is insensitive to sliding velocity at the lowest velocities investigated, but increases significantly at slip velocities of 16 or 18 $\mu\text{m/s}$. The positive correlation between slip hardening rate and normal stress may reflect an underlying inverse relation between sample thickness and the slip hardening rate, with sample thickness decreasing with increasing normal stress. In a few experiments, we measured final thickness of one of the shear zones by microscopic investigation, but no systematic decrease was found with increasing applied normal stress (Table 2.1).

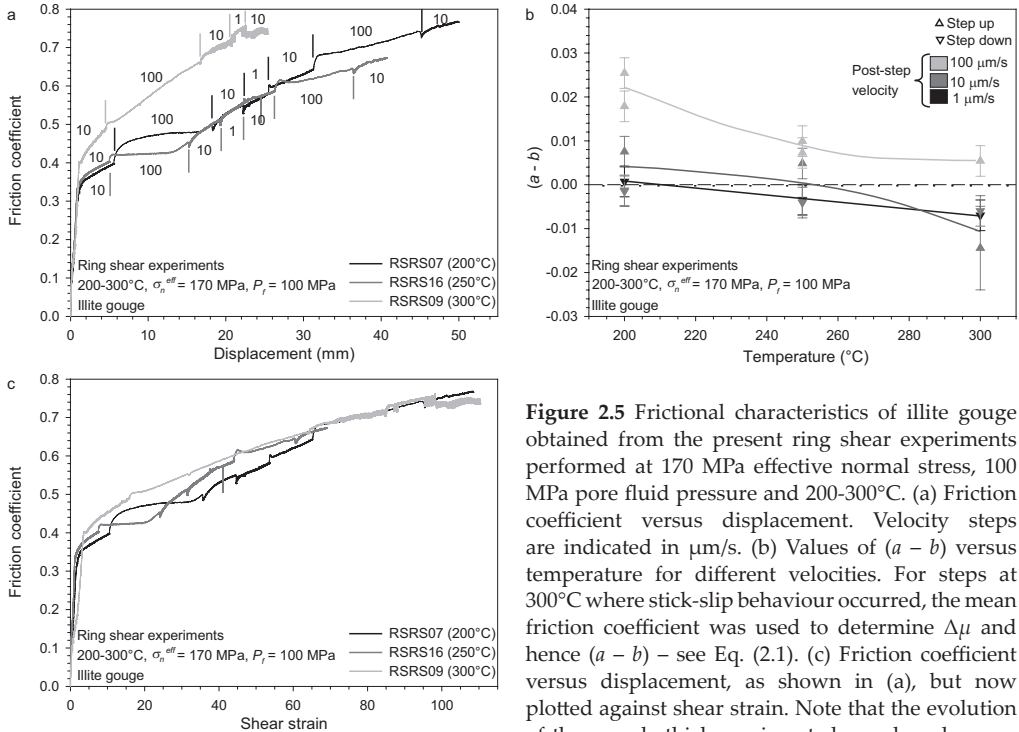


Figure 2.5 Frictional characteristics of illite gouge obtained from the present ring shear experiments performed at 170 MPa effective normal stress, 100 MPa pore fluid pressure and 200–300 $^{\circ}\text{C}$. (a) Friction coefficient versus displacement. Velocity steps are indicated in $\mu\text{m/s}$. (b) Values of $(a - b)$ versus temperature for different velocities. For steps at 300 $^{\circ}\text{C}$ where stick-slip behaviour occurred, the mean friction coefficient was used to determine $\Delta\mu$ and hence $(a - b)$ – see Eq. (2.1). (c) Friction coefficient versus displacement, as shown in (a), but now plotted against shear strain. Note that the evolution of the sample thickness is not shown here because the error was relatively large ($\sim 5\text{--}10\%$).

2.3.1.3 Ring shear data on illite

The friction coefficient versus displacement curves obtained from the ring shear experiments at temperatures of 200, 250 and 300°C are shown in Fig. 2.5a. Experiments performed at 200°C and 250°C show a rapid initial increase in the coefficient of friction followed by an apparent yield point at a coefficient of friction of 0.35 and by subsequent slip hardening towards friction coefficients at 10 mm displacement of 0.47 and 0.42 at 200°C and 250°C, respectively. At 300°C, the initial apparent yield point occurs at a coefficient of friction of 0.4. Subsequent slip hardening occurs at a higher rate and the friction coefficient at a displacement of 10 mm is increased to 0.57. The friction coefficients obtained at 200-250°C are thus similar to those obtained for illite gouges at room temperature and at lower normal stresses, while that at 300°C is significantly higher. Velocity strengthening behaviour is visible in many of the velocity steps imposed at 200 and 250°C, whereas velocity weakening and stick-slip are seen at 300°C (Fig. 2.5a). This velocity dependence of friction is expressed in terms of $(a - b)$ values in Fig. 2.5b. For steps to and from the lowest velocities of 1 and 10 $\mu\text{m/s}$, the trend in $(a - b)$ crosses the $(a - b) = 0$ line, i.e. the velocity strengthening to weakening transition, between 210°C and 250°C. The $(a - b)$ values are the highest and positive for velocity steps from 10 to 100 $\mu\text{m/s}$, and suggest a transition to negative values at temperatures above 300°C at these rapid slip rates.

All friction coefficients versus displacement curves presented in Fig. 2.5a show strong slip hardening at a rate that is significantly higher at 300°C than at 200°C and 250°C. However, the gouge layer thickness at 300°C was 50-65% less than at 200 and 250°C (Table 2.1). In Fig. 2.5c, we re-plot the friction curves for the ring shear experiments with shear strain on the horizontal axis instead of the displacement. As opposed to the evolution of the coefficient of friction with displacement (Fig. 2.5a), the evolution with shear strain (Fig. 2.5c) is very similar at the three different temperatures. In the comparison of the shear stress as a function of the (effective) normal stress for the ring shear experiments with the biaxial experiments, therefore, a constant shear strain is used instead of a constant displacement. A displacement of 10 mm corresponds to a shear strain of ~20 on average for the ring shear experiments. The shear stresses attained in the ring shear experiments at a shear strain of 20, measured at the effective normal stress of 170 MPa are included in Fig. 2.4b for the three different temperatures. The biaxial and ring shear results are consistent and together define a near-linear increase in the shear stress with normal stress, despite the slight upward curvature at low normal stresses.

In order to compare the slip hardening rate obtained at the high effective normal stresses addressed in the ring shear experiments (Fig. 2.5a) with those at the lower (effective) normal stresses used in the biaxial experiments on illite, we included the rates obtained for the ring shear sample with a thickness most similar to the biaxial samples (i.e. the 300°C sample, Table 2.1) in Fig. 2.4d. The slip hardening rate obtained at high normal stress in the ring shear machine fits quite well with the trend obtained in the biaxial experiments on illite gouge. Together, these data show a positive correlation between slip hardening rate and effective normal stress, which seems to approach an asymptotic value at high normal stresses (Fig. 2.4d - note the break in the horizontal axis). Note, however, that in contrast to the biaxial experiments, the ring shear experiments consistently give the highest slip hardening rate at the lowest slip velocity.

2.3.2 Microstructural observations

2.3.2.1 Biaxial experiments

The microstructures of the ODP samples and illite gouge tested at room temperature in the biaxial machine are shown in Fig. 2.6 and Fig. 2.7, respectively. Closely similar features were observed in both materials. Micrographs of the pre-compacted samples are presented in Figs. 2.6a and 2.7a. The starting microstructures developed in both materials show a more or less homogenous mixture of relatively large (up to $\sim 30\ \mu\text{m}$) particles of mainly quartz embedded in a chaotically foliated matrix of fine clay minerals. The microstructures seen in both the ODP and illite gouges, after deformation in the biaxial machine (Figs. 2.6b, 2.7b and 2.7c), show a much more pervasive and strongly-orientated clay mineral foliation. This foliation is anastomosing in nature and lies roughly in the P-shear orientation of Logan et al. (1992), i.e. at $\sim 20^\circ$ to the shear plane. In addition, numerous sharp discontinuities are visible in the P-orientation, which we interpret as discrete P-shears (Figs. 2.6b, 2.7b and 2.7c). The foliation is cross-cut by sharp, planar Y-shears mostly of limited lateral extend and R_1 -shears at ~ 20 - 30° to the shear plane (Fig. 2.6b and 2.7c). Discontinuous, undulating Y-shears are visible near the boundaries of some samples (Fig. 2.7b). The R_1 -shears are usually seen as sharp, relatively widely spaced discontinuities, but sometimes define a foliation or form open cracks. The various foliations and shears were slightly more pronounced in the illite gouge samples than in the ODP materials. Although it is not easy to distinguish individual grains in Figs. 2.6 and 2.7, the starting and final grain sizes appeared similar or slightly finer after deformation. There was no clear difference in the microstructure displayed by samples sheared at different normal stresses, or by different types of ODP material.

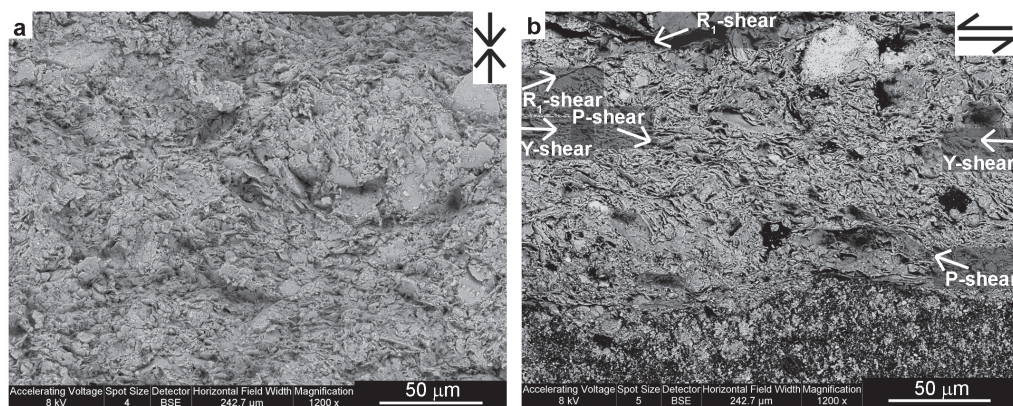


Figure 2.6 Microstructure of ODP-IN-A material tested at room temperature in the biaxial machine, as imaged using the FEG-SEM. (a) Starting microstructure, after pre-compaction at a normal stress of 20 MPa (compaction direction as indicated). (b) Microstructure of BODP-IN-A02, sheared in velocity stepping mode at a normal stress of 10 MPa.

2.3.2.2 Ring shear experiments

The microstructure of illite gouge pre-pressed at room temperature, before deformation in the ring shear machine, as imaged with the FIB-SEM, is shown in Fig. 2.8a. The deformed samples could only be studied in the FIB-SEM because of handling difficulties. This starting microstructure shows sub-rounded quartz grains (dark in backscatter mode) and occasional fragments of phyllosilicates of ~ 1 - $5\ \mu\text{m}$ in diameter, surrounded by a matrix of

clay minerals with an anastomosing preferred orientation. Similar features are visible in the starting material using FEG-SEM imaging (Fig. 2.8b). Whereas the general appearance of the starting microstructures imaged with the different machines is distinctly different, both show a similar anastomosing preferred orientation of clay minerals wrapping around the coarser clast phases. Moreover, in the case of deformed illite samples, both the foliation and discrete shears can be observed in both types of images (compare for example Figs. 2.7b and 2.8c). On this basis, we argue that the imaging method used does not influence our main observations.

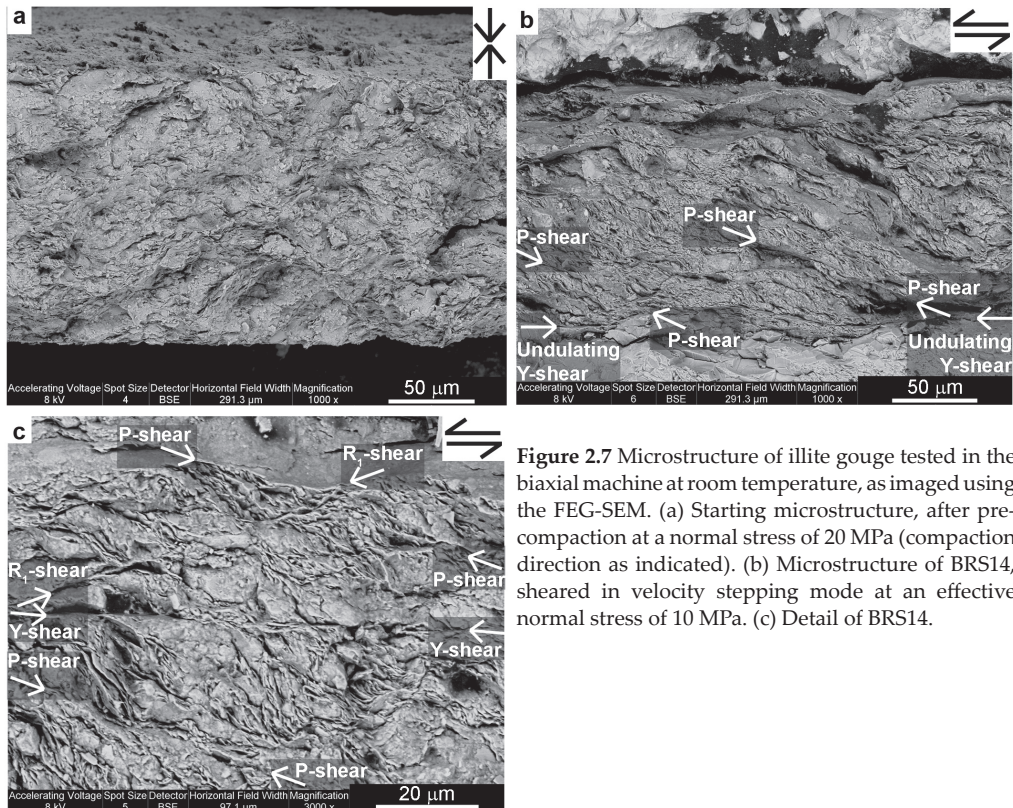


Figure 2.7 Microstructure of illite gouge tested in the biaxial machine at room temperature, as imaged using the FEG-SEM. (a) Starting microstructure, after pre-compaction at a normal stress of 20 MPa (compaction direction as indicated). (b) Microstructure of BRS14, sheared in velocity stepping mode at an effective normal stress of 10 MPa. (c) Detail of BRS14.

Representative micrographs of the illite gouge samples after shearing in the ring shear machine at 250 and 300°C are shown in Figs. 2.8c and 2.8d, respectively and show very similar microstructures. Compared to the starting microstructure (Fig. 2.8a), the deformed samples appear to have a slightly higher proportion of quartz grains, which are more angular, more equidimensional and generally smaller ($\sim 0.5\text{--}2\text{ }\mu\text{m}$) than in the pre-compacted starting material (note the different scale bars in Fig. 2.8). In the matrix of the deformed samples (Fig. 2.8c and d), a foliation oriented parallel to the P-orientation is defined by a phyllosilicate mineral with a light appearance in backscatter mode (indicated with “ma”). This phase was too small to identify by EDX measurements. Locally, the foliation has a folded appearance, wrapping around the bigger quartz grains (Fig. 2.8c, denoted “f”).

Several horizontal, dilated, Y-shears were observed in the deformed samples, which either cross-cut quartz grains without offsetting them (Fig. 2.8c) or follow the boundaries of quartz grains (Fig. 2.8d). Most of the porosity seen in the deformed samples is concentrated in these dilated Y-shears or along the boundaries of quartz grains (Fig. 2.8c and d). We did not observe R_1 shears in the ring sheared samples using the FIB-SEM. However, the samples showed a tendency to break along through going fractures spaced at the millimetre scale, with an orientation similar to R_1 shears. Hence, we propose that R_1 shears were important during the deformation of the illite-rich samples in the ring shear machine at 200-300°C, but that they were too widely spaced to be observed in the FIB-milled sections.

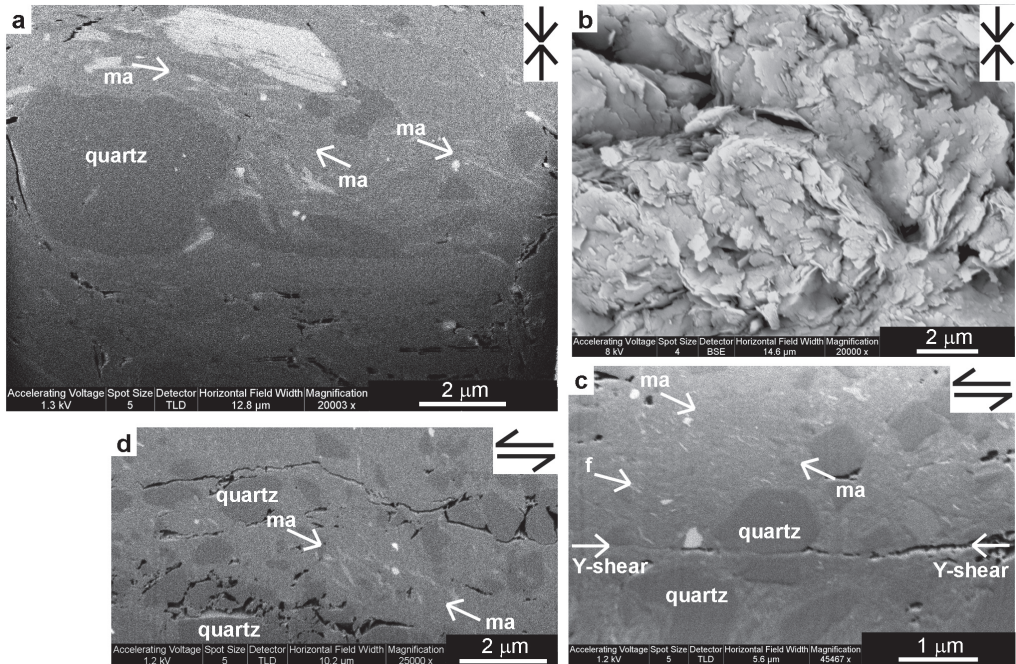


Figure 2.8 Microstructures of illite gouge tested in the ring shear machine, as imaged with the FIB-SEM (except b). Mineral alignments are indicated with “ma” and “f” indicates regions where the foliation appears folded. (a) Starting microstructure, after pre-pressing and before insertion into the ring shear apparatus. Compaction direction as indicated. Here “ma” indicates the flattening fabric developed during pre-pressing. (b) Starting microstructure, after pre-pressing; non-polished surface imaged using the FEG-SEM. The orientation of the sample is as in (a). (c) Microstructures developed in RSR516, sheared at 250°C. (d) Microstructure of RSR509, sheared at 300°C.

2.4 Discussion

2.4.1 Comparison with previous data

Our biaxial experiments on ODP material from both inside and outside the sampled décollement consistently showed velocity strengthening behaviour. All ODP samples were further characterized by friction coefficients of 0.33-0.41 at 10 mm displacement (corresponding to shear strains of ~51-113, Table 2.1), increasing to ~0.40-0.50 at 20 mm displacement (Fig. 2.3). Some evidence was found for an increase of the slip hardening rate and friction coefficient with normal stress. The observed velocity dependence and

associated ($a - b$) values agree well with those obtained for similar (I)ODP and smectite-rich materials deformed wet at room temperature in previous studies (Ikari and Saffer, 2011; Ikari et al., 2009a; Tembe et al., 2010), both in sign and magnitude (generally $< \sim 0.007$). In comparing friction coefficients, we note that the shear strains attained in previous studies of similar materials are much lower than those in the current study. When compared at the low shear strain previously reached (~ 5 -9, corresponding to displacements of ~ 0.5 -1.7 mm in our tests on ODP samples – Fig. 2.3), our friction coefficients agree well with the values of 0.20-0.28 reported previously for samples from the décollement zone at Site 1174 at the Nankai Trough by Ikari and Saffer (2011) and values of ~ 0.2 for mixtures of smectite and illite with $\sim 10\%$ quartz (Tembe et al., 2010). These data were also obtained at room temperature, similar velocities and relatively low effective normal stresses (25 and 40 MPa, respectively). Agreement is less good with the μ -values of 0.32-0.44 obtained at low shear strains (~ 5) for samples recovered from the Nankai megathrust fault system during IODP Expedition 316 (Ikari and Saffer, 2011; Ikari et al., 2009a), perhaps reflecting differences in composition and fabric (Ikari, personal communication 2011). Kopf and Brown (2003) reported friction coefficients of 0.16-0.24, lower than those obtained here, for samples from the Nankai Trough at ODP Site 808. This difference may be due to the very low effective normal stress (< 2 MPa) used in that study and the dependence of μ on normal stress observed here (Fig. 2.3).

As for the ODP materials, the velocity strengthening behaviour observed in our biaxial experiments on illite-rich gouge is in agreement with previous studies (Ikari et al., 2009b; Morrow et al., 1992; Saffer and Marone, 2003; Tembe et al., 2010). Our friction coefficients for this material ranged from 0.30 to 0.43 at a displacement of 10 mm (shear strains of ~ 10 -90, Table 2.1) under the room temperature conditions of the biaxial experiments. Comparing at similar shear strain, these values agree favourably with those obtained at room temperature and low effective normal stresses by Ikari and Saffer (2011) for the same material (0.27-0.32) under wet conditions and with values of ~ 0.30 -0.50 previously reported by Tembe et al. (2010) for wet illite with 0-50 wt% quartz. Values of 0.22 and ~ 0.25 obtained by Brown et al. (2003) and Kopf and Brown (2003) for Rochester illite and 70/30 illite/quartz mixtures are lower, again perhaps due to the lower effective normal stress (< 2 MPa) used by these authors. Coefficients of friction obtained in the current study also differ from those reported by Saffer and Marone (2003). Their samples were not water saturated but equilibrated with room humidity. As a result, the friction coefficient reported by these authors at low normal stresses (0.54-0.63 at 5-30 MPa) is higher than obtained here, consistent with the observed weakening effect of water saturation on phyllosilicates (e.g. Morrow et al., 2000). By contrast, the μ values measured by Saffer and Marone (2003) at high normal stresses (0.41 at 150 MPa) are only a little higher than our biaxial values at 15 MPa, perhaps reflecting increasing (adsorbed) water saturation caused by compaction at these high normal stresses.

The ring shear experiments, performed at a much higher effective normal stress (170 MPa) and temperature (200-300°C), showed increased values of the coefficient of friction of illite compared to the biaxial experiments (Fig. 2.4b), reaching values of 0.43-0.51 at displacements of 6-13 mm (shear strain of 20). The value of 0.41 measured by Saffer and Marone (2003) at 150 MPa is similar to our values of 0.36-0.44 at low shear strains (~ 4 -8), supporting our

suggestion above of an effect of normal stress on water saturation in their experiments. Our values of 0.38-0.43 at a shear strain of 7 also agree reasonably well with those of 0.45-0.47 measured for wet Fithian illite by Morrow et al. (1992; 1982) at room temperature, 200-300 MPa confining pressure and the same shear strain. This, combined with the very similar friction coefficients for our experiments at different elevated temperatures, implies that the increase of μ in our ring shear experiments compared to the biaxial experiments is an effect of the elevated effective normal stress rather than the increased temperature. At temperatures above 300°C, however, an increase of the coefficient of friction with temperature is suggested by the results of Moore et al. (1986a, b, 1989).

In their appendix, Tembe et al. (2009) report friction coefficients for illite-rich gouge ranging between 0.42 and 0.68 at 189°C and 349°C, respectively, at effective normal stresses of 76 and 150 MPa, a pore fluid pressure of 100 MPa and at a shear strain of ~3.7. These values are higher than we obtained in our ring shear tests at low strain (0.36-0.4). The difference may reflect the somewhat different composition of the samples of Tembe et al. (2009), which were derived from an inactive strand of the San Andreas Fault. Despite the higher μ -values reported by Tembe et al. (2009), this study supports our finding of a transition to unstable, velocity weakening behaviour at a temperature of 250-300°C at low velocity (1-10 $\mu\text{m/s}$). At temperatures between 266°C and 283°C, a pore fluid pressure of 100 MPa, effective normal stresses of 76-226 MPa and a sliding rate of 0.05-0.5 $\mu\text{m/s}$, velocity weakening behaviour was observed, whereas velocity strengthening occurred at temperatures below 266°C and above 283°C. Values of $(a - b)$ obtained by Tembe et al. (2009) at 189-349°C lay between -0.0056 and +0.0122, compared with the values of -0.0144 to +0.0254 that we observed. In addition, Moore et al. (1986a, b, 1989) reported the occurrence of stick-slip events in saw cut experiments at constant velocity on (Fithian) illite at temperatures of 400°C and 600°C. This behaviour was seen at virtually all confining pressures between 25 and 250 MPa, pore fluid pressures between 0.1 and 100 MPa and slip velocities of either 0.048 $\mu\text{m/s}$ or 4.8 $\mu\text{m/s}$, and suggests either velocity neutral or velocity weakening slip behaviour at high temperatures.

Looking at our entire set of experiments on both gouges, using both machines, at effective normal stresses ≥ 10 MPa, our experiments all showed slip hardening at a rate that increased with increasing normal stress. The very high shear strains reached (up to >200 in the biaxial tests) result in friction curves in which the effect of this hardening behaviour is more apparent than in some earlier experimental studies attaining much lower shear strains. Nevertheless, slip hardening behaviour was also reported by Moore et al. (1986a, b, 1989), Morrow et al. (1982) and Tembe et al. (2010). Tembe et al. (2010) measured strain hardening rates (equivalent to slip hardening rate, since a constant sample thickness of 1 mm was assumed) between 0.0022 and 0.0148 for mixtures of illite or illite/smectite with quartz. This is similar to the range seen in our tests on illite gouge (Fig 4d). Friction coefficients obtained in experiments must therefore be treated with care, since they may not represent true steady state or in-situ fault behaviour. Moreover, the implications for slip hardening in determining $(a - b)$ values from Eq. (2.1), or in determining the full set of RSF parameters, remains unclear. This matter deserves further attention in future studies.

2.4.2 Microscopic shear mechanisms

The microstructures developed in all of our samples after deformation (Figs. 2.6b, 2.7b, 2.7c, 2.8c and 2.8d) show clay mineral alignment forming a foliation in the P-orientation, oriented at about 20° to the shear plane and shear direction. If this foliation represents a preferred alignment parallel to the extension axis of the finite strain ellipse developed by passive rotation of clay particles during homogeneous simple shear, it would reflect a shear strain of ~ 2 (Ramsay and Huber, 1983). This is much less than the shear strains imposed in our experiments, suggesting two possible microscale shearing mechanisms. In the first, the foliation formed due to distributed, homogeneous deformation and passive clay rotation until a shear strain of ~ 2 was reached. Beyond this point, P-shearing would have been easy on the foliation, leading to on-going localized deformation by P-shearing plus R_1 -slip and (minor) Y-shear to accommodate the overall imposed strain. The alternative possibility is that deformation was dominated by combined P-, R_1 - and Y-shearing from the outset, with the 20° foliation developing due to a prevalence of P-shearing. We favour the first explanation because all of our samples show macroscopic yield at a shear strain of between 1 and 2, suggesting a major change in dominant microscale processes. We found no sign of prominent, flat Y-shears at the sample boundaries of the type reported in illite gouge by Moore et al. (1989). Y-shear features were observed to be less widespread than P- and R_1 -shears in all deformed samples and those present near the sample boundaries were undulating rather than sharp. Apparently, Y-shear activity during deformation was relatively minor. This is supported by the fact that μ -values in our tests show better reproducibility when measured at fixed shear strain rather than fixed displacement (Fig. 2.5a versus 2.5c), demonstrating the importance of gouge thickness and ruling out major localization on discrete Y-shears. This implies that the stick-slip behaviour observed in illite-rich gouge deformed at 300°C in the ring shear machine (Fig. 2.5a) may not be associated with persistent localization on Y-shears, as often suggested in other studies (e.g. Marone, 1998).

From the present microstructures, no alternative explanation could be deduced for the unstable, velocity weakening behaviour seen at 300°C in our ring shear test on illite. Specifically, no obvious differences were visible in the microstructures seen in samples showing velocity strengthening behaviour versus those showing velocity weakening behaviour with stick-slip (Fig. 2.8c versus 2.8d). Tembe et al. (2009) attributed the velocity weakening behaviour they observed in illite-containing gouge at temperatures between 266 and 283°C to (i) failure to achieve steady state in the brief velocity steps employed (0.5 mm displacement), (ii) transient increases in pore fluid pressure as a result of velocity stepping, (iii) chemical changes, or (iv) dehydration reactions. Considering the close agreement between their findings and the current results, it seems unlikely that velocity weakening is an experimental artefact such as (i). Transient increases in pore fluid pressure seem unlikely as our ring shear samples are only 3 mm in width and trial pore fluid pressure stepping tests showed no significant effect on μ . Regarding chemical changes, no significant changes were found in the XRD patterns obtained for deformed samples, compared to undeformed samples. However, we cannot exclude the possibility that illite was (partially) transformed to muscovite. This is expected to occur (slowly) at ~ 200 – 300°C (Merriman and Frey, 1999), but would result in only very subtle changes of the basal plane XRD peak (spacing of 10 Å; Meunier and Velde, 2004). Dehydration reactions are not likely to be important in our

illite gouge, because the hydrous mineral smectite was not detected in these samples. Moreover, if it would have been present, it would already have dehydrated at 120-150°C (Pytte and Reynolds, 1988). In illite, water molecules in interlayer sites are also extracted from the crystal structure at temperatures below 200°C (Meunier and Velde, 2004) and are therefore not expected to play a role in the transition to velocity weakening behaviour seen at temperatures of ~250°C.

Remaining possibilities for the observed transition from velocity strengthening to velocity weakening behaviour not considered by Tembe et al. (2009) include (i) a decrease in the amount of adsorbed water on the surface of the clay minerals with increasing temperature (Mackenzie, 1957), in accordance with expectations of site adsorption theory (Masel, 1996), or (ii) the onset of compaction by thermally activated diffusive mass transport such as pressure solution, which has been shown to be capable of inducing velocity weakening in granular gouge materials (Niemeijer and Spiers, 2007). Pressure solution has been observed in laboratory experiments on quartz and quartz/muscovite mixtures at temperatures $\geq 350^\circ\text{C}$. Moreover, extrapolating the pressure solution rate versus grain size data obtained by Niemeijer et al. (2002) to the $\sim 1\text{--}5\ \mu\text{m}$ quartz grain size characterizing our ring shear samples implies that pressure solution will certainly occur. The possibility that a thermally activated process such as pressure solution is involved in controlling the transition to velocity weakening behaviour seen at $\sim 250^\circ\text{C}$ is further supported by the fact that the transition temperature tends to decrease with decreasing slip velocity, as seen in Fig. 2.5b. The transition may accordingly occur at significantly lower temperatures at velocities below the minimum of $\sim 10^{-6}\ \text{m/s}$ investigated here. However, neither of these possibilities can be confirmed by the present data.

At present, we can also only speculate on the possible causes of the effects of normal stress and/or velocity that we observed on μ , on $(a - b)$ values and on the slip hardening rate. A possible mechanism underlying the effects of normal stress is the progressive crushing and distribution of quartz grains throughout the gouge zone. A similar interpretation was put forward by Tembe et al. (2010), who observed a higher strain hardening rate for a mixture of clay and quartz with an increase in the quartz proportion. An increase in the applied (effective) normal stress may result in more severe crushing and mixing of the quartz grains, or even preferential loss of clay from the samples, yielding a higher strain hardening rate and thus also a higher value of the coefficient of friction.

2.4.3 Implications for seismogenesis

At room temperature, all ODP gouges showed velocity strengthening behaviour, in agreement with previous studies on similar materials (Ikari and Saffer, 2011; Ikari et al., 2009a; Tembe et al., 2010). The illite gouge also exhibited velocity strengthening behaviour at room temperature, in line with the findings of Saffer and Marone (2003) for the same material deformed at room temperature and room humidity. On the basis of their results, Saffer and Marone (2003) rejected the hypothesis put forward by Vrolijk (1990) that the dehydration of smectite to illite may be responsible for the updip seismogenic limit in subduction zones. Recently, alternative hypotheses have been put forward to explain the onset of seismogenesis, such as a threshold lithification state of megathrust fault gouges (e.g. Marone and Saffer, 2007; Moore et al., 2007). However, the present ring shear experiments at

200–300°C demonstrate that temperature is an important control on the velocity dependence of friction in illite gouge, and that a transition from velocity strengthening to velocity weakening behaviour occurs at ~250°C. Our results show not only velocity weakening in illite at 250°C, but also evidence for a sliding velocity dependence suggesting the onset of velocity weakening at temperatures significantly below ~250°C at velocities below 10^{-6} m/s (Fig. 2.5b), i.e. at initial slip nucleation velocities. On this basis, we suggest that the upper limit of the seismogenic zone could still be related to the transformation from smectite to illite, if illite is velocity weakening at the in-situ conditions of the transformation (120–150°C). Alternatively, the top of the seismogenic zone might simply reflect the onset of velocity weakening in the illite-dominated reaches of subduction megathrusts, beyond the smectite-illite transition.

At levels well within the seismogenic zone, muscovite-rich fault rocks must ultimately replace illite-rich gouge, since at temperatures of 200–300°C illite starts to transform into muscovite (Merriman and Frey, 1999). Simulated muscovite gouge has recently been shown by Van Diggelen et al. (2010) to exhibit a similar friction coefficient to our illite gouge under comparable conditions, as well as showing stick-slip behaviour at 400–500°C, which compares favourably with our observation of unstable behaviour in illite at 300°C. These findings, coupled with the gradual nature of the illite-muscovite transition, with the close structural similarity between illite and muscovite, and with the velocity dependence of $(a - b)$ seen in our ring shear tests, suggest that our results for illite-rich gouge may be relevant to earthquake nucleation over a significant portion of the seismogenic zone, i.e. into the muscovite-dominated zone. Nonetheless, further work is clearly needed on both muscovite and illite to confirm this.

Though limited, our room temperature data for ODP materials point to an increase in friction coefficient and slip hardening rate with normal stress (Fig. 2.3). Our room temperature data for illite show a clear increase in friction coefficient, in the velocity dependence parameter $(a - b)$ and in slip hardening rate with normal load, and, broadly speaking, with sliding velocity (Fig. 2.4). All of these trends will tend to promote unstable slip behaviour at low effective normal stresses and at low sliding velocities, thus favouring nucleation of both regular earthquakes and SSEs when effective normal stresses are low. If present in illite at higher temperatures, and if pore fluid pressures are high, these trends may further reduce the temperature and hence depth of the transition from velocity strengthening to weakening in this material, beyond the effects of sliding velocity mentioned above. Turning to SSEs, our biaxial experiments on ODP and illite-rich gouges showed velocity strengthening behaviour at room temperature and normal stresses of 5–30 MPa (Fig. 2.3c and 2.4c, respectively), indicating that a relatively low normal stress alone is not enough to trigger the velocity weakening behaviour required to generate SSEs. The effect of temperature on the velocity dependence of illite gouge that we found in our ring shear tests may therefore also be important for the generation of SSEs as well as for conventional seismogenesis.

2.4.4 Implications for modelling studies

Both regular earthquakes and SSEs have been reproduced in recent modelling studies of subduction zone megathrust behaviour (Hori et al., 2004; Kato, 2003; Liu and Rice, 2005, 2007, 2009; Matsuzawa et al., 2010; Shibazaki et al., 2010; Shibazaki and Iio, 2003; Shibazaki

and Shimamoto, 2007). Several of these studies have made use of data on the velocity dependence of friction coefficients obtained from experiments, such as the dry halite data of Shimamoto (1986), shown in Fig. 2.9. These data show a transition from velocity weakening to velocity strengthening behaviour at sliding velocities of 10^{-6} - 10^{-5} m/s. Our ring shear results for illite gouge relevant for the temperatures in the seismogenic zone (200-300°C) are included in Fig. 2.9 for comparison. These suggest that if a similar transition in frictional behaviour occurs in illite gouge, then it would be displaced to higher velocities at temperatures above 200°C compared with the data of Shimamoto (1986), being displaced by at least one order of magnitude at 300°C.

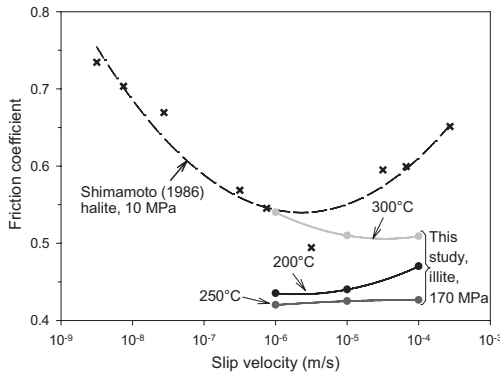


Figure 2.9 Coefficients of friction versus the logarithm of slip velocity for different materials. The results of Shimamoto (1986) are for dry halite deformed in a saw cut assembly at room temperature and at a confining pressure of 10 MPa. The present ring shear results are presented for a shear strain of 20 and temperatures of 200-300°C. Trend lines are added for clarity.

Aside from assuming a velocity dependence such as that in Fig. 2.9, most models of seismogenesis or SSE activity typically assume some dependence of $(a-b)$ upon temperature and/or depth (Hori et al., 2004; Liu and Rice, 2005, 2007, 2009; Matsuzawa et al., 2010; Shibazaki et al., 2010; Shibazaki and Iio, 2003; Shibazaki and Shimamoto, 2007). The $(a-b)$ dependencies on depth assumed by Liu and Rice (2005) and by Shibazaki and Shimamoto (2007) are shown in Fig. 2.10, for the example of the southwest Japan subduction zone (Shikoku). These are based in part on data of wet granite (Blanpied et al., 1995) and dry halite (Shimamoto, 1986), respectively. For comparison, our $(a-b)$ data for ODP and illite-rich gouge are added. Our biaxial results are plotted for the lowest normal stresses of 5 MPa and 10 MPa employed in our room temperature tests on illite gouge and ODP material, assuming these data to be the most realistic for low temperatures and shallow depths. The ring shear results include data obtained in velocity steps between 1 and 10 $\mu\text{m/s}$ only, as these most closely approach the velocities relevant for earthquake and SSE nucleation. Fig. 2.10 clearly shows that the transition from velocity strengthening to velocity weakening behaviour seen in our ring shear tests occurs at significantly higher temperatures (250°C versus $\sim 100^\circ\text{C}$) and greater depths than in the modelling studies by Liu and Rice (2005) and by Shibazaki and Shimamoto (2007) for the case of the Shikoku subduction zone. At the same time, our high temperature data for illite showed a tendency for the transition temperature to decrease to $\sim 210^\circ\text{C}$ at the lowest velocities investigated. This suggests that the transition may well occur at lower temperatures and depths in the subduction zone megathrust environment. Model assumptions made to date regarding transition temperature and depth (Fig. 2.10) may therefore still prove to be appropriate. To resolve this question, the frictional properties of realistic illite and muscovite fault gouges must be

investigated under realistic in-situ conditions, including at rates below $0.1 \mu\text{m/s}$.

Based on experimental studies of dry halite (Shimamoto, 1986), wet granite (Blanpied et al., 1998) and wet gabbro gouges (He et al., 2007), the modelling studies of earthquake or SSE nucleation of the type discussed above, incorporate not only a transition to velocity weakening but also a transition back to velocity strengthening behaviour at temperatures $\geq 350^\circ\text{C}$ (Fig. 2.10). This means that experiments on realistic megathrust fault gouges are also needed at temperatures exceeding those used here. Interestingly, results on SAFOD material presented by Tembe et al. (2009) do suggest such a switch back to velocity strengthening at $\sim 350^\circ\text{C}$, but it is important to note that these data are for smectite-bearing gouge, which will not survive at depth.

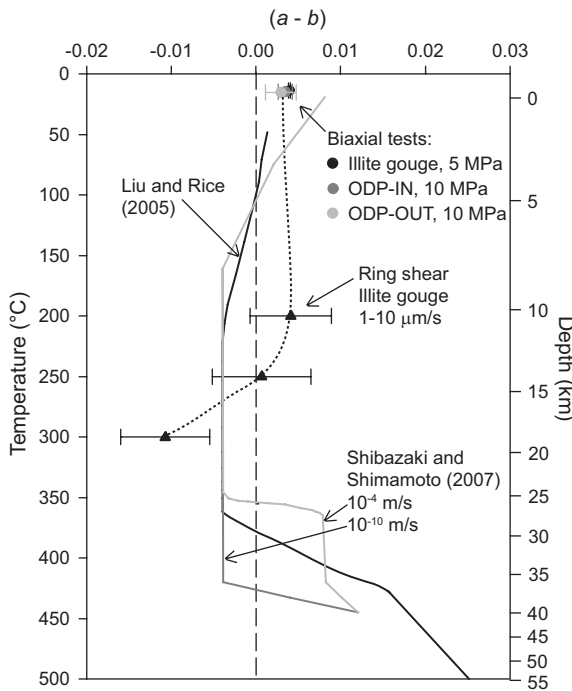


Figure 2.10 Values of $(a-b)$ versus temperature assumed by Liu and Rice (2005) and Shibazaki and Shimamoto (2007), for the example of the Shikoku subduction zone. Two profiles of Shibazaki and Shimamoto (2007) are given, for different sliding velocities. The profiles by the two respective studies are based in part on data for wet granite (Blanpied et al., 1998) and dry halite (Shimamoto, 1986) respectively, which are not representative for true subduction zones. Data for megathrust clays from the current study are added for comparison, where results for the biaxial experiments are those obtained at an applied normal stress of 5 MPa and 10 MPa for the illite gouge and ODP materials, respectively. The ring shear results include velocity steps involving 1 and $10 \mu\text{m/s}$ only. The error bars represent plus or minus one standard deviation. The dotted trend line is added to data obtained in the present study for clarity. The pressure-temperature path for Shikoku of Peacock (2009) is used.

In summary, our experiments have provided insight into effects of temperature and normal stress that may be important for unstable frictional behaviour related to the nucleation of earthquakes and perhaps SSEs. However, they also clearly demonstrate a need for future experiments which address materials that more realistically represent the deeper parts of the subduction interface (i.e. materials rich in muscovite and quartz) and which explore low effective normal stresses (1-50 MPa) combined with high temperatures ($300-550^\circ\text{C}$) and low slip rates ($<0.1 \mu\text{m/s}$). Only in this way, and by establishing a mechanistic basis for extrapolation to even lower slip rates, can a reliable basis be established for modelling frictional behaviour at the conditions of nucleation of earthquakes and SSEs in subduction zones.

2.5 Conclusions

In this study, we aimed to investigate the influence of effective normal stress and temperature in independently varied ranges relevant for the frictional properties of (simulated) subduction zone megathrust fault gouges. We conducted biaxial (double direct shear) experiments on both Nankai ODP (Leg 190, Site 1174) and Rochester illite gouge materials under wet conditions, at room temperature, low (effective) normal stresses of 5-30 MPa, at sliding velocities stepped in the range 0.16 to 18 $\mu\text{m/s}$. In addition, ring shear experiments were conducted on illite gouge, at temperatures of 200-300°C, an effective normal stress of 170 MPa and a pore fluid pressure of 100 MPa, at sliding velocities stepped in the range 1 to 100 $\mu\text{m/s}$. Our findings can be summarized as follows:

1. ODP material from inside and outside the décollement zone cored at Site 1174 showed velocity strengthening behaviour characterized by coefficients of friction of 0.33-0.41 at 10 mm displacement at (effective) normal stresses of 10-15 MPa and at room temperature. The friction coefficient was found to increase (weakly) with increasing normal stress.
2. At room temperature, illite gouge also showed velocity strengthening behaviour with the coefficient of friction increasing from 0.30 to 0.43, at a displacement of 10 mm, for normal stresses in the range 5-30 MPa. The velocity strengthening behaviour became more marked with increasing effective normal stress and broadly speaking with sliding velocity.
3. At room temperature and normal stresses above 5 MPa, both the ODP and illite gouges showed slip hardening at a rate that increased with applied normal stress and sliding velocity. This behaviour favours earthquake nucleation and SSE activity at low effective stresses.
4. The ring shear experiments performed on simulated illite gouge at 200-300°C displayed friction coefficients of 0.36-0.57 at displacements of 2-10 mm (shear strain 4-20). Above ~250°C, a transition from velocity strengthening to velocity weakening behaviour (with stick-slip at 300°C) was observed. The transition temperature decreased with decreasing sliding velocity. This means that despite the velocity strengthening seen in previous experiments at room temperature, velocity weakening in illite-rich fault gouge may well play a role in determining the depth of the updip limit of the seismogenic zone.
5. The microstructures of all of our deformed samples suggest a microscale shear mechanism that is initially controlled by distributed deformation and passive clay rotation, forming a foliation, and later by P- and R_1 -shearing with minor Y-shear activity at shear strain >1 or 2.
6. Our data for illite at 200-300°C suggest that key transitions between velocity strengthening and weakening in megathrust faults may occur at significantly different slip rates and temperatures than implied by experimental data on halite, granite and gabbro gouges that have been incorporated in modelling studies to date. This emphasises the need for friction studies on realistic megathrust fault rock materials, such as illite-quartz and muscovite-quartz materials, under true subduction zone conditions.

Acknowledgements

We thank Chris Marone and Brett Carpenter of the Pennsylvania State University for providing the illite gouge. We also thank Takehiro Hirose and Osamu Tadaï of Kochi Institute for Core Sample Research, JAMSTEC for help in conducting XRD analyses of

our starting materials. Tetsuhiro Togo and Keishi Okazaki are thanked for their assistance with the biaxial experiments at Hiroshima. Gert Kastelein, Thony van de Gon Netscher, Eimert de Graaff and Peter van Krieken provided technical assistance at Utrecht. We thank Martyn Drury for his guidance with the FIB-SEM work. Data analysis was performed using the XLook program developed at Pennsylvania State University. We also benefitted from discussions with André Niemeijer. This research used samples provided by IODP. This work was funded by means of a Toptalent grant awarded by the Netherlands Organisation for Scientific Research (NWO) to SdH (Dossier number 021.002.025).

Chapter 3

New constraints on megathrust slip stability under subduction zone P - T conditions

Sabine A.M. den Hartog, André R. Niemeijer and Christopher J. Spiers

Earth and Planetary Science Letters 353-354, 240-252, 2012

Abstract

To understand and model subduction zone seismogenesis, data are needed on the frictional properties of (meta)pelitic subduction zone materials under in-situ megathrust conditions. Here, we report the results of rotary shear friction experiments on simulated illite-quartz fault gouge at an effective normal stress of 170 MPa, a pore fluid pressure of 100 MPa, at 150-500°C and sliding velocities of 1-100 $\mu\text{m/s}$. The results show three temperature-dependent regimes, characterized by velocity-strengthening at 150-250°C, velocity-weakening at 250-400°C and velocity-strengthening at 400-500°C. The regimes are defined by a decrease in the rate and state friction (RSF) parameter ($a-b$) at 150-300°C followed by an increase at 300-500°C. These trends correlate with systematic changes in other RSF parameters, as well as an increase in friction coefficient above 300°C. We explain the effects of increasing temperature in terms of a transition from frictional granular flow (150-250°C), through granular flow whereby dilatation is balanced by thermally activated compaction involving stress corrosion cracking (SCC) of quartz clasts (250-400°C), to non-dilatant slip on the phyllosilicates with accommodation at quartz clasts by SCC (400-500°C). Taking into account the effects of sliding velocity, the observed velocity-weakening regime broadly explains the extent of the seismogenic zone within subduction megathrusts.

3.1 Introduction

The M_w 9.0 Tohoku-Oki earthquake of 11 March 2011 (e.g. Ide et al., 2011; Simons et al., 2011) dramatically illustrated the need to improve seismic and tsunami hazard evaluation capability. Such improvements depend on understanding seismic slip nucleation and propagation on subduction zone megathrusts.

Nucleation of earthquakes on megathrusts occurs in the seismogenic zone, bound at its up-dip and down-dip extremities by (conditionally) stable, aseismic zones (e.g. Hyndman et al., 1997; Schwartz and Rokosky, 2007). From focal depth data, the location of these boundaries appears thermally controlled, with the up-dip limit occurring at 100-150°C and the down-dip limit at approximately 350°C (Hyndman et al., 1997; Oleskevich et al., 1999). Where the fore-arc mantle wedge is reached at shallower depths than the 350°C isotherm, the down-dip limit moves to correspondingly shallower levels, probably due to the presence of aseismically deforming (talc-)serpentine (e.g. Hyndman and Peacock, 2003; Peacock and Hyndman, 1999).

The onset of seismogenesis at the up-dip limit on subduction megathrusts has often been attributed to the dehydration of smectites present in clay-rich accretionary sediments to form illite (Vrolijk, 1990), which also occurs at temperatures of ~100-150°C (e.g. Hower et al., 1976; Jennings and Thompson, 1986). However, experimental studies designed to test this hypothesis do not support it, showing only inherently stable (“velocity-strengthening”), aseismic behaviour in illite-rich gouge (Brown et al., 2003; Saffer and Marone, 2003; see also Ikari et al., 2009; Morrow et al., 1992; Tembe et al., 2010), at least at room temperature. An alternative hypothesis for the onset of seismogenesis on megathrusts at 100-150°C involves temperature- and depth-dependent lithification of the fault rock, which is argued to lead to potentially unstable (“velocity-weakening”) shear localization (e.g. Byrne et al., 1988; Marone and Scholz, 1988; Moore et al., 2007; Moore and Saffer, 2001). It has further been proposed that decreasing compaction and fluid production rates at temperatures beyond 150°C lead to diminishing fluid overpressures and hence higher effective normal stresses, destabilizing the megathrust (Marone and Saffer, 2007; Moore and Saffer, 2001). However, this would still require velocity-weakening material properties.

When thermally controlled, the down-dip seismogenic limit is widely believed to be determined by the transition from brittle to ductile behaviour (Hyndman and Wang, 1993; Hyndman et al., 1997; Peacock and Hyndman, 1999; Scholz, 1998). This is based on friction experiments on wet granite gouge, which show velocity-weakening behaviour at ~100-350°C but velocity-strengthening above this temperature (Blanpied et al., 1991; 1995; 1998). Similar trends have been observed using wet gabbro (He et al., 2007) and San Andreas Fault gouges (SAF; Tembe et al., 2009). However, it is unknown to what extent these data apply to subduction zone fault rocks (metapelites) and conditions. Nonetheless, the frictional properties of wet granitic, gabbroic, and dry halite (Shimamoto, 1986) gouges are widely used for modelling subduction zone seismicity (e.g. Liu and Rice, 2009; Matsuzawa et al., 2010; Shibazaki et al., 2010). The transition from velocity-strengthening to velocity-weakening shown by these materials at low temperatures, along with the reverse transition at higher temperatures, offers a possible explanation for the depth extent of the seismogenic zone (Scholz, 1988). At the same time, they remain poorly representative of the fault rocks

expected in subduction megathrusts (Den Hartog et al., 2012, Chapter 2). It follows that to model earthquake nucleation in subduction zones on a sound basis, friction experiments on realistic, pelitic materials, under in-situ megathrust conditions are needed.

Den Hartog et al. (2012, Chapter 2) recently presented preliminary data on the frictional behaviour of illite-rich gouge deformed at 170 MPa effective normal stress, 100 MPa pore fluid pressure and 200-300°C. These suggested a transition from velocity-strengthening to weakening at ~250°C. Here, we extend this dataset from 150 to 500°C, exploring frictional properties, including velocity dependence, at temperatures spanning the entire seismogenic zone within subduction megathrusts.

3.2 Material and methods

3.2.1 Sample material

The material used here consisted of crushed, illite-rich Rochester Shale (Folk, 1962), sieved to a grain size below 106 μm (Ikari et al., 2009). Saffer and Marone (2003) reported the same material to contain 59% illite clay, 23% quartz, 9% kaolinite/dickite clays and 4% plagioclase. Our own X-Ray Diffraction (XRD) analysis showed similar results but with minor chlorite instead of plagioclase and kaolinite/dickite.

3.2.2 Experimental apparatus and procedure

Frictional sliding experiments were performed using the ring shear machine (Fig. 3.1) described by Niemeijer et al. (2008). In this machine, a ~1 mm thick, ring-shaped sample is sandwiched between two roughened René 41 Superalloy pistons and kept in place by inner and outer confining rings (Fig. 3.1c). The sample-piston assembly is located inside an internally heated, 300 MPa pressure vessel filled with distilled water, which forms the pore fluid (Fig. 3.1a and b). Normal stress is applied via a pressure-compensated upper loading piston (Fig. 3.1b) and externally controlled using a 100 kN Instron loading frame. A servo-controlled motor and gearbox rotate the vessel and lower piston to produce shearing velocities of ~0.010 to ~300 $\mu\text{m/s}$. Rotary shear of the sample generates a shear stress and torque measured externally via the non-rotating upper piston. Note that normal stress (σ_n) is applied to the sample in excess of the fluid pressure (P_f) measured in the vessel, so that the effective normal stress (σ_n^{eff}) is equal to σ_n , assuming that the small sample is penetrated by the fluid, at pore fluid pressure P_f (demonstrated by P_f -stepping tests).

Rotary shear experiments were performed on pre-pressed rings of gouge, at an applied normal stress of 170 MPa, a fluid pressure of 100 MPa and temperatures of 150-500°C. Pre-pressing was conducted in the presence of water vapour, at 170 MPa for ~20 minutes at room temperature in a specially designed die, yielding porosities of ~12-19%, taking into account errors in volume and mass determination. The sliding velocity imposed during shear was either stepped between 1, 10 and 100 $\mu\text{m/s}$ or held constant at one of these velocities. Two experiments were performed under vacuum ("dry") at 200°C and 350°C, using otherwise identical conditions. Shear displacement (resolution $\pm 1 \mu\text{m}$), axial displacement ($\pm 0.05 \mu\text{m}$), normal force ($\pm 0.05 \text{ kN}$) and torque ($\pm 6 \text{ Nm}$) were measured externally and the corresponding signals logged, together with the pore fluid pressure ($\pm 0.005 \text{ MPa}$) and sample temperature ($\pm 1^\circ\text{C}$), using a 16 bit A/D converter at a frequency of 1-100 Hz.

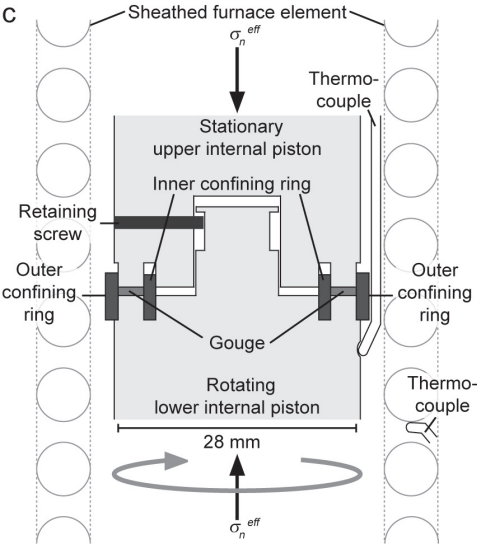
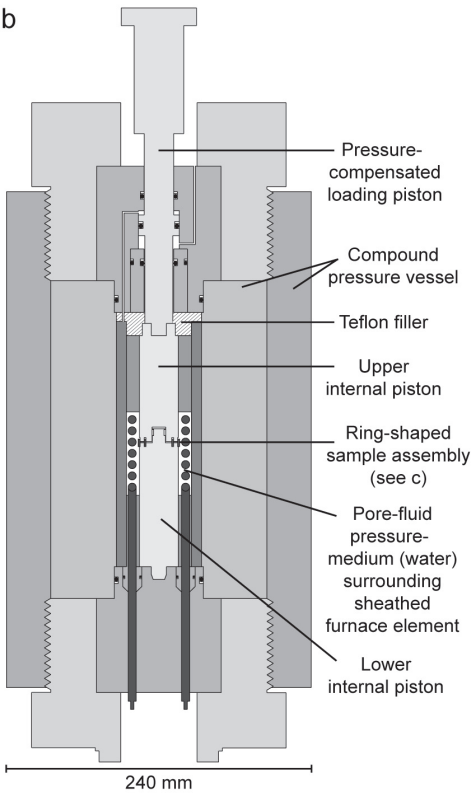
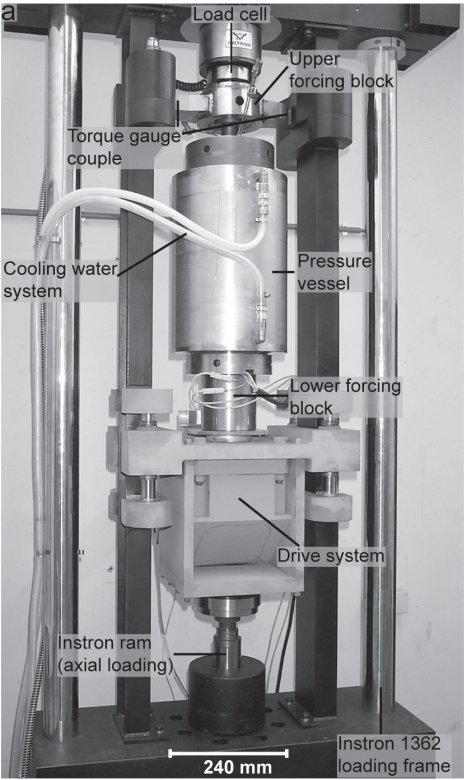


Figure 3.1 Ring shear machine used in the present study (after Niemeijer et al., 2008). (a) The rotary shear drive system and pressure vessel mounted inside the Instron loading frame. (b) Semi-schematic cross section of the pressure vessel. (c) Schematic cross section of the sample assembly. σ_n^{eff} = effective normal stress.

3.2.3 Data processing

Torque and normal force data were corrected for seal friction, and shear displacement for machine stiffness. The seal friction correction is estimated to be accurate to within ~9 Nm and ~0.2 kN for the torque and normal force, respectively. The corrected torque was converted to a shear force acting on the sample surface at the mean sample radius of 12.5 mm. The apparent coefficient of friction μ was calculated as $\mu = \tau / \sigma_n^{eff}$. Shear strain (γ) was obtained from the ratio of shear displacement to instantaneous sample thickness, determined from the final piston-sample assembly length and the axial displacement measured during each experiment. We used these data only to estimate the evolution of shear strain, because the axial displacement measurement included effects of extrusion of sample material and measurement errors in sample thickness (~5-10%) related to the remote location of the displacement transducer from the sample. This also made it impossible to reliably determine changes in porosity of the sample associated with compaction/dilatation.

The velocity dependence of friction was interpreted using the rate and state dependent friction (RSF) theory (Dieterich, 1978, 1979; Ruina, 1983), with the empirical Dieterich type ("slowness") formulation:

$$\mu = \mu_0 + a \ln\left(\frac{V}{V_0}\right) + b \ln\left(\frac{V_0 \theta}{d_c}\right) \quad \text{with} \quad \frac{d\theta}{dt} = 1 - \frac{V\theta}{d_c} \quad (3.1)$$

(e.g. Marone, 1998). Here, θ is an internal state variable, a represents the magnitude of the instantaneous change in μ upon a step change in sliding velocity from a value V_0 to a value $V = eV_0$, b reflects the magnitude of the change in μ during subsequent evolution to a new steady state value over a critical sliding distance d_c , and μ_0 is the friction coefficient measured at velocity V_0 . For changes in steady state friction coefficient ($\Delta\mu_{ss}$) resulting from a stepwise change in velocity, Eq. (3.1) yields:

$$(a - b) = \frac{\Delta\mu_{ss}}{\Delta \ln V} \quad (3.2)$$

(e.g. Marone, 1998). A positive ($a-b$) value indicates an increase in friction coefficient with increasing velocity, i.e. velocity-strengthening slip behaviour, which is inherently stable (e.g. Scholz, 1998). A negative ($a-b$) value means that the behaviour is velocity-weakening, which is potentially unstable.

Though Eq. (3.2) strictly applies only to steady state behaviour, friction experiments typically show slip hardening. We followed standard practice by detrending the μ versus displacement curves for background slip hardening or softening (inset in Fig. 3.2a), as described by Blanpied et al. (1998) and Tembe et al. (2010). In addition, a , b and d_c were determined individually by solving Eq. (3.1), coupled with an equation describing elastic interaction with the testing machine, using the fitting method described by Marone (1998) and Blanpied et al. (1998). Fitting solutions were highly sensitive to data quantity and quality per velocity step. For this reason, we used ($a-b$) values determined using Eq. (3.2), retaining individual a , b and d_c values when the fitted inversion fell within the error bars of the experimental data and when ($a-b$) matched the results of Eq. (3.2).

Table 3.1 List of experiments, conditions and key data. σ_n^{eff} = effective normal stress, T = temperature, P_f = pore fluid pressure, V = sliding velocity, μ = coefficient of friction and γ = shear strain.

Experiment	σ_n^{eff} (MPa)	T (°C)	P_f (MPa)	V ($\mu\text{m/s}$)	Final μ	Final gouge thickness (mm)	Final displacement (mm)	Final γ	Occurrence of stick-slip
RSRS07	170	200	100	10-100-10-1-10-100	0.79	0.46	49.2	107	no
RSRS09	170	300	100	10-100-10-1	0.77	0.23	23.6	102	at 1 and 10 $\mu\text{m/s}$
RSRS12	170	300	100	10	0.71	0.64	26.8	42	yes
RSRS16	170	250	100	10-100-10-1-10-100	0.69	0.59	40.1	68	no
RSRS18	170	250	100	10-100-10-1-10-100-10	0.75	0.48	39.6	82	no
RSRS28	170	200	100	100	0.76	0.54	56.5	105	no
RSRS38	170	350	100	10-100-10-1-10-100	0.81	0.64	33.9	53	at 10 and 100 $\mu\text{m/s}$
RSRS39	170	400	100	10-100-10-1-10-100	0.89	0.48	35.0	73	at 10 $\mu\text{m/s}$
RSRS40	170	450	100	10-100-10-1-10-100-10	0.91	0.52	40.6	78	no
RSRS43	170	500	100	10-100-10-1-10-100-10	0.95	0.66	47.5	72	no
RSRS46	170	350	100	10	0.93	0.42	41.8	99	yes
RSRS47	170	350	100	100	0.89	0.46	67.2	146	yes
RSRS48	170	350	100	1	0.92	0.56	43.6	78	yes
RSRS50	170	150	100	10	0.83	0.60	76.4	127	no
RSRS51	170	500	100	10	0.96	0.50	66.5	133	no
RSRS57	170	150	100	100	0.80	0.62	73.7	119	no
RSRS58	170	500	100	100	0.85	0.42	70.1	167	no
RSRS64	170	350	dry	10-100-10-1-10-100-10	0.82	0.80	40.3	50	no
RSRS65	170	200	dry	10-100-10-1-10-100-10	0.72	0.68	40.2	59	no
RSRS73	170	150	100	10-100-10-1-10-100-10	0.68	0.62	39.9	64	no

3.2.4 Microstructural methods

Microstructures were examined using an XL30S FEG Scanning Electron Microscope (SEM), a Focused Ion Beam (FIB) SEM (Nova 600) and Tecnai-20 FEG Transmission EM (TEM), all equipped with Energy-Dispersive X-ray (EDX) detectors. The FIB-SEM was used to mill cross-sections and TEM lamellae (< 100 nm thick) oriented tangentially to the rotary shear direction and perpendicular to the shear plane of the samples. Cross-sections were investigated in the FIB-SEM and lamellae in the TEM. High resolution images were analysed using SIS Scandium software to obtain average 2D grain diameters, and ImageJ to determine the area fraction of SEM-visible porosity (defined by setting an appropriate greyscale threshold).

3.3 Results

3.3.1 Mechanical data

Experimental conditions and key mechanical data are listed in Table 3.1. The evolution of μ with shear displacement and shear strain is shown in Fig. 3.2a and b, for a representative

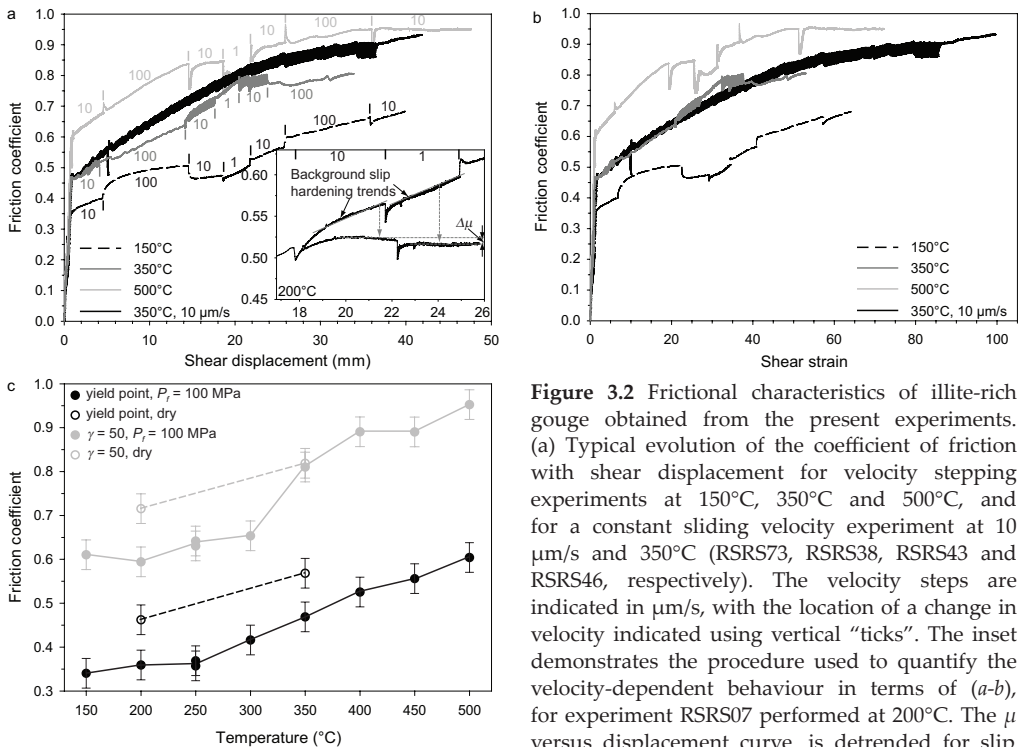


Figure 3.2 Frictional characteristics of illite-rich gouge obtained from the present experiments. (a) Typical evolution of the coefficient of friction with shear displacement for velocity stepping experiments at 150°C, 350°C and 500°C, and for a constant sliding velocity experiment at 10 $\mu\text{m/s}$ and 350°C (RSRS73, RSRS38, RSRS43 and RSRS46, respectively). The velocity steps are indicated in $\mu\text{m/s}$, with the location of a change in velocity indicated using vertical "ticks". The inset demonstrates the procedure used to quantify the velocity-dependent behaviour in terms of $(a-b)$, for experiment RSRS07 performed at 200°C. The μ versus displacement curve is detrended for slip

hardening based on the hardening rates measured in each consecutive step. (b) Same as (a) but with shear strain instead of displacement on the horizontal axis. (c) Friction coefficient versus temperature for velocity stepping experiments. The μ values are taken at either the yield point or at a shear strain of 50 and apply to a sliding velocity of 10 $\mu\text{m/s}$ (interpolated or extrapolated where necessary). Standard error propagation analysis showed that the error bar in friction coefficient is at most ± 0.034 . At 350°C, the mean and minimum μ -values obtained for stick-slip sliding behaviour differ by less than this error. Note that the increase in μ from 300°C to 400°C is three and seven times larger than the error bar at yield and at $\gamma = 50$, respectively. In (a) and (b), "noisy" portions of individual curves correspond to periods of stick-slip.

subset of experiments. All experiments showed a rapid increase in μ until apparent yielding at a displacement of ~ 1 mm ($\gamma \sim 1$ -2; Fig. 3.2a and b). This was followed by significant slip or strain-hardening (Fig. 3.2a and b) superimposed on the velocity steps (where applied), resulting in final friction coefficients (Table 3.1) ranging from 0.68 (150°C; velocity stepping) to 0.96 (500°C; 10 $\mu\text{m/s}$). At 150-300°C, the strain-hardening rate was roughly constant with shear strain (Fig. 3.2b). At temperatures of 350-500°C, however, the strain-hardening rate decreased with strain and steady state friction was approached from $\gamma \approx 35$. Unstable, oscillatory (stick-slip) events (Fig. 3.2a and b; Table 3.1) were occasionally observed at 300-400°C.

In general, higher friction coefficients were measured at higher temperatures (Table 3.1).

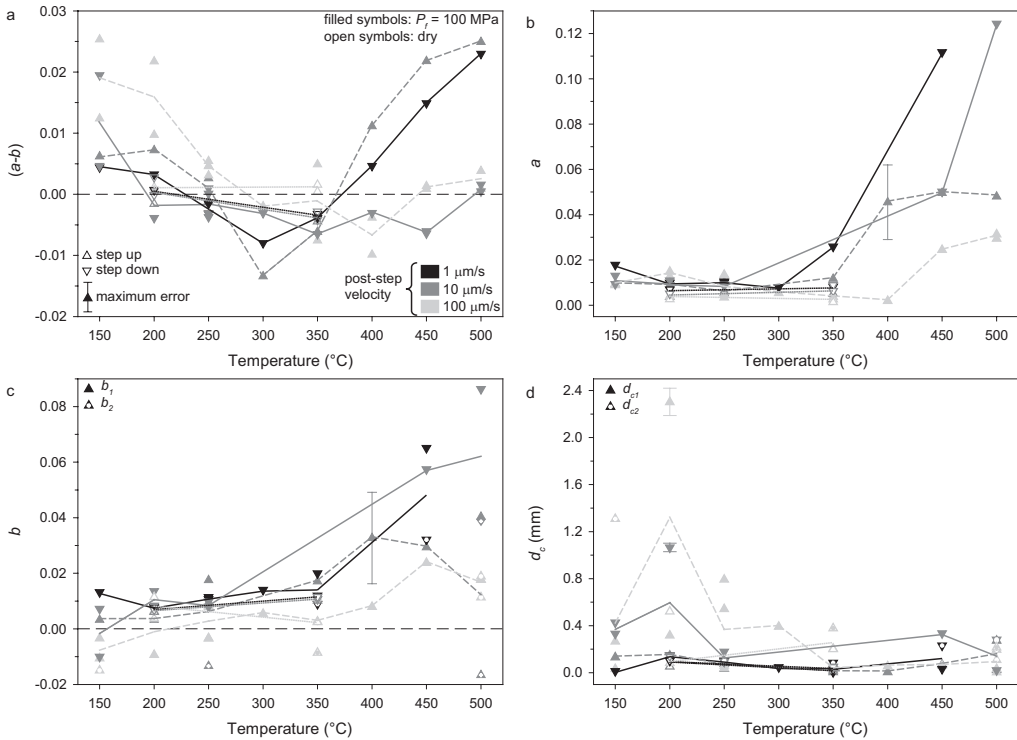


Figure 3.3 RSF parameters as a function of temperature obtained for the present illite-rich gouge. Grey-scales indicate the magnitude of the velocity imposed in performing each upward or downward velocity step - see (a). Solid tie-lines designate a step down in velocity, dashed a step up. Dotted tie-lines are fitted to the data for dry experiments, not distinguishing between steps up and down, since the results were similar. In the case of oscillatory (stick-slip) behaviour, average friction coefficients were used to obtain the various parameters. Peak μ values yield the same trends. The error in (a-b) is estimated to be within ± 0.0024 , as shown by the error bar inserted to the bottom left of (a). Error bars in (b)-(d) are smaller than the symbol size except where shown, and represent plus or minus one standard deviation. (a) Velocity dependence parameter $(a-b)$ versus temperature. Note that slight differences between the results shown here and shown previously by Den Hartog et al. (2012, Chapter 2) for the experiments at 200-300°C are due to improvements in data correction. (b) Values of a versus temperature. (c) Values of b versus temperature. A poor fit could sometimes be improved by using a version of Eq. (3.1) with an additional evolution term $b_2 \ln([V_0 \theta_2]/d_c)$ (e.g. Blanpied et al., 1998; Appendix 3.A, Fig. 3.A2). (d) Values of d_e versus temperature.

This is illustrated in Fig. 3.2c, which shows μ versus temperature at 10 $\mu\text{m/s}$ in the velocity stepping experiments. The μ values for the wet-tested illite-rich gouge at yield remain roughly constant at ~ 0.35 up to 250°C , increasing steadily to ~ 0.60 at 500°C . At a shear strain of 50, μ remains at ~ 0.6 up to 300°C . At 350°C , it increases to 0.81 and to ~ 0.9 at 400 – 500°C . A similar, slightly more rapid increase in μ was observed at $\sim 350^\circ\text{C}$ at all shear strains ($\gamma > 5$) and slip velocities.

The velocity dependence of friction is represented in Fig. 3.3a in terms of $(a-b)$ versus temperature. Three regimes can be identified for the wet experiments: predominantly velocity-strengthening ($[a-b] > 0$) below 250°C (Regime 1), mainly velocity-weakening ($[a-b] < 0$) between 250 and 400°C (Regime 2), and again mainly velocity-strengthening ($[a-b] > 0$) above 400°C (Regime 3). The transitions from velocity-strengthening to weakening and back at the boundaries between these regimes tend to occur at lower temperatures for steps between 1 and 10 $\mu\text{m/s}$ than those between 10 and 100 $\mu\text{m/s}$. Unlike the velocity stepping experiments, $(a-b)$ data obtained from the constant velocity experiments (Table 3.1) show no consistent sign or trends, probably reflecting sample-to-sample variability.

Individual values of a , b and d_c are shown versus temperature in Fig. 3.3b–d. Both a and b for the wet tests show a sharp increase from 300°C . At these temperatures (and sometimes lower in the case of b), both parameters decrease towards higher velocity. At 150 – 300°C , a and b are roughly constant. On average, d_c decreases with increasing temperature up to $\sim 300^\circ\text{C}$, and is generally higher at higher sliding velocities (Fig. 3.3d).

The dry control experiments show higher μ values, notably at yield (Fig. 3.2c), but reach steady state at a displacement of 20–30 mm ($\gamma \sim 30$ – 40), yielding lower average strain-hardening rates than the wet experiments. As in the wet experiments, the dry experiments show an increase in μ from 200°C to 350°C (Fig. 3.2c). However, the $(a-b)$ values obtained for dry samples are near neutral (Fig. 3.3a) and a , b and d_c show little or no effect of temperature.

3.3.2 Microstructural observations

SEM inspection of pre-pressed ring material demonstrated strong reduction of the quartz grain size from an initial value of ~ 20 – $60\ \mu\text{m}$ to $< 10\ \mu\text{m}$ during the pre-pressing stage. In the FIB-SEM, this material shows sub-rounded quartz grains of ~ 0.5 – $5\ \mu\text{m}$ in diameter, surrounded by a matrix of fine phyllosilicates (~ 0.4 – $5\ \mu\text{m}$ in length by ~ 0.1 – $0.6\ \mu\text{m}$ in width) with a sub-horizontal preferred orientation, anastomosing around the quartz grains (Fig. 3.4a). Elongated pores are visible at both grain and interphase boundaries. The SEM-detectable porosity is ~ 10 – 12% , in reasonable agreement with ~ 12 – 19% calculated from the sample volume, mass and mineral densities.

The microstructure developed after wet deformation at 150°C (Fig. 3.4b) shows a marked reduction in porosity and phyllosilicate matrix grain size. Sub-rounded, angular and fractured quartz grains of ~ 0.5 – $3\ \mu\text{m}$ are embedded in the fine phyllosilicate matrix, with little discernible foliation visible at the SEM-scale. Elongated pores up to $\sim 3\ \mu\text{m}$ in length are concentrated at quartz-phyllosilicate interfaces and account for an SEM-visible porosity of ~ 1 – 2% . The microstructures of samples sheared at 250°C and 300°C show a progressive

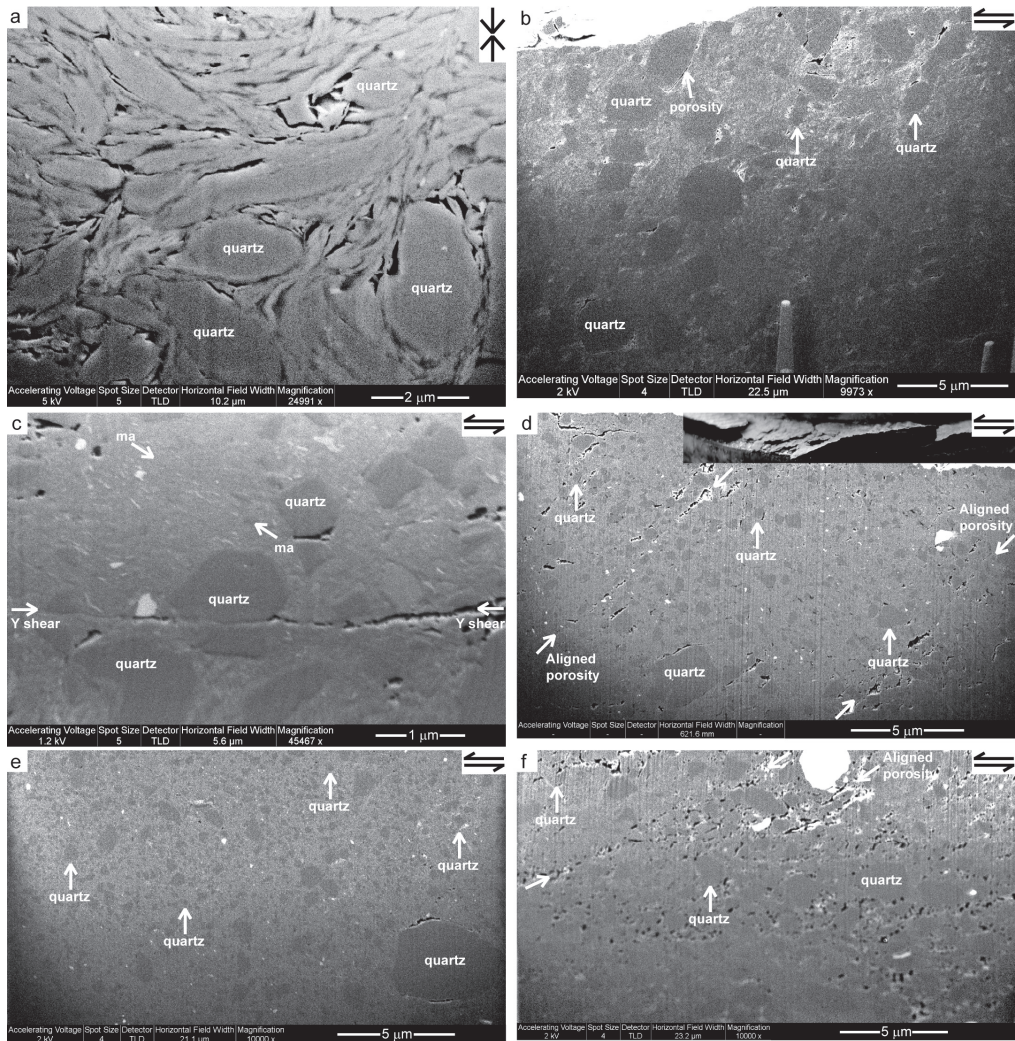


Figure 3.4 Sample microstructures, as imaged using FIB-SEM in backscatter mode. Compaction and shear directions are as indicated with black arrows. (a) Starting microstructure, after pre-pressing but before shearing. (b), (c), (d) and (e) Microstructures of respectively RRS50, RRS16, RRS46 and RRS51, sheared at a pore fluid pressure of 100 MPa and temperatures of 150°C, 250°C, 350°C and 500°C, either at a constant velocity of 10 $\mu\text{m/s}$ (b, d and e) or in velocity stepping mode (c). Note that the horizontal white streaks in (b) are the result of charging effects emanating from pores. In (c), the alignment of phyllosilicates in the P shear orientation is denoted as a mineral alignment, “ma”. In (d), sample handling resulted in anticlockwise rotation of the shear plane from the horizontal by about 30°. The original orientation is shown in the inset. Note the prominent R_1 shears in both images. (f) Microstructure of RRS64, performed dry, at sliding velocities stepped between 1 and 100 $\mu\text{m/s}$ at a temperature of 350°C.

decrease in quartz grain size to $\sim 1 \mu\text{m}$ and the development of a weak alignment of sub-micron phyllosilicates in the P shear orientation of Logan et al. (1992) (Fig. 3.4c). SEM-visible porosity remains $\sim 1\text{-}2\%$, the pores being concentrated in occasional Y shears and at quartz grain margins. Note that potential effects of decompression and cooling on porosity

are expected to be similar for all experiments, so these should not affect the comparison between samples.

The sample deformed wet at 350°C (Fig. 3.4d) shows slightly finer, sub-angular quartz grains, with mean grain size $\sim 0.4 \mu\text{m}$. Porosity is again visible, amounting to $\sim 1\text{-}2\%$, with the pores partly concentrated in bands in the R_1 -direction. The sample deformed wet at 500°C (Fig. 3.4e) shows similar, very fine (generally $< 1 \mu\text{m}$), sub-angular to oval quartz grains embedded in the sub-micron phyllosilicate matrix. No foliation or internal shear band structures are observed at the SEM-scale. Moreover, pores are no longer visible, apart from a very few at the boundaries of larger quartz grains.

The SEM microstructures of the wet-tested samples (Fig. 3.4b-e) show porous bands in the R_1 shear orientation at 350°C only (Fig. 3.4d). However, during recovery, samples deformed at 150-350°C disintegrated along spaced fractures in the R_1 -direction, especially at 350°C, suggesting the presence of spaced R_1 shear bands, which may not always be visible due to SEM sampling effects. Neither R_1 -oriented fractures nor porous bands were apparent in the samples deformed above 350°C.

TEM images of our wet-tested samples are depicted in Fig. 3.5. Phyllosilicate lattice spacings measured from high-resolution images of all samples (e.g. high-resolution versions of Fig. 3.5a, b, d-f) show an interlayer spacing mostly corresponding to that of illite (10 \AA) and/or muscovite (10.04 \AA), and occasionally chlorite (14.3 \AA) or kaolinite (7.15 \AA ; cf. Meunier, 2005; Meunier and Velde, 2004). Interlayer spacing determined from electron diffraction patterns yielded average values of 9.9 \AA , consistent with illite. Neither the lattice spacing nor electron diffraction data show systematic differences in phyllosilicate structure between the starting (Fig. 3.5a) and deformed material (Fig. 3.5b-f) over the range 150-500°C. This was confirmed by XRD measurements (Appendix 3.A, Fig. 3.A1). No dislocations could be imaged in the phyllosilicates, but bending (Fig. 3.5d and f) may indicate increased crystal plasticity at 350-500°C. Compared to the phyllosilicates in the starting material, which show a grain size of $\sim 100\text{-}350 \text{ nm}$ length by $\sim 30 \text{ nm}$ width and larger in the TEM (Fig. 3.5a, cf. SEM image Fig. 3.4a), those in the wet-deformed samples are reduced to only $\sim 40\text{-}100$ by $\sim 10\text{-}40 \text{ nm}$ at all temperatures (Fig. 3.5b-f). At 150°C, these nano-grains locally show an alignment (Fig. 3.5b) that anastomoses around the quartz clasts. At 350°C, the phyllosilicates also wrap around the clasts, forming a microstructure with no overall preferred orientation and with pores clearly developed in the neighbourhood of the clasts (Fig. 3.5c). At 500°C, the phyllosilicate foliation again anastomoses around the quartz grains but now shows an overall alignment roughly in the P shear orientation, i.e. at $\sim 20\text{-}30^\circ$ to the shear plane (Fig. 3.5e and f).

The microstructure of the sample deformed dry at 350°C, as imaged using the FIB-SEM (Fig. 3.4f), displays a lower quartz/phyllosilicate ratio than the wet equivalent (Fig. 3.4d), and has higher visible porosity ($\sim 3\%$) and slightly larger mean quartz grain size ($\sim 0.9 \mu\text{m}$). The visible porosity in the dry sample is partly concentrated in bands in an R_1 shear orientation, similar to that observed under wet conditions at 350°C (Fig. 3.4d). Like the wet sample, the dry ones fractured on macroscopic R_1 shears during sample recovery.

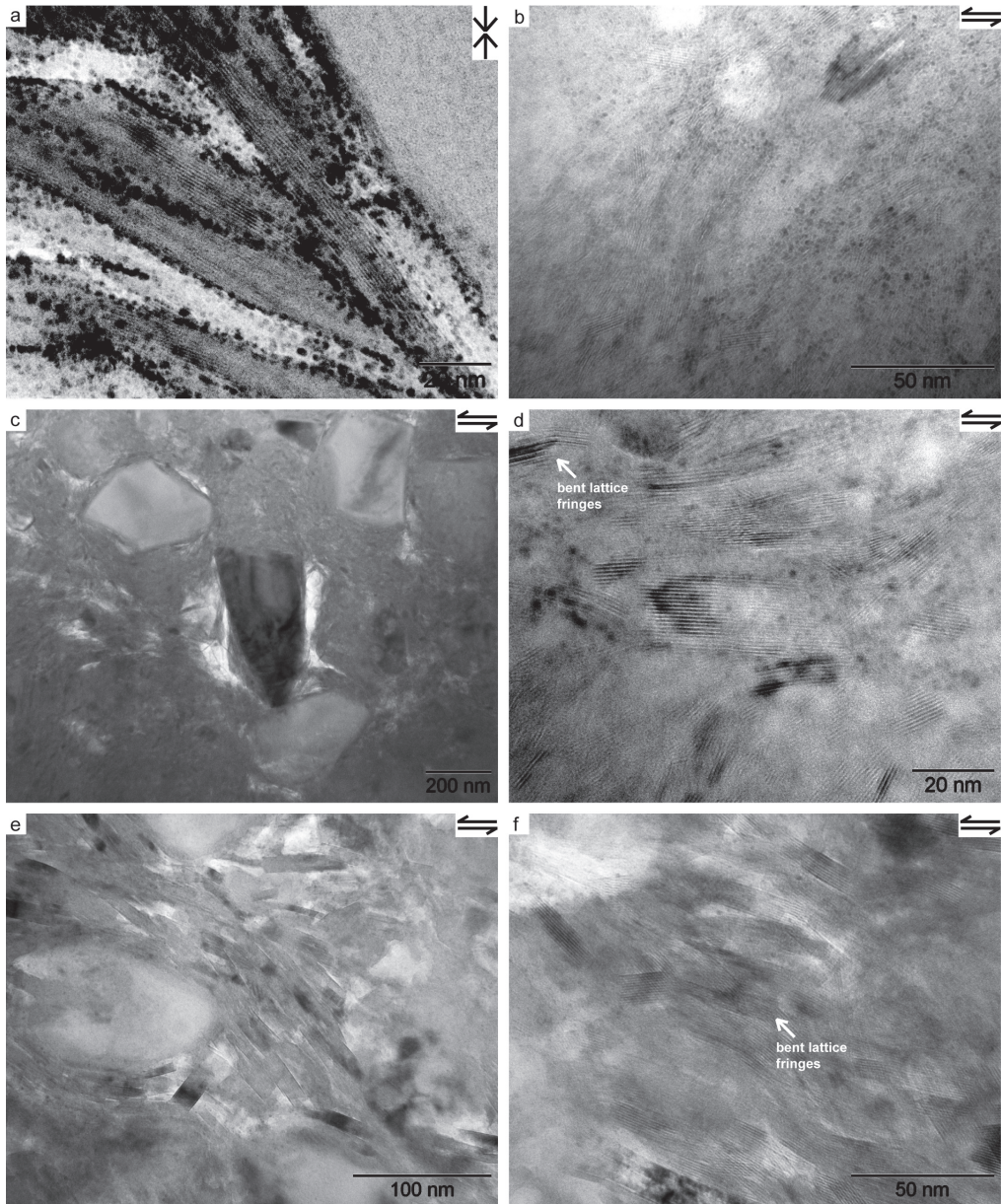


Figure 3.5 Microstructures of the phyllosilicate matrix imaged using TEM (bright field). Compaction/shear directions as indicated. (a) Starting microstructure, after pre-pressing but before shearing. (b)-(f) Microstructures of RSR50 (150°C; b), RSR546 (350°C; c and d), and RSR551 (500°C; e and f), sheared at a pore fluid pressure of 100 MPa and a sliding velocity of 10 $\mu\text{m/s}$. Note the pores around the clasts in (c), visible as light patches, and the phyllosilicates wrapping around individual quartz clasts.

3.4 Discussion

The current experiments on wet illite-rich gouge show three regimes of velocity dependence (Fig. 3.3a), essentially characterized by velocity-strengthening at 150-250°C (Regime 1), velocity-weakening at 250-400°C (Regime 2) and velocity-strengthening at 400-500°C (Regime 3). These regimes reflect a decrease in $(a-b)$ up to ~300-350°C and an increase at higher temperatures. This change in behaviour is also reflected in other frictional parameters, with (i) a decrease of d_c between 150°C and 300-350°C, and (ii) an increase of μ , a and b above ~300-350°C. In addition, the deformed gouges showed clearly developed R_1 shears only at temperatures $\leq 350^\circ\text{C}$, a reduction in quartz grain size from Regime 1 to 2, and development of SEM-visible porosity in Regimes 1 and 2 compared with Regime 3. The dry experiments exhibited near neutral velocity dependence and little or no dependence of μ , $(a-b)$, a , b or d_c on temperature, at least up to 350°C. In the following, we compare our result with previous work, attempt to explain our findings and assess their implications.

3.4.1 Temperature-dependent frictional properties: present versus previous work

Similar three-regime behaviour has been observed for wet SAF (illite-smectite-quartz gouge; Tembe et al., 2009), wet granite (Blanpied et al., 1991; 1995; 1998) and wet quartz-biotite gabbro gouges (He et al., 2007), deformed in saw-cut shear experiments. Particular similarity exists regarding the temperature dependence of $(a-b)$, with the velocity-weakening regime (Regime 2) falling in roughly the same temperature range for all these materials. Though less complete, the data on wet quartz gouge obtained by Chester and Higgs (1992; see also Blanpied et al., 1998) at similar conditions also point to velocity-weakening around 300°C with velocity-strengthening occurring at 23°C and 600°C. In experiments on illite-rich gouge performed at 200, 400 and 600°C, and at similar normal stress, pore fluid pressure and velocity conditions to our tests, Moore et al. (1986, 1989) found stick-slip behaviour at 400°C only, also suggesting three-regime behaviour.

The correspondence of the “slip-stability” regimes observed for these different materials suggests that the mechanisms controlling the velocity-dependent behaviour seen in our wet illite-rich gouge, and in other materials, are not specific to illite-rich materials, but reflect more general properties of the silicates present, the influence of mineral changes, the effects of common mineralogical components (quartz, phyllosilicate), or else fluid or fluid-rock interaction effects. A role of fluids is supported by the fact that dry samples tested in this study, and by others at similar temperatures (Blanpied et al., 1991; 1995; 1998; Chester and Higgs, 1992; He et al., 2006), show near velocity-neutral behaviour.

Besides the decrease in $(a-b)$ exhibited by our wet samples at 150-300°C, followed by the increase at 300-500°C (Fig. 3.3a), our data show that μ , a and b are almost independent of temperature below 300°C but increase with temperature above 300°C. An increase in μ between 200 and 600°C is also reported by Moore et al. (1986, 1989) for illite-rich gouge. Similarly, an increase in μ was observed by Tembe et al. (2009) for SAF gouge, from 0.41 at 96°C to 0.73 at 431°C, with the largest increase occurring between 250 and 350°C, though σ_n^{eff} was increased alongside the temperature. Finally, for muscovite-rich fault gouge sheared at effective normal stresses of 20-100 MPa, a pore fluid pressure of 100 MPa and 20-700°C, Van Diggelen et al. (2010) reported an increase in μ from a near constant value of ~0.4 below 250°C to ~0.55 at 450-700°C, as well as stick-slip events at 400-500°C versus otherwise stable

sliding (cf. Mariani et al., 2006, who reported stick-slip behaviour in muscovite-rich gouge at 600°C also). The resemblance of these results to our findings suggests that illite-rich and muscovite-rich gouges behave similarly under wet conditions at elevated temperatures. Hence, our results may be of broader relevance for metapelitic subduction zone materials below the up-dip seismogenic limit, even beyond the illite-muscovite transition at ~200–300°C (Merriman and Frey, 1999).

3.4.2 Microscopic shear mechanisms

The present data for wet illite-rich gouge imply a change in microscale processes controlling frictional strength and stability between 150 and 500°C, leading not only to the three regimes of behaviour observed but to a decrease in $(a-b)$ at 150–300°C, an increase in $(a-b)$ above ~300°C, and increases in μ , a and b above ~300°C.

Possible phenomena and processes that might explain these changes with increasing temperature include (i) a change in the mineralogy or phyllosilicate structure (illite → muscovite), (ii) a change in the properties of water, notably around the critical point, (iii) an increase in the importance of crystal plasticity and (iv) an increase in the importance of fluid-assisted deformation processes. Changes in mineralogy or structure (i) are not likely to have been important, since the XRD patterns for samples deformed at different temperatures closely resembled each other and the interlayer spacing of the phyllosilicates showed no consistent change with temperature. Regarding (ii), the temperature range investigated here encompasses the critical temperature of water (374°C), at which point its properties (e.g. density, solute-bearing capacity) change sharply depending on pressure (Lemmon et al., 2010; Wagner and Pruss, 2002). However, at the fluid pressure we used (100 MPa), these sharp changes are absent (Lemmon et al., 2010; Wagner and Pruss, 2002). This, combined with the observed effect of velocity on the transition-temperature from Regime 2 to 3 (Fig. 3.3a), makes explanation (ii) unlikely.

The onset of crystal plasticity (explanation iii) is sometimes put forward to explain the changes in $(a-b)$ with temperature in granite, gabbro and quartz gouges, notably the transition from velocity-weakening to strengthening above ~350°C (Scholz, 1998). However, at the conditions of our experiments, negligible plastic flow occurs in quartz (see data given by Hirth and Tullis, 1994; Rutter and Brodie, 2004). Much more evidence exists for stress corrosion cracking (SCC) and for the onset of pressure solution in quartz at 300–350°C (explanation iv); Schutjens, 1991). Previous work does suggest plastic deformation of phyllosilicates already at room temperature (Mares and Kronenberg, 1993; Saffer and Marone, 2003), but the flow strength is relatively temperature-insensitive (Kronenberg et al., 1990; Mares and Kronenberg, 1993; Mariani et al., 2006). Moreover, we observed only minor plastic bending of phyllosilicates (Fig. 3.5) at and above 350°C. Velocity-dependent grain boundary frictional behaviour controlled by asperity micro-plasticity involving an atomic jump process at the micro-/nano-asperity scale in the quartz or phyllosilicate (e.g. Rice et al., 2001) also fails to explain our results as this would imply a linear increase of a with temperature. In addition, a series of experiments on pure muscovite (crushed, optical-quality, single crystals), to be reported elsewhere, showed predominantly velocity-strengthening at 200–600°C. Taking into account the almost indistinguishable structure of illite (K-deficient muscovite; Rieder et al., 1998) and muscovite, these results demonstrate

that plasticity or fluid-rock interaction occurring in the phyllosilicates alone cannot explain our results, i.e. quartz plays an essential role.

On this basis, noting that the three-regime behaviour seen in our wet tests is absent in dry samples, we suggest that the observed changes in frictional behaviour and microstructure are likely related to increasing contributions of pressure solution and/or SCC of quartz grains with increasing temperature (see also Blanpied et al., 1991; 1995; 1998; Chester and Higgs, 1992). However, a monotonic increase in the rate of these thermally activated processes would not lead to the observed three regimes. One model which does predict such behaviour is that suggested by Niemeijer and Spiers (2007) for three-regime behaviour in muscovite/halite mixtures (fault gouge analogue) undergoing shear deformation at conditions favouring pressure solution of the halite plus intergranular slip on the phyllosilicates. This model for fault gouge behaviour should apply to any soluble solid plus phyllosilicate mixture. It predicts that at low temperatures or rapid slip rates, where pressure solution is too slow to accommodate significant shear deformation or compaction, deformation will occur by frictional (critical state) granular flow producing velocity-neutral or velocity-strengthening behaviour, depending on whether intergranular slip on the phyllosilicate phase is itself velocity-neutral (as assumed by Niemeijer and Spiers, 2007) or velocity-strengthening, as often observed in experiments on pure phyllosilicates (e.g. Ikari et al., 2011). At higher temperatures or lower slip rates, pressure solution becomes fast enough to allow compaction (to sub-critical state porosities) at a rate that balances dilation due to granular flow, while being too slow to contribute significantly to shear deformation. Under these conditions, increasing the slip velocity increases the granular dilation rate thus increasing the porosity until grain contacts are small enough, and contact stresses high enough, to enable the rate of pressure solution compaction to balance that of dilation. This produces a steady state porosity that increases with sliding velocity (Niemeijer and Spiers, 2007). Since the dilation angle associated with granular flow must decrease with increasing porosity (as critical state is approached), the frictional strength of the material accordingly decreases with increasing velocity, yielding velocity-weakening slip. At still higher temperatures or lower velocities, compaction by pressure solution is efficient enough to eliminate the porosity so that the strength of the gouge approaches the Byerlee failure strength for the dense material (Byerlee, 1978), yielding transitional, velocity-neutral behaviour. At even higher temperatures or lower rates, pressure solution is fast enough to contribute to shear deformation by accommodating slip on the phyllosilicates with zero porosity development but with the development of a foliation. Frictional sliding on this foliation, accommodated by pressure solution of the intervening pressure-dissolving clasts, then leads to velocity-strengthening as the resistance to deformation is controlled by frictional sliding plus serial pressure solution, the latter obeying a classical rate law (Bos et al., 2000; Bos and Spiers, 2002; Niemeijer and Spiers, 2005, 2006).

The three-regime behaviour predicted by the Niemeijer and Spiers (2007) model closely resembles that seen in the present experiments. Applying it directly yields the following interpretation. At the lowest temperatures, thermally activated compaction by pressure solution or SCC is negligible, yielding a relatively high porosity and low dilatation angle. As a result, velocity-strengthening behaviour measured for (near-)pure phyllosilicates (e.g. Ikari et al., 2011; Moore and Lockner, 2008) dominates. As temperatures approach ~300-

350°C, more efficient, thermally activated compaction results in a denser microstructure, characterized by a higher dilatation angle, causing a larger increase in porosity and hence a decrease in frictional strength in an upward velocity step. Competition between intergranular dilatation and thermally activated compaction by pressure solution or SCC can therefore explain the observed decrease of $(a-b)$ with increasing temperature at 150–350°C, as well as the transition from Regime 1 to 2. Above ~300–350°C, thermally activated compaction is expected to become still more efficient. Following the Niemeijer and Spiers (2007) model, we suggest it results in a microstructure that is sufficiently dense (cf. Fig. 3.4e) that the frictional strength increases to approach Byerlee's rule. With ongoing increase in temperature, the thermally activated mechanism of pressure solution or SCC causing compaction will become so efficient that it can fully accommodate slip on or between the phyllosilicates, so that dilatation is no longer needed, yielding the observed switch to velocity-strengthening.

The above interpretation fits the main changes observed in $(a-b)$, μ and visible sample porosity with temperature (Fig. 3.3a, 3.2c and 3.4). The clast/matrix microstructures observed in Regimes 1 and 2 are also largely consistent with the granular flow implied by the model for lower temperatures where thermally activated processes cannot accommodate slip between the phyllosilicates. However, in Regime 3, while we observed a phyllosilicate foliation anastomosing around the quartz clasts at the TEM-scale, we could find no evidence for deformation of the quartz by pressure solution to form tailed porphyroclasts (cf. Bos et al., 2000; Niemeijer and Spiers, 2007). In this regime, the quartz clasts were sub-angular or oval, and reduced in size compared with Regime 2. Moreover, a simple calculation (cf. Niemeijer and Spiers, 2005) of the rate of pressure solution, for the present conditions and quartz grain size, yields a strain rate that is at least one order too low to accommodate the strain rate imposed. We therefore infer that the dominant thermally activated mechanism in our experiments is SCC, perhaps accompanied by minor pressure solution. The higher porosity observed in the dry sample (Fig. 3.4f) supports the importance of a fluid-assisted mechanism in bringing about compaction. Progressive refinement of quartz by SCC followed by increased mixing with phyllosilicates, could also contribute to the observed slip/strain-hardening (Den Hartog et al., 2012, Chapter 2). It remains difficult to explain the R_1 shears developed at temperatures $\leq 350^\circ\text{C}$ in terms of the Niemeijer-Spiers model (2007). Though we did not observe boundary shears, we cannot exclude their occurrence. However, the strongly and pervasively reduced grain size suggests a major role of distributed deformation consistent with the Niemeijer and Spiers (2007) model.

3.4.3 Implications for seismogenesis

The observed changes from velocity-strengthening to weakening and back, with increasing temperature, correspond to those expected downwards along a subduction megathrust. Regime 2 could thus be considered as equivalent to the seismogenic zone, assuming elastic stability conditions are also met (e.g. Paterson and Wong, 2005; Scholz, 1998). If this comparison is valid, the boundaries between Regimes 1 and 2 and Regimes 2 and 3 correspond to the up- and down-dip seismogenic limits, respectively. In our data, the temperature range encompassed by velocity-weakening (Fig. 3.3a) depends on sliding velocity. The tie-lines fitted to $(a-b)$ data for a velocity step from 1 to 10 $\mu\text{m/s}$ (shear strain rate $\sim 10^{-2} \text{ s}^{-1}$) yield transition temperatures of $\sim 255^\circ\text{C}$ and $\sim 370^\circ\text{C}$. The latter temperature

corresponds well with that of 350°C associated with the down-dip limit of the seismogenic zone, but the former is ~100°C higher than the 150°C associated with the up-dip limit (e.g. Hyndman et al., 1997). On the other hand, displacement rates during earthquake nucleation are expected to be 1-5 orders lower than applied here, with the lowest rates approaching plate velocities of $\sim 10^{-9}$ m/s (Segall and Rice, 2006), equivalent to shear strain rates of 10^{-9} - 10^{-6} s $^{-1}$ in a 1 m – 1 mm wide shear zone. Viewed in this context, the velocity dependence of the low temperature boundary of Regime 2 (Fig. 3.3a) suggests a shift towards the up-dip limit of 150°C at natural strain rates. However, the same reasoning would yield too low a temperature for the down-dip limit, unless there are additional effects on (*a-b*) of factors such as σ_n^{eff} (He et al., 2007). The present data are too limited to allow reliable extrapolation, but reasonable correspondence is seen between our data and the temperatures characterizing the seismogenic zone.

Returning to the widely cited hypothesis that it is the growth of illite from smectite that causes the onset of seismogenesis at the up-dip seismogenic limit at ~150°C, it will be recalled that this is not supported by previous room temperature experiments on illite-rich gouge (Brown et al., 2003; Ikari et al., 2009; Morrow et al., 1992; Saffer and Marone, 2003; Tembe et al., 2010). Our findings suggest that the necessary velocity-weakening behaviour at temperatures > 150°C is caused by the presence of illite, quartz or the combination, with quartz likely playing an important role.

Besides velocity-weakening, earthquake nucleation and unstable slip generally require strain-neutral or softening behaviour (e.g. Rice, 1983). However, our wet experiments showed strain-hardening, reaching a steady state friction coefficient only above ~350°C at $\gamma > \sim 35$ (Fig. 3.2b). At lower temperatures, a steady state may be achievable, but at shear strains exceeding those attained here ($\gamma \approx 130$). Thus, unstable behaviour should be favoured towards higher temperature and strain rate, where strain-hardening is least. On the other hand, the reduced strain-hardening rates in the dry experiments suggest that strain-hardening may be largely due to preferential loss of phyllosilicates, an effect that would not occur in natural fault zones. Moreover, strain-hardening is expected to be counteracted in nature by broadening of the fault zone (e.g. Ben-Zion and Sammis, 2003) or by the development of an interconnected phyllosilicate fabric (e.g. Collettini et al., 2009; Niemeijer et al., 2010).

3.4.4 Implications for modelling studies

To date, models reproducing earthquake nucleation in subduction zones (e.g. Hori et al., 2004; Liu and Rice, 2005), or generating Slow Slip Events (SSEs) (e.g. Liu and Rice, 2009; Matsuzawa et al., 2010; Shibazaki and Shimamoto, 2007), have relied on assumed frictional characteristics or on those determined for materials such as dry halite (Shimamoto, 1986), wet granite (Blanpied et al., 1991; 1995; 1998) or gabbro gouges (He et al., 2007). These models typically require a depth and/or temperature distribution of (*a-b*). Den Hartog et al. (2012, Chapter 2) provided such a distribution based on experiments on illite-rich gouge at temperatures up to 300°C and compared this with the distributions used in modelling studies by Liu and Rice (2005) and Shibazaki and Shimamoto (2007), for the example of the southwest Japan subduction zone (Shikoku). A revised and extended version of this distribution is shown in Fig. 3.6a, based on the full three-regime behaviour determined

here for illite-rich fault gouge under in-situ P - T conditions. The transition from velocity-strengthening to weakening based on the illite data, at $\sim 255^\circ\text{C}$, lies at a higher temperature than the $\sim 100^\circ\text{C}$ assumed by Liu and Rice (2005) and Shibazaki and Shimamoto (2007), but may correspond better at natural strain rates in accordance with the decrease of transition temperature with decreasing strain rate evident in Fig. 3.3a. The transition back to velocity-strengthening found here, on the other hand, occurs at similar temperatures to those assumed in the modelling studies. A significant difference in the $(a-b)$ profile produced from our data is seen in the magnitude of our minimum and maximum $(a-b)$ values. These are more negative and positive, respectively, in the velocity-weakening and high temperature (450-500 $^\circ\text{C}$) velocity-strengthening fields than in the above modelling studies. To complement our $(a-b)$ profile, a , b , d_c and μ profiles are added in Fig. 3.6b.

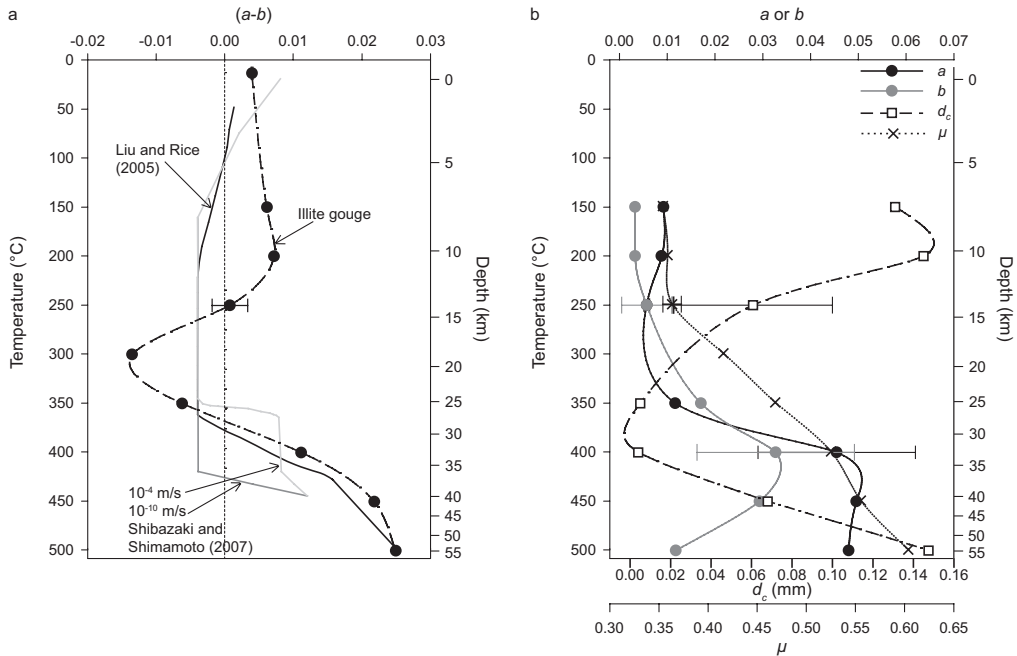


Figure 3.6 (a) Comparison of present and previously assumed $(a-b)$ values versus temperature. The profile of Liu and Rice (2005) for the example of the Shikoku subduction zone plus two profiles of Shibazaki and Shimamoto (2007) are given, for different sliding velocities. The profiles given in the two respective studies are based in part on data for wet granite (Blanpied et al., 1998) and dry halite (Shimamoto, 1986), respectively. Data for illite-rich gouge from the current study are added for comparison, taking the room temperature data from Den Hartog et al. (2012, Chapter 2), who performed biaxial experiments at 5 MPa normal stress under water-wet conditions. Higher temperature $(a-b)$ values are those calculated from velocity steps from 1 to 10 $\mu\text{m/s}$, obtained in the present study. The error bars represent plus or minus one standard deviation. The dashed trend line is added to data obtained in the present study for clarity. The pressure-temperature path for Shikoku of Peacock (2009) is used. (b) Profiles of a , b , d_c and μ versus temperature. Values of a , b and d_c apply to velocity steps from 1 to 10 $\mu\text{m/s}$, obtained in the present study. Values of μ are taken at the yield point, to exclude effects of strain hardening. Error bars represent plus or minus one standard deviation.

The present results provide frictional characteristics, under approximate in-situ conditions, of material that is a much more realistic representation of the fault rocks expected in

subduction megathrust fault zones than the data used for modelling so far. The results are surprisingly similar to those for granite in terms of the general effect of temperature on (a - b) and on the observed three-regime behaviour. At the same time, there are important differences that should be incorporated in modelling work. In addition, illite undergoes a transition to muscovite at ~ 200 - 300°C (Merriman and Frey, 1999), which might influence the profiles shown in Fig. 3.6. Though likely similar to illite-quartz gouge, the frictional characteristics of muscovite-quartz mixtures under in-situ conditions therefore need to be investigated to obtain a better understanding of friction in the deeper portions of megathrust seismogenic zones. Moreover, the microphysical model used to explain our results needs to be quantitatively compared with the experimental results for relevant materials to more reliably extrapolate (a - b) to the in-situ conditions within megathrusts.

3.5 Conclusions

In this study, we aimed to determine the frictional characteristics of realistic subduction zone materials under in-situ megathrust conditions. We performed rotary shear friction experiments on illite-rich fault gouge at an effective normal stress of 170 MPa, a pore fluid pressure of 100 MPa, at 150 - 500°C and sliding velocities of 1 - $100\ \mu\text{m/s}$. Our main findings are as follows:

1. Three temperature-dependent regimes exist, essentially characterized by velocity-strengthening at 150 - 250°C (Regime 1), velocity-weakening at 250 - 400°C (Regime 2) and velocity-strengthening at 400 - 500°C (Regime 3). These regimes are reflected in the microstructures of the gouge after deformation, showing a reduction in quartz grain size from Regime 1 to 2, a decrease in visible porosity from Regime 2 to 3 and clearly developed R_1 shears only in Regimes 1 and 2.
2. The frictional behaviour shows a marked change at $\sim 300^\circ\text{C}$. At lower temperatures, (a - b) and d_c decrease with increasing temperature and a and b are roughly constant, whereas at higher temperatures (a - b) as well as a and b increase with increasing temperature and d_c is approximately constant. In addition, μ shows an increase at temperatures above $\sim 300^\circ\text{C}$.
3. With increasing temperature, the processes operating at the microscale are inferred to change from predominantly granular flow controlled by velocity-strengthening friction in the phyllosilicates, to competition between dilatation and compaction by thermally activated stress corrosion cracking (SCC) of quartz grains plus possible pressure solution. This gives way to slip on the phyllosilicates accommodated by deformation of quartz grains mainly by SCC at the highest temperatures investigated. The importance of a fluid-assisted mechanism in causing velocity-weakening was confirmed by dry control experiments, which showed near zero values of (a - b) at 200 and 350°C .
4. Taking into account the effects of sliding velocity, Regime 2 broadly corresponds to the seismogenic zone on subduction megathrusts. On the basis of our data, the presence of illite, quartz, or the combination, therefore seems to be responsible for the occurrence of velocity-weakening behaviour in the seismogenic zone.
5. The frictional characteristics of illite-rich fault gouge obtained here, including the temperature- and hence depth-distribution of (a - b), show significant differences compared with previous data based on experiments on dry halite, wet granite and gabbro, notably in the magnitude of (a - b).

Acknowledgements

We thank Chris Marone and Brett Carpenter of the Pennsylvania State University for providing the illite gouge and XLook program. Gert Kastelein, Thony van de Gon Netscher, Eimert de Graaff and Peter van Krieken provided technical assistance. Matthijs de Winter, Hans van Meeldijk, Martyn Drury and Gill Pennock helped with the FIB-SEM and TEM work. Some XRD measurements were made at Kochi Core Centre. We thank Chris Marone and an anonymous reviewer for their helpful reviews. SdH is supported by a Toptalent grant awarded by the Netherlands Organisation for Scientific Research (NWO) (Project 021.002.025). AN is supported by an NWO VENI-grant No 863.09.013.

Appendix 3.A: Supplementary data

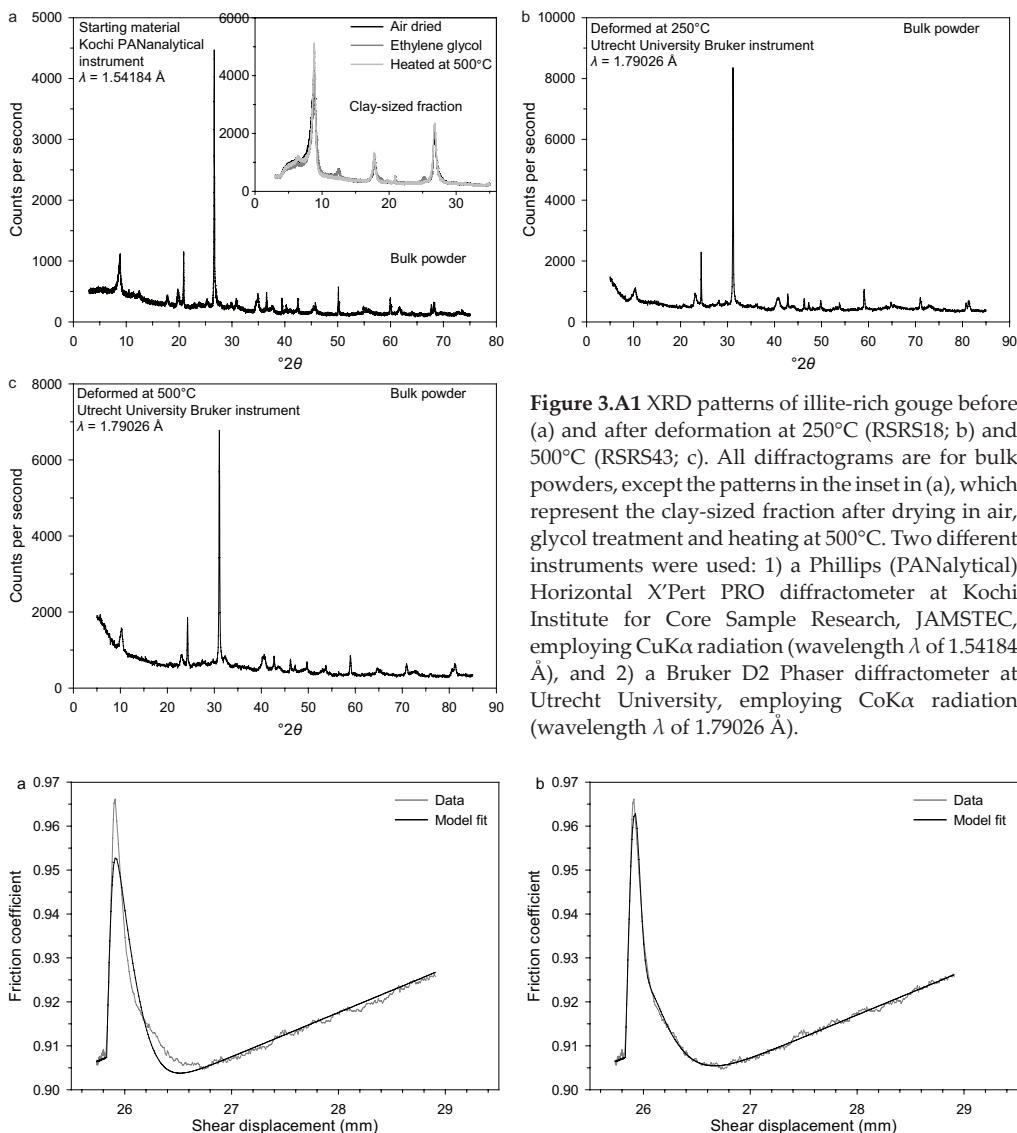


Figure 3.A1 XRD patterns of illite-rich gouge before (a) and after deformation at 250°C (RSRS18; b) and 500°C (RSRS43; c). All diffractograms are for bulk powders, except the patterns in the inset in (a), which represent the clay-sized fraction after drying in air, glycol treatment and heating at 500°C. Two different instruments were used: 1) a Phillips (PANalytical) Horizontal X'Pert PRO diffractometer at Kochi Institute for Core Sample Research, JAMSTEC, employing CuK α radiation (wavelength λ of 1.54184 Å), and 2) a Bruker D2 Phaser diffractometer at Utrecht University, employing CoK α radiation (wavelength λ of 1.79026 Å).

Figure 3.A2 Illustration of the RSF modelling results for the fifth velocity step in RSR543 (i.e. from 10 to 100 $\mu\text{m/s}$). (a) Model fit when using one state variable. (b) Model fit when using two state variables. The fit is improved significantly when using two instead of one state variable.

Chapter 4

Influence of subduction zone conditions and gouge composition on frictional slip stability of megathrust faults

Sabine A.M. den Hartog and Christopher J. Spiers

Tectonophysics, in press

Abstract

To understand the temperature/depth distribution of destructive earthquakes in subduction megathrusts, and the mechanisms of nucleation of these events, data on the frictional behaviour of phyllosilicate/quartz-rich megathrust fault gouges under in-situ conditions are needed. We performed rotary shear friction experiments at effective normal stresses of 25-200 MPa, pore fluid pressures of 50-200 MPa, at 140-600°C and sliding velocities of 1-100 $\mu\text{m/s}$, using gouge mixtures with an illite:quartz ratio between 65:35 and zero. Experiments on 65:35 mixtures, deformed at an effective normal stress (σ_n^{eff}) of 170 MPa, a pore fluid pressure (P_f) of 100 MPa and 150-500°C provided a reference dataset. This showed three temperature-dependent slip stability regimes with potentially unstable, velocity-weakening behaviour at 250-400°C and velocity-strengthening at lower and higher temperatures. The velocity-weakening regime was found to shift towards higher temperatures with decreasing σ_n^{eff} , being located at ~350-600°C at 50 MPa. Increasing quartz content and decreasing sliding velocity also displaced the velocity-weakening regime towards lower temperatures. Increasing P_f increased $(a-b)$ at all temperatures, narrowing the temperature extent of the velocity-weakening regime. We explain our results qualitatively in terms of a microphysical model in which changes in friction coefficient and $(a-b)$ with velocity and temperature are brought about by changes in the relative importance of deformation of the clast phase, by thermally activated stress corrosion cracking and pressure solution, versus athermal granular flow of the mixture accompanied by dilatation. Our results imply that the depth extent of the seismogenic zone on subduction megathrusts depends not only on temperature and that to predict its location, it is essential to have well-constrained depth profiles for pore fluid pressure and effective normal stress.

4.1 Introduction

It is widely believed that the depth range of the seismogenic portion of subduction megathrusts is thermally controlled, with the up- and down-dip limits being located at ~ 150 and $\sim 350^\circ\text{C}$, respectively (Hyndman et al., 1997). This view is based on focal depth distribution data (cf. Oleskevich et al., 1999; Tichelaar and Ruff, 1993), on experiments showing dehydration of smectite-rich sediments to form illite-rich rock at around 150°C (Hower et al., 1976; Jennings and Thompson, 1986), and on experiments showing a transition from unstable to stable sliding in simulated granitic fault gouge at $\sim 350^\circ\text{C}$ (Blanpied et al., 1991; 1995; 1998). However, the seismogenic zone does not coincide with the temperature range of 150 – 350°C in all subduction zones (e.g. McCaffrey et al., 2008). Moreover, illite gouge does not seem to be capable of supporting unstable slip, at least in experiments at room temperature (e.g. Saffer and Marone, 2003), and granitic gouge is unlikely to be representative for the behaviour of the metapelitic fault rocks believed to be present in many subduction megathrusts (e.g. Underwood, 2007). The basis for our understanding of the extent of the seismogenic zone is therefore open to question.

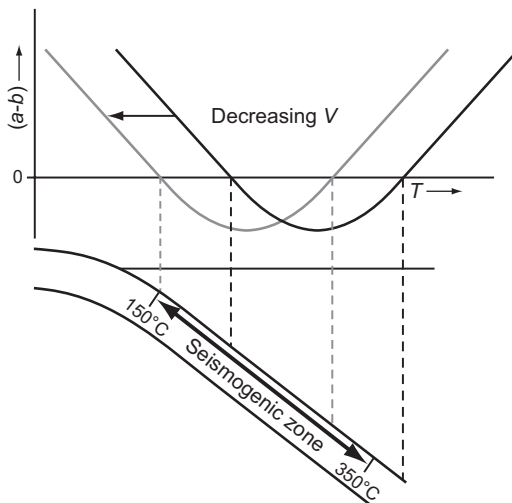


Figure 4.1 Schematic figure of the rate and state friction parameter ($a-b$) versus temperature curve reported by Den Hartog et al. (2012a, Chapter 3) in experiments on illite-rich fault gouge, showing three slip stability regimes as a function of temperature and the experimentally observed effect of decreasing the slip velocity. The experiments were performed at an effective normal stress of 170 MPa, a pore fluid pressure of 100 MPa and slip velocities of 1–100 $\mu\text{m/s}$. A positive ($a-b$) value indicates inherently stable velocity-strengthening slip behaviour, whereas a negative ($a-b$) value indicates velocity-weakening behaviour, which is potentially unstable. The schematic cross section of the subduction zone shows the discrepancy between the temperature-range of velocity-weakening found in the experiments (black curve) versus the generally accepted temperature-range of the seismogenic zone on subduction zone megathrusts. Den Hartog et al. (2012a, Chapter 3) proposed that extrapolating the ($a-b$) data to in-situ velocities would move the velocity-weakening region into correspondence with the seismogenic zone.

To understand the depth/temperature range of destructive earthquakes in subduction zones, and the mechanisms of nucleation of these events, data are needed on the frictional behaviour of realistic, metapelitic (i.e. phyllosilicate/quartz-rich) megathrust fault gouges under in-situ pressure, temperature and velocity conditions. However, only a few experimental studies have been performed using appropriate materials and conditions. Recently, Den Hartog et al. (2012a, Chapter 3) presented the results of ring shear experiments performed on simulated illite-quartz fault gouge at pressure conditions corresponding to ~ 10 km depth on a subduction megathrust (effective normal stress of 170 MPa, pore fluid pressure of 100 MPa), at sliding velocities of 1–100 $\mu\text{m/s}$ and covering temperatures in the range 150 – 500°C . These confirmed the importance of temperature in controlling subduction zone

seismogenesis, showing a switch from predominantly stable (“velocity-strengthening”) sliding behaviour to potentially unstable (“velocity-weakening”) behaviour at $\sim 255^{\circ}\text{C}$, as well as a reverse transition at $\sim 370^{\circ}\text{C}$ (Fig. 4.1). At the same time, however, the temperature of these transitions was observed to depend on sliding velocity, being displaced towards lower temperatures with decreasing velocity. In-situ nucleation velocities are believed to be close to plate velocities of $\sim 10^{-9}$ m/s (e.g. Segall and Rice, 2006). On this basis, it was proposed that the observed velocity effect might explain the discrepancy between the onset of velocity-weakening behaviour observed at 255°C and the temperature of 150°C typically associated with the up-dip seismogenic limit (Fig. 4.1).

The role of temperature in determining the occurrence of velocity-strengthening versus velocity-weakening slip has also been observed in experiments on other materials besides illite-rich gouge. Specifically, wet quartz (Chester and Higgs, 1992; cf. Kanagawa et al., 2000; cf. Niemeijer et al., 2008), granite (Blanpied et al., 1991; 1995; 1998), gabbro (He et al., 2007) and San Andreas Fault (SAF; Tembe et al., 2009) gouges all show three frictional “slip stability” regimes. These are characterized by velocity-weakening behaviour at respectively 300°C , $100\text{--}350^{\circ}\text{C}$, $170^{\circ}\text{C}\text{--}310^{\circ}\text{C}$ and $266\text{--}283^{\circ}\text{C}$, with velocity-strengthening occurring at lower and higher temperatures. The broad similarity of these temperature ranges with each other, and with that observed for velocity-weakening in illite-rich fault gouge is surprising, not only because of the differences in materials studied, but also because significantly different sliding velocities, effective normal stresses and pore fluid pressures were often used.

These considerations raise the question of to what extent the three-regime behaviour displayed by illite-rich megathrust fault gouge depends on variables such as sliding velocity, composition, effective normal stress and pore fluid pressure. Understanding the effects of these variables on velocity-strengthening versus velocity-weakening behaviour may be crucial for modelling seismogenesis on subduction zone megathrusts and for establishing better constraints on the temperature/depth range of the seismogenic zone. In this paper, we report experiments designed to systematically evaluate the impact of these factors on the frictional strength and slip stability of illite-quartz fault gouge. We add new friction experiments to our previous dataset to cover effective normal stresses in the range 25–200 MPa, pore fluid pressures ranging from 50 to 200 MPa and temperatures in the range $140\text{--}600^{\circ}\text{C}$. In addition, we examine the effect of composition by varying the quartz content of the gouge from ~ 35 to 100%. The lowest temperature investigated was chosen to match our best estimate of the temperature at the source region of the Tohoku-Oki earthquake ($140 \pm 11^{\circ}\text{C}$), derived using a source depth of 24 km (Japan Meteorological Agency, JMA) and the temperature versus depth profile given by Peacock and Wang (1999). The range of quartz contents investigated was intended to allow for variability in subducted sediment input, including sands (Kitamura and Kimura, 2012; Underwood, 2007), and cherts as in the Tohoku region (Kameda et al., 2012). We show that all variables investigated affect the temperature range at which velocity-weakening behaviour occurs in metapelitic subduction zone gouges, and we consider the implications for the temperature/depth range of the seismogenic zone.

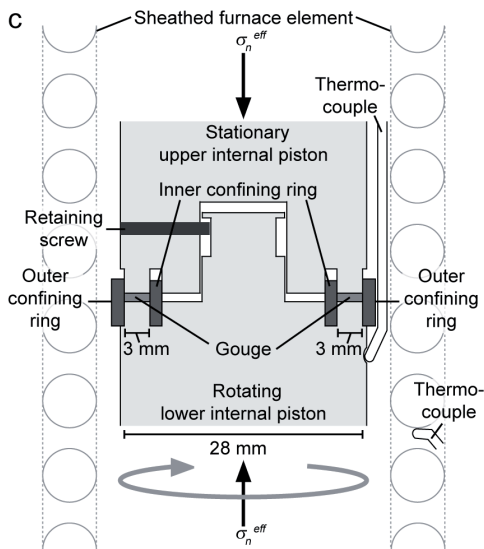
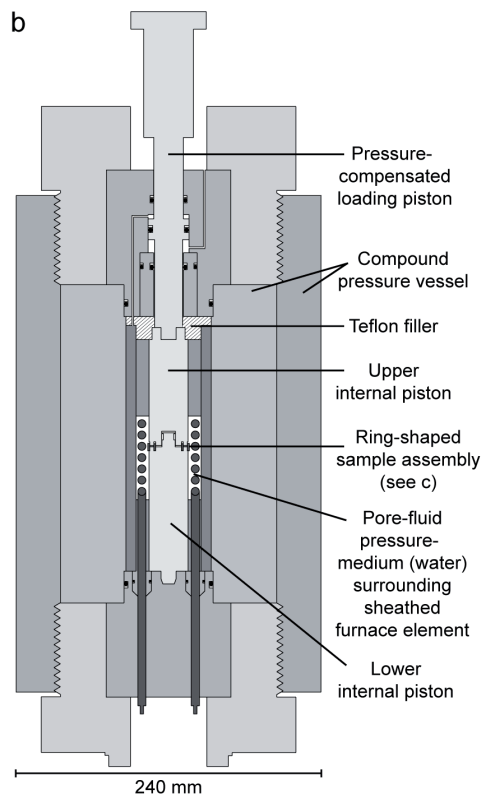
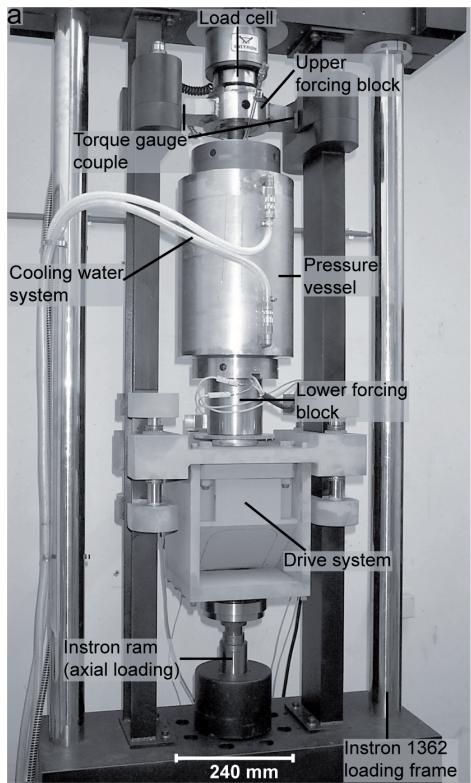


Figure 4.2 Ring shear machine used in the present study (after Den Hartog et al., 2012a, Chapter 3). (a) The rotary shear drive system and pressure vessel mounted inside the Instron loading frame. (b) Semi-schematic cross section of the pressure vessel. (c) Semi-schematic cross section of the sample assembly. σ_n^{eff} = effective normal stress.

4.2 Material and methods

4.2.1 Sample material

The reference material used in this study, and in our previous work (Den Hartog et al.,

2012a, Chapter 3), consisted of crushed illite-rich Rochester Shale (Folk, 1962), sieved to obtain a grain size below 106 μm (Ikari et al., 2009). Saffer and Marone (2003) reported the same material to contain 59% illite, 23% quartz, 9% kaolinite/dickite and 4% plagioclase. Our own X-Ray Diffraction (XRD) analysis showed similar results, but with minor chlorite instead of plagioclase and kaolinite/dickite. Varying the illite:quartz content of this material was achieved by adding SIL-CO-SIL 49, obtained from US Silica, to the crushed Rochester Shale. This material has a median grain size of $\sim 11 \mu\text{m}$. Ring shaped samples were made by pre-pressing mixtures of $\sim 0.5 \text{ g}$ gouge and $\sim 0.04 \text{ g}$ distilled water at $\sim 170 \text{ MPa}$ for $\sim 20 \text{ min}$. in a hydraulic press (see Den Hartog et al., 2012b, Chapter 2).

4.2.2 Experimental apparatus and procedure

Frictional sliding experiments were performed using the hydrothermal ring shear machine (Fig. 4.2) described by Den Hartog et al. (2012a, Chapter 3; 2012b, Chapter 2) and Niemeijer et al. (2008). In this machine, a $\sim 1 \text{ mm}$ thick, ring-shaped sample is sandwiched between two roughened René 41 Superalloy pistons, and kept in place by inner and outer confining rings of the same material, coated with a graphite powder suspension (Fig. 4.2c). The sample-piston assembly is located inside an internally heated, 300 MPa pressure vessel, filled with distilled water which forms the pore fluid (Fig. 4.2a and b). Normal stress is applied via a pressure-compensated upper loading piston (Fig. 4.2b) and controlled using a 100 kN servo-controlled Instron loading frame. A servo-controlled motor-gearbox system rotates the vessel and lower piston at sliding velocities ranging from $\sim 10 \text{ nm/s}$ to $\sim 300 \mu\text{m/s}$ relative to the non-rotating upper piston, generating rotary shear deformation of the sample. The resulting shear stress and torque are measured externally via the stationary upper piston set.

Note that the use of the pressure-compensated upper loading piston means that normal stress is applied to the sample in excess of the fluid pressure (P_f) measured in the vessel, so that the effective normal stress (σ_n^{eff}) experienced by the sample is equal to the axially applied stress, assuming that the small sample is penetrated by the fluid at pore fluid pressure P_f (Den Hartog et al., 2012a, Chapter 3). This implies that the effective normal stress is not affected by changes in the pore fluid pressure. Also note that two experiments were performed in the absence of a (pressurized) pore fluid, but under a vacuum, generated using a vacuum pump with a capacity better than 1 mbar.

The experimental procedure followed is described by Den Hartog et al. (2012b, Chapter 2). The experiments were performed under the conditions shown in Table 4.1, grouped into datasets that each addresses the effect of one specific variable. All experiments performed were velocity stepping tests, employing slip velocities of 1, 10 and 100 $\mu\text{m/s}$, imposed after initial sliding at 10 $\mu\text{m/s}$ for a displacement of $\sim 5 \text{ mm}$. To enable proper cross-comparison, the experiments listed in Table 4.1 include 11 experiments reported previously by Den Hartog et al. (2012a, Chapter 3) plus 18 new experiments. We define Dataset 1 (Table 4.1) as a reference set of tests. These were performed on Rochester Shale ($\sim 65\%$ illite and $\sim 35\%$ quartz) at an effective normal stress of 170 MPa, a pore fluid pressure of 100 MPa, and at 150-500°C. This dataset shows the effect of temperature on the velocity dependence of the reference illite-rich gouge. Three additional sets of experiments on the same material also show the effect of temperature, but at $\sigma_n^{\text{eff}} = 50 \text{ MPa}$ and $P_f = 100 \text{ MPa}$ (Dataset 2), at $\sigma_n^{\text{eff}} = 170$

MPa and $P_f = 50$ MPa (Dataset 3), and at $\sigma_n^{eff} = 170$ MPa under vacuum (“dry”) conditions (Dataset 4). When compared to Dataset 1, Datasets 2-4 show the effects of σ_n^{eff} , P_f and the presence of water. The effect of σ_n^{eff} is addressed explicitly in Datasets 5 and 6, obtained for Rochester reference material at 350°C and $P_f = 100$ MPa, and at 140°C and $P_f = 200$ MPa, respectively. Dataset 7 explicitly shows the effect of pore fluid pressure, at $\sigma_n^{eff} = 170$ MPa and 350°C. Dataset 8 shows the effect of varying the quartz content of the illite-quartz mixture, at $\sigma_n^{eff} = 100$ MPa, 140°C and $P_f = 200$ MPa.

4.2.3 Data acquisition and processing

Shear displacement (resolution $\pm 1 \mu\text{m}$), axial displacement ($\pm 0.05 \mu\text{m}$), normal force (± 0.05 kN) and torque (better than ± 6 Nm) were measured externally and the corresponding signals logged, together with the pore fluid pressure (± 0.005 MPa) and temperature ($\pm 1^\circ\text{C}$) signals, using a 16 bit A/D converter and a logging frequency of 1-100 Hz. Torque and normal force data were corrected for seal friction, employing calibrations performed at experimental pressures, and temperatures up to 200°C, using an internal load/torque cell of known pressure-sensitivity, in combination with graphite-coated pairs of PEEK sample rings of known frictional strength. Shear displacement was corrected for machine stiffness using calibrations determined by replacing the sample-piston set by a solid steel (Remanit 1.4122) column of known elastic properties. The seal friction correction is estimated to be accurate to within ~ 9 Nm and ~ 0.2 kN for the torque and normal force, respectively. The corrected torque was converted to a shear force acting on the sample surface at the mean sample radius of 12.5 mm. The corrected shear and normal force were divided by the sample area to obtain shear stress (τ) and applied normal stress, respectively. The apparent coefficient of friction μ was calculated as $\mu = \tau / \sigma_n^{eff}$. Shear strain γ was obtained from the ratio of shear displacement to instantaneous sample thickness, determined from the final piston-sample assembly length and the axial displacement measured during each experiment. We used these data only to estimate the evolution of shear strain, because the axial displacement measurement included effects of extrusion of sample material and measurement errors in sample thickness (5-10%) related to the remote location of the displacement transducer from the sample. This also made it impossible to reliably determine changes in porosity of the sample associated with compaction/dilatation (cf. Den Hartog et al., 2012a, Chapter 3; 2012b, Chapter 2).

The velocity dependence of friction was interpreted using the Dieterich type rate and state dependent friction (RSF) model (“slowness law”; Dieterich, 1978; 1979; Marone, 1998; Ruina, 1983) written:

$$\mu = \mu_0 + a \ln\left(\frac{V}{V_0}\right) + b \ln\left(\frac{V_0 \theta}{d_c}\right) \quad \text{with} \quad \frac{d\theta}{dt} = 1 - \frac{V\theta}{d_c} \quad (4.1)$$

(e.g. Marone, 1998). Here, θ is a gouge state variable, a determines the absolute magnitude of the instantaneous change in μ upon a given step change in sliding velocity from a reference value V_0 to a new value V , b reflects the magnitude of the change in μ during the evolution to a new steady state value over a critical sliding distance d_c , and μ_0 is the steady state friction coefficient measured at the reference velocity V_0 . For changes in steady state friction coefficient ($\Delta\mu_{ss}$) resulting from a stepwise change in slip velocity this yields:

Table 4.1 List of experiments, conditions and key data. σ_n^{eff} = effective normal stress, T = temperature, P_f = pore fluid pressure, V = sliding velocity, μ = coefficient of friction and γ = shear strain. Some experiments are part of multiple datasets, in which case they are shown in grey after their first appearance. The occurrence of stick-slip events is reported in the last column by specifying the velocity at which stick-slip was observed (N = no stick-slip observed), and by underlining in the V -column, the corresponding stages in the velocity-stepping-sequence.

Experiment	Composition	σ_n^{eff} (MPa)	T (°C)	P_f (MPa)	V ($\mu\text{m/s}$)	μ_{final}	Final gouge thickness (mm)	Final displacement (mm)	γ_{final}	Occurrence of stick-slip
Dataset 1: effect of T at constant $\sigma_n^{eff} = 170$ MPa, $P_f = 100$ MPa^a										
RSRS73	65% ill, 35% qtz	170	150	100	10-100-10-1-10-100-10	0.68	0.62	39.9	64	N
RSRS07	65% ill, 35% qtz	170	200	100	10-100-10-1-10-100-10	0.79	0.46	49.2	49	N
RSRS16	65% ill, 35% qtz	170	250	100	10-100-10-1-10-100-10	0.69	0.59	40.1	68	N
RSRS18	65% ill, 35% qtz	170	250	100	10-100-10-1-10-100-10	0.75	0.48	39.6	82	N
RSRS09	65% ill, 35% qtz	170	300	100	10-100- <u>10-1-10</u> -10	0.77	0.23	23.6	102	1, 10 $\mu\text{m/s}$
RSRS38	65% ill, 35% qtz	170	350	100	<u>10-100-10-1-10-100</u>	0.81	0.64	33.9	53	10, 100 $\mu\text{m/s}$
RSRS39	65% ill, 35% qtz	170	400	100	10-100-10-1- <u>10-100</u>	0.89	0.48	35.0	73	10, 100 $\mu\text{m/s}$
RSRS40	65% ill, 35% qtz	170	450	100	10-100-10-1-10-100-10	0.91	0.52	40.6	78	N
RSRS43	65% ill, 35% qtz	170	500	100	10-100-10-1-10-100-10	0.95	0.66	47.5	72	N
Dataset 2: effect of T at constant $\sigma_n^{eff} = 50$ MPa, $P_f = 100$ MPa										
RSRS56	65% ill, 35% qtz	50	200	100	10-100-10-1-10-100-10	0.59	0.72	40.3	56	N
RSRS60	65% ill, 35% qtz	50	200	100	10-100-10-1-10-100-10	0.50	0.26	40.7	156	N
RSRS53	65% ill, 35% qtz	50	350	100	10-100-10-1-10-100-10	0.79	0.38	42.0	111	1 $\mu\text{m/s}$
RSRS59	65% ill, 35% qtz	50	500	100	<u>10-100-10-1-10-100-10</u>	1.00	0.60	40.0	67	10 $\mu\text{m/s}$
RSRS62	65% ill, 35% qtz	50	600	100	10-100-10-1-10-100	1.14	0.64	40.7	64	N
Dataset 3: effect of T at constant $\sigma_n^{eff} = 170$ MPa, $P_f = 50$ MPa										
RSRS82	65% ill, 35% qtz	170	150	50	10-100-10-1-10-100-10	0.57	0.54	40.2	75	N
RSRS81	65% ill, 35% qtz	170	350	50	<u>10-100-10-1-10-100-10</u>	0.74	0.54	39.6	73	10, 100 $\mu\text{m/s}$
RSRS84	65% ill, 35% qtz	170	500	50	<u>10-100-10-1-10-100-10</u>	0.86	0.42	40.3	96	10, 100 $\mu\text{m/s}$
Dataset 4: effect of T at constant $\sigma_n^{eff} = 170$ MPa, dry^a										
RSRS65	65% ill, 35% qtz	170	200	dry	10-100-10-1-10-100-10	0.72	0.68	40.2	59	N
RSRS64	65% ill, 35% qtz	170	350	dry	10-100-10-1-10-100-10	0.82	0.80	40.3	50	N

Table 4.1 (continued)

Experiment	Composition	σ_n^{eff} (MPa)	T (°C)	P_f (MPa)	V ($\mu\text{m/s}$)	μ_{final}	Final gouge thickness (mm)	Final displacement (mm)	γ_{final}	Occurrence of stick-slip
Dataset 5: effect of σ_n^{eff} at constant $T = 350^\circ\text{C}$, $P_f = 100$ MPa										
RSRS53	65% ill, 35% qtz	50	350	100	10-100-10-1-10-100-10	0.79	0.38	42.0	111	1 $\mu\text{m/s}$
RSRS54	65% ill, 35% qtz	90	350	100	10-100-10-1-10-100-10	0.83	0.58	38.9	67	10 $\mu\text{m/s}$
RSRS55	65% ill, 35% qtz	130	350	100	10-100-10-1-10-100-10	0.85	0.50	37.5	75	10 $\mu\text{m/s}$
RSRS38	65% ill, 35% qtz	170	350	100	10-100-10-1-10-100-10	0.81	0.64	33.9	53	10, 100 $\mu\text{m/s}$
Dataset 6: effect of σ_n^{eff} at constant $T = 140^\circ\text{C}$, $P_f = 200$ MPa										
RSRS77	65% ill, 35% qtz	25	140	200	10-100-10-1-10-100-10	0.59	0.60	40.5	67	N
RSRS76	65% ill, 35% qtz	50	140	200	10-100-10-1-10-100-10	0.52	0.62	40.6	65	N
RSRS75	65% ill, 35% qtz	100	140	200	10-100-10-1-10-100-10	0.51	0.58	40.0	69	N
RSRS79	65% ill, 35% qtz	200	140	200	10-100-10-1-10-100-10	0.65	0.52	39.6	76	N
Dataset 7: effect of P_f at constant $\sigma_n^{eff} = 170$ MPa, $T = 350^\circ\text{C}$										
RSRS81	65% ill, 35% qtz	170	350	50	10-100-10-1-10-100-10	0.74	0.54	39.6	73	10, 100 $\mu\text{m/s}$
RSRS38	65% ill, 35% qtz	170	350	100	10-100-10-1-10-100-10	0.81	0.64	33.9	53	10, 100 $\mu\text{m/s}$
RSRS85	65% ill, 35% qtz	170	350	200	10-100-10-1-10-100-10	0.84	0.42	40.4	96	10 $\mu\text{m/s}$
Dataset 8: effect of composition (quartz content) at constant $\sigma_n^{eff} = 100$ MPa, $T = 140^\circ\text{C}$, $P_f = 200$ MPa										
RSRS75	65% ill, 35% qtz	100	140	200	10-100-10-1-10-100-10	0.51	0.58	40.0	69	N
RSRSQ1	35% ill, 65% qtz	100	140	200	10-100-10-1-10-100-10	0.76	0.66	39.2	59	N
RSRSQ2	15% ill, 85% qtz	100	140	200	10-100-10-1-10-100-10	0.70	0.70	40.4	58	N
RSQ1 ^b	100% qtz	100	140	200	10-100-10-1-10-100-10	0.73	0.80	39.5	49	10, 100 $\mu\text{m/s}$

^aReported previously by Den Hartog et al. (2012a).

^bPre-pressed in the ring shear machine at 170 MPa (as opposed to external pre-pressing at 170 MPa in a hydraulic press – other experiments).

$$(a-b) = \frac{\Delta\mu_{ss}}{\Delta \ln V} \quad (4.2)$$

(e.g. Marone, 1998; Paterson and Wong, 2005; Scholz, 2002), where positive $(a-b)$ values indicate an increase in friction coefficient with increasing velocity, i.e. velocity-strengthening slip behaviour, while negative $(a-b)$ values signify velocity-weakening (e.g. Paterson and Wong, 2005; Scholz, 1998). Values of $(a-b)$ were calculated using Eq. (4.2), after detrending the μ versus displacement curves for background slip hardening or softening, as described by Den Hartog et al. (2012b, Chapter 2).

4.3 Results

Key mechanical data obtained are listed in Table 4.1 per dataset.

4.3.1 Frictional strength

The evolution of apparent friction coefficient $\mu = \tau / \sigma_n^{eff}$ with shear displacement for representative subsets of experiments is shown in Fig. 4.3. The friction versus displacement curves obtained in the experiments were mostly similar. All experiments showed a rapid increase in μ until apparent yielding at the “knee” in the μ versus displacement curves, occurring at a displacement of ~ 1 mm, i.e. within the initial sliding stage of 5 mm at 10 $\mu\text{m/s}$. In some cases, the yield point was followed by a small drop in μ . This was usually followed by significant slip-hardening, superimposed on the mostly modest response to subsequent velocity steps. Note that the yield point (“knee”) characterizing each individual experiment was taken as the point of maximum rate of change of the hardening rate (h), i.e. $\partial h / \partial x = \max$, where x is displacement. Temperature, effective normal stress, pore fluid pressure and quartz proportion were found to have systematic influences on the frictional strength, as described below.

First, the dependence of shear stress (τ), supported at yield, on σ_n^{eff} is shown in Fig. 4.4 for our reference illite-rich gouge (65% illite, 35% quartz). At $T = 200^\circ\text{C}$ and $P_f = 100$ MPa, as well as at $T = 350^\circ\text{C}$ and $P_f = 100$ MPa, these data can be described by a linear trend passing through or close to the origin, supporting the use of an apparent μ to describe shear strength. However, at $T = 500^\circ\text{C}$ and $P_f = 100$ MPa and at $T = 140^\circ\text{C}$ and $P_f = 200$ MPa, the τ -axis of Fig. 4.4 is crossed at 5-6 MPa, suggesting 5-6 MPa of cohesion under these conditions. This may reflect an initially over-consolidated state of samples tested at low σ_n^{eff} , produced by pre-pressing at 170 MPa normal stress. The apparent friction coefficient μ should therefore be interpreted with caution at low values of σ_n^{eff} .

Second, the apparent friction coefficient (μ) clearly increases with temperature at comparable displacement values (Fig. 4.3a, Table 4.1). This is shown explicitly in Fig. 4.5a, where μ at yield is plotted versus temperature for Datasets 1-4. It will be recalled that in these datasets the effect of varying temperature was tested, at the fixed effective normal stresses and pore fluid pressures defined in Table 4.1. The friction coefficient at the yield point was selected for comparison of μ values, in order to exclude effects of slip-hardening. For wet samples, the friction coefficient increases from ~ 0.35 at 150 - 250°C (Datasets 1-3), to ~ 0.6 at 500°C for a normal stress of 170 MPa (Datasets 1 and 3), reaching ~ 0.7 at 500°C and almost 0.9 at 600°C when the normal stress is 50 MPa (Dataset 2). The increase in μ with temperature tends to

be sharpest at around 350°C (Fig. 4.5a), at least for $\sigma_n^{eff} = 170$ MPa and $P_f = 100$ MPa (Dataset 1). At these conditions, temperature also affects the slip-hardening behaviour, yielding a relatively constant hardening rate at the lowest temperatures explored (e.g. 150°C; Fig. 4.3a), giving way to hardening followed by steady state slip at the highest temperatures explored (e.g. at 500°C; Fig. 4.3a). For dry samples (Dataset 4), μ is typically 25% higher than for wet samples (Fig. 4.5a). Unstable, oscillatory (stick-slip) events were occasionally observed in the wet experiments (Fig. 4.3a, Table 4.1), at 300–400°C for $\sigma_n^{eff} = 170$ MPa and $P_f = 100$ MPa (Dataset 1) and at 350–500°C for $\sigma_n^{eff} = 50$ MPa and $P_f = 100$ MPa (Dataset 2) and for $\sigma_n^{eff} = 170$ MPa and $P_f = 50$ MPa (Dataset 3).

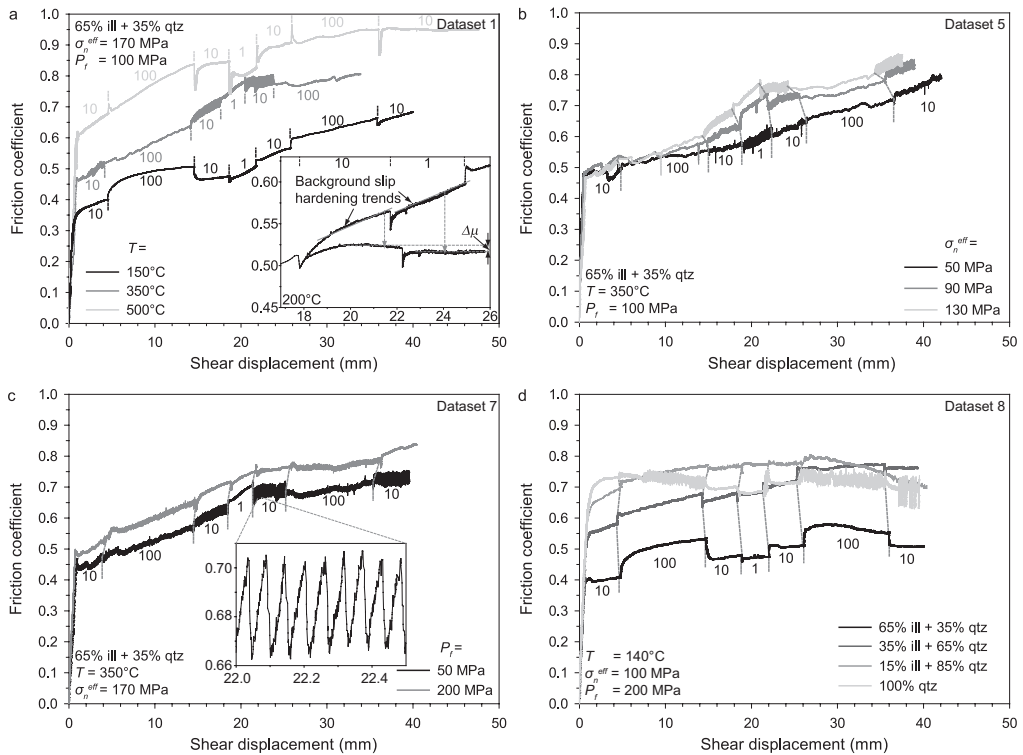


Figure 4.3 Typical evolution of friction coefficient with shear displacement obtained in the present experiments. Velocity steps are indicated in $\mu\text{m/s}$, with the location of a change in velocity indicated using vertical “ticks”, connected with dashed lines to the same velocity step in different experiments in (b-d). (a) Effect of temperature on frictional strength, shown for Dataset 1, on mixtures of ~65% illite and ~35% quartz sheared at $\sigma_n^{eff} = 170$ MPa and $P_f = 100$ MPa (RSRS73, RSRS38 and RSRS43). The inset demonstrates the procedure used to quantify the term $(a-b)$, for experiment RSRS07 performed at 200°C. The μ versus displacement curve is detrended for slip hardening based on the hardening rates measured in each consecutive step. (b) Effect of σ_n^{eff} on frictional strength, shown for Dataset 5, on mixtures of ~65% illite and ~35% quartz tested at $T = 350^\circ\text{C}$ and $P_f = 100$ MPa (RSRS53, RSRS54 and RSRS55). (c) Effect of P_f on frictional strength, shown for Dataset 7, on mixtures of ~65% illite and ~35% quartz, sheared at $T = 350^\circ\text{C}$ and $\sigma_n^{eff} = 170$ MPa (RSRS81 and RSRS85). The inset shows details of stick-slip behaviour. (d) Effect of quartz content on frictional strength, shown for experiments of Dataset 8, performed at $T = 140^\circ\text{C}$, $\sigma_n^{eff} = 100$ MPa and $P_f = 200$ MPa (RSRS75, RSRSQ1, RSRSQ2 and RSQ1).

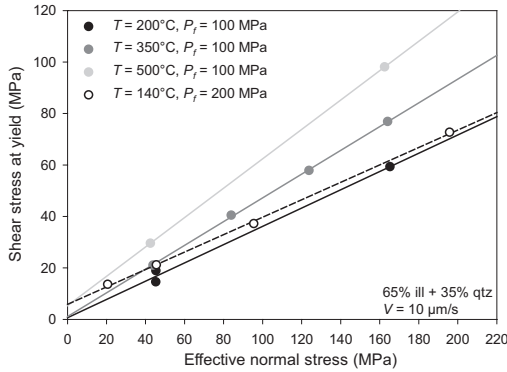


Figure 4.4 Shear strength at yield versus effective normal stress for the current experiments on the reference material (65% illite, 35% quartz). Data are presented for different temperature and pore fluid pressure conditions. Linear trend lines and corresponding data points are colour-coded. The dashed line is a fit to the data represented by the open symbols.

The effect of σ_n^{eff} on the frictional strength of our illite-quartz gouge is illustrated via Dataset 5 ($T = 350^\circ\text{C}$, $P_f = 100\text{ MPa}$) and Dataset 6 ($T = 140^\circ\text{C}$, $P_f = 200\text{ MPa}$) – refer Table 4.1. The μ versus displacement curve for Dataset 5, obtained at an effective normal stress of 170 MPa, is included in Fig. 4.3a, whereas those obtained at 50, 90 and 130 MPa are shown in Fig. 4.3b. These curves show similar μ -values at yield (0.47-0.48) demonstrating little or no effect of σ_n^{eff} on μ at low displacements at 350°C (Fig. 4.3b and 4.5b). However, the slip-hardening rate does increase with increasing σ_n^{eff} (Fig. 4.3b). By contrast, at 140°C and a pore fluid pressure of 200 MPa (Dataset 6), the friction coefficients at yield show, in line with the cohesion measured at these conditions (Fig. 4.4), an inverse normal stress dependence (Fig. 4.5b), but little effect of normal stress on slip-hardening rate (cf. Table 4.1). Stick-slip events were observed at all effective normal stresses for $T = 350^\circ\text{C}$ and $P_f = 100\text{ MPa}$ (Dataset 5), generally occurring at higher sliding velocity at a higher σ_n^{eff} (Fig. 4.3b, Table 4.1). No such events occurred in the experiments comprising Dataset 6 (Table 4.1).

Friction coefficient versus displacement curves for different pore fluid pressures, obtained at an effective normal stress of 170 MPa and 350°C , are shown in Fig. 4.3c. Together with the 350°C curve in Fig. 4.3a, these data define Dataset 7. The friction curves are similar at different pore fluid pressures, and show very similar μ -values at yield (0.47-0.50; Fig. 4.5c). At large displacements, μ -values measured at pore fluid pressures of 100 or 200 MPa are larger than at 50 MPa pore fluid pressure by an absolute amount of ~ 0.1 . Stick-slip events occurred at 10 and/or 100 $\mu\text{m/s}$ at all pore fluid pressures investigated (Fig. 4.3c, Table 4.1).

The friction curves obtained for gouges with different quartz contents, at a constant effective normal stress of 100 MPa, temperature of 140°C and pore fluid pressure of 200 MPa (Dataset 8), are shown in Fig. 4.3d. For this dataset, the μ -value at yield increases with quartz content from 0.39 at 35% quartz to 0.69 at 100% quartz (Fig. 4.5d). At larger displacements, the difference in μ -value between samples with different quartz contents decreases or reverses in direction (Fig. 4.3d; Table 4.1), due to a decrease in slip hardening rate in the most quartz-rich samples. Stick-slip events were observed only in the 100% quartz experiment (Fig. 4.3d, Table 4.1).

4.3.2 Velocity dependence of friction

The velocity dependence of μ , expressed in terms of $(a-b)$, is shown in Fig. 4.6-4.8, which respectively illustrate the effect of temperature (Fig. 4.6), effective normal stress (Fig. 4.7), and pore fluid pressure, quartz content and sliding velocity (Fig. 4.8). Note that the detrending procedure used to determine $(a-b)$ from our velocity step data is illustrated in Fig. 4.3a.

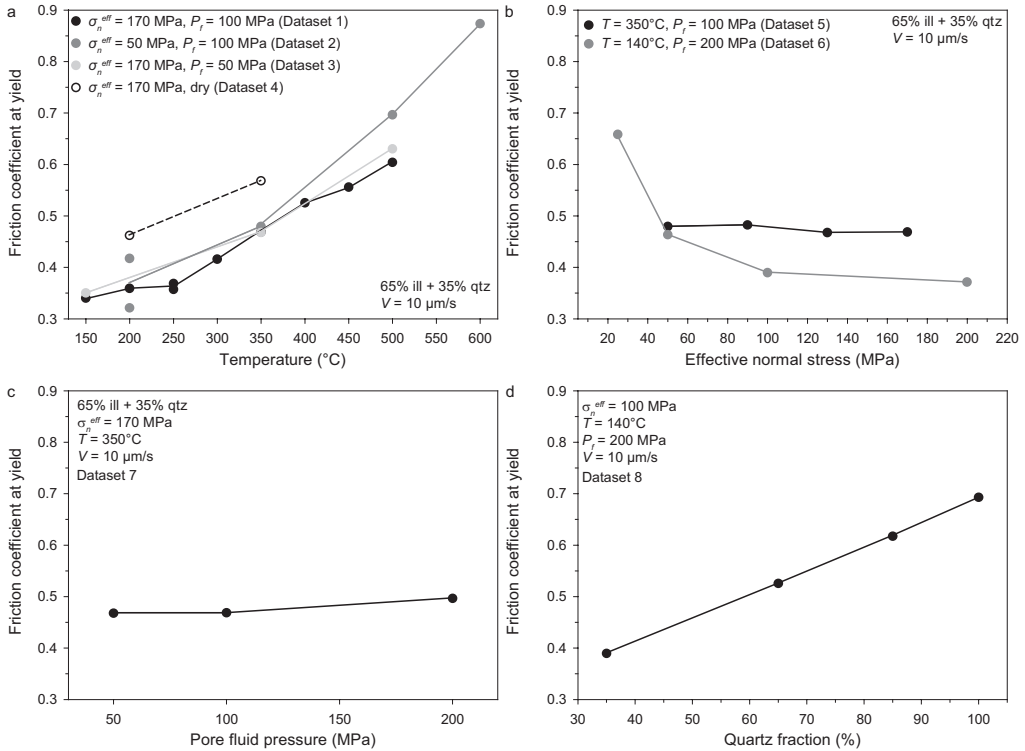


Figure 4.5 Friction coefficient at yield (i.e. at the initial sliding velocity of 10 $\mu\text{m/s}$), versus the different variables investigated in the present experiments. (a) Friction coefficient versus temperature for mixtures of ~65% illite and ~35% quartz, deformed at different combinations of σ_n^{eff} and P_f (or dry), as indicated (Dataset 1-4). (b) Friction coefficient versus effective normal stress for mixtures of ~65% illite and ~35% quartz, deformed at different combinations of temperature and P_f , as indicated (Dataset 5 and 6). (c) Friction coefficient versus pore fluid pressure for mixtures of ~65% illite and ~35% quartz, deformed at a temperature of 350°C and $\sigma_n^{eff} = 170$ MPa (Dataset 7). (d) Friction coefficient versus quartz fraction for experiments performed at a temperature of 140°C, $\sigma_n^{eff} = 100$ MPa and $P_f = 200$ MPa (Dataset 8).

Datasets 1-3, in which the effect of temperature was tested for wet samples at constant σ_n^{eff} and P_f show a broad, U-shaped $(a-b)$ versus temperature curve produced by a decrease in $(a-b)$ at low temperatures (e.g. 150-300°C for Dataset 1), followed by an increase at high temperatures (e.g. 300-500°C for Dataset 1; Fig. 4.6a – see also Den Hartog et al., 2012a, Chapter 3). These trends define three regimes of behaviour characterized by positive $(a-b)$ values (i.e. velocity-strengthening behaviour) at the lowest temperatures, negative values (i.e. velocity-weakening) at intermediate temperatures and again positive values at

the highest temperatures investigated. The temperature range of the velocity-weakening regime shifts upward with decreasing normal stress, lying at $\sim 250\text{--}400^\circ\text{C}$ at $\sigma_n^{\text{eff}} = 170\text{ MPa}$ and $P_f = 100\text{ MPa}$ (Dataset 1; Fig. 4.6a) but at $\sim 350\text{--}600^\circ\text{C}$ at $\sigma_n^{\text{eff}} = 50\text{ MPa}$ and $P_f = 100\text{ MPa}$ (Dataset 2; Fig. 4.6b). At $\sigma_n^{\text{eff}} = 170\text{ MPa}$ and $P_f = 50\text{ MPa}$ (Dataset 3; Fig. 4.6c), the velocity-weakening regime again occurs at $\sim 250\text{--}400^\circ\text{C}$, indicating relatively little effect of P_f in the range 50–100 MPa. In dry samples, the $(a-b)$ values are near zero, i.e. the behaviour is near velocity-neutral, in the temperature range investigated (Dataset 4; Fig. 4.6d).

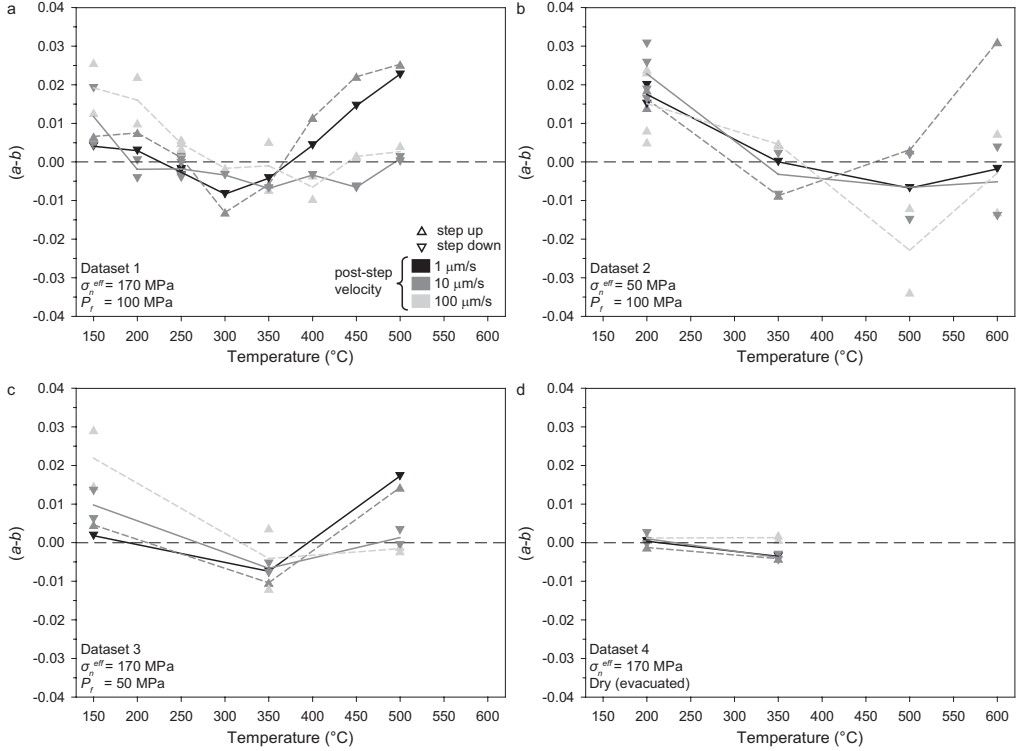


Figure 4.6 Values of the velocity dependence parameter $(a-b)$ versus temperature as obtained in the present experiments on mixtures of $\sim 65\%$ illite and $\sim 35\%$ quartz. Grey-scales indicate the magnitude of the velocity imposed in performing each upward or downward velocity step, as defined in (a). Solid tie-lines designate a step down in velocity, dashed a step up. In the case of oscillatory (stick-slip) behaviour, the average friction coefficient was used to obtain $(a-b)$. Using peak μ values instead of the average friction value yields the same trends. (a) Data obtained at $\sigma_n^{\text{eff}} = 170\text{ MPa}$ and $P_f = 100\text{ MPa}$ (Dataset 1). (b) Data obtained at $\sigma_n^{\text{eff}} = 50\text{ MPa}$ and $P_f = 100\text{ MPa}$ (Dataset 2). (c) Data obtained at $\sigma_n^{\text{eff}} = 170\text{ MPa}$ and $P_f = 50\text{ MPa}$ (Dataset 3). (d) Values of $(a-b)$ versus temperature for experiments performed at $\sigma_n^{\text{eff}} = 170\text{ MPa}$ and dry (Dataset 4).

The effect of σ_n^{eff} on $(a-b)$ in the mainly velocity-weakening regime is shown explicitly in Fig. 4.7a, at $T = 350^\circ\text{C}$ and $P_f = 100\text{ MPa}$ (Dataset 5). Compared with the reference data seen in Fig. 4.6a, for $\sigma_n^{\text{eff}} = 170\text{ MPa}$, Fig. 4.7a shows that $(a-b)$ attains minimum values at $\sigma_n^{\text{eff}} = 90\text{ MPa}$. At 140°C , i.e. in the low temperature velocity-strengthening regime (cf. Fig. 4.6a), and at $P_f = 200\text{ MPa}$, a modest decrease of $(a-b)$ with increasing effective normal stress is seen (Dataset 6; Fig. 4.7b), approaching velocity-neutral/weakening behaviour at $\sigma_n^{\text{eff}} = 200\text{ MPa}$

at the slowest velocities investigated. A plot of $(a-b)$ versus pore fluid pressure is shown in Fig. 4.8a (Dataset 7) for $T = 350^\circ\text{C}$ and $\sigma_n^{\text{eff}} = 170 \text{ MPa}$, i.e. for the velocity-weakening regime of Fig. 4.6a. These data show a slight increase in $(a-b)$ with increasing pore fluid pressure from the lowest values of about -0.01 at $P_f = 50 \text{ MPa}$ to values around 0.05 at $P_f = 200 \text{ MPa}$. Comparison of Fig. 4.6a and c suggests a similar slight increase in $(a-b)$ with increasing pore fluid pressure at 150 and 500°C .

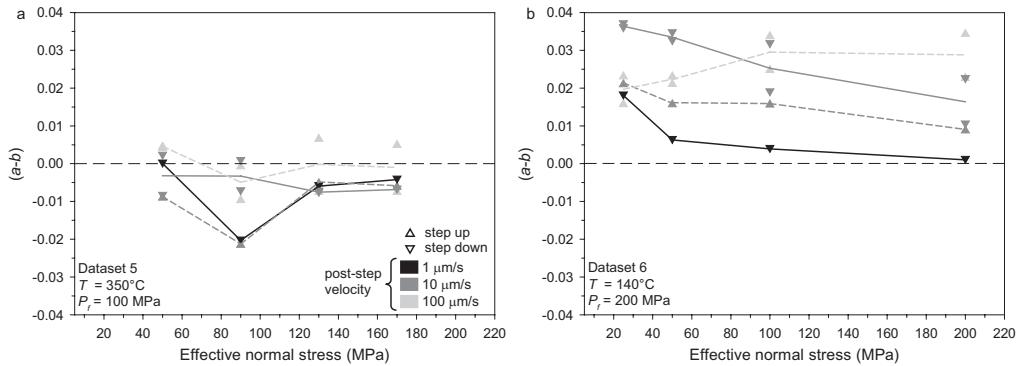


Figure 4.7 Velocity dependence parameter $(a-b)$ versus effective normal stress obtained in the present experiments on mixtures of $\sim 65\%$ illite and $\sim 35\%$ quartz. Grey-scales indicate the magnitude of the velocity imposed in performing each upward or downward velocity step, as defined in (a). Solid tie-lines designate a step down in velocity, dashed a step up. In the case of oscillatory (stick-slip) behaviour, the average friction coefficient was used. (a) Values of $(a-b)$ versus σ_n^{eff} for experiments performed at $T = 350^\circ\text{C}$ and $P_f = 100 \text{ MPa}$ (Dataset 5). (b) Values of $(a-b)$ versus σ_n^{eff} for experiments performed at $T = 140^\circ\text{C}$ and $P_f = 200 \text{ MPa}$ (Dataset 6).

The effect of an increase in quartz content on the velocity-dependent behaviour of our illite-quartz gouges is shown in Fig. 4.8b for experiments performed at 140°C , $\sigma_n^{\text{eff}} = 100 \text{ MPa}$ and $P_f = 200 \text{ MPa}$. With increasing quartz content, the value of $(a-b)$ shows a general tendency to decrease, except at the highest quartz proportions investigated (i.e. 100% quartz as compared to 85% quartz). At a quartz content of 85% , both positive and slightly negative $(a-b)$ values were obtained (Fig. 4.8b). The 100% quartz sample showed positive $(a-b)$ values, along with marked stick-slip and negative $(a-b)$ values measured using peak μ values.

Our data show a broad correspondence between negative or near-neutral $(a-b)$ values and the occurrence of stick-slip events (Fig. 4.6-4.8; Table 4.1). A few points associated with stick-slip fall in the velocity-strengthening field, but only by a margin that falls within or close to the error in $(a-b)$ (± 0.0024 ; Den Hartog et al., 2012a, Chapter 3). A notable exception is the experiment at 400°C , $\sigma_n^{\text{eff}} = 170 \text{ MPa}$ and $P_f = 100 \text{ MPa}$ (Dataset 1, Fig. 4.6a), which showed a short period of stick-slip behaviour following velocity-strengthening in an upward step in velocity from 1 to $10 \mu\text{m/s}$ (Table 4.1).

Comparison of the $(a-b)$ versus temperature data plotted for different sliding velocities in Fig. 4.6 suggests a tendency for the three slip stability regimes to shift towards higher temperatures at higher sliding velocities. This effect is illustrated also in Fig. 4.8c, where $(a-b)$ is plotted versus sliding velocity for a selection of experiments on the $\sim 65\%$ illite and

~35% quartz reference samples, performed at an effective normal stress of 170 MPa and a pore fluid pressure of 100 MPa (Dataset 1). At 150°C, $(a-b)$ tends to increase with increasing sliding velocity, whereas it is insensitive to sliding velocity at 350°C, and decreases with sliding velocity at 500°C. Apart from a few exceptions, plots of $(a-b)$ versus sliding velocity derived from the other datasets show the same trends.

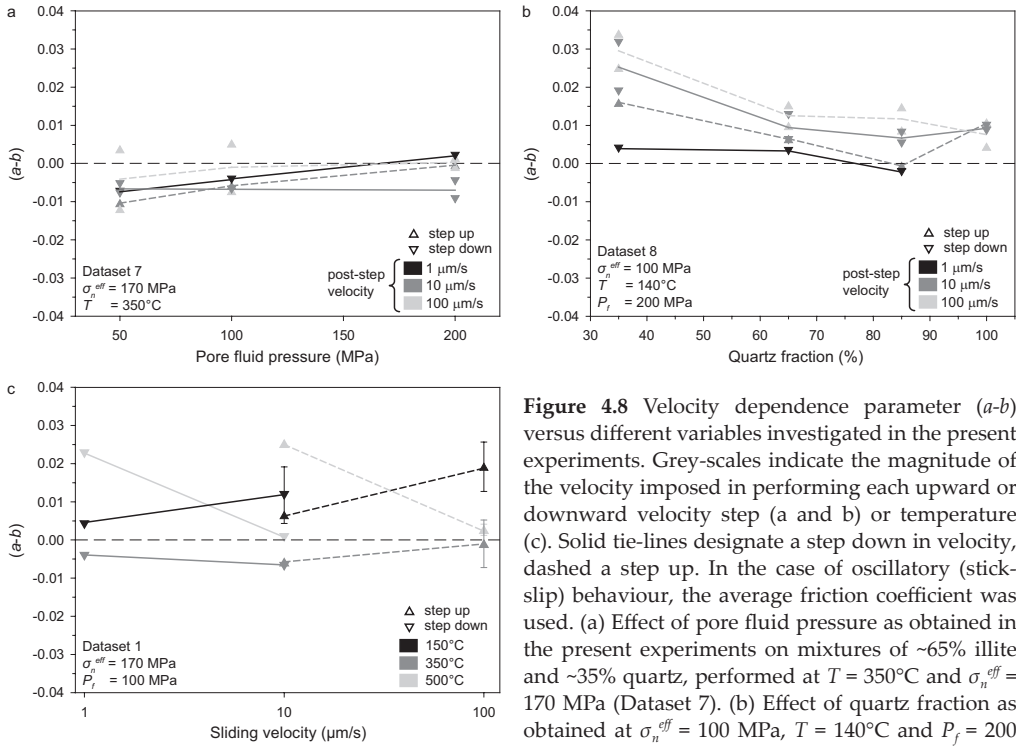


Figure 4.8 Velocity dependence parameter $(a-b)$ versus different variables investigated in the present experiments. Grey-shades indicate the magnitude of the velocity imposed in performing each upward or downward velocity step (a and b) or temperature (c). Solid tie-lines designate a step down in velocity, dashed a step up. In the case of oscillatory (stick-slip) behaviour, the average friction coefficient was used. (a) Effect of pore fluid pressure as obtained in the present experiments on mixtures of ~65% illite and ~35% quartz, performed at $T = 350^\circ\text{C}$ and $\sigma_n^{\text{eff}} = 170$ MPa (Dataset 7). (b) Effect of quartz fraction as obtained at $\sigma_n^{\text{eff}} = 100$ MPa, $T = 140^\circ\text{C}$ and $P_f = 200$ MPa (Dataset 8). (c) Effect of sliding velocity as

obtained in the present experiments on the reference mixtures of ~65% illite and ~35% quartz, performed at $\sigma_n^{\text{eff}} = 170$ MPa, $P_f = 100$ MPa and representative temperatures (Dataset 1). For simplicity, mean $(a-b)$ values are plotted, using range bars to indicate the full range of $(a-b)$ actually measured. Note that the trends seen at the three temperatures considered imply a shift in velocity-weakening regime to higher temperatures with increasing velocity.

4.4 Discussion

As reported by Den Hartog et al. (2012a, Chapter 3), the experiments constituting Dataset 1 here (i.e. the effect of temperature at $\sigma_n^{\text{eff}} = 170$ MPa and $P_f = 100$ MPa), show a U-shaped trend linking $(a-b)$ to temperature (refer Fig. 4.6a). This defines three temperature-dependent slip stability regimes characterized by predominantly velocity-strengthening slip ($[a-b] > 0$) at temperatures below ~250°C (Regime 1), mainly velocity-weakening ($[a-b] < 0$) between 250°C and 400°C (Regime 2), and again mainly velocity-strengthening ($[a-b] > 0$) above ~400°C (Regime 3). The current experiments show that these three regimes, and the defining U-shaped curve, shift with changing deformation conditions, as summarized schematically in Fig. 4.9. Our data demonstrate that with a change in σ_n^{eff} or V , $(a-b)$ either increases or decreases, depending on the temperature (Fig. 4.6a, 4.6b, 4.7 and 4.8c). These

changes imply a horizontal shift of the U-shaped ($a-b$) curve towards higher temperatures as effective normal stress decreases (Fig. 4.9a) and as sliding velocity increases (Fig. 4.9d). The effect of pore fluid pressure is minor, but increasing it increases ($a-b$) at most temperatures, thus displacing the ($a-b$) versus T curve vertically towards higher ($a-b$) values and reducing the extent of the velocity-weakening regime (Fig. 4.6a, 4.6c, 4.8a and 4.9b). However, based on the current data, we cannot eliminate the possibility of a shift of the curve horizontally towards lower temperatures with increasing P_f (cf. Fig. 4.6a and c). Turning to composition effects, an increase in quartz content results in a decrease of ($a-b$), at least in Regime 1 (Fig. 4.8b). This implies either a shift of all three regimes towards lower temperatures with increasing quartz content, or else a decrease in ($a-b$) values without a shift in temperature (i.e. vertical depression of the curve). We believe the first explanation is the most likely one (Fig. 4.9c), as discussed below. Lastly, note that deforming the gouge dry instead of wet appears to render ($a-b$) neutral and more or less independent of temperature (Fig. 4.9e).

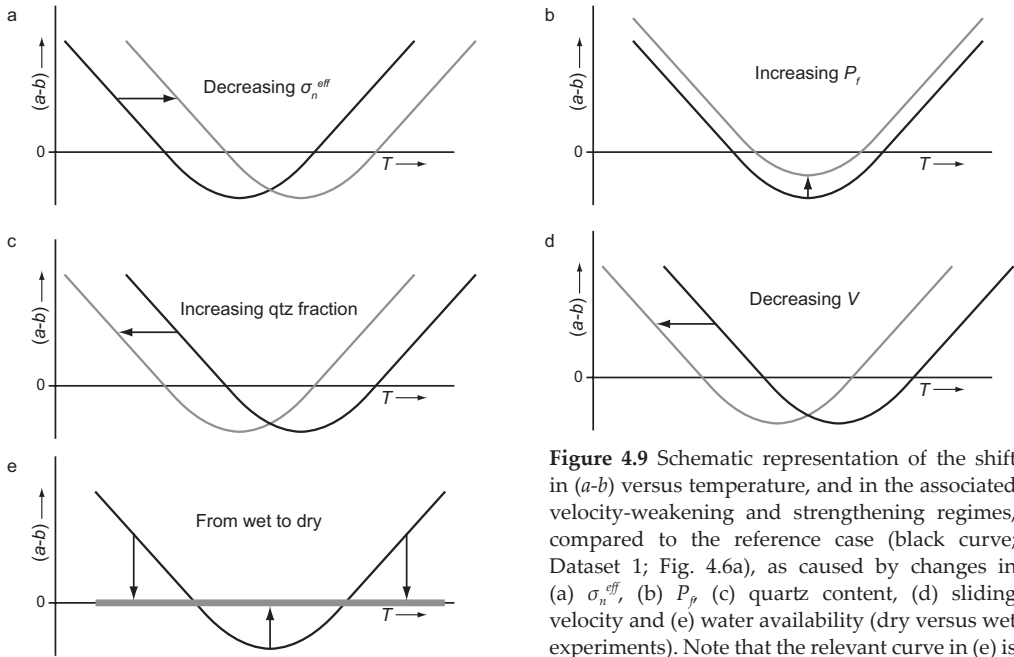


Figure 4.9 Schematic representation of the shift in ($a-b$) versus temperature, and in the associated velocity-weakening and strengthening regimes, compared to the reference case (black curve; Dataset 1; Fig. 4.6a), as caused by changes in (a) σ_n^{eff} , (b) P_f , (c) quartz content, (d) sliding velocity and (e) water availability (dry versus wet experiments). Note that the relevant curve in (e) is horizontal and coincides with the horizontal axis.

It will be recalled that along with the U-shaped trend linking ($a-b$) to temperature, our data also show an increase in μ with temperature, increasing most sharply in Regime 2 for $\sigma_n^{\text{eff}} = 170$ MPa and $P_f = 100$ MPa (Fig. 4.5a). Increasing the quartz content or performing the experiments dry instead of wet also resulted in an increase in μ (Fig. 4.5d and 4.5a). An increase in σ_n^{eff} resulted in a decrease of μ at 140 and 500°C, but did not have any effect at 350°C (Fig. 4.5a and 4.5b). No effect of P_f on μ was observed (Fig. 4.5c). In addition, all of our samples showed slip hardening behaviour except those with $\geq 85\%$ quartz (Fig. 4.3).

In the following, we attempt to explain qualitatively the above trends in (a-b) and μ versus temperature in terms of a previously published microphysical model. We then go on to compare the model predictions on the effects of V , quartz content, σ_n^{eff} and P_f with the effects reported here and we compare our findings with previous studies. Finally, we discuss the implications for subduction zone seismogenesis by roughly quantifying the effects of V , quartz content, σ_n^{eff} and P_f on the slip stability of illite-quartz gouges.

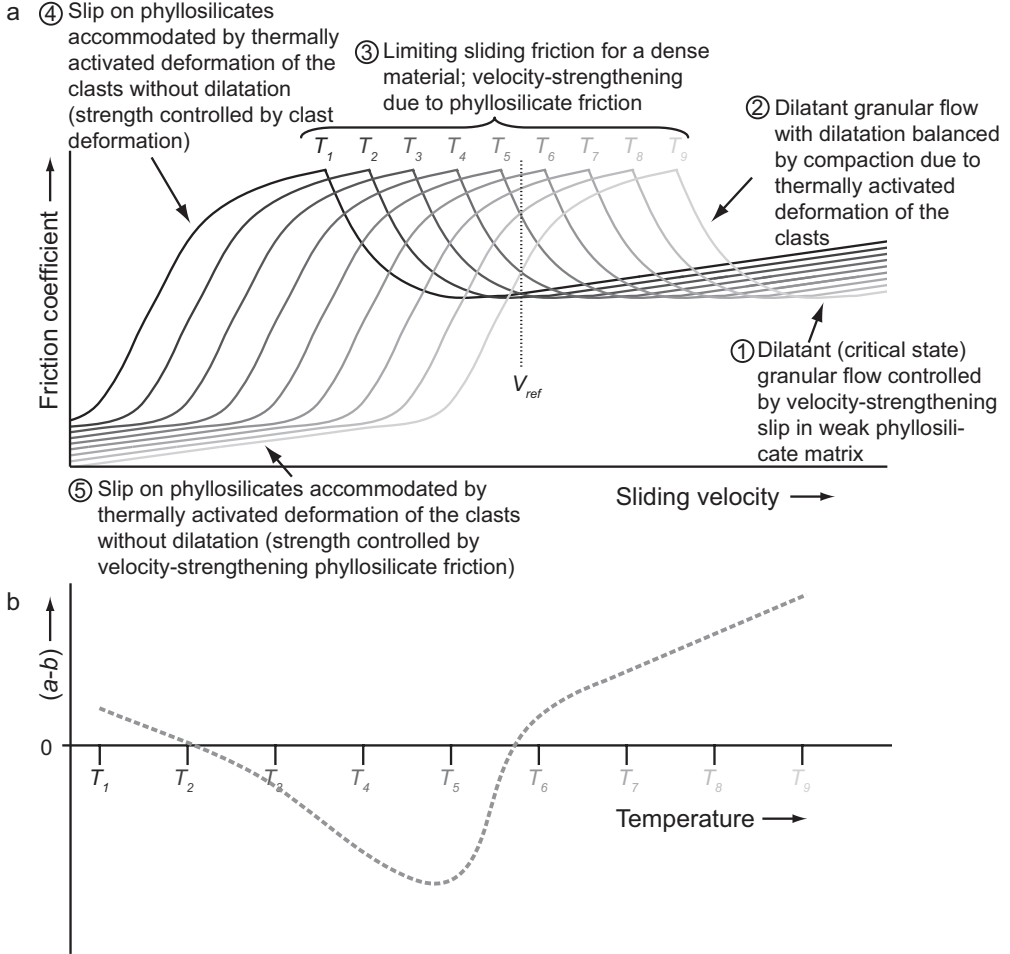


Figure 4.10 Schematic diagram illustrating the microphysical model by Niemeijer and Spiers (2007) used to explain our results. (a) Friction coefficient predicted by the model as a function of velocity for different temperatures (increasing from T_1 to T_9). Note that the asymptotic values of the friction coefficient that are approached at the lowest and highest velocity increase with sliding velocity, in contrast to the constant values assumed originally by Niemeijer and Spiers (2007). This is the consequence of taking the phyllosilicate matrix to be velocity strengthening in line with experimental data for pure phyllosilicates (e.g. Ikari et al., 2011), whereas Niemeijer and Spiers (2007) assumed velocity-neutral phyllosilicate friction. (b) Values of $(a-b)$ as a function of temperature at the fixed velocity (V_{ref}) indicated by the dotted line in (a). Note that $(a-b) = \partial\mu / \partial \log V$ is the slope of the μ versus sliding velocity curve at the corresponding temperature in (a).

4.4.1 Microscopic shear mechanisms: microphysical model versus results

4.4.1.1 Predicted and observed effects of temperature

The three regimes of velocity-dependence observed for 65:35 illite-quartz mixtures sheared at $\sigma_n^{eff} = 170$ MPa and $P_f = 100$ MPa (Dataset 1; Fig. 4.6a) were explained by Den Hartog et al. (2012a, Chapter 3) in the framework of the microphysical model proposed by Niemeijer and Spiers (2007; see also Bos and Spiers, 2002) for steady state shear flow of salt-clay and quartz-mica mixtures. The basic idea of this model is that changes in friction coefficient and $(a-b)$ with velocity and temperature are brought about by changes in the relative importance of deformation of the clast phase, by a thermally activated mechanism, versus athermal granular flow of the mixture accompanied by dilatation. The dependence of μ at steady state on sliding velocity and temperature and the resulting dependence of $(a-b)$ on temperature predicted by this model are illustrated schematically in Fig. 4.10, and the operative microscale processes are indicated (see also Niemeijer and Spiers, 2007). On the basis of microstructural evidence, and since dry samples did not show significant velocity-dependence (cf. Fig. 4.6d), it was argued by Den Hartog et al. (2012a, Chapter 3) that the relevant thermally activated process most likely involved fluid-assisted stress corrosion cracking (SCC), perhaps accompanied by pressure solution.

Applying the qualitative concepts of the Niemeijer and Spiers (2007) model, and allowing for velocity-dependent phyllosilicate friction, yields the following interpretation for the effect of temperature at a fixed reference velocity V_{ref} (Fig. 4.10). First, at the lowest temperatures investigated (150-250°C), thermally activated deformation of the quartz clasts and phyllosilicate matrix will be negligible, leading to dilatational granular flow involving frictional slip on the weak phyllosilicates in the matrix. Under these conditions, porosity (Φ) will develop, due to dilatation, in a manner similar to that familiar in soil mechanics, i.e. it will develop with shear strain at a rate determined by the dilatation angle defined $\tan \psi = \partial \varepsilon / \partial \gamma$ where ε is dilatational strain (cf. Paterson, 1995). In granular media, this angle decreases with increasing porosity, reaching zero at a steady state value known as the critical state porosity (e.g. Gerogiannopoulos and Brown, 1978). During steady state deformation at the critical state, intergranular friction in the weaker phyllosilicate matrix will determine the macroscopic friction. As a result, the velocity-strengthening behaviour expected for phyllosilicates (e.g. Ikari et al., 2011) will dominate (temperatures T_1 and T_2 in Fig. 4.10b).

Second, with increasing temperature ($T_2 - T_5$; Fig. 4.10), the model predicts that more efficient thermally activated deformation of the quartz clasts, by processes such as pressure solution or SCC, results in compaction (porosity reduction) competing with dilatation. When these balance (at steady state), a denser microstructure than that seen at low temperatures results, characterized by an increased frictional strength. This increase occurs because, according to the relation

$$\tau = \frac{(\tilde{\mu} + \tan \Psi)}{(1 - \tilde{\mu} \tan \Psi)} \sigma_n^{eff} \quad (4.3)$$

given by Niemeijer and Spiers (2007), the resistance to overall shear increases with decreasing porosity and increasing dilatation angle. Here $\tilde{\mu}$ is the friction coefficient within

the phyllosilicates. Upward velocity steps from a given steady state cause an increase in porosity, and thus a decrease in dilation angle. Hence, the macroscopic frictional strength will progressively decrease in consecutive upward velocity steps. Competition between intergranular dilatation and increasingly efficient thermally activated compaction can therefore explain the observed decrease of $(a-b)$ with increasing temperature seen in the range 150-350°C, as well as the transition from velocity-strengthening to velocity-weakening behaviour seen at ~250°C (compare Fig. 4.6a with temperatures T_2 - T_5 in Fig. 4.10).

Finally, at still higher temperatures, the Niemeijer-Spiers (2007) model predicts that thermally activated compaction becomes yet more efficient, yielding a steady state microstructure that is sufficiently dense that the frictional strength increases to approach a limiting value, characteristic of zero porosity (T_6 in Fig. 4.10a). Under these conditions, upward steps in velocity will exhibit velocity-strengthening caused by the velocity-strengthening nature of the weak phyllosilicate matrix (e.g. Ikari et al., 2011). This offers an explanation for the observed switch back to velocity-strengthening behaviour beyond 350°C. With ongoing increase in temperature, thermally activated deformation of the quartz clasts will ultimately become so efficient, that they will begin to shear “internally”, accommodating slip on an increasingly well developed phyllosilicate foliation (Bos et al., 2000; Bos and Spiers, 2001) and leading to a serial, strongly velocity-strengthening slip process (T_7 - T_9 in Fig. 4.10; velocity-strengthening mylonitic textural regime of Bos et al., 2000; Bos and Spiers, 2001; 2002; Niemeijer and Spiers, 2005; 2006; 2007).

4.4.1.2 Predicted and observed effects of other variables on $(a-b)$

Most of the newly observed effects of σ_n^{eff} , P_f , quartz content and sliding velocity reported in the present paper can also be qualitatively understood in the framework of the model presented by Niemeijer and Spiers (2007). From the model, increasing effective normal stress and decreasing sliding velocity are both expected to lead to an increase in the relative importance of thermally activated deformation and/or compaction by SCC or pressure solution of the quartz clasts, relative to athermal granular flow plus dilatation at any given temperature. This increase in compaction/deformation rate would be broadly equivalent to an increase in temperature and hence results in a shift of the three frictional slip stability regimes towards lower temperatures (cf. Fig. 4.10). Such effects are indeed observed with increasing effective normal stress (Figs. 4.6a, 4.6b, 4.7 and 4.9a) and decreasing sliding velocity (Figs. 4.6a, 4.8c and 4.9d).

Though more difficult to assess, an increase in quartz content is also expected to increase the thermally activated compaction/deformation rate, because, in the Niemeijer and Spiers (2007) model, it is the quartz that deforms by thermally activated processes. A larger proportion of quartz is thus expected to again have similar effects to increasing the temperature at any given porosity, shifting the three slip stability regimes towards lower temperatures. This is in good agreement with the observed decrease of $(a-b)$ with increasing quartz content seen in Regime 1 (Fig. 4.8b and 4.9c). On the other hand, the relative proportions of quartz and phyllosilicates may also influence the rate of dilation accompanying granular flow, perhaps complicating this picture.

Finally, we consider the presently observed effects of P_f . An increase in pore fluid pressure

in the range 50-200 MPa is not expected to enhance pressure solution or SCC significantly in quartz, as quartz solubility and surface reaction rates in aqueous solution are insensitive to fluid pressure, at least above 100 MPa (e.g. Walther and Helgeson, 1977). On this basis, P_f is expected to have little influence on the rate of thermally activated compaction or on the temperature location of the three slip stability regimes seen in our ($a-b$) versus T data. Our data indeed show only a slight increase in ($a-b$) with increasing pore fluid pressure over the limited range investigated (Fig. 4.6c, 4.8a and 4.9b), which is therefore reasonably consistent with our model.

4.4.1.3 Predicted and observed trends in μ

A key characteristic of the above microphysical model is the increase in the thermally activated deformation rate of quartz clasts with increasing temperature. In the model framework, this leads to compaction becoming significant in the velocity-weakening region and subsequently decreasing in importance at higher temperatures, where the microstructure is too dense for compaction to proceed. Compaction of the gouge yields a denser microstructure, and hence a higher friction coefficient. Therefore, the model predicts an increase in friction coefficient with increasing temperature in the velocity-weakening field (Fig. 4.10), which is in broad agreement with our observations (Fig. 4.5a). At $\sigma_n^{eff} = 170$ MPa and $P_f = 100$ MPa (Dataset 1), our data indeed show the sharpest increase in μ in Regime 2 (Fig. 4.5a). The continued increase from Regime 2 to 3 can be explained by the complete elimination of porosity (T_5-T_6 in Fig. 4.10a). The enhancement of thermally activated compaction with increasing quartz content implied by the model also agrees with the observed increase in friction coefficient for an increase in the quartz fraction (Fig. 4.5d). Similarly, an increase in effective normal stress should also promote thermally activated compaction. However, the expected accompanying increase in μ with σ_n^{eff} is not observed. Instead, μ decreases with increasing σ_n^{eff} at 140°C and 500°C (Fig. 4.5a and b). With reference to the plot of τ versus σ_n^{eff} shown in Fig. 4.4, though, it is evident that this is related to use of the apparent friction coefficient, defined $\mu = \tau / \sigma_n^{eff}$. In this definition, τ and μ include the cohesion S_0 of the gouge, which in the experiments at 140°C and 500°C is significant (though possibly an artefactual contribution of seal friction). Cohesion is negligible at other temperatures (Fig. 4.4). In line with our observations (Fig. 4.5c), the microphysical model does not predict an effect of P_f on μ .

Turning to the role of water, the fact that the friction coefficient increases strongly when samples are deformed dry as opposed to wet (Fig. 4.5a), is consistent with the generally accepted notion that water decreases the frictional strength of phyllosilicate-rich fault gouges by adsorbing onto the phyllosilicates and providing a low-resistance slip interface (e.g. Morrow et al., 2000). This effect apparently outweighs the decrease in μ expected in Regimes 1 and 2 by the inhibition of compaction by SCC or pressure solution in dry samples compared with wet. It is possible that viscous water films coating the phyllosilicate surfaces could lead to temperature and velocity dependent changes in strength and compaction behaviour of the phyllosilicates (e.g. Hüpers and Kopf, 2009). This, or other thermally activated processes, at the grain scale or at the intergranular asperity scale, in the phyllosilicates, could conceivably also influence ($a-b$) versus temperature in our wet experiments.

Finally, we address the slip hardening effect on μ seen in the present experiments (Fig. 4.3). Den Hartog et al. (2012b, Chapter 2), following Tembe et al. (2010), explained this as due to progressive crushing and dispersion of quartz grains throughout the gouge. This may have been further enhanced by preferential loss of clay, from samples sheared at high σ_n^{eff} , involving extrusion past the rings confining the samples (Fig. 4.2c; see also Den Hartog et al., 2012a, Chapter 3). Note, however, that the influence of slip hardening on our μ and (*a-b*) data, and on the comparison with the steady state model of Niemeijer and Spiers (2007), has been minimised through our use of μ at yield and by the detrending procedure employed to obtain (*a-b*) values.

In order to fully understand the effects of temperature, σ_n^{eff} , sliding velocity, quartz content and P_f on the frictional strength and stability regimes of illite-rich fault gouge, the model of Niemeijer and Spiers (2007) clearly needs to be quantitatively applied, including the effects of all of the main variables. The resulting model should be capable of predicting (*a-b*) and μ versus temperature profiles for a chosen set of conditions, which can then be compared with those reported here. Such a modelling effort requires full quantification of the operative SCC and possible pressure solution processes and is beyond the scope of the present article but will be attempted in a future paper.

4.4.2 Comparison with previous work on other gouge compositions

The proposed microphysical processes governing the slip stability of illite-quartz mixtures as a function of temperature can be expected to operate in other phyllosilicate-quartz or similar granular mineral aggregates, leading to similar trends in frictional behaviour. This indeed seems to be the case for wet quartz (Chester and Higgs, 1992), granite (Blanpied et al., 1991; 1995; 1998), gabbro (He et al., 2007) and San Andreas Fault (SAF; Tembe et al., 2009) gouges. Like our samples, the gouges showed three-regime behaviour with velocity-weakening occurring at temperatures of, respectively, 300°C, 100-350°C, 170°C-310°C and 266-283°C, with velocity-strengthening at higher and lower temperatures. Based on microstructural evidence, Chester and Higgs (1992) suggested that at temperatures up to 300°C deformation of the quartz gouge occurred by heterogeneous cataclastic deformation, giving way to cataclastic flow assisted by solution-precipitation processes at 450-600°C, broadly in line with our microphysical model. Blanpied et al. (1991; 1995; 1998) also proposed fluid-assisted processes such as pressure solution and subcritical crack growth to be important in their experiments at high temperature.

Despite differences in the conditions leading to velocity-weakening behaviour, some of the other trends in (*a-b*) seen in the present experiments on illite-quartz gouge were also observed for the above-mentioned materials. For example, the data on granite gouge presented by Blanpied et al. (1995; 1998) point to an increase in (*a-b*) with an increase in pore fluid pressure from 10 MPa to 100 MPa, at least in the high temperature velocity-strengthening regime (600°C). Similarly, He et al. (2007) observed an increase in (*a-b*) (i.e. a less negative value) for the same increase in pore fluid pressure in the velocity-weakening regime for gabbro gouge (252°C). Both findings are consistent with our observation of an increase in (*a-b*) with increasing pore fluid pressure (Figs. 4.6a, 4.6c, 4.8a and 4.9b). Like our data, the data of Blanpied et al. (1995; 1998) also show an increase in the transition temperature from velocity-weakening (Regime 2) to strengthening (Regime 3) with an

increase in slip rate. In addition, He et al. (2007) report an effect of effective normal stress on the slip stability of gabbro gouges. These authors observed a shift from three-regime behaviour to exclusively velocity-strengthening behaviour when the effective normal stress was increased from 200 MPa to 300 MPa. This may suggest a general increase in $(a-b)$ with increasing effective normal stress rather than the shift of the $(a-b)$ versus T curve towards lower temperatures observed by us (Figs. 4.6a, 4.6b, 4.7 and 4.9a). Such a discrepancy could reflect an effect of gouge composition, or might point to a possible influence of the much lower displacements reached (~ 4.3 mm) in the experiments of He et al. (2007). Note that an effect of displacement was reported by Beeler et al. (1996), characterized by decreasing $(a-b)$ values with displacement at displacements of ~ 20 – 40 mm ($\gamma \sim 20$ – 40). Analysis of our $(a-b)$ versus displacement data shows a broad scatter, with a weak negative correlation, perhaps indicating a slight effect of displacement.

Our results of the effect of velocity on $(a-b)$ are also largely consistent with the results of Shimamoto (1986), even though these experiments were performed on halite at room temperature. Shimamoto (1986) showed a change from velocity-strengthening at $\sim 10^{-9}$ – 10^{-7} m/s to velocity-weakening at $\sim 10^{-7}$ – 10^{-5} m/s and back to strengthening at $\sim 10^{-5}$ – 10^{-4} m/s. With reference to Fig. 4.9d, the same trend is present in our data, at a constant temperature.

Some of the trends in μ seen in our data and predicted by our model have also been observed in the above materials. For example, the three-regime behaviour in $(a-b)$ versus temperature visible in the data reported by Tembe et al. (2009) for SAF gouge was accompanied by an increase of μ with temperature, particularly in the neighbourhood of the velocity-weakening regime. In addition, although no $(a-b)$ values were determined, Van Diggelen et al. (2010) found an increase in μ for muscovite gouge, the high temperature equivalent of illite, concentrated in the range 200–500°C. Though relatively minor, wet granite and gabbro gouges show a similar increase in μ with temperature, but only at the low temperature end of the velocity-weakening regime.

Drawing together all of the foregoing discussion, it seems that the microphysical processes inferred to operate in our illite-quartz samples very probably explain the behaviour seen in other (wet) gouge systems at elevated temperatures. Finally, our data at 140°C show a linear increase in friction coefficient with increasing quartz content (Fig. 4.5d), in good agreement with previous room temperature data presented by Tembe et al. (2010) for illite-quartz mixtures tested at 40 MPa effective normal stress (cf. Brown et al., 2003). This behaviour contrasts with the non-linear dependence on quartz content generally observed in soil mechanics (e.g. Lupini et al., 1981), where the friction of clay-quartz mixtures becomes dominated by the end-member phases at a concentration of $>75\%$. The difference remains hard to explain at present, but may reflect differences in applied effective normal stress, sample porosity (water content), clay mineral type, or strain hardening behaviour (cf. Tembe et al., 2010).

4.4.3 Implications for seismogenesis under in-situ megathrust conditions

The three-regime behaviour for illite-rich fault gouge reported by Den Hartog et al. (2012a, Chapter 3) and forming Dataset 1 here (Fig. 4.6a), involved velocity-weakening at ~ 255 – 370°C for upward velocity steps at the lowest sliding velocity, i.e. from 1 to 10 $\mu\text{m/s}$.

This three-regime behaviour closely resembles the sequence of aseismic - seismogenic - aseismic behaviour seen with increasing temperature and depth within subduction zone megathrusts. However, the onset of velocity-weakening behaviour occurs at a temperature $\sim 100^\circ\text{C}$ higher than that of 150°C typically associated with the up-dip seismogenic limit (Hyndman et al., 1997). Den Hartog et al. (2012a, Chapter 3) recognized that the velocity-weakening regime is positioned at lower temperatures for velocity steps involving 1 and $10\ \mu\text{m/s}$ than for those involving 10 and $100\ \mu\text{m/s}$ (cf. Fig. 4.6a) and proposed that this may explain the 100°C discrepancy, taking into account the low nucleation velocities expected in nature compared with our lab-imposed velocities. We have shown here, that apart from the sliding velocity, the effective normal stress, pore fluid pressure and quartz content also affect the temperature-extent of the three slip stability regimes characterizing illite-quartz gouges. In the following, we will try to quantify roughly the dependence of $(a-b)$ on the variables investigated and to assess the implications of these trends for seismogenesis in subduction zones. We take our $(a-b)$ data for the upward step in velocity at the lowest sliding velocity studied (i.e. from 1 to $10\ \mu\text{m/s}$) in Dataset 1 as the reference case for determining the sensitivity of $(a-b)$ to V , quartz content, P_f and σ_n^{eff} , as these low velocities are the most relevant to earthquake nucleation. A basic assumption made is that the effects of the different variables investigated are independent.

4.4.3.1 Sensitivity of $(a-b)$ to sliding velocity

We begin with the effect of sliding velocity on $(a-b)$. This varies between $+0.01$ per order of magnitude increase in velocity at 150°C , through $+0.004$ at 250°C , to -0.02 per order at 500°C , changing in sign between 350°C and 400°C (Fig. 4.6a and 4.8c). With reference to Fig. 4.6a, for an upward step in velocity, this results in a shift of the transition temperature marking the onset of velocity-weakening behaviour (i.e. the equivalent of the up-dip seismogenic limit) of $\sim 32^\circ\text{C}$ per order of magnitude increase in velocity. The boundary between Regime 2 and 3, which we assume is equivalent to the down-dip seismogenic limit, in turn, moves up in temperature by $\sim 75^\circ\text{C}$ per order increase in velocity. If we assume that the sliding velocity during the initiation of an earthquake increases by one order of magnitude from a value close to plate velocities of $\sim 10^{-9}\ \text{m/s}$ (Segall and Rice, 2006), the current data accordingly imply a velocity-weakening regime starting at a temperature of $\sim 155^\circ\text{C}$ (that is a shift of $\Delta T = -32^\circ\text{C} \times \log(10^{-9}/10^{-6})$ from the transition in Fig. 4.6a). This temperature indeed agrees much better with the generally accepted temperature of 150°C at the up-dip seismogenic limit than the value of 255°C shown by our data for velocity steps from 1 to $10\ \mu\text{m/s}$ in Fig. 4.6a. The extrapolated temperature for the down-dip seismogenic limit, on the other hand, would be only $\sim 142^\circ\text{C}$ and thus much too low, being even less than that at the up-dip seismogenic limit. This may point to the importance of taking into account additional factors, such as changes in effective normal stress with depth or the thickness of the gouge layer that accommodates deformation (i.e. slip velocity versus shear strain), but could also reflect “over-extrapolation” of the observed $(a-b)$ versus temperature trend.

4.4.3.2 Sensitivity of $(a-b)$ to quartz content

At $T = 140^\circ\text{C}$, $\sigma_n^{\text{eff}} = 100\ \text{MPa}$, $P_f = 200\ \text{MPa}$ and for velocity steps of $1\text{--}10\ \mu\text{m/s}$, an increase in the quartz content results in a decrease of $(a-b)$ with a sensitivity ranging between $\sim 8.3 \times 10^{-5}$ and $\sim 3.3 \times 10^{-4}$ for a 1% increase in quartz (Fig. 4.8b). In addition, our data shows that under these conditions, a fault gouge will become velocity-weakening for a quartz content

of ~82%. Thus, velocity-weakening behaviour may be expected to start at relatively low temperatures in quartz-rich subduction zones. When taking into account the decrease in $(a-b)$ with decreasing sliding velocity for Regime 1 as quantified above (Fig. 4.8c), $(a-b)$ values become negative over the entire range of quartz contents measured at 140°C at earthquake nucleation slip rates (cf. Fig. 4.8b). Noting that the Japan Trench sediments are relatively siliceous (Kameda et al., 2012), this de-stabilizing effect of quartz could perhaps help to explain the estimated relatively low temperature of ~140°C (JMA; Peacock and Wang, 1999) pertaining at the focal depth of the M_w 9.0 Tohoku-Oki earthquake (NE Japan) of 11 March 2011 (e.g. Ide et al., 2011; Ozawa et al., 2011; Simons et al., 2011).

4.4.3.3 Sensitivity of $(a-b)$ to P_f and σ_n^{eff}

The present data show that an increase in pore fluid pressure seems to result in an increase in $(a-b)$ in all three slip stability regimes (Fig. 4.6c and 4.8a). A linear fit to our $(a-b)$ versus P_f data for velocity steps from 1 to 10 $\mu\text{m/s}$ (Fig. 4.8a) indicates a sensitivity of $(a-b)$ to P_f of $\sim 6.5 \times 10^{-5}$ per MPa. The implication of such an effect of P_f on $(a-b)$ at all temperatures is that the temperature-extent of the velocity-weakening region shrinks with increasing P_f by $\sim 4^\circ\text{C}$ per 10 MPa.

The effect of σ_n^{eff} on $(a-b)$ can be roughly quantified by comparing obtained results at $\sigma_n^{eff} = 170$ MPa (Fig. 4.6a) and at $\sigma_n^{eff} = 50$ MPa (Fig. 4.6b), and presented in Fig. 4.7. These data show a sensitivity of $(a-b)$ to σ_n^{eff} that is different for each of the three regimes. In Regime 1, the data at 200°C suggest a decrease in $(a-b)$ by $\sim 7.3 \times 10^{-5}$ per MPa increase in σ_n^{eff} above 50 MPa, whereas at 500°C (Regime 3) $(a-b)$ increases by 1.9×10^{-4} per MPa. At 350°C (Regime 2), the sensitivity of $(a-b)$ to σ_n^{eff} depends on the range of σ_n^{eff} considered, decreasing by $\sim 3.1 \times 10^{-4}$ per MPa increase in σ_n^{eff} at $\sigma_n^{eff} < 90$ MPa, increasing by $\sim 4.1 \times 10^{-4}$ per MPa at $90 < \sigma_n^{eff} < 130$ MPa, and again decreasing at $\sigma_n^{eff} > 130$ MPa, by $\sim 2.3 \times 10^{-5}$ per MPa increase in σ_n^{eff} . At a pore fluid pressure of 200 MPa, the decrease in $(a-b)$ per MPa increase in σ_n^{eff} in Regime 1 is similar, being $\sim 6.1 \times 10^{-5}$ at 140°C (Fig. 4.7b).

4.4.3.4 Extrapolation to in-situ conditions

The significance of the effects of the above variables for extrapolation purposes can be assessed by comparing the corresponding sensitivities to the temperature sensitivity of $(a-b)$. The sensitivity of $(a-b)$ to temperature varies between $\sim 2.0 \times 10^{-5}$ and 3.5×10^{-4} per $^\circ\text{C}$, with an average value of around 1.70×10^{-4} per $^\circ\text{C}$. This means, that to change $(a-b)$ by for example 0.004 (~10% of the total range in the reference case; 1-10 $\mu\text{m/s}$; Fig. 4.6a), a change in temperature of $\sim 24^\circ\text{C}$ is required. Alternatively, the sensitivities determined above imply that the same change can be achieved by a change of 0.2-1.1 orders of magnitude in V , a change of 12-48% in quartz content, 62 MPa in P_f or a change of 10-177 MPa in σ_n^{eff} . This comparison illustrates that, as well as temperature, other variables, in particular the sliding velocity, pore fluid pressure and the effective normal stress, are expected to have significant effects on the slip stability of illite-quartz gouge within the range of variability expected for these quantities under subduction zone megathrust conditions (V : 10^{-9} - 10^{-6} m/s; P_f : hydrostatic-lithostatic; σ_n^{eff} : zero-lithostatic). Thus, the generally accepted view that the depth extent of the seismogenic zone of subduction megathrusts is thermally controlled (e.g. Hyndman et al., 1997) is one that neglects important other effects.

The question now arises as to the temperatures and depths at which we can expect velocity-weakening behaviour under in-situ conditions. However, the present data is too limited to allow reliable extrapolation over the relevant ranges of P_f and σ_n^{eff} . Moreover, the manner in which P_f and hence σ_n^{eff} vary with depth is largely unknown at depths greater than a few km in subduction zone megathrust environments (e.g. Saffer and Tobin, 2011). Fluid overpressures (i.e. above hydrostatic) are believed to be significant at depths just above the up-dip seismogenic limit, as a result of compaction and dehydration reactions (Moore and Saffer, 2001; Saffer and Tobin, 2011). This is supported by observations of Very Low Frequency Earthquakes (VLFES; Ito and Obara, 2006) and tectonic tremor (Obana and Kodaira, 2009) at these depths. Such events are associated with unusual seismological characteristics, such as ultra-low shear wave velocities, anomalously high Poisson's ratios and high P to S wave velocity ratios, suggesting elevated pore fluid pressures (e.g. Beroza and Ide, 2011; Kato et al., 2010; Kodaira et al., 2004). Similarly, observations of (V)LFEs, tremor and Slow Slip Events (SSEs), at depths just beyond the down-dip seismogenic limit, suggest the existence of high fluid overpressures there too (e.g. Beroza and Ide, 2011; Saffer and Tobin, 2011; Shelly et al., 2006). By contrast, the fluid overpressure in the seismogenic zone itself is believed to be only moderate compared to that beyond its up- and down-dip limits (Saffer and Tobin, 2011), lying between hydrostatic and lithostatic and reaching lithostatic values in the adjacent aseismic zones (Saffer and Tobin, 2011). This all implies a complicated depth profile for the pore fluid pressure, with rapid changes around the limits of the seismogenic zone. As a result, the effective normal stress is expected to be higher in the seismogenic zone than in the neighbouring aseismic regions up- and down-dip. We can only conclude that, since an increase in σ_n^{eff} relative to our experimental reference value results in a shift of the three slip stability regimes towards lower temperatures and vice versa (Fig. 4.6a, 4.6b and 4.7), the $(a-b)$ versus depth profile along a subduction megathrust will be critically dependent on the evolution of the pore fluid pressure with depth. At present, this profile is largely a matter of speculation (Saffer and Tobin, 2011). Clearly, then, to map the depth extent of velocity-weakening behaviour on subduction zone megathrusts, it is crucial to obtain (i) better insight into the pore fluid pressure distribution that may be expected in-situ, and (ii) more data to constrain extrapolation of the effects of V , quartz content, P_f and σ_n^{eff} on $(a-b)$, and to enable calibration of the proposed microphysical model. In addition, the quartz content is not the only possible compositional variable and some subduction zones show the presence of materials such as chalk (e.g. Spinelli and Underwood, 2004).

4.4.3.5 Stiffness, strength and stability

So far, we have focused on the velocity-dependence of friction in determining the conditions under which megathrust fault gouge behaviour can be seismogenic or not. However, the stability of faults also depends on the elastic stiffness of the material surrounding the slipping portion of a fault, compared to a critical stiffness value. This critical value is defined in terms of the spring stiffness in an equivalent spring-slider model for the fault (e.g. Beeler, 2007), and is given:

$$K_c = \frac{-(a-b)\sigma_n^{eff}}{d_c} \quad (4.4)$$

Earthquake nucleation requires the elastic stiffness (K) of the material surrounding the slip

zone to be less than this critical value, when expressed in terms of a spring-slider model. Non-destructive events observed up- and down-dip of the seismogenic zone, on the other hand, are believed to be related to the criterion given in Eq. (4.4) being closely approached (e.g. Liu and Rice, 2005; Segall et al., 2010). Once again then, through the appearance of σ_n^{eff} in this stability criterion, the effective normal stress and fluid pressure are seen to be of key importance in determining the frictional stability of megathrust faults, further highlighting the need for a better understanding of the P_f and σ_n^{eff} versus depth profiles characterizing subduction zone megathrusts.

Once the conditions for unstable behaviour are met, i.e. $(a-b) < 0$ and $K < K_c$, the magnitude of the stress drop during an earthquake will depend on the friction coefficient. We have shown that μ increases with temperature (Fig. 4.5a), which suggests potentially larger stress drops at greater depths. This is consistent with stress drop estimates as a function of depth by Bilek and Lay (1999). A full analysis of earthquake nucleation would, in addition, require that effects of inertia and energy release rate be taken into account (e.g. Dieterich, 1992; Rubin and Ampuero, 2005). Such an analysis, however, is beyond the scope of the present paper.

4.5 Conclusions

We have aimed to determine how the frictional strength and velocity-dependence ($a-b$) of illite-rich fault gouge deformed under in-situ megathrust conditions depend on temperature, effective normal stress, pore fluid pressure, phyllosilicate versus quartz content and sliding velocity. We performed rotary shear friction experiments on illite-quartz fault gouge at effective normal stresses in the range 25-200 MPa, pore fluid pressures ranging from 50 to 200 MPa and temperatures in the range 140-600°C. In addition, we examined the effect of composition by using gouge mixtures with increasingly large proportions of quartz (~35-100%). Our conclusions are as follows:

1. The three temperature-dependent slip stability regimes recognized previously by Den Hartog et al. (2012a, Chapter 3), i.e. a predominantly velocity-strengthening regime at 150-250°C (Regime 1), a mostly velocity-weakening regime at 250-400°C (Regime 2) and a mainly velocity-strengthening regime at 400-500°C (Regime 3), move towards higher temperatures with an increase in sliding velocity, and conversely to lower temperature with a decrease in velocity.
2. An increase in quartz fraction results in a decrease of $(a-b)$, at least in Regime 1, suggesting a shift of the velocity-weakening regime towards lower temperatures with increasing quartz content. An increase in the quartz content also results in an increase in the friction coefficient, linearly from ~0.4 to ~0.7 at yield, for an increase in quartz content from 35 to 100%, at 140°C and $\sigma_n^{eff} = 100$ MPa and $P_f = 200$ MPa. This effect of quartz content is in line with the findings of Tembe et al. (2010) in experiments at room temperature.
3. The pore fluid pressure has on average only a minor effect on the frictional slip stability across the range investigated, increasing $(a-b)$ at all temperatures explored. The friction coefficient shows no dependence on the pore fluid pressure.
4. The three slip stability regimes shift towards higher temperatures with a decrease in effective normal stress. At an effective normal stress of 50 MPa, the boundaries between Regime 1 and 2 and between 2 and 3 lie at ~350°C and ~600°C, respectively. The friction

- coefficient is relatively insensitive to changes in the effective normal stress.
5. These qualitative trends in friction coefficient and velocity-dependence (*a-b*) can largely be explained in terms of a microphysical model previously proposed by Niemeijer and Spiers (2007), modified to include velocity-strengthening of the phyllosilicates. This model describes the frictional behaviour of mixtures of phyllosilicates with a granular material (quartz clasts) capable of deforming by a thermally activated, hence time-dependent, deformation mechanism. With increasing temperature, the processes operating at the microscale are inferred to change from (i) dilatant granular flow controlled by velocity-strengthening slip within the weaker phyllosilicates (Regime 1), to (ii) competition between dilatation due to granular flow and compaction by thermally activated stress corrosion cracking (SCC) of quartz grains plus possible pressure solution (Regime 2), resulting in velocity-weakening. At still higher temperatures, compaction becomes more efficient and the limiting frictional strength of a fully dense material is approached, resulting in velocity-strengthening behaviour controlled by the properties of the weaker phyllosilicate matrix (Regime 3). Ultimately, thermally activated deformation of the clasts becomes so easy that the clasts can deform to accommodate slip on the phyllosilicates, leading to a decrease in frictional strength but increased velocity-strengthening.
 6. In this model, an increase in the effective normal stress, decrease in the sliding velocity and increase in quartz content are all expected to enhance thermally activated deformation of the quartz clasts, thus resulting in a shift towards lower temperatures of the three-regime behaviour, as observed.
 7. Our results show that the depth extent of the seismogenic zone on subduction megathrusts is significantly influenced not only by temperature as often assumed, but also by other variables, shifting to lower temperatures hence shallower levels with a decrease in the sliding velocity, an increase in the quartz content or an increase in σ_n^{eff} , and narrowing in extent with an increase in P_f . A first attempt to use the observed trends to predict the temperature hence depth extent of velocity-weakening behaviour on megathrusts under in-situ conditions shows that, to achieve this, it is essential to find a way to quantify the dependence of pore fluid pressure on depth.

Acknowledgements

K. Kanagawa encouraged us to contribute to the Kochi conference. We thank C. Marone and B. Carpenter of the Pennsylvania State University for providing the illite gouge and the XLook program for obtaining RSF parameters. G. Kastelein, T. van de Gon Netscher, E. de Graaff and P. van Krieken provided technical assistance. We thank Guest Editor G. Di Toro and Reviewers M. Ikari and H. Noda for their helpful reviews. This work was funded by means of a Toptalent grant awarded by the Netherlands Organisation for Scientific Research (NWO) to SdH (Dossier number 021.002.025).

Chapter 5

Friction on subduction megathrust faults: beyond the illite-muscovite transition

Sabine A.M. den Hartog, André R. Niemeijer and Christopher J. Spiers

Submitted to Earth and Planetary Science Letters

Abstract

Previous experimental studies addressing subduction megathrust friction have focused on shallow fault gouges, dominated by smectite, illite and quartz. Here, we aim to determine the effect of the transition to muscovite-rich fault rock at depths beyond the illite-dominated region of the seismogenic zone. To achieve this, rotary friction experiments were performed on simulated muscovite-quartz (65:35) gouge at 100-600°C, an effective normal stress of 170 MPa, pore pressures of 100 and 200 MPa, and sliding velocities of 1-100 $\mu\text{m/s}$. We distinguished the effects of muscovite versus quartz by shearing pure muscovite gouge at 200-600°C, under otherwise identical conditions. At low shear strains ($\gamma \approx 1$), muscovite-quartz gouge showed a friction coefficient μ of 0.4-0.5, while muscovite gouge exhibited $\mu \approx 0.3$. Both gouges showed an increase in μ with γ and temperature. The muscovite-quartz gouge was characterised by velocity-strengthening or neutral behaviour at 100-350°C, velocity-weakening at 350-500°C and velocity-strengthening at 500-600°C. Pure muscovite gouge showed predominantly velocity-strengthening or neutral behaviour, demonstrating a key role of quartz in producing velocity-weakening. The velocity-weakening regime in the mixed gouge extends that recently reported for illite-quartz gouge from 250-400°C up to 500°C. Taken together, these data help explain the depth extent of seismogenesis along subduction megathrusts. Interestingly, comparison with previous microphysical models suggests that the underlying mechanism causing velocity-weakening in phyllosilicate-quartz gouge is one of granular flow involving competition between shear-induced dilation and compaction through thermally activated quartz deformation.

5.1 Introduction

The slip behaviour of subduction megathrusts changes with depth and temperature from predominantly aseismic in the shallow, up-dip region at temperatures below $\sim 150^{\circ}\text{C}$, through seismic at intermediate depths and temperatures (10–40 km, $150\text{--}350^{\circ}\text{C}$), to again aseismic at greater depths (e.g. Hyndman et al., 1997). Slip is believed to be localized in the subducted sediments present at the interface between the subducting and overlying plates (Moore, 1989; Saffer et al., 2012; Shipboard Scientific Party, 2001a, 2003). In the case of subduction zones dominated by pelitic input, such as Nankai or Barbados (e.g. Underwood, 2007), it is therefore reasonable to expect that the observed transitions in seismogenic behaviour may be related to the progressive diagenesis and ultimately metamorphism of the subducted clay-rich sediments.

Previous studies attempting to explain the depth-dependence of subduction megathrust seismicity have focused on the diagenetic transformation of smectite clays to illite. This is because the temperature of this transition ($\sim 100\text{--}150^{\circ}\text{C}$; see Hower et al., 1976; Jennings and Thompson, 1986) corresponds roughly with that at the presumed up-dip seismogenic limit (Hyndman et al., 1997). Vrolijk (1990) was among the first to suggest that it is this transition that causes the onset of seismogenic behaviour. Experimental studies subsequently performed on illite-rich gouge at room temperature appear to refute this hypothesis, showing only stable, “velocity-strengthening” frictional behaviour (Brown et al., 2003; Ikari et al., 2009; Morrow et al., 1992; Saffer and Marone, 2003; Tembe et al., 2010). However, more recent experiments (Den Hartog et al., 2012a, Chapter 3; 2012b, Chapter 2) have shown that illite-rich fault gouge does exhibit the velocity-weakening behaviour required for unstable behaviour and seismogenesis, when deformed at near in-situ pressures and at temperatures above $155\text{--}250^{\circ}\text{C}$, depending on sliding rate.

In contrast to the smectite-illite transition, almost no attention has been paid to the transformation of illite to muscovitic micas at temperatures of $\sim 200\text{--}300^{\circ}\text{C}$ (Hunziker, 1986; Merriman and Frey, 1999; Van de Kamp, 2008), despite the clear relevance of this transformation to the deeper portions of the seismogenic zone and beyond. Indeed, the velocity-dependence of friction for muscovite-rich gouges at in-situ megathrust pressures and temperatures is unknown at present, though the potential for unstable, velocity-weakening behaviour at these conditions is implied by the experimental studies reported by Van Diggelen et al. (2010) and Mariani et al. (2006), both of which showed stick-slip behaviour in muscovite-dominated gouges at $400\text{--}600^{\circ}\text{C}$.

Alongside the phyllosilicates, metapelitic megathrust fault gouges invariably contain quartz (e.g. Marone and Saffer, 2007; Shipboard Scientific Party, 2001b; Underwood et al., 1993). Quartz was present in all of the illite- and muscovite-rich fault gouges that showed stick-slip or velocity-weakening behaviour in experiments performed to date (Den Hartog et al., 2012a, Chapter 3; 2012b, Chapter 2; Mariani et al., 2006; Van Diggelen et al., 2010). Quartz is affected by thermally activated deformation processes like pressure solution and stress corrosion cracking (SCC), which become progressively faster with increasing temperature and hence depth (e.g. Schutjens, 1991; Spiers et al., 2004). The question therefore arises as to what extent the slip stability of subduction megathrusts is governed by the presence, concentration and behaviour of quartz, in the associated fault rocks, as

opposed to phyllosilicates.

In this paper, we investigate the velocity-dependent frictional behaviour of 65:35 muscovite-quartz and 100% pure muscovite fault gouges, under near in-situ subduction zone conditions. Our aim was to determine the frictional behaviour of megathrust fault rocks at depths beyond the illite-muscovite transition (i.e. beyond 200-300°C) and to determine the specific role of quartz versus muscovite at these depths.

5.2 Material and methods

5.2.1 Sample material

The synthetic fault gouge used in this study consisted of mixtures of muscovite (Mica S) and quartz (SIL-CO-SIL 75), or else of pure muscovite (crushed optical crystals). The Mica S was obtained from Aspang, Austria (Internatio B.V. Zutphen, the Netherlands) and has a mean, particle size grain size of 37 μm and a median grain size of 28 μm . The SIL-CO-SIL 75 was obtained from Mill Creek, Oklahoma (US Silica) and has mean and median grain sizes of ~ 21 and ~ 16 μm , respectively. We prepared mixtures of $\sim 65\%$ muscovite and $\sim 35\%$ quartz by weight from these materials, taking into account the presence of up to ~ 10 vol% quartz in the Mica S (Van Diggelen et al., 2010).

Pure muscovite gouge, with a mean, particle size grain size of 42 μm and a median grain size of 36 μm , was prepared from sheets of “grade 4” muscovite, obtained from SPI Supplies. The sheets were cleaved by hand and subsequently ground using a Retsch Ultra Centrifugal Mill ZM 200 and an agate ball mill. To obtain a similar grain size distribution to the Mica S, the crushed pure muscovite material was sieved to obtain particles < 50 μm in size, and subjected to gravity settling to partially remove grains smaller than ~ 8 μm .

Ring-shaped samples of both gouges, measuring ~ 1 mm in thickness and with inner and outer diameters of 22 and 28 mm, were prepared by pre-pressing mixtures of 0.5 g gouge and ~ 0.04 g distilled water. Pressing was done at ~ 170 MPa for 20 minutes at room temperature, using a specially designed die. This yielded a starting porosity of ~ 20 - 26% , determined from the sample mass, dimensions and mineral densities plus composition.

5.2.2 Experimental apparatus and procedure

Rotary frictional sliding experiments were performed using the hydrothermal ring shear machine (Fig. 5.1) described in detail by Den Hartog et al. (2012a, Chapter 3; 2012b, Chapter 2) and Niemeijer et al. (2008). In this machine, the pre-pressed, ring-shaped sample is sandwiched between two, roughened (~ 0.1 mm grooved), René 41 Superalloy pistons. These are located in an internally heated pressure vessel filled with distilled water, which forms the pore fluid phase. To inhibit extrusion, the sample is confined between the loading pistons by steel rings (Fig. 5.1c). Normal stress is applied to the small, porous sample, in excess of the pore fluid pressure (P_f) measured in the vessel, via a pressure-compensated upper loading piston, so that the effective normal stress (σ_n^{eff}) experienced by the sample is equal to the axially applied stress (see Den Hartog et al., 2012a, Chapter 3). Rotation of the vessel and lower piston allow shearing of the sample at constant rate, while the shear stress (τ) generated is measured externally via the non-rotating upper piston.

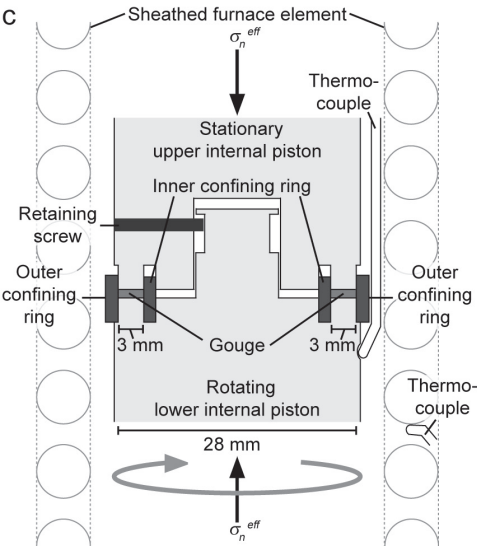
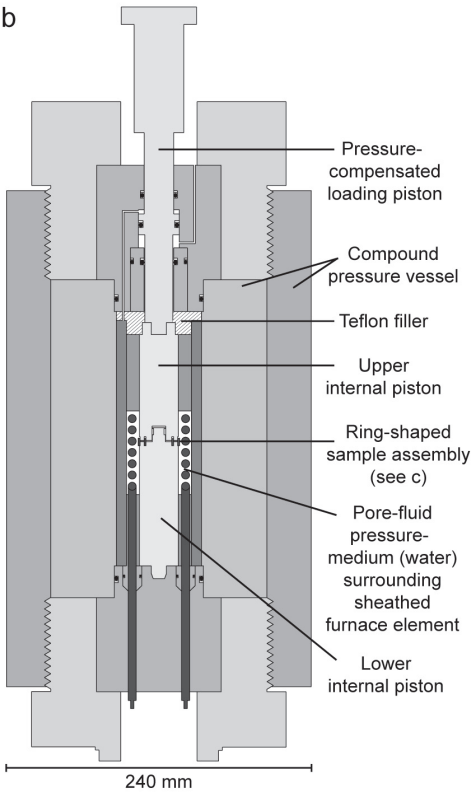
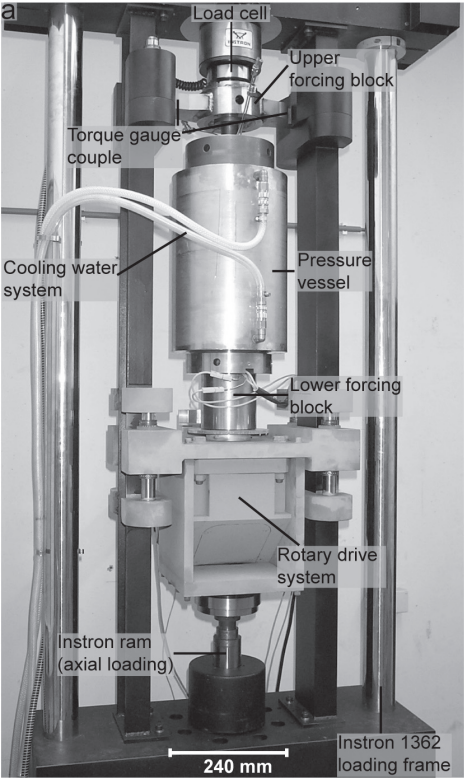


Figure 5.1 Ring shear machine used in the present study (after Den Hartog et al., 2012a, Chapter 3). (a) Rotary shear drive system and pressure vessel mounted inside the Instron loading frame used to apply normal stress to the sample. (b) Semi-schematic cross section of the pressure vessel. (c) Semi-schematic cross section of the sample assembly. σ_n^{eff} = effective normal stress.

The experimental procedure followed has been described by Den Hartog et al. (2012b, Chapter 2). Rotary shear experiments were performed at an effective normal stress of 170 MPa, a pore fluid pressure of 100 MPa, temperatures of 100-600°C and at sliding velocities

stepped between 1, 10 and 100 $\mu\text{m/s}$. The temperature range of 100-600°C was selected (i) to cover the seismogenic zone of subduction megathrusts and (ii) to cover the temperature range over which illite-quartz gouge previously showed 3 regimes of distinct behaviour (Den Hartog et al., 2012a, Chapter 3). A single experiment was performed at 200 MPa pore fluid pressure (at 500°C) to assess any effects of this variable. In all experiments, a sliding velocity of 10 $\mu\text{m/s}$ was imposed for the first 5 mm of shear displacement, before initiating velocity-stepping. Shear was terminated at a displacement of ~ 40 mm, to prevent gouge thinning to the point where the pistons would touch.

5.2.3 Data processing

Shear displacement (resolution $\pm 1 \mu\text{m}$), axial displacement ($\pm 0.05 \mu\text{m}$), normal force ($\pm 0.05 \text{ kN}$) and torque (better than $\pm 6 \text{ Nm}$) were measured externally and the corresponding signals logged, together with the pore fluid pressure ($\pm 0.005 \text{ MPa}$) and temperature ($\pm 1^\circ\text{C}$) signals, using a 16 bit A/D converter and a logging frequency of 1-100 Hz. Torque and normal force data were corrected for pre-determined seal friction to obtain the shear stress (τ) and effective normal stress (σ_n^{eff}) acting on the sample. Shear displacement was corrected for machine distortion. The evolution of the layer thickness could not be determined accurately due to (minor) sample extrusion and machine distortion effects. Shear strain (γ) could therefore be determined only approximately ($\pm 5\text{-}10\%$), using the procedures described previously by Den Hartog et al. (2012a, Chapter 3). The data obtained allowed shear strength and apparent friction coefficient ($\mu = \tau / \sigma_n^{\text{eff}}$, ignoring cohesion) to be plotted versus shear displacement.

The velocity dependence of friction, measured in the velocity-stepping procedure applied to the samples after initial shearing at 10 $\mu\text{m/s}$, was quantified in the framework of the rate- and state-dependent friction model (RSF; Dieterich, 1978, 1979; Ruina, 1983), using the parameter:

$$(a - b) = \frac{\Delta\mu_{ss}}{\Delta \ln V} \quad (5.1)$$

(e.g. Marone, 1998). Here a represents the absolute magnitude of the instantaneous change in apparent friction coefficient μ upon a step change in sliding velocity from a reference value V_0 , characterized by a steady state friction coefficient μ_{ss} , to a new velocity V , while b reflects the magnitude of the change in μ during evolution to a new steady state. The overall change in steady state friction coefficient is denoted $\Delta\mu_{ss}$. Positive $(a-b)$ values indicate an increase in friction coefficient with increasing velocity, i.e. velocity-strengthening, which ensures stable slip behaviour, while negative $(a-b)$ values signify velocity-weakening and potentially unstable behaviour (e.g. Scholz, 1998). Though Eq. (5.1) strictly applies only to steady state behaviour, friction experiments generally show some degree of slip hardening (increasing μ with displacement at constant velocity) due to effects such as gouge extrusion (Den Hartog et al., 2012a, Chapter 3). To obtain $\Delta\mu_{ss}$ and hence $(a-b)$, we detrended the μ versus displacement curves to remove the effects of background slip hardening, as described by Blanpied et al. (1998) and Tembe et al. (2010).

Table 5.1 List of experiments, conditions and key data. σ_n^{eff} = effective normal stress, T = temperature, P_f = pore fluid pressure, V = sliding velocity, μ = coefficient of friction defined as $\mu = \tau / \sigma_n^{eff}$ and γ = shear strain. Sample-scale fracture orientations are classified following Logan et al. (1992), where R denotes R₁-shear, Y represents Y-shear and P denotes P-shear. Question marks indicate uncertainties associated with exact orientation hence identity in the Logan et al. (1992) terminology.

Experiment	Material (mus%/qtz%)	σ_n^{eff} (MPa)	T (°C)	P_f (MPa)	V (μ m/s)	Final μ	Final gouge thickness (mm)	Final shear displacement (mm)	Final γ	Stick-slip (Y/N)	Steady state reached (Y/N)	Sample-scale fracture orientation on removal from apparatus
RSMQ4	65/35	170	300	100	10-100-10-1-10-100-10	0.74	0.62	39.7	64	N	N	R
RSMQ5	65/35	170	400	100	10-100-10-1-10-100-10	0.80	0.66	38.2	58	Y (at 10 and 100 μ m/s)	N	R?
RSMQ6	65/35	170	600	100	10-100-10-1-10-100-10	0.82	0.52	39.5	76	Y (at 10 μ m/s) ^a	Y (at 13 mm)	?
RSMQ7	65/35	170	200	100	10-100-10-1-10-100-10	0.66	0.64	39.5	62	N	N	R?
RSMQ8	65/35	170	500	100	10-100-10-1-10-100-10	0.84	0.54	39.7	74	Y (at 100 μ m/s)	Y (at 24 mm)	R
RSMQ9	65/35	170	100	100	10-100-10-1-10-100-10	0.56	0.64	39.9	62	Y (at 100 μ m/s) ^b	N	Y?
RSMQ10	65/35	170	500	200	10-100-10-1-10-100-10	0.80	0.52	39.7	76	N	Y (at 19 mm)	?
RSMQ11	65/35	170	200	100	10-100-10-1-10-100-10	0.67	0.66	40.0	61	N	N	R?
RSMQ12	65/35	170	600	100	10-100-10-1-10-100-10	0.85	0.52	41.2	79	Y (at 10 μ m/s) ^a	Y (at 12 mm)	R??
RSM1	100/0	170	400	100	10-100-10-1-10-100-10	0.57	0.58	40.8	70	N	Y (at 24 mm)	P
RSM2	100/0	170	600	100	10-100-10-1-10-100-10	0.67	0.65	39.8	61	Y (at 10 μ m/s)	Y (at 38 mm)	P
RSM3	100/0	170	200	100	10-100-10-1-10-100-10	0.46	0.66	40.6	61	N	Y (at 26 mm)	P?

^aDuring initial loading-up only; ^bOnly at 34.1-34.5 mm displacement.

5.2.4 Microstructural methods

Upon sample recovery after shearing, all samples broke into annular fragments, or into flakes oriented mainly parallel or at a slight angle to the shear plane. Selected fragments of both gouges were vacuum impregnated with epoxy, then wafer-sawn perpendicular to the shear plane and tangential to the rotary shear direction. The sectioned surfaces obtained were again impregnated with epoxy and polished by hand. Other fragments were prepared for investigation of the principal surfaces along which the samples broke. To obtain fracture surfaces of the same orientation as the sectioned samples, fragments of the muscovite-quartz samples were scored with a scalpel and then fractured by bending. All samples were carbon or platinum coated. Microstructures were examined using either an XL30S FEG SEM (Scanning Electron Microscope), or a Focused Ion Beam (FIB) SEM (Nova 600 NanoLab DualBeam). High resolution images were analysed using SIS Scandium software to obtain average apparent 2D grain diameters, and ImageJ to determine the area fraction of SEM-visible porosity (defined by setting an appropriate greyscale threshold).

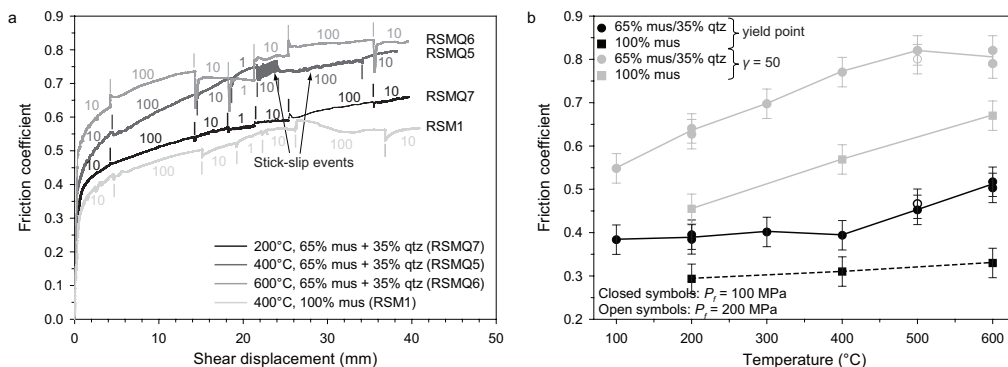


Figure 5.2 Representative friction data for the muscovite-quartz and pure muscovite gouges tested in the present experiments. (a) Typical evolution of the coefficient of friction with shear displacement for experiments on muscovite-quartz gouge at 200°C, 400°C and 600°C, and on pure muscovite gouge at 400°C (all tests at 100 MPa pore fluid pressure). The applied velocity steps are indicated in $\mu\text{m/s}$, with the location of a change in velocity indicated using vertical “ticks”. Shear strain γ is not indicated on the horizontal axis as it was different for all samples (for final gouge thickness and γ -values, see Table 5.1). (b) Friction coefficient versus temperature. The μ -values are taken at either the apparent yield point (see a) or at a shear strain γ of 50 and apply to a sliding velocity of 10 $\mu\text{m/s}$ (interpolated where necessary). Standard error propagation analysis showed that the error bar in friction coefficient is at most ± 0.034 . Solid and dashed tie-lines are added to the data for the muscovite-quartz and pure muscovite gouges, respectively.

5.3 Results: mechanical data

A list of experimental conditions and key mechanical data is provided in Table 5.1. We describe first our results for the muscovite-quartz samples, then our data for the pure muscovite gouge.

5.3.1 Muscovite-quartz samples

Representative curves of μ versus shear displacement for the muscovite-quartz gouges are shown in Fig. 5.2a for experiments performed at different temperatures (200, 400 and 600°C) at 100 MPa fluid pressure. Similar behaviour was observed in the single test performed at 200 MPa fluid pressure. At displacements up to 0.3–0.7 mm ($\gamma \approx 0.4$ to 1), μ increased

rapidly and more or less linearly to values of ~ 0.38 - 0.52 , at which point apparent yielding occurred. Between yield and the maximum shear strain of 58-79 (Table 5.1), the friction coefficient continued to increase (i.e. slip harden) with displacement, but at a steadily decreasing rate, resulting in final μ values 50-100% higher than at yield. At temperatures $< 500^\circ\text{C}$, steady state was not reached, even at displacements of 40 mm ($\gamma \approx 64$; Fig. 5.2a; Table 5.1). At 500 and 600°C , steady state was attained at displacements of ~ 13 mm and ~ 19 - 24 mm, respectively. At 100 MPa pore fluid pressure, sustained periods of regular stick-slip were common at 400 and 500°C , while only short periods of stick-slip occurred at 100 and 600°C (Fig. 5.2a; refer Table 5.1). Apparent frictional strength increased with temperature, especially at higher displacements (Fig. 5.2a; Table 5.1). This is illustrated further in Fig. 5.2b for μ at the yield point and at $\gamma = 50$ (displacement ≈ 26 - 34 mm), for a sliding velocity of $10 \mu\text{m/s}$ (interpolated where needed). The value of μ at yield remained constant at ~ 0.39 in the range 100 - 400°C , but increased at higher temperatures, reaching a value of ~ 0.51 at 600°C . In contrast, at $\gamma = 50$, μ increased steadily from 0.55 at 100°C to 0.82 at 500°C , but hardly changed from 500°C to 600°C .

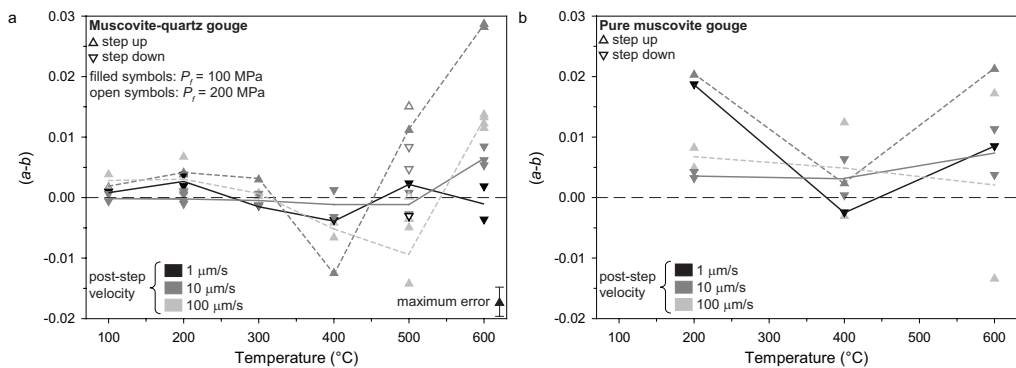


Figure 5.3 Values of the velocity dependence parameter ($a-b$) as a function of temperature, as obtained from the present experiments. Grey-scales indicate the magnitude of the post-step velocity imposed in performing each upward or downward velocity step. Solid tie-lines designate a step down in velocity, while dashed lines designate a step up. In the case of oscillatory (stick-slip) behaviour, average friction coefficients were used to obtain μ and ($a-b$). Peak μ values yield the same broad trend. Errors in ($a-b$) are estimated to lie within ± 0.0024 (see error bar in the upper plot). (a) Results for muscovite-quartz gouges. (b) Results for pure muscovite gouge. Note that the data point in (b) at 600°C with a negative ($a-b$) value corresponds to the first velocity step. This was performed just after apparent yield and was preceded by stick-slip at $10 \mu\text{m/s}$, just before the step.

Values of ($a-b$) for the muscovite-quartz mixtures are shown in Fig. 5.3a as a function of temperature. Overall, ($a-b$) decreases in the range 100 or 200°C to 400°C and increases in the range 400 or 500°C to 600°C . Three regimes of velocity dependence can therefore be distinguished: velocity-strengthening or near-neutral behaviour at ~ 100 - 350°C (Regime 1), velocity-weakening at ~ 350 - 500°C (Regime 2) and velocity-strengthening at ~ 500 - 600°C (Regime 3). Note that velocity-weakening behaviour in Regime 2 is expressed by clear stick-slip events at 400°C (Fig. 5.2a). In Regimes 2 and 3, the spread in ($a-b$) values at a fixed temperature is larger than in Regime 1, with data obtained in velocity steps with the same sign and post-step velocity clustering together. For steps up in velocity, changes in ($a-b$) with temperature are more pronounced than for steps down. The temperature extent of the

velocity-weakening regime also tends to decrease with decreasing velocity, notably in the higher temperature region of velocity-weakening (upward velocity steps). No clear strain dependence of $(a-b)$ was observed.

The single experiment on muscovite-quartz gouge performed at a pore fluid pressure of 200 MPa, at 500°C, showed very similar values of μ to the equivalent test performed at 100 MPa fluid pressure (Fig. 5.2b). However, in all but one velocity step (from 10 to 1 μs), the $(a-b)$ -values obtained at 200 MPa were higher by ~ 0.007 (Fig. 5.3a).

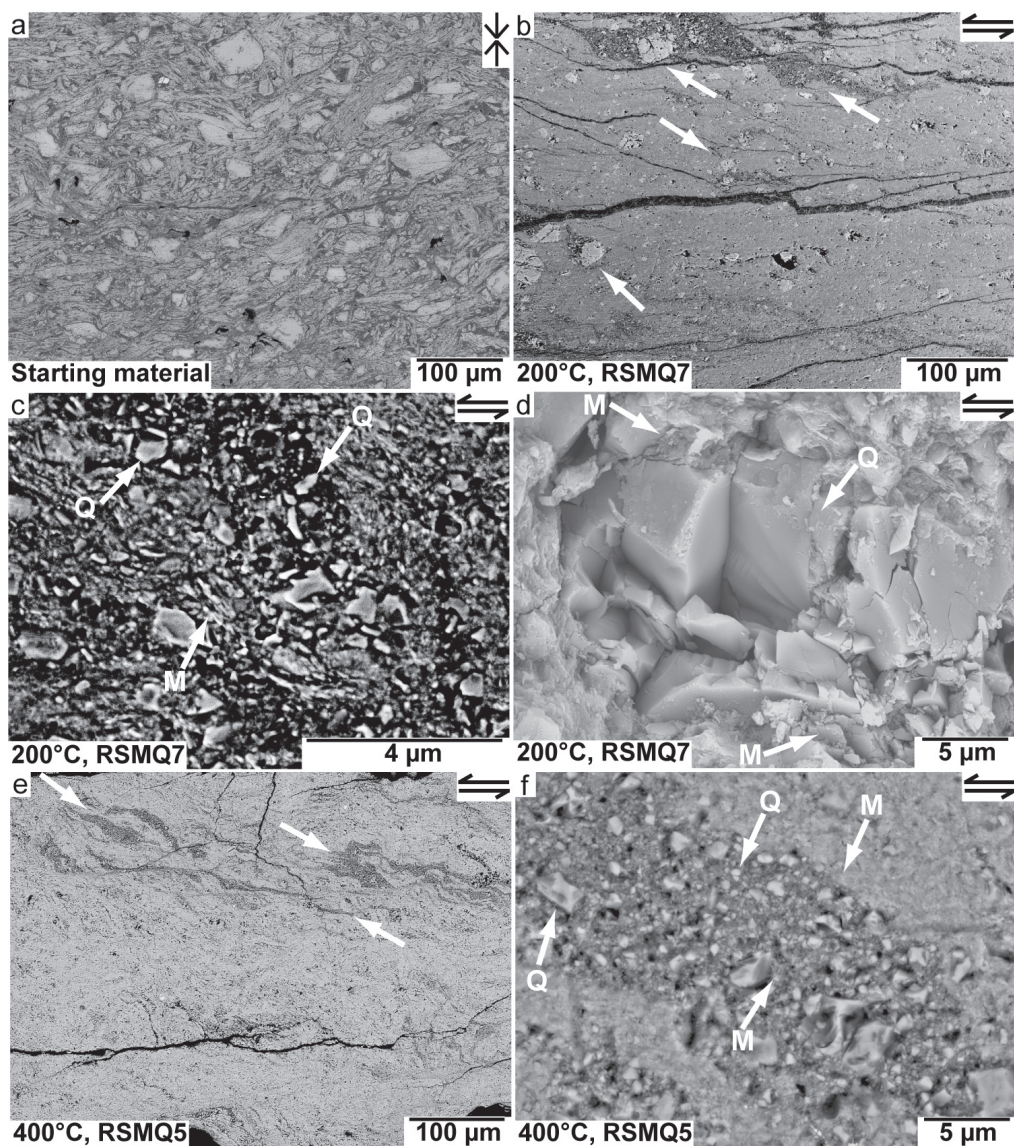


Figure 5.4 (caption on next page)

5.3.2 Pure muscovite samples

The evolution of the friction coefficient with shear displacement for the pure muscovite gouges was similar at all temperatures investigated and is shown in Fig. 5.2a for the experiment performed at 400°C. The pure muscovite gouges showed a 17-35% lower friction coefficient than the muscovite-quartz mixtures, at all temperatures investigated (Fig. 5.2a and b; Table 5.1). The friction coefficient increased with temperature, as in the muscovite-quartz mixtures, with a similar sensitivity (Fig. 5.2b).

In contrast to the muscovite-quartz gouge, the experiments on pure muscovite gouge attained steady state friction at all temperatures investigated, at displacements beyond ~24-38 mm. Stick-slip was observed, but only just after yield at 600°C (Table 5.1). Unlike the mixed gouge, the (*a-b*) values obtained for pure muscovite were almost always positive or neutral, though they still showed a minimum at ~400°C (cf. Fig. 5.3a versus 5.3b).

5.4 Results: microstructural observations

5.4.1 Sectioned samples

5.4.1.1 Starting microstructure muscovite-quartz samples

The microstructure of the pre-pressed rings of muscovite-quartz gouge, observed in section before shearing, shows sub-angular quartz clasts surrounded by elongate muscovite grains

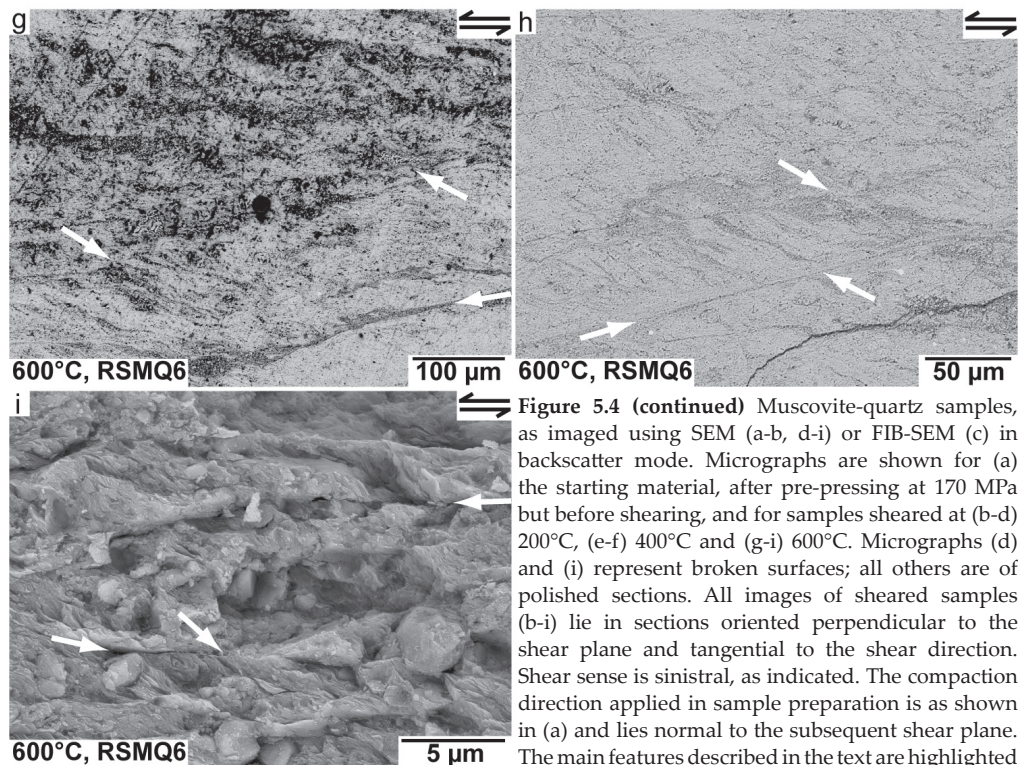


Figure 5.4 (continued) Muscovite-quartz samples, as imaged using SEM (a-b, d-i) or FIB-SEM (c) in backscatter mode. Micrographs are shown for (a) the starting material, after pre-pressing at 170 MPa but before shearing, and for samples sheared at (b-d) 200°C, (e-f) 400°C and (g-i) 600°C. Micrographs (d) and (i) represent broken surfaces; all others are of polished sections. All images of sheared samples (b-i) lie in sections oriented perpendicular to the shear plane and tangential to the shear direction. Shear sense is sinistral, as indicated. The compaction direction applied in sample preparation is as shown in (a) and lies normal to the subsequent shear plane. The main features described in the text are highlighted with arrows. Where mineral phase is indicated, “M” denotes muscovite and “Q” indicates quartz.

with a sub-horizontal preferred orientation (Fig. 5.4a). Analysis of more than 400 quartz and muscovite grains (564 quartz and 425 muscovite grains in 10 and 11 SEM micrographs, respectively) yielded a mean quartz clast diameter of $14 \pm 9 \mu\text{m}$ and mean muscovite dimensions of $37 \pm 18 \mu\text{m}$ length by $5 \pm 2 \mu\text{m}$ width (aspect ratio 8:1).

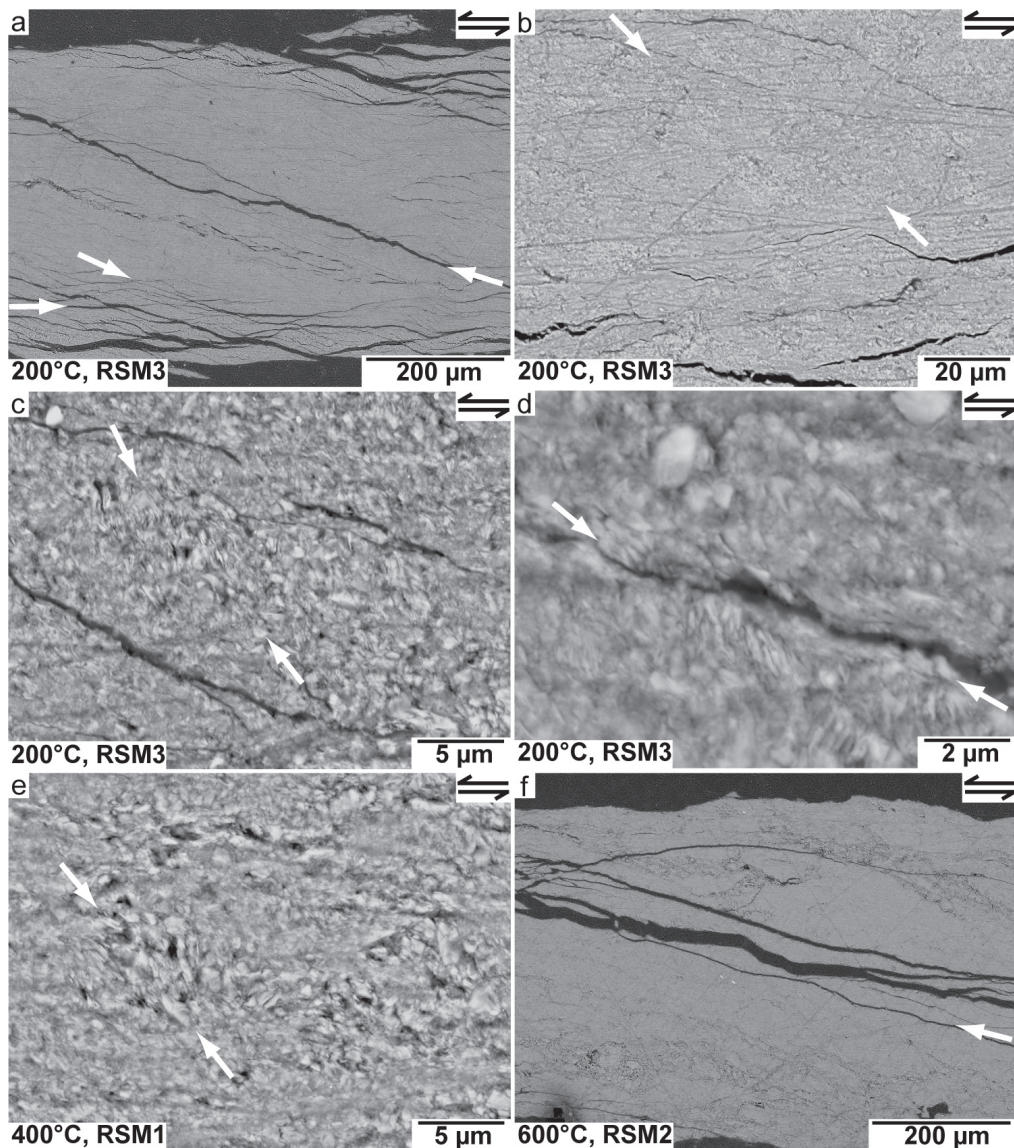


Figure 5.5 Microstructures observed in pure muscovite samples, as imaged using SEM in backscatter mode. All images are of polished sections cut perpendicular to the shear plane and tangential to the shear direction. The sense of shear is sinistral in all cases, as indicated. The main features described in the text are highlighted with arrows. Micrographs are shown for samples sheared at (a-d) 200°C, (e) 400°C and (f) 600°C.

5.4.1.2 Sheared muscovite-quartz samples

The microstructures seen in cross sections of muscovite-quartz gouges sheared at 200°C, 400°C and 600°C, i.e. in Regimes 1, 2 and 3, are shown in Figs. 5.4b-d, e-f and g-i, respectively. Compared to the microstructure before shearing, the quartz grains are strongly reduced in size (generally $<1\text{ }\mu\text{m}$; Fig. 5.4c and f), being concentrated in fine, polycrystalline quartz-dominated clusters or streaks containing minor, submicron muscovite (Fig. 5.4c, d and f). The clusters are often roughly sigmoidal in shape (Fig. 5.4b, e, g and h) and display a classical “stair-stepping” form (Passchier and Trouw, 2005), defining foliations in the P- and Y-shear orientations of Logan et al. (1992). These foliations become better developed towards higher temperature (Fig. 5.4e, g and h versus Fig. 5.4b). At 200°C, fractured quartz clasts up to $\sim 40\text{ }\mu\text{m}$ in diameter can still be recognized, located in the cores of the fine, quartz-rich grain clusters (Fig. 5.4b and d). At 400°C and 600°C, these larger clasts are almost absent (Fig. 5.4e, g and h). At all temperatures, the porosity within the fine quartz-rich clusters appears relatively high ($\sim 10\%$; Fig. 5.4c and f), though preferential dislodgement of quartz grains during section preparation cannot be excluded. At all temperatures, the muscovite matrix grains are also strongly reduced in size, to lengths below $\sim 0.5\text{ }\mu\text{m}$, with an aspect ratio of typically $\sim 5:1$, where visible in the SEM (Fig. 5.4c, f and i). Along with the fine, sigmoidal quartz-rich clusters, those that are SEM-visible define a foliation in the P-shear orientation (Fig. 5.4c and i). The muscovites also define a closely spaced foliation in the Y-shear orientation, notably at 600°C (Fig. 5.4i). At 600°C, both muscovites and fine-grained quartz streaks also define an R_1 shear band fabric, with a regular spacing of $50\text{--}100\text{ }\mu\text{m}$ (Fig. 5.4g, h; nomenclature after Logan et al., 1992).

5.4.1.3 Sheared pure muscovite samples

Cross sections of the pure muscovite samples show a fine-grained microstructure, with a foliated appearance, at the sample scale, produced by conspicuous unloading/extraction fractures (Fig. 5.5a, f). These are predominantly developed in the P-shear orientation, but also in the R_1 -orientation and occasionally the Y-shear orientation. Those in the P- and R_1 -shear orientations are often short (several tens of μm) and link together to form anastomosing networks (Fig. 5.5a). Though difficult to resolve with the SEM, fine muscovite grains appear aligned at fracture margins (Fig. 5.5d). As in the mixed samples, roughly sigmoidal regions can be distinguished in muscovite gouges deformed at all temperatures (Fig. 5.5b-e). However, these are now composed of muscovite grains that are coarse ($\sim 600\text{--}800\text{ nm}$ in length and $\sim 110\text{ nm}$ thick; aspect ratio $\sim 1:6$; Fig. 5.5c-e) compared to the surrounding matrix grains, which are not clearly resolvable. The muscovites in these sigmoidal regions show a preferred orientation in a direction that is steeper than the main P-shear orientation (Fig. 5.5c-e). No microstructural differences were found between the pure muscovite gouges deformed at different temperatures.

5.4.2 Fracture surfaces

5.4.2.1 Sheared muscovite-quartz samples

All samples showed sample-scale fractures formed during unloading and recovery. Fractures formed in the muscovite-quartz samples developed parallel to the R_1 -shear orientation, and occasionally the Y-shear orientation, at all temperatures investigated (Table 5.1). The surfaces of several such fractures in the mixed gouges are shown in Fig. 5.6a and b. These surfaces have a rough, granular and crudely layered or platy appearance, with faint

striations on the layering. Embedded quartz clasts and fine (quartz) debris respectively cross cutting or coating the striations, are common (Fig. 5.6a). At 200°C, the embedded quartz clasts are relatively large (~10-20 µm; Fig. 5.6a), whereas at 400°C and 600°C they are difficult to discern from “loose” surface debris, being in general <5 µm and often sub-micron in diameter. However, sub-spherical voids lined with phyllosilicates can be recognized in the sample surfaces, apparently delineating the position of formerly embedded but now dislodged quartz particles (Fig. 5.6b).

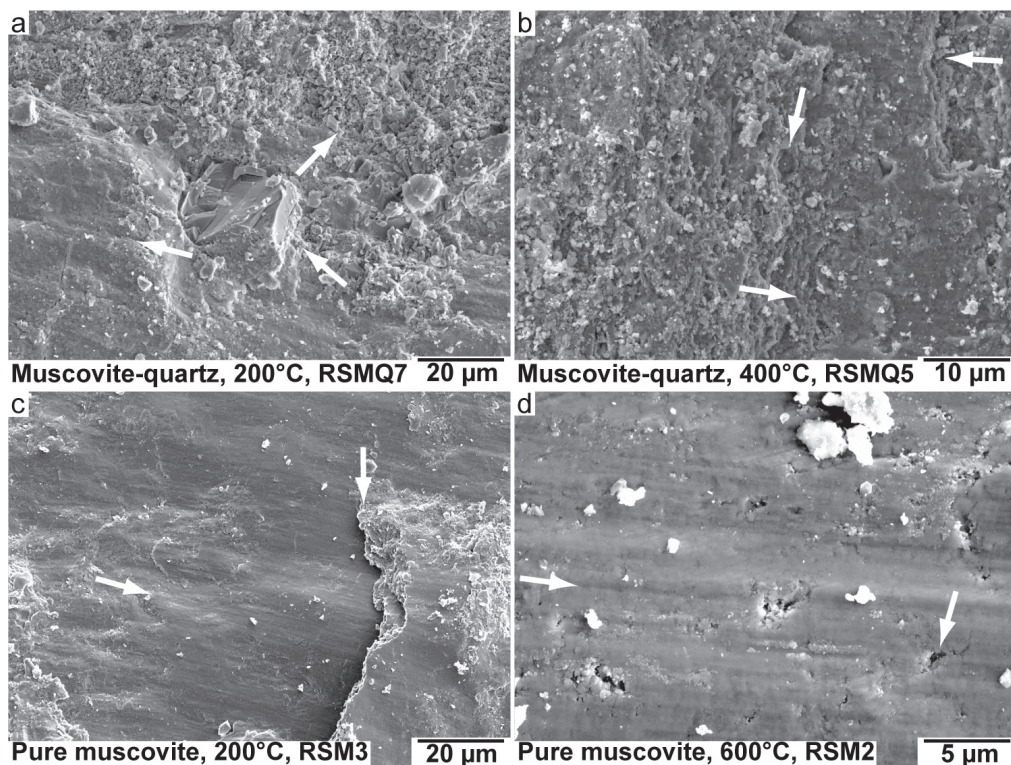


Figure 5.6 Striated surfaces of sample fragments imaged using SEM in secondary electron mode. Movement on all surfaces was top (removed material) to the left, generally at a slight angle to the horizontal image boundaries and/or to the surface (i.e. the plane of the page). The main features described in the text are highlighted with arrows. Micrographs are shown for muscovite-quartz samples deformed at (a) 200°C and (b) 400°C, as well as for pure muscovite samples deformed at (c) 200°C and (d) 600°C.

5.4.2.2 Sheared pure muscovite samples

In contrast to the mixed gouge, the pure muscovite samples showed fractures only in the P-shear orientation (Table 5.1). Compared to the 65:35 gouge mixtures, the pure muscovite gouges show much smoother fracture surfaces, characterized by larger, continuously striated, platy foliae imparting a well-layered structure to the sample surface (Fig. 5.6c and d). The layers or foliae are conspicuously corrugated parallel to the striations. At 600°C, they show the additional development of porous patches around 1-2 µm in diameter, surrounded by equidimensional submicron muscovite grains (Fig. 5.6d).

5.5 Discussion

The current experiments on wet 65:35 muscovite-quartz gouges have revealed three slip stability regimes characterized by velocity-strengthening or neutral behaviour at 100-350°C, velocity-weakening at 350-500°C and velocity-strengthening at 500-600°C. By contrast, pure muscovite gouges showed velocity-strengthening or neutral behaviour at 200-600°C, but with minimum (*a-b*) values at 400°C. Both gouge types showed an increase in the friction coefficient with temperature, with 17-35% lower values for pure muscovite than for the mixed gouge at all temperatures investigated. In the following, we compare our results with previous work on muscovite- and/or quartz-bearing gouges, in an effort to determine the role of muscovite versus quartz in controlling mixed gouge frictional behaviour. We then attempt to explain our results in terms of microphysical mechanisms. Finally, we assess the implications of our results for subduction megathrust behaviour by combining our data with those reported recently for illite-quartz gouges (Den Hartog et al., 2012a, Chapter 3).

5.5.1 Role of muscovite versus quartz in controlling friction

Previous studies addressing muscovite frictional behaviour have focused on near-pure muscovite. These have yielded μ -values in the range ~0.31-0.46 at room temperature (Behnsen and Faulkner, 2012; Moore and Lockner, 2004; Morrow et al., 2000; Niemeijer and Spiers, 2005; Scruggs and Tullis, 1998). At 150-600°C, Van Diggelen et al. (2010) obtained friction coefficients of 0.45-0.58 at $\gamma = 40$, which is very similar to the value of 0.42-0.64 obtained here for pure muscovite even though the muscovite used by Van Diggelen et al. (2010) contained minor quartz (<10 vol%). Our μ -values for pure muscovite at low strains are also similar to the values of ~0.28-0.35 reported by Mariani et al. (2006) for near-pure muscovite gouge (<1% quartz, plus feldspar, plus apatite) sheared at 300-600°C. In addition, the 17-35% lower coefficient of friction measured here for pure muscovite gouge, compared to our 65:35 muscovite-quartz mixture, is quantitatively similar to previous data on μ versus phyllosilicate:quartz ratio (Brown et al., 2003; Kopf and Brown, 2003; Saffer and Marone, 2003; Tembe et al., 2010). Overall then, our data on the frictional strength of muscovite and on the effects of admixed quartz and temperature on frictional strength are consistent with previous work.

Regarding slip stability, however, the data reported for pure muscovite gouge by Van Diggelen et al. (2010) and Mariani et al. (2006) compare more favourably with our data for mixed muscovite-quartz gouge. Specifically, the stick-slip events that they observed at 400 to 500°C (Van Diggelen et al., 2010), and at 400 to 600°C (Mariani et al., 2006), fall roughly in our velocity-weakening regime for the mixed gouge (Regime 2 at 350-500°C ; Fig. 5.3a), where we also observed stick-slip in some runs (see Table 5.1, Fig. 5.2a). Although apparatus effects and effects of differences in normal stress cannot be excluded, the few percent of quartz present in the samples of Van Diggelen et al. (2010) and Mariani et al. (2006) therefore seems able to produce unstable slip, similar to that seen in our gouges with 35% quartz at similar temperatures.

Focusing specifically on the velocity dependence of friction, while our mixed samples showed velocity-weakening at 350-500°C, our pure muscovite samples were dominated by velocity-strengthening or velocity-neutral slip at all temperature investigated. Most pure

phyllosilicates show velocity-strengthening behaviour, at least at room temperature (e.g. Ikari et al., 2009; Moore and Lockner, 2008). The implication is that the presence of quartz is pre-requisite for velocity-weakening behaviour in muscovite gouge - and perhaps in phyllosilicate-rich gouges in general (cf. Ikari et al., 2007; Moore et al., 2007). The presence of quartz as an even more general requirement for velocity-weakening is supported by the fact that other gouge materials that have been shown to exhibit three-regime behaviour, similar to that found here for muscovite-quartz gouge, all contain quartz. These include wet illite-quartz (Den Hartog et al., 2012a, Chapter 3), pure quartz (Chester and Higgs, 1992; cf. Kanagawa et al., 2000; cf. Niemeijer et al., 2008), granite (Blanpied et al., 1991; 1995; 1998), gabbro (He et al., 2007) and San Andreas Fault gouge (SAF gouge; Tembe et al., 2009). A key role of quartz has also been suggested based on field observations, of ubiquitous quartz veining, cementation and pressure solution in exhumed accretionary prisms exposed to temperatures above ~200°C (Moore et al., 2007; Moore and Saffer, 2001).

5.5.2 Microphysical mechanisms

The three-regime behaviour that we found previously for illite-quartz gouge (see also Den Hartog et al., 2012a, Chapter 3; Den Hartog and Spiers, in press, Chapter 4), deformed under similar conditions to those applied here, we explained in terms of a modified, qualitative version of the microphysical model originally proposed by Bos et al. (2000) and Bos and Spiers (2001, 2002) and extended by Niemeijer and Spiers (2005, 2006, 2007). The modified model includes velocity-strengthening of the phyllosilicates as opposed to the velocity-neutral phyllosilicate friction assumed originally. It describes the steady state frictional behaviour of phyllosilicates mixed with a granular clast phase capable of deforming by a thermally activated, hence time-dependent, deformation mechanism. At low temperatures, the process operating at the microscale in wet illite-quartz gouge sheared at constant velocity was inferred to be granular flow, at critical state porosity, controlled by velocity-strengthening slip within the weaker phyllosilicates (low temperature, velocity-strengthening Regime 1). At higher temperatures, deformation was predicted to be controlled by a competitive balance between dilatation due to granular flow, at sub-critical state porosity, and compaction by thermally activated stress corrosion cracking (SCC) and perhaps pressure solution of quartz grains (Regime 2). This balance results in an increase in porosity with increasing velocity and hence velocity-weakening. At still higher temperatures, it was argued that more efficient thermally activated compaction leads to the elimination of porosity such that the limiting frictional strength of a fully dense material is approached, resulting in velocity-strengthening behaviour controlled by the weaker phyllosilicate matrix (Regime 3). Alongside the effects of velocity, increasing temperature was accordingly predicted to lead to an increase in steady state friction strength. Ultimately, thermally activated deformation of the clasts was envisaged to become so easy that the clasts deform to accommodate slip on the phyllosilicates, leading then to a decrease in frictional strength but increased velocity-strengthening.

The above model is equally applicable to describe qualitatively the behaviour of muscovite-quartz mixtures, since (i) the main gouge components (phyllosilicate and quartz) are similar or equivalent in properties to those in the illite-quartz system, (ii) the deformation conditions were largely identical to those applied for illite-quartz and (iii) similar three-regime behaviour was observed for both phyllosilicate-quartz gouges. This conceptual model accordingly

predicts that it is compaction by thermally activated deformation of the quartz component of our muscovite-quartz gouge, competing with dilatation accompanying granular flow of the mixture, that causes (i) velocity-weakening and three-regime behaviour in the present experiments and (ii) the observed increase in μ with temperature. We suggest that the shift in temperature of the velocity-weakening regime in muscovite-quartz, compared to illite-quartz, may be related to the concentration of quartz in clusters in the muscovite-quartz mixtures, as opposed to being distributed in the illite-quartz gouge. Alternatively, the difference between the two gouges may imply a minimum in $(a-b)$ for pure illite that is shifted downwards in temperature compared to pure muscovite (refer Fig. 5.3b).

Based on microstructural evidence, Den Hartog et al. (2012a, Chapter 3) inferred the thermally activated mechanism controlling quartz clast deformation in the illite-quartz system to be SCC plus possible pressure solution. Similarly, the present microstructures for muscovite-quartz gouge (Fig. 5.4) suggest microcracking as the dominant quartz shear deformation mechanism, as they show pervasive fragmentation of the clasts rather than the formation of tailed porphyroclasts expected from pressure solution (cf. Bos et al., 2000; Niemeijer and Spiers, 2007). On the other hand, the quartz-rich clusters do display a broadly sigmoidal shape, suggesting that the fine-grained quartz produced by microcracking, and concentrated in these clusters, may subsequently deform by pressure solution. Interestingly, Van Diggelen et al. (2010) also observed fractured quartz clasts in a mixture of >90% muscovite and <10% quartz, deformed up to 500°C, with some evidence for indentation, suggesting minor pressure solution, at 600°C.

The mechanisms controlling the frictional behaviour of pure phyllosilicate gouges, such as muscovite, are poorly understood. Based on a correlation with interlayer bond strength and hence cleavage-plane surface energy, Moore and Lockner (2004) suggested that the strength of wet phyllosilicate gouges is controlled by the strength of bonding of water films to the surfaces of the constituent phyllosilicate grains. However, an alternative explanation for the correlation between gouge strength and interlayer bond strength may be found in dislocation processes (e.g. Dahl and Dorais, 1996). Superficially, neither viscous slip on thin intergranular water films, nor intracrystalline dislocation motion, are able to explain the increase in μ or changes in $(a-b)$ with T (i.e. the minimum in $a-b$ at 400°C) observed in our experiments on pure muscovite, since both processes are expected to be thermally activated and hence velocity-strengthening (Frost and Ashby, 1982; Israelachvili, 1986). This suggests that, as in our muscovite-quartz mixtures, the behaviour of pure muscovite gouges may be governed by competition between multiple mechanisms, of which at least one is time-dependent and thermally activated.

5.5.3 Present results versus data for illite-quartz gouge and implications for subduction zone seismogenesis

With increasing depth and hence temperature along a subduction megathrust, dioctahedral clay minerals undergo a transition from smectite to illite and finally to muscovite (e.g. Merriman, 2002; Merriman and Peacor, 1999), or else structurally similar muscovite micas, such as phengite, if magnesium and iron are present in sufficient concentration. The implications of the smectite to illite transition for the seismogenic potential of megathrusts have been considered in several previous studies (Den Hartog et al., 2012a, Chapter 3;

2012b, Chapter 2; Ikari et al., 2007; Kopf and Brown, 2003; Saffer et al., 2012; Saffer and Marone, 2003), but the importance of the transformation of illite to muscovitic mica has generally been overlooked. By comparing and combining the present dataset with that for illite-quartz gouges reported previously by Den Hartog et al. (2012a, Chapter 3; see also Den Hartog et al., 2012b, Chapter 2), we can extend our insight into the frictional properties of megathrusts to greater depths, encompassing the illite-to-muscovite transition.

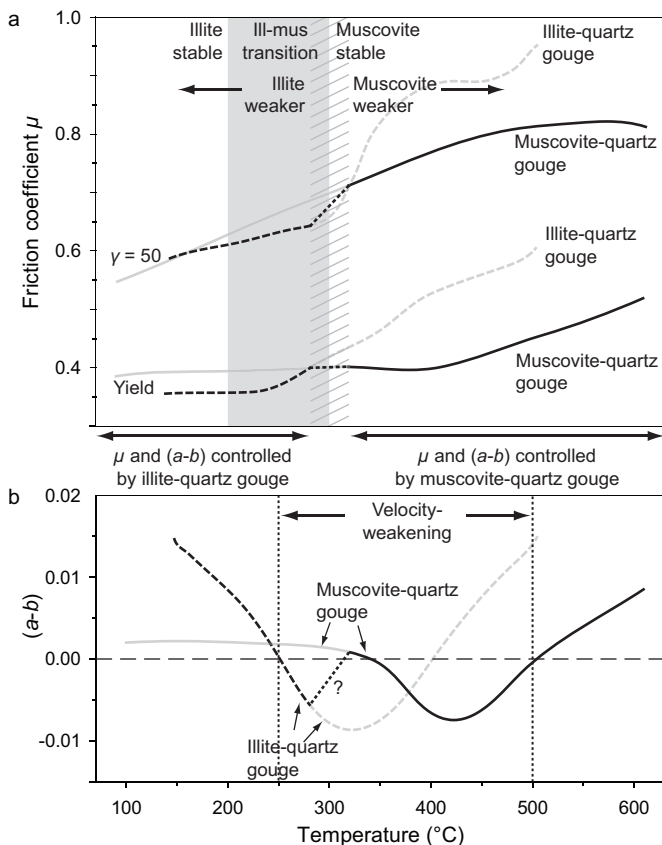


Figure 5.7 Synoptic diagram showing the present results for muscovite-quartz gouges together with those previously reported for illite-quartz gouge (Den Hartog et al., 2012a, Chapter 3). (a) shows friction coefficient (μ) versus temperature, at yield and at a shear strain of 50, whereas (b) shows $(a-b)$ versus temperature. The curves corresponding to muscovite-quartz gouge are solid and those corresponding to illite-quartz gouge are dashed. The temperature range within which illite transforms into muscovite is shown by the grey window in (a). The temperature range around $\sim 300^\circ\text{C}$ within which the strength-controlling phyllosilicate changes from illite to muscovite is indicated with grey oblique-hatching. The curves governing net frictional behaviour at a given temperature are shown in black.

We begin by comparing the results for μ and $(a-b)$ obtained here for 65:35 muscovite-quartz gouge with those that we previously obtained for illite-quartz gouge of similar quartz content. In both cases, the phyllosilicate:quartz ratio falls in the range exhibited by many accretionary wedge sediments (e.g. Nankai, Steurer and Underwood, 2003; Barbados, Underwood and Deng, 1997). In our experiments at an effective normal stress of 170 MPa, a pore fluid pressure of 100 MPa, at 100-600°C and at sliding velocities of 1-100 $\mu\text{m/s}$, both illite-quartz (Den Hartog et al., 2012a, Chapter 3) and muscovite-quartz fault gouge (this study) show a temperature dependence of $(a-b)$, with velocity-weakening behaviour occurring at temperatures of, respectively, ~ 250 -400°C and ~ 350 -500°C. At the pressure conditions of our experiments, which are equivalent to a depth of ~ 10 km, the behaviour of natural megathrust fault gouge may therefore be expected to be velocity-weakening in

the overlapping temperature range of ~350-400°C. Outside this temperature range, the stability of sliding will depend on whether illite or muscovite is present. Illite is believed to transform to muscovite at temperatures of ~200-300°C, forming progressively coarser muscovite at temperatures of ~300-500°C (Van de Kamp, 2008). This means that at ~200-300°C, both illite and muscovite are likely to be present in subduction zone megathrusts. We assume that the frictional behaviour will be governed by the weaker phyllosilicate-quartz mixture. Comparison of the μ and ($a-b$) data presented by Den Hartog et al. (2012a, Chapter 3; their Fig. 2c/3.2c) and our Fig. 5.2b shows that illite-quartz mixtures will usually have the lower friction coefficient at temperatures up to ~300-350°C, above which muscovite-quartz gouge becomes the weaker (Fig. 5.7a). Taking into account the uncertainty in this strength transition temperature, along with that in the temperature of (i) the transitions in velocity-strengthening versus weakening and (ii) the transformation of illite into muscovite, we may therefore expect velocity-weakening behaviour to dominate across the entire temperature range of ~250-500°C (Fig. 5.7b), at least at the laboratory pressure and velocity conditions addressed here and previously (Den Hartog et al., 2012a, Chapter 3).

Inspection of the temperature range characterised by the velocity-weakening behaviour seen in our combined dataset for muscovite-quartz and illite-quartz gouges (Fig. 5.7b), shows that this is similar in extent to the natural seismogenic zone (~250°C versus 200°C), but displaced towards higher temperatures compared to the generally assumed upper and lower seismogenic limits of ~150°C and ~350°C (e.g. Hyndman et al., 1997). However, Den Hartog and Spiers (in press, Chapter 4) showed that, for illite-quartz gouge, this range, and the overall ($a-b$) versus temperature profile, are affected by sliding velocity, effective normal stress, pore fluid pressure and the quartz content. In particular, the transition from velocity-strengthening to weakening shifts to lower temperatures with decreasing sliding velocity (i.e. shear strain rate). Natural slip nucleation strain rates are likely to be 3-6 orders of magnitude lower than the shear strain rates of 10^{-1} - 10^{-3} s $^{-1}$ applied here (Den Hartog et al., 2012a, Chapter 3; Segall and Rice, 2006). Thus, the temperature corresponding to the onset of velocity-weakening behaviour derived from the experiments on illite-quartz gouge might agree better with the up-dip seismogenic limit when extrapolated to natural slip nucleation strain rates. More rigorous extrapolation to in-situ megathrust conditions requires accurate profiles of in-situ pore fluid pressure and effective normal stress at depths >~5-8 km, which are typically estimated only indirectly and as spatially averaged quantities (Kitajima and Saffer, 2012; Saffer and Tobin, 2011), and better constraining these quantities presents an important challenge for future work.

Given the similar dependences of μ and ($a-b$) upon temperature exhibited by both muscovite-quartz and illite-quartz gouges, it is likely that the three slip stability regimes reported here for muscovite-quartz gouge are influenced by other variables besides temperature, as observed for illite-rich material. Indeed, the current data for muscovite-quartz do suggest an increase in ($a-b$) with an increase in pore fluid pressure (Fig. 5.3a), similar to the trend seen for illite-quartz samples (Den Hartog and Spiers, in press, Chapter 4). A velocity dependence of ($a-b$) for muscovite-quartz mixtures is also suggested by the differences in ($a-b$) values obtained for different velocity steps above 300°C (Fig. 5.3a). Unfortunately, however, these data are too limited to determine whether a systematic relationship exists between ($a-b$) and velocity for muscovite-quartz gouge. Nonetheless, when considering steps up in velocity

only, the data do suggest a narrowing of the velocity-weakening regime with decreasing sliding velocity, perhaps resulting in a decrease of the temperature at which muscovite-quartz fault gouge switches behaviour from velocity-weakening to strengthening, yielding better agreement with the down-dip seismogenic limit.

Finally, our interpretation of the microscale processes active in both illite-quartz and muscovite-quartz fault gouges means that velocity-weakening behaviour in both materials is caused by time-dependent compaction due to thermally activated deformation of the quartz clasts, competing with dilatation. The rough correspondence of the velocity-weakening region defined by these materials taken together, with the seismogenic zone of subduction megathrusts, therefore implies that seismogenesis is also caused by compaction due to a thermally activated process. The implication is that the seismogenic limits are the result of compaction by a thermally activated deformation mechanism becoming sufficiently efficient to compete with dilation at the up-dip limit and of compaction leading to zero dilation at the down-dip limit - with the thermally activated mechanism presumably allowing some ductile shearing. At temperatures beyond those of the down-dip seismogenic limit, i.e. beyond about 350°C (or at low slip velocities) crystal plasticity will eventually become an important thermally activated deformation mechanism (cf. Scholz, 1998). However, exhumed natural fault rocks show more evidence for solution transfer processes around the brittle-ductile transition (e.g. Moore et al., 2007), suggesting that the transition from seismic to aseismic behaviour is associated with pressure solution. In addition, the transition from velocity-weakening to velocity-strengthening in our experiments cannot be explained by the onset of crystal plasticity, since data by Hirth and Tullis (1994) and Rutter and Brodie (2004) points towards negligible plastic flow in quartz at the conditions of our experiments. Much more evidence exists for SCC and pressure solution at the conditions of our experiments, notably for the onset of pervasive pressure solution in quartz at 300–350°C (Schutjens, 1991).

5.6 Conclusions

This study has investigated the effects of the transition to muscovite-rich fault rock, at depths beyond the illite-dominated region of the seismogenic zone, on the frictional behaviour of subduction megathrusts at temperatures beyond 200–300°C where the transition occurs. This was approached using rotary shear friction experiments performed on simulated 65:35 muscovite-quartz gouges and on pure muscovite gouge at near in-situ megathrust conditions, i.e. an effective normal stress of 170 MPa, a pore fluid pressure of 100 or 200 MPa, at temperatures in the range 100–600°C and at sliding velocities of 1–100 $\mu\text{m/s}$. Our conclusions are as follows:

1. Muscovite-quartz gouge shows an increase in friction coefficient with temperature, from 0.38 to 0.52 (yield) and from 0.55 to 0.82 ($\gamma=50$) over the range 100–600°C.
2. Pure muscovite gouge is weaker than muscovite-quartz gouge at all displacements and temperatures investigated. As for muscovite-quartz gouge, μ for pure muscovite increases with temperature, from 0.29 to 0.33 (yield) and from 0.46 to 0.67 ($\gamma=50$) over the range 200–600°C.
3. Three regimes of velocity dependence were observed for muscovite-quartz gouge, characterized by velocity-strengthening or else neutral behaviour at 100–350°C, velocity-weakening at 350–500°C and velocity-strengthening at 500–600°C. These regimes are

- associated with decreasing ($a-b$) in the range 100-400°C, a minimum (negative) ($a-b$) at 350-400°C and increasing ($a-b$) from 400-600°C.
4. In contrast to the muscovite-quartz mixtures, pure muscovite gouges showed predominantly velocity-strengthening behaviour at 200-600°C, with a minimum though positive value of ($a-b$) at 400°C.
 5. The absence of velocity-weakening behaviour in experiments on pure muscovite gouge demonstrates the key role played by quartz in causing velocity-weakening behaviour in phyllosilicate-quartz mixtures. The role of quartz can be explained in terms of a conceptual model previously used to explain three-regime behaviour in illite-quartz gouge. This accounts for three-regime behaviour in terms of competition between a) thermally activated shear and compaction, involving deformation of the clast phase, and b) dilatant granular flow involving slip on the intervening phyllosilicates. More specifically, the model implies that velocity-weakening is caused by competition between compaction through thermally activated deformation of the quartz and athermal, shear-induced dilatation. In the muscovite-quartz system, the microstructure reported here suggests that SCC is one of the thermally activated deformation mechanisms affecting the quartz clasts, perhaps giving way to pressure solution as the clasts become comminuted, thus producing the observed sigmoidal quartz-rich clusters.
 6. For in-situ megathrust conditions, and for slip rates similar to laboratory rates (1-100 $\mu\text{m/s}$), our results imply that the temperature range of ~250-400°C in which velocity-weakening behaviour occurs in illite-quartz mixtures, should be extended up to temperatures of ~500°C, to take into account the illite-muscovite transition and the switch to muscovite frictional properties at temperatures beyond ~200-300°C. Our data for both illite-quartz and muscovite-quartz suggest that this temperature window of 250-500°C may shift to lower values more closely matching the seismogenic range of 150-350°C at in-situ nucleation velocities.
 7. Finally, the present microphysical interpretation of the mechanism causing velocity-weakening in phyllosilicate-quartz gouges (Conclusion 5) has the interesting implication that rupture nucleation in subduction zone megathrusts is ultimately controlled by competition between shear-induced dilation and compaction through thermally activated quartz deformation.

Acknowledgements

Gert Kastelein, Thony van de Gon Netscher, Eimert de Graaff and Peter van Krieken provided technical assistance. We thank Matthijs de Winter and Martyn Drury for their help with the (FIB-)SEM work. Kyu Kanagawa and Demian Saffer provided helpful reviews during the paper review process (taken into account only partially here). SdH is supported by a Toptalent grant awarded by the Netherlands Organisation for Scientific Research (NWO) (Project 021.002.025). AN is supported by an NWO VENI-grant No 863.09.013.

Chapter 6

A microphysical model for fault gouge friction and slip stability applied to subduction megathrusts

Sabine A.M. den Hartog and Christopher J. Spiers

Abstract

A microphysical model is developed for the steady state frictional behaviour and slip stability of illite-quartz fault gouge, suitable for application to subduction megathrust P - T conditions. The model assumes a phyllosilicate-supported microstructure in which rate-independent frictional slip on aligned phyllosilicates and thermally activated deformation of intervening quartz clasts occurs. At low slip rates or high temperatures, thermally activated deformation of the clasts is easy, accommodating slip on the phyllosilicate foliation. With increasing velocity (decreasing temperature), shear of the quartz clasts by the thermally activated mechanism becomes more difficult, increasing the shear stress, until slip is activated on phyllosilicates anastomosing around the clasts. Slip on this curved foliation leads to dilation, balanced at steady state by compaction through thermally activated clast deformation. Model predictions, taking pressure solution as the thermally activated mechanism, show broad agreement with previous experiments on illite-quartz gouge. Both show three regimes of velocity dependence, with velocity-weakening occurring at intermediate temperatures. Changing the slip rate, effective normal stress and quartz fraction in the model shifts the three regimes in temperature, as seen experimentally. Extrapolation of the model to earthquake nucleation slip rates successfully predicts the onset of velocity-weakening behaviour at the temperatures associated with the up-dip seismogenic limit. The results suggest that the location of the seismogenic zone on subduction megathrusts is controlled by fault rock compaction through pressure solution of quartz clasts, operating in competition with dilatation due to slip on anastomosing phyllosilicates.

6.1 Introduction

Numerical modelling of subduction zone seismogenesis, and of Slow Slip Events or SSEs (e.g. Hori et al., 2004; Liu and Rice, 2005; 2007; 2009; Matsuzawa et al., 2010; Noda and Lapusta, 2013; Perfettini and Ampuero, 2008; Shibazaki et al., 2011), relies on input parameters describing the frictional properties of the fault zone, hence fault rock, under in-situ pressure (P) and temperature (T) conditions. The relevant P - T conditions, slip velocities and shear strains present enormous challenges for laboratory determination of these parameters and have only rarely been approached in friction experiments on compositionally representative materials (e.g. Moore et al., 1986a; 1986b; 1989; Morrow et al., 1992; Saffer and Marone, 2003).

Recently, Den Hartog et al. (2012a, Chapter 3; submitted, Chapter 5) reported the first friction experiments investigating realistic megathrust gouge compositions under in-situ P - T conditions and reaching large shear strains (up to ~ 170). Simulated 65:35 illite-quartz and muscovite-quartz gouges were used, to capture the progressive metamorphic evolution of the pelitic (accretionary) fault rocks typically expected at seismogenic depths within subduction megathrusts (i.e. at ~ 5 -40 km; ~ 150 -350°C; Hyndman et al., 1997), assuming illite to be stable at ~ 150 -200°C, with muscovite replacing it above 200-300°C (e.g. Hower et al., 1976; Van de Kamp, 2008). The experiments were typically conducted at an effective normal stress (σ_n^{eff}) of 170 MPa, a pore fluid pressure (P_f) of 100 MPa and sliding velocities (V) of 1-100 $\mu\text{m/s}$. At temperatures in the range 100-600°C, both gouges showed three regimes of velocity-dependent frictional behaviour, superimposed on an overall increase in frictional strength. In the terminology of the Rate and State Friction model (RSF; Dieterich, 1978; 1979; Ruina, 1983), both gouges showed stable, velocity-strengthening (or near-neutral) behaviour at low temperatures (Regime 1), potentially unstable, velocity-weakening behaviour at intermediate temperatures (Regime 2) and velocity-strengthening at the highest temperatures investigated (Regime 3) (Den Hartog et al., 2012a, Chapter 3; submitted, Chapter 5). The observed behaviour is illustrated for illite-quartz gouge in Fig. 6.1. In this case, velocity-weakening (Regime 2) occurs at temperatures between $\sim 250^\circ\text{C}$ and $\sim 400^\circ\text{C}$ (Fig. 6.1a). Closely similar behaviour was observed for muscovite-quartz gouge, but with Regime 2 displaced upward in temperature to fall in the range 350 to 500°C. This three-regime behaviour closely resembles that reported for granitic and gabbroic fault gouge (Blanpied et al., 1991; 1995; 1998; He et al., 2007), with the overlapping velocity-weakening regimes of the two phyllosilicate-rich gouges studied offering an appealing explanation for the temperature/depth location of the seismogenic zone within subduction zone megathrusts (Den Hartog et al., submitted, Chapter 5).

The possibility that the observed three-regime behaviour might explain the location of the seismogenic zone on subduction megathrusts is supported by the fact that illite-quartz gouge shows a shift of Regime 2 (velocity-weakening) behaviour towards lower temperatures with decreasing sliding velocity (Fig. 6.1a and c), moving Regime 2 towards the window of 150-350°C characterizing the seismogenic zone (Hyndman et al., 1997) - where rupture nucleation is believed to occur at initial slip velocities of $\sim 10^{-9}$ m/s (e.g. Segall and Rice, 2006). This trend, along with effects of quartz content and effective normal stress on the temperature location of Regime 2 seen in illite-quartz gouge (Den Hartog and Spiers, in press, Chapter 4; Fig. 6.1), offer a means of extrapolating the frictional behaviour seen

in experiments to true in-situ megathrust conditions. However, the observed trends are too poorly constrained to allow meaningful extrapolation, especially over many orders of magnitude in sliding velocity (Den Hartog and Spiers, in press, Chapter 4). This highlights the need for a mechanism-based model to constrain extrapolation to nature.

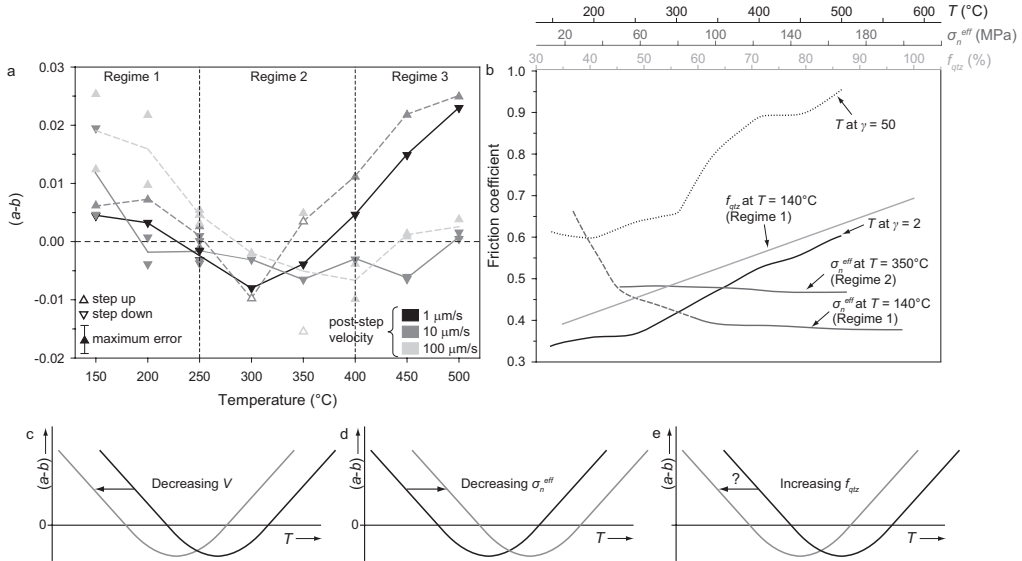


Figure 6.1 Synoptic diagram summarizing the key results obtained by Den Hartog and Spiers (in press, Chapter 4; see also Den Hartog et al., 2012a, Chapter 3) from ring shear experiments on illite-quartz gouges, at near in-situ megathrust conditions. (a) Rate and state friction parameter ($a-b$) versus temperature for the sliding velocity steps shown. Data obtained at reference conditions of $\sigma_n^{\text{eff}} = 170$ MPa, $P_f = 100$ MPa using gouge with initial composition of 65:35 illite:quartz. Open symbols are calculated using peak friction values of stick-slip events and differ from the ($a-b$) values for stick-slip events originally reported by Den Hartog et al. (2012a, Chapter 3; see also Den Hartog and Spiers, in press, Chapter 4), which were based on mean friction values. (b) Main trends observed in friction coefficient versus temperature (T), effective normal stress (σ_n^{eff}) and quartz fraction (f_{qtz}). The friction coefficient is defined as the ratio of shear stress to effective normal stress and neglects cohesion. All curves represent μ at the apparent yield point, except the black dotted curve, which gives μ versus temperature at a shear strain of 50. The curve showing the effect of σ_n^{eff} at low temperatures (i.e. falling in Regime 1 of (a)) is dashed at low effective normal stresses where the sample cohesion is significant. (c-e) Schematic representation of the displacement of the ($a-b$) versus temperature curve shown in (a) (black curve) as a result of changes in: slip rate (c), effective normal stress (d) and quartz content (e). The question mark in (d) indicates uncertainty in the interpretation of the effect of quartz content on the ($a-b$) versus temperature profile; the experimental data could also be explained by vertical depression of the curve.

Previously, we explained the behaviour of the above illite- and muscovite-quartz gouges, qualitatively, in the framework of the microphysical model for steady state shearing of halite-phyllsilicate and quartz-phyllsilicate fault gouges proposed by Bos and Spiers (2001; 2002) and extended by Niemeijer and Spiers (2005; 2006; 2007). This model assumes shear by thermally activated deformation of the halite or quartz clasts, by pressure solution, plus (dilatant) inter-granular slip on the subordinate phyllsilicate phase. However, the Bos-Niemeijer-Spiers model (2001; 2005; 2007) is not appropriate for quantitative

comparison with our experiments on illite- and muscovite-quartz gouges or for modelling phyllosilicate-rich megathrust gouges in general. This is because the model assumes a clast-supported microstructure, with the clasts being separated by only a thin film of phyllosilicates, as opposed to the matrix-supported microstructure of phyllosilicate-rich gouges. In addition, since grain size reduction was often observed, the dominant thermally activated deformation mechanism affecting the clasts in our experiments on illite-quartz and muscovite-quartz gouges was inferred to be Stress Corrosion Cracking (SCC), with pressure solution likely playing a subordinate role. The relative importance of these mechanisms could not be quantitatively established, however.

In this paper, we derive a quantitative model for the steady state frictional behaviour of matrix-supported phyllosilicate-quartz gouges deforming by frictional slip on the phyllosilicate foliation plus thermally activated deformation of the quartz clasts. The approach adopted resembles that employed in the Niemeijer-Spiers (2007) model for clasts supported gouge, but avoids a number of unnecessary assumptions. We base our model on the microstructures developed in our experiments on illite-quartz mixtures, which are somewhat simpler than those seen in the muscovite-quartz gouge. Since deformation involving SCC is too poorly understood to model quartz clasts deformation in a meaningful way, we focus on the much better constrained process of pressure solution, with the aim of evaluating to what extent this process, combined with friction on the phyllosilicates, can explain the behaviour seen in our experiments on illite-quartz gouge. Favourable agreement is obtained, suggesting that pressure solution was more important in our experiments than inferred from the sample microstructures alone. Assuming the same deformation mechanisms to operate in natural megathrust gouges, we go on to apply our model to determine the temperature range in which velocity-weakening is predicted to occur at in-situ nucleation velocities.

6.2 Microstructural model

We start model development by summarizing the main microstructural features developed in our previous experiments on illite-quartz gouges. These are used as a basis for defining an idealised microstructure and the operative deformation mechanisms to be modelled. An explanatory list of all symbols used can be found in Table 6.1.

6.2.1 Microstructural observations

Our experiments on illite-quartz gouges sheared at (near) in-situ megathrust P - T conditions (Den Hartog et al., 2012a, Chapter 3; 2012b, Chapter 2) show the development of a relatively uniform microstructure composed of equiaxed, micron-sized quartz clasts embedded in a finer phyllosilicate matrix (Fig. 6.2). The phyllosilicates are frequently aligned (Fig. 6.2a, e-g and i), forming a foliation that anastomoses around the quartz clasts (Fig. 6.2e, f and i). Such phyllosilicate alignments or foliations often form in the P -shear orientation of Logan et al. (1992; Fig. 6.2a, e, f and i) or in the R_1 - or Y -orientation (Fig. 6.2g). The quartz clasts are more or less homogeneously distributed throughout the phyllosilicate matrix, with elongate pores accounting for a porosity of several percent developed preferentially at clast/matrix interfaces oriented favourably for extension and hence for debonding – i.e. oriented at a high angle to the local incremental extension direction (Fig. 6.2a-f and h). No specific evidence was visible for deformation of individual clasts by pressure solution, such

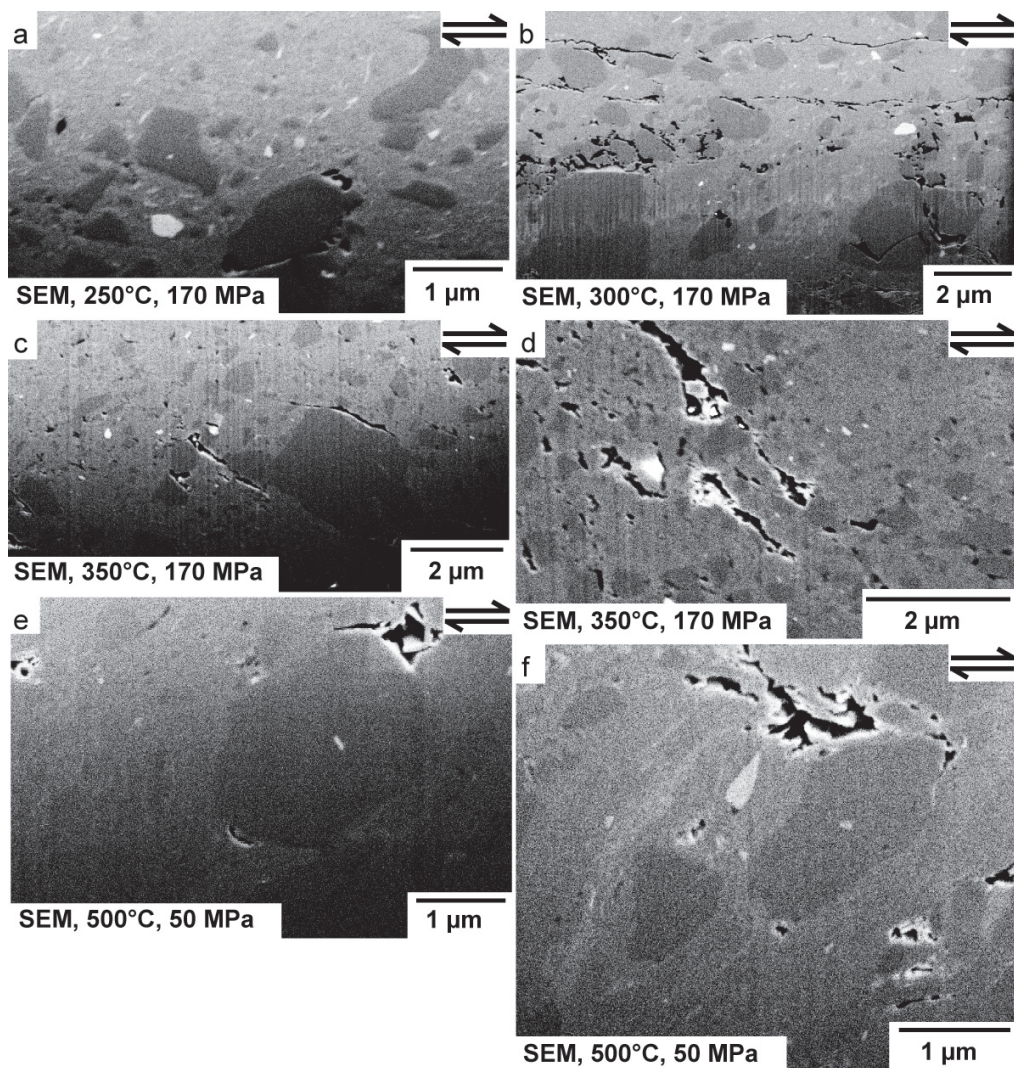


Figure 6.2 (caption on next page)

as the development of tailed porphyroclasts. Rather, the blocky or sub-angular to rounded shape of the quartz clasts, plus the reduction in clast size compared to the starting material (0.5-5 μm ; Den Hartog et al., 2012a, Chapter 3), seen notably at high temperature (Fig. 6.2e, f, h and i), suggests deformation, or at least a phase of grain size reduction, by cataclastic processes such as (thermally activated) SCC. However, this does not rule out small compactional strains by pressure solution, or small shear strains. Indeed, the oval shape of the finest quartz clasts (Fig. 6.2i) may point to deformation by pressure solution. Clearly, key features of the microstructure of our illite-quartz samples are that the phyllosilicate content is high enough to allow matrix support, and that dilatant porosity is observed to develop at extensional quartz-phylosilicate interfaces.

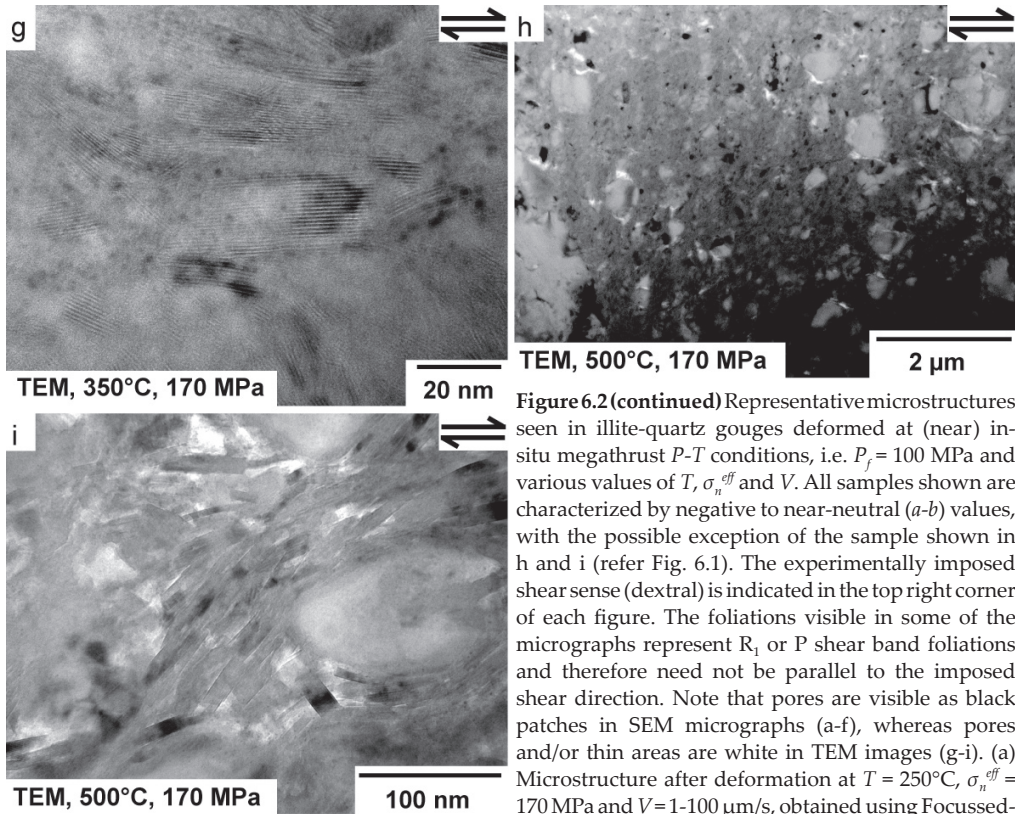


Figure 6.2 (continued) Representative microstructures seen in illite-quartz gouges deformed at (near) in-situ megathrust P - T conditions, i.e. $P_f = 100$ MPa and various values of T , σ_n^{eff} and V . All samples shown are characterized by negative to near-neutral (a - b) values, with the possible exception of the sample shown in h and i (refer Fig. 6.1). The experimentally imposed shear sense (dextral) is indicated in the top right corner of each figure. The foliations visible in some of the micrographs represent R_1 or P shear band foliations and therefore need not be parallel to the imposed shear direction. Note that pores are visible as black patches in SEM micrographs (a - f), whereas pores and/or thin areas are white in TEM images (g - i). (a) Microstructure after deformation at $T = 250^\circ\text{C}$, $\sigma_n^{eff} = 170$ MPa and $V = 1$ - 100 $\mu\text{m/s}$, obtained using Focussed-

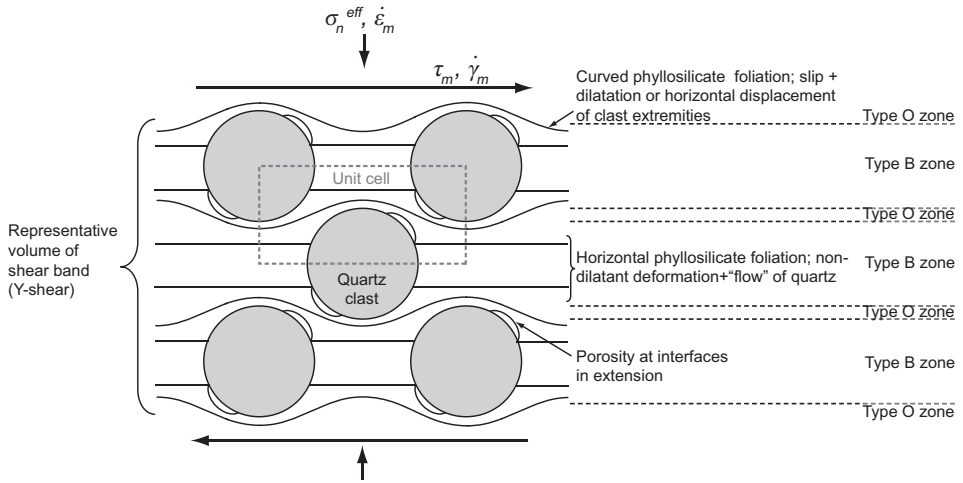
Ion Beam Scanning Electron Microscopy (FIB-SEM). (b) FIB-SEM microstructure after deformation at $T = 300^\circ\text{C}$, $\sigma_n^{eff} = 170$ MPa and $V = 1$ - 100 $\mu\text{m/s}$. (c) FIB-SEM microstructure after deformation at $T = 350^\circ\text{C}$, $\sigma_n^{eff} = 170$ MPa and $V = 10$ $\mu\text{m/s}$. (d) FIB-SEM microstructure after deformation at $T = 350^\circ\text{C}$, $\sigma_n^{eff} = 170$ MPa and $V = 10$ $\mu\text{m/s}$. (e) FIB-SEM microstructure after deformation at $T = 500^\circ\text{C}$, $\sigma_n^{eff} = 50$ MPa and $V = 1$ - 100 $\mu\text{m/s}$. (f) FIB-SEM microstructure after deformation at $T = 500^\circ\text{C}$, $\sigma_n^{eff} = 50$ MPa and $V = 1$ - 100 $\mu\text{m/s}$. (g) Microstructure after deformation at $T = 350^\circ\text{C}$, $\sigma_n^{eff} = 170$ MPa and $V = 10$ $\mu\text{m/s}$, obtained using Transmission Electron Microscopy (TEM). (h) TEM microstructure after deformation at $T = 500^\circ\text{C}$, $\sigma_n^{eff} = 170$ MPa and $V = 10$ $\mu\text{m/s}$. (i) TEM microstructure after deformation at $T = 500^\circ\text{C}$, $\sigma_n^{eff} = 170$ MPa and $V = 10$ $\mu\text{m/s}$.

6.2.2 Idealised microstructural model

On the basis of the above, we infer that shear deformation of the illite-quartz samples investigated by Den Hartog et al. (2012a, Chapter 3; 2012b, Chapter 2; cf. Den Hartog and Spiers, in press, Chapter 4) occurred via slip on internally foliated P -, R_1 - and Y -shear bands. Deformation within these bands appears to have involved slip on the phyllosilicate foliation accommodated by (i) deformation of the intervening quartz clasts through processes such as SCC and/or pressure solution, or (ii) dilatation occurring at clast-matrix interfaces subject to extensional displacements.

In line with this interpretation, we assume that the strength of the illite-quartz samples was controlled by the frictional properties of the active shear bands. To model this, we will focus on Y -shears, noting that the simple angular relationship between Y -, P - and R_1 -shears means that overall gouge behaviour will be insensitive to the dominant shear band type.

a



b

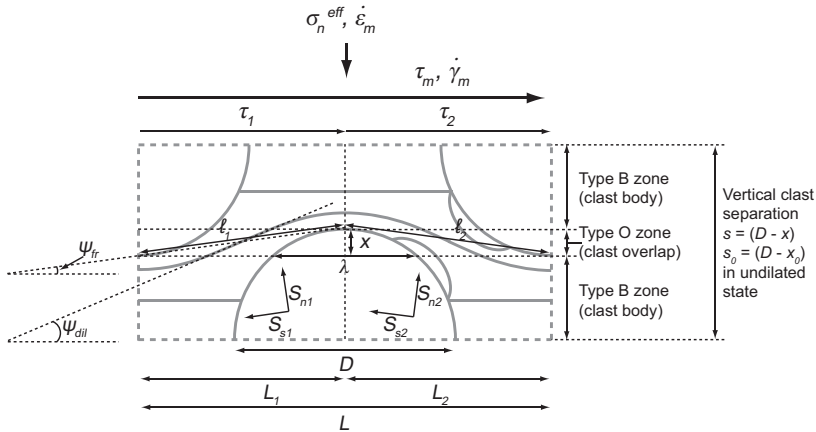


Figure 6.3 Assumed model microstructure for illite-quartz gouge undergoing shear deformation. (a) Representative volume of the basic shear band microstructure, showing cylindrical quartz clasts embedded in a matrix of aligned phyllosilicates. The phyllosilicates define both horizontal and curved foliations, the latter anastomosing around the quartz clasts. Note the porosity developed at the quartz-phyllosilicate interfaces undergoing extension. The main microstructural elements, and related deformation processes, are indicated. Type B zones indicate regions containing a horizontal phyllosilicate foliation and quartz bodies and are characterized by slip on the horizontal phyllosilicates and clast body shear. Type O zones contain anastomosing phyllosilicates and clast overlaps and deform by slip on the phyllosilicates at the zone margins plus clast overlap shearing, or by slip on the anastomosing foliation. (b) Model unit cell and associated microstructural state variables. The unit cell dimension perpendicular to the plane of view is D .

Our idealised model for the steady state microstructure of illite-quartz gouge deforming by horizontal (Y-) shear is shown in Fig. 6.3. The model is quasi two-dimensional in that it consists of cylindrical quartz clasts of diameter and length D embedded in a phyllosilicate matrix. The clasts are uniformly distributed in the matrix according to a regular packing characterised by a constant horizontal clast spacing L and a vertical spacing s , i.e. by the unit cell shown in Fig. 6.3. Adjacent horizontal rows of clasts overlap by an amount x , such that $s = D - x < D$. Strictly speaking, this matrix-supported geometry limits applicability of

the model to quartz contents of 39-79%, or perhaps 30-85% if the clasts are sub-ellipsoidal, subspherical or blocky, rather than perfectly cylindrical. On average, the phyllosilicates are aligned parallel to the shear band boundaries (i.e. parallel to the macroscopic shear stress τ_m and shear strain rate $\dot{\gamma}_m$ measured at the boundaries), but locally anastomose around the quartz clasts. Given the assumed vertical overlap of adjacent clast layers (by x , or x_0 at zero porosity), i.e. given sufficient quartz content, a through-going horizontal foliation is absent.

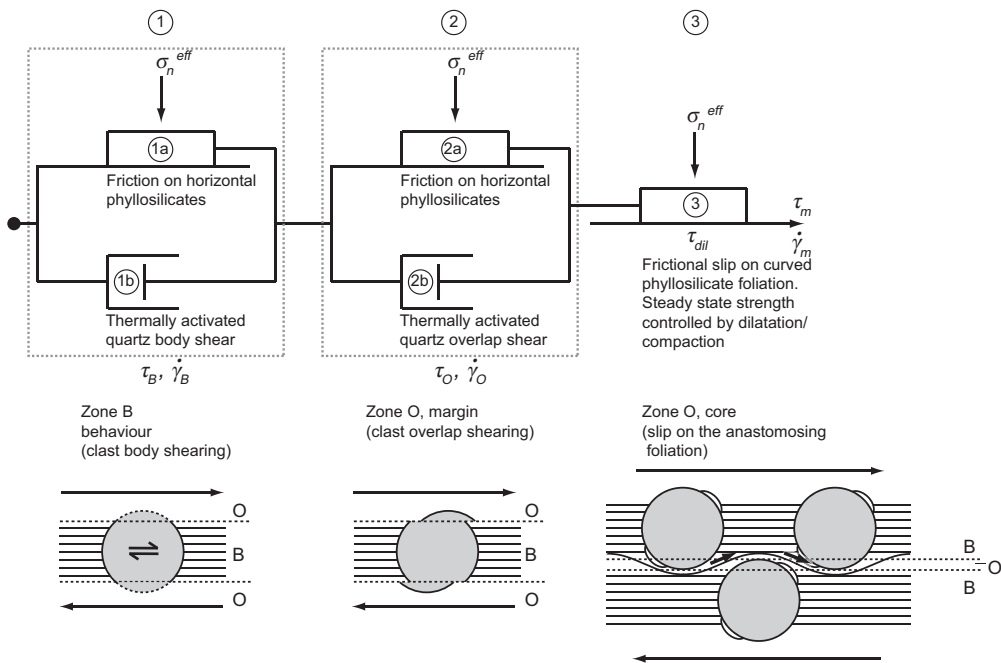


Figure 6.4 Mechanical analogue diagram for the deformation of illite-quartz gouges by slip on the phyllosilicate foliation (elements 1a and 2a), accommodated by thermally activated deformation of the quartz clast bodies (1b) and overlaps (2b), and by dilatant slip (3). Elements 1, 2 and 3 correspond to the deformation processes assumed to operate in zones B and O of the model microstructure (refer Fig. 6.3). The variables are defined in the text. Note that by definition, serial-sequential transport processes appear as elements in parallel in the mechanical analogue diagram, while parallel-concurrent processes appear as serial elements.

6.2.3 Assumed deformation process

Within the model microstructure, shear deformation can occur either within the horizontal “clast body” zones containing a horizontal phyllosilicate foliation (Type B zones, Fig. 6.3a) or in the alternating “clast overlap” regions containing anastomosing phyllosilicates (Type O zones, Fig. 3a). The horizontal foliation in the Type B zones abuts against the quartz clasts, so that sliding on this foliation requires shear of the clast “bodies”. By contrast, in the Type O zones, the illite foliation anastomoses around the clast “overlaps”. In these zones, deformation can occur either by slip on the phyllosilicates at the zone margins accommodated by shearing of the clast overlaps, or by slip on the curved foliation accompanied by dilatation at extensional clast-matrix interface sites (Fig. 6.3a). Assuming that sliding on the foliation is a frictional process, slip on the curved foliation will not occur

unless a critical value of the macroscopic shear stress, τ_{dil} , is attained. When the shear stress reaches τ_{dil} , slip on the anastomosing foliation will be activated, causing dilatation and porosity development. Based on the microstructures observed in deformed illite-quartz gouges (Fig. 6.2), we assume that the porosity concentrates at the quartz-illite interfaces (Fig. 6.3), at the portions experiencing extension, rather than along the curved foliation. This results in a decrease in the clast overlap distance x , and hence in the inclination of the curved foliation. This in turn causes a decrease in the rate of dilation per unit horizontal displacement on the inclined foliation, or, in the terminology of soil mechanics (Bolton, 1986), a decrease in the dilatation angle Ψ_{dil} with increasing porosity. Following Niemeijer and Spiers (2007), we assume that, at the same time, the development of porosity accelerates compaction by thermally activated deformation of the clasts, in competition with dilatation. At steady state, dilation due to slip on the curved foliation and compaction by the thermally activated mechanism must balance. This competition is of key importance since it will lead to higher steady state porosities and a flatter foliation as sliding velocity increases, and hence to velocity-weakening slip.

The deformation processes envisaged to be active in the illite-quartz gouge, and the way in which they are coupled, are shown in the mechanical analogue diagram in Fig. 6.4. Slip on the foliation is assumed to be purely frictional (i.e. rate-independent) and is therefore represented by sliders (elements 1a, 2a and 3). Thermally activated, rate-dependent shear deformation of the quartz clast bodies and overlaps, on the other hand, is represented by dash-pots (elements 1b and 2b). In the Type B zones of the microstructure (Fig. 6.3 and 6.4), frictional slip on the horizontal foliation (1a) is accommodated by serial, thermally activated deformation of the quartz clast bodies (1b), supporting shear stress τ_B . At the margins of the Type O zones, deformation occurs by slip on the horizontal foliation plus shearing of the clast overlap regions (2a plus 2b), supporting shear stress τ_O . Provided slip on the horizontal foliation is activated, these two processes of combined frictional sliding plus thermally activated deformation (elements 1 and 2 in Fig. 6.4) operate as parallel-concurrent processes, both contributing to the total measured shear strain rate $\dot{\gamma}_m$, while supporting shear stresses equal to the macroscopic, measured shear stress τ_m ($\tau_B = \tau_O = \tau_m$; Fig. 6.4). With increasing slip rate or decreasing temperature, the shear resistance to deformation exerted by thermally activated quartz (body/overlap) deformation will increase, until the point that the shear stress needed to activate deformation on the anastomosing foliation (τ_{dil} ; element 3) is exceeded (Fig. 6.4). When this critical shear stress is reached, dilatant slip on the curved foliation will operate in parallel with non-dilatant slip on the horizontal foliation, so that elements 1, 2 and 3 will all be active, all contributing to the measured strain rate $\dot{\gamma}_m$ under the action of a shear stress of magnitude $\tau_m = \tau_{dil} = \tau_B = \tau_O$. In this state, the appearance of porosity will trigger compaction by the same thermally activated creep process producing shear of the clasts, under the action of the vertical effective normal stress, σ_n^{eff} . During steady state shearing this will balance dilatation maintaining a steady state porosity, dilatation angle and shear strength $\tau_m = \tau_{dil} = \tau_B = \tau_O$. As the sliding velocity is increased further (or the temperature decreased), increasingly competitive dilatation will lead to an increase in steady state porosity and a decrease in shear strength until a limiting or critical state porosity is reached (cf. Niemeijer and Spiers, 2007).

Table 6.1 Explanation of symbols used in the current paper.

Symbol	Meaning	Symbol	Meaning
A_x	Horizontal position along phyllosilicate foliation [m]	$\dot{\epsilon}_{comp}$	Rate of compaction by a thermally activated mechanism [s^{-1}]
a	Fraction of grain boundary segment occupied by pore [-]	ϵ_{dil}	(Dilational) strain normal to anastomosing phyllosilicates [-]
A_{pore}	Pore area available for quartz-on-quartz precipitation [m^2]	$\dot{\epsilon}_{dil}$	Rate of dilatation due to slip on anastomosing phyllosilicates [s^{-1}]
A_{pore-c}	Pore area per clast at critical state [m^2]	$\dot{\epsilon}_m$	Macroscopic rate of compaction [s^{-1}]
A_p	Area of precipitation [m^2]	ϕ	Porosity [-]
A_{qtz-b}	Average horizontal area occupied by a single clast body [m^2]	ϕ_c	Porosity at critical state [-]
A_{qtz-o}	Area over which an overlap displaces during slip [m^2]	$\dot{\gamma}$	Shear strain rate [s^{-1}]
A_s	Area of dissolution [m^2]	$\dot{\gamma}_B$	Shear strain rate due to slip on the horizontal foliation and clast body deformation [s^{-1}]
A'_{seg}	Area of clast segment in overlap zone, perpendicular to shear plane [m^2]	$\dot{\gamma}_{dil}$	(Shear) strain parallel to anastomosing phyllosilicates [-]
D	Clast diameter and length [m]	$\dot{\gamma}'_{dil}$	Shear strain rate due to dilatant slip on anastomosing phyllosilicates [s^{-1}]
f_{qtz}	Volume fraction of quartz [-]	$\dot{\gamma}_m$	Macroscopic or imposed shear strain rate [s^{-1}]
I	$k_s \Omega$ [ms^{-1}]	$\dot{\gamma}_{non-dil}$	Shear strain rate due to non-dilatant deformation [s^{-1}]
k_+	Reaction rate coefficient for quartz [$mol \cdot m^{-2} s^{-1}$]	$\dot{\gamma}_O$	Shear strain rate due to slip on the horizontal foliation and clast overlap deformation [s^{-1}]
k_f	Constant depending on the 3D clast shape, $\frac{1}{4}$ for cylinder assumed here [-]	$\dot{\gamma}_{qtz-b}$	Shear strain rate due to thermally activated deformation of quartz clast bodies [s^{-1}]
L	Horizontal clast spacing, unit cell length [m]	$\dot{\gamma}_{qtz-o}$	Shear strain rate due to thermally activated deformation of quartz clast overlaps [s^{-1}]
L_1	Length of unit cell over which the anastomosing foliation displays a positive inclination [m]	λ	Width at the base of the clast overlap [m]
L_2	Length of unit cell over which the anastomosing foliation displays a negative inclination [m]	μ	Macroscopic or measured friction coefficient [-]
ℓ_1	(Length of) line approximating anastomosing foliation with positive inclination [m]	$\tilde{\mu}$	Friction coefficient within phyllosilicates [-]
ℓ_2	(Length of) line approximating anastomosing foliation with negative inclination [m]	$\Delta\mu_{ps}$	Chemical potential drop associated with pressure solution [$Jmol^{-1}$]
M_s	Volume of quartz dissolved/precipitated per second [$m^3 s^{-1}$]	$\Delta\mu_p$	Chemical potential drop associated with precipitation [$Jmol^{-1}$]
n	Exponent in relation describing pore area, pore shape evolution parameter [-]	$\Delta\mu_s$	Chemical potential drop associated with dissolution [$Jmol^{-1}$]
R	Gas constant [$Jmol^{-1} K^{-1}$]	σ_A	Largest principal normal stress [Pa]
s	Vertical clast spacing, unit cell height [m]	σ_B	Smallest principal normal stress [Pa]
S_{n1}	Normal stress component on ℓ_1 [Pa]	σ_n^{eff}	Macroscopic effective normal stress [Pa]
S_{s1}	Shear stress component on ℓ_1 [Pa]	τ_1	Portion of macroscopic shear stress that acts over distance L_1 [Pa]
T	Temperature [K]	τ_2	Portion of macroscopic shear stress that acts over distance L_2 [Pa]
V	Sliding velocity [ms^{-1}]	τ_{dil}	Shear stress to activate/maintain slip on anastomosing foliation [Pa]
V_b	Horizontal shear velocity contribution due to clast body shear to shear of the unit cell [ms^{-1}]	τ_m	Macroscopic shear stress [Pa]
V_p	Velocity of precipitation [ms^{-1}]	τ_O	Shear stress due to slip on the horizontal foliation and clast overlap deformation [Pa]
V_{qtz-o}	Velocity of overlap dissolution relative to clast body [ms^{-1}]	τ_{ph}	Shear stress associated with frictional slip on phyllosilicates [Pa]
V_s	Velocity of dissolution [ms^{-1}]	τ_{qtz-b}	Shear stress associated with deformation of quartz clast bodies [Pa]
V_u	Unit cell volume [m^3]	τ_{qtz-o}	Shear stress associated with deformation of quartz clast overlaps [Pa]
w	Average sample thickness [m]	Ω	Molar volume of quartz [$m^3 mol^{-1}$, $2.27 \cdot 10^{-5} m^3 mol^{-1}$]
\dot{w}	Mechanical work rate related to shear deformation [$J s^{-1}$]	Ψ_{dil}	Dilatation angle [$^\circ$]
x	Overlap of adjacent horizontal rows of clasts [m]	Ψ_{fr}	Mean inclination of anastomosing foliation [$^\circ$]
x_0	Overlap of adjacent horizontal rows of clasts in the undiluted (dense) state [m]		

6.2.4 Microstructural state variables

As shown in Fig. 6.3b, the assumed steady state microstructure can be described in terms of a unit cell with length L , height $s = D - x$ and depth or thickness D . We now define some additional microstructural descriptors. Consider first the curved foliation. This displays a positive inclination over the distance L_1 and a negative inclination over L_2 (Fig. 6.3b). Shear on this foliation will result in an increase of L_2 at the expense of L_1 , as pores open at the extensional clast interfaces. However, since steady state porosities are expected to be relatively small under in-situ megathrust conditions, we take $L_1 \approx L_2 \approx L/2$. From the geometry of the unit cell (Fig. 6.3b), it is now easily shown that

$$L = \frac{k_f \pi D^2}{(D - x_0) f_{q\kappa}} \quad (6.1)$$

where k_f is a factor accounting for clast shape ($1/4$ for cylindrical clasts), x_0 is the vertical overlap of the clasts when the porosity is zero, and $f_{q\kappa}$ is the volume fraction of quartz in the illite-quartz mixture. The vertical clast overlap at zero porosity can hence be written as

$$x_0 = D - \sqrt{\frac{k_f \pi D^2}{2 f_{q\kappa}}} \quad (6.2)$$

As porosity ϕ increases due to dilational slip on the curved foliation, this overlap decreases from x_0 to x according to the relation $x = x_0 - [(D - x_0)\phi]/(1 - \phi)$. The decrease in overlap in turn leads to a decrease in the width (λ) of overlapping clast segments (Fig. 6.3b), described by $\lambda = 2\sqrt{(Dx - x^2)}$. In addition, as ϕ increases and x decreases, the amplitude and hence inclination of the curved foliation decrease, producing a decrease in the dilatation angle Ψ_{dil} represented in Fig. 6.3b. To define Ψ_{dil} , we treat the curved foliation in our model as a sine function with period L and amplitude $x/2$, on which slip-induced dilatation is controlled by the steepest portion. The dilatation angle Ψ_{dil} is then given by:

$$\tan \Psi_{dil} = \frac{\partial [(x/2) \sin(2\pi A_x/L)]}{\partial A_x} \bigg|_{A_x=0} = \frac{(D - x_0) f_{q\kappa}}{k_f D^2} x = \frac{\partial \varepsilon_{dil}}{\partial \gamma_{dil}} \quad (6.3)$$

where A_x represents the horizontal position along the foliation, ε_{dil} is the (dilational) strain normal to the foliation and γ_{dil} the (shear) strain parallel to the foliation. Since x decreases with increasing porosity, this angle decreases with increasing porosity, reaching zero at a limiting or "critical state porosity" (e.g. Gerogiannopoulos and Brown, 1978; Rutter and Glover, 2012), $\phi_c = x_0/D$, attained when $x = 0$.

From the above, it is clear that that model microstructure is characterized by 13 state variables in total, namely $D, s, L, L_1, L_2, x, x_0, \lambda, f_{q\kappa}, \phi, \phi_c, \Psi_{dil}$ and k_f . Of these, inspection of Eq. [6.1]-[6.3], plus the additional equations given in the text, shows that only two are independent, e.g. D and $f_{q\kappa}$. The porosity ϕ_c is determined by x_0/D . the instantaneous porosity ϕ and dilatation angle Ψ_{dil} are key microstructural state variables that are dynamically determined by the model, i.e. by the imposed deformation conditions and sliding velocity.

6.3 Macroscopic shear stress balance and kinematic relations

The macroscopic shear stresses and kinematic relations governing the deformation of our model gouge by frictional slip on the phyllosilicate foliation combined with thermally activated deformation of the quartz clasts can be derived from the mechanical analogue diagram in Fig. 6.4.

6.3.1 Non-dilatant deformation

At sufficiently low imposed sliding velocities, or at high temperatures, thermally activated shear deformation (creep) of the quartz clasts will be easy. The total resistance to slip on the horizontal foliation will then be lower than the shear stress τ_{dil} needed to activate slip and dilatation on the anastomosing foliation. Under these conditions, non-dilatant deformation takes place by the parallel processes of (1) slip on the horizontal foliation with serial shear of the clast bodies in the B zones of the microstructure (elements 1a and 1b in Fig. 6.4), plus (2) slip on the horizontal phyllosilicates with serial shear of clast overlaps at the margin of the overlap (O) zones (elements 2a and 2b in Fig. 6.4). As indicated previously, stress equilibrium between the B and O zones requires that $\tau_m = \tau_B = \tau_O$. In addition, the parallel shear processes operating in the O and B zones mean that the total, measured shear strain rate during non-dilatant deformation of a representative volume of gouge (integer number of unit cells) is given $\dot{\gamma}_m = \dot{\gamma}_B + \dot{\gamma}_O$, where $\dot{\gamma}_B$ and $\dot{\gamma}_O$ denote the shear strain rates contributed by deformation of the clast body and overlap zones, respectively. The serial coupling of rate-independent slip on the phyllosilicates (elements 1a and 2a) with thermally activated deformation of clasts (elements 1b and 2b) now implies that $\dot{\gamma}_B = \dot{\gamma}_{qtz-b}$ and $\dot{\gamma}_O = \dot{\gamma}_{qtz-o}$ so that $\dot{\gamma}_m = \dot{\gamma}_{qtz-b} + \dot{\gamma}_{qtz-o}$ where $\dot{\gamma}_{qtz-b}$ and $\dot{\gamma}_{qtz-o}$ are the shear strain rates due to thermally activated deformation of the clast bodies and clast overlaps, respectively. Lastly, since compaction by thermally activated processes is impossible during non-dilatational deformation of the dense microstructure ($\phi = 0$), we can write $\dot{\epsilon}_{comp} = 0$ for the (positive) compaction strain rate occurring normal to the shear plane.

6.3.2 Dilatant deformation

At high slip rates or low temperatures, thermally activated shear deformation of the quartz clasts (elements 1b and 2b in Fig. 6.4) will become difficult, leading to an increase in the total resistance to shear on the horizontal foliation, ultimately activating slip on the curved phyllosilicates in the overlap (O) zones of the microstructure (element 3 in Fig. 6.4). Under these conditions, all elements in Fig. 6.4 are active, with elements 1, 2 and 3 operating in parallel. The measured shear strength is now equal to that required to activate slip on the anastomosing foliation, which, coupled with stress equilibrium between B and O zones, means, $\tau_m = \tau_{dil} = \tau_B = \tau_O$. The total, measured shear strain rate $\dot{\gamma}_m$, in turn, is given by $\dot{\gamma}_m = \dot{\gamma}_B + \dot{\gamma}_O + \dot{\gamma}_{dil}$ or equivalently $\dot{\gamma}_m = \dot{\gamma}_{qtz-b} + \dot{\gamma}_{qtz-o} + \dot{\gamma}_{dil}$ where $\dot{\gamma}_{dil}$ is the shear strain rate due to dilatant slip on the curved phyllosilicates. This mechanism produces an associated dilatational strain rate, $\dot{\epsilon}_{dil}$ which, following the classical soil mechanics approach to granular flow (Bolton, 1986), is related to $\dot{\gamma}_{dil} = d\gamma_{dil} / dt$ via the dilatation angle Ψ_{dil} such that:

$$\dot{\epsilon}_{dil} = \left(\frac{d\epsilon_{dil}}{d\gamma_{dil}} \right) \frac{d\gamma_{dil}}{dt} = (-\tan\Psi_{dil})\dot{\gamma}_{dil} \quad (6.4)$$

where compaction is taken positive. The porosity generated will induce compaction by

thermally activated deformation of the quartz clasts at a rate $\dot{\epsilon}_{comp}$. The total, measured compaction strain rate is therefore given by $\dot{\epsilon}_m = \dot{\epsilon}_{comp} + \dot{\epsilon}_{dil}$. At steady state, dilatation and compaction must balance, resulting in a steady state porosity corresponding to the condition that $\dot{\epsilon}_m = 0$ or $\dot{\epsilon}_{comp} = -\dot{\epsilon}_{dil}$.

6.4 Microscopic stress balance and shear resistance to deformation

6.4.1 Clast body zones

During non-dilatant deformation at low slip rates and/or high temperatures, but also during dilatant deformation, the total shear stress, acting over the shear plane of area LD per unit cell (Fig. 6.3b), is supported, in the B zone of the cell, by slip on the horizontal phyllosilicates plus thermally activated deformation of the clast bodies (element 1, Fig. 6.4), each contributing in proportion to the horizontal area occupied. This means that

$$\tau_B = \tau_{ph} \left(1 - \frac{A_{q\kappa-b}}{LD} \right) + \tau_{q\kappa-b} \frac{A_{q\kappa-b}}{LD} \quad (6.5)$$

where τ_{ph} is the shear stress needed to drive frictional slip on the horizontal phyllosilicate foliation and $\tau_{q\kappa-b}$ is that needed to drive thermally activated clast body deformation at the imposed shear rate. $A_{q\kappa-b}$ represents the average horizontal area occupied by a single clast body within zone B of the unit cell, and is given by $A_{q\kappa-b} = [(1/4)\pi D^2 - 2A'_{seg}D]/(D - 2x)$, where, following Harris and Stocker (1998), $A'_{seg} = [16x^2(D - x) + 3x^3]/[12\sqrt{(Dx - x^2)}]$ is the area of an individual clast segment located in the overlap zone of the cell in the plane of Fig. 6.3b.

6.4.2 Clast overlap zones

Similarly, during both non-dilatant and dilatant deformation, the shear stress supported in the overlap (O) region of the unit cell is given by:

$$\tau_O = \tau_{ph} \left(1 - \frac{A_{q\kappa-o}}{LD} \right) + \tau_{q\kappa-o} \frac{A_{q\kappa-o}}{LD} \quad (6.6)$$

where $\tau_{q\kappa-o}$ is now the shear stress needed to drive thermally activated deformation of the quartz overlaps and $A_{q\kappa-o} = \lambda D = 2D\sqrt{(Dx - x^2)}$ is the area over which the overlap is displaced by slip at its base.

To quantify τ_{ph} in Eq. [6.5] and [6.6], sliding on the horizontal foliation can be described by a rate-independent, cohesionless friction law given $\tau_{ph} = \tilde{\mu}\sigma_n^{eff}$, where $\tilde{\mu}$ is the friction coefficient within the phyllosilicates and σ_n^{eff} is the macroscopic, effective normal stress. The resistance to shear offered by the quartz clast bodies and overlaps ($\tau_{q\kappa-b}$ and $\tau_{q\kappa-o}$) depends on the mechanism by which thermally activated deformation occurs. In principle, this could be any creep mechanism, though later we assume that it is pressure solution.

6.4.3 Stress supported during dilatant deformation

The shear stress needed to activate slip on the curved foliation in the overlap zones (O) can be obtained from Fig. 6.3b by considering the balance of forces acting on the anastomosing foliation. We approximate the mean trajectory of the curved foliation by straight lines (ℓ_1

and ℓ_2) joining the tops and bottoms of adjacent clasts as shown in Fig. 6.3b. For the mean inclination (Ψ_{fr}) of the curved foliation, this yields

$$\tan \Psi_{fr} = \frac{2(D - x_0) f_{q\zeta}}{k_f \pi D^2} x \quad (6.7)$$

which, since $L_1 \approx L_2$, holds for both halves of the unit cell. Balancing the normal and shear forces on ℓ_1 now yields:

$$S_{n1} \ell_1 D = \sigma_n^{eff} L_1 D \cos \Psi_{fr} + \tau_1 L_1 D \sin \Psi_{fr} \quad (6.8)$$

$$S_{s1} \ell_1 D = \tau_1 L_1 D \cos \Psi_{fr} - \sigma_n^{eff} L_1 D \sin \Psi_{fr} \quad (6.9)$$

where S_{n1} and S_{s1} are the normal and shear stress components on ℓ_1 , and τ_1 is the portion of the macroscopic shear stress that acts over distance L_1 . The normal and shear stress components on ℓ_1 are linked via the microscopic friction coefficient $\tilde{\mu}$, i.e. via $S_{s1} = \tilde{\mu} S_{n1}$. Using, in addition, $\cos \Psi_{fr} = L_1/\ell_1$, Eq. [6.8] and [6.9] thus yield $\tau_1 = [(\tilde{\mu} + \tan \Psi_{fr})/(1 - \tilde{\mu} \tan \Psi_{fr})] \sigma_n^{eff}$.

Following a similar approach, the portion of the shear stress τ_2 acting over distance L_2 can be obtained. The macroscopic shear strength is subsequently obtained by adding τ_1 and τ_2 , accounting for the lengths $L_1 \approx L_2 \approx L/2$ over which they act. This yields for the shear stress required to activate or maintain slip on the curved foliation:

$$\tau_{dil} = \left\{ \frac{\tilde{\mu} (1 + \tan^2 \Psi_{fr})}{1 - \tilde{\mu}^2 \tan^2 \Psi_{fr}} \right\} \sigma_n^{eff} \quad (6.10)$$

6.5 Thermally activated deformation of quartz

As explained in the Introduction, SCC is too poorly constrained to model clast deformation by this mechanism. We therefore focus on pressure solution as the thermally activated mechanism operating in our model. The required flow laws for clast deformation by pressure solution are derived in Appendices A-C. In these derivations, we assume that pressure solution is controlled by the interfacial reactions of dissolution and precipitation. A simple order of magnitude calculation shows that for fine grained materials such as gouges, diffusion is too fast to be rate controlling. To describe the dissolution/precipitation kinetics, we use a linear dissolution/growth law valid for low driving forces, i.e. for low stresses, as opposed to the full exponential form (Spiers et al., 2004). This does not significantly affect the result in the range of stresses considered here. The flow law obtained in Appendix 6.A for clast body shear by pressure solution, in terms of the strain rate contributed to the unit cell, is

$$\dot{\gamma}_{q\zeta-b} = \frac{\pi I \tau_{q\zeta-b} \Omega}{RT} \frac{D - 2x}{D(D - x)} \quad (6.11)$$

where I is the product of the reaction rate coefficient k_+ and molar volume Ω of quartz,

and where R is the gas constant. The corresponding shear strain rate contribution due to shearing of the clast overlaps by pressure solution is, in turn, given from Appendix 6.B by

$$\dot{\gamma}_{qtz-o} = \frac{2I\tau_{qtz-o}\Omega}{RT} \frac{1}{\sqrt{Dx-x^2}} \quad (6.12)$$

The compaction rate of the unit cell due to pressure solution transfer from illite-quartz interfaces to dilated quartz interfaces (pore walls), derived in Appendix 6.C, is written

$$\dot{\epsilon}_{comp} = \frac{2I\sigma_n^{eff}\Omega}{RT} \frac{A_{pore}}{(D-x)DL} \quad (6.13)$$

The pore surface area A_{pore} available for quartz-on-quartz precipitation is assumed to be describable using a power law function of ϕ , written $A_{pore} = (A_{pore-c}/2)(\phi/\phi_c)^n$ where ϕ_c and A_{pore-c} are the porosity and pore area per grain, respectively, at the critical state. The exponent $n < 1$ is used to account for an initially large pore length to width ratio at the onset of dilatation (clast interface debonding), evolving to a smaller one, consistent with expectations from the observed microstructure (Fig. 6.2). Note that A_{pore-c} is equal to the maximum geometrically possible value of one half of the cylindrical grain surface area and is given by $A_{pore-c} = (\pi D^2)/2$.

6.6 Final model assembly and implementation

We now combine the foregoing equations to provide a framework for the construction of curves showing the macroscopic, steady state friction coefficient ($\mu = \tau_m/\sigma_n^{eff}$) versus shear strain rate or slip velocity, and we specify the input parameters implemented in our model calculations.

6.6.1 Determining shear strength as a function of slip velocity

6.6.1.1 Non-dilatant deformation

During non-dilatant deformation at low slip velocities and/or high temperatures, the total shear stress supported is defined as $\tau_m = \tau_B = \tau_O$ and the shear strain rate as $\dot{\gamma}_m = \dot{\gamma}_B + \dot{\gamma}_O$ (elements 1 and 2, Fig. 6.4). The shear stress or strength τ_m can be obtained from either Eq. [6.5] or [6.6], which define τ_B and $\tau_{O'}$ respectively. For τ_{ph} in these relations, we use $\tilde{\mu}\sigma_n^{eff}$. To obtain τ_{qtz-B} in Eq. [6.5], we use the flow law for pressure solution of the quartz bodies, defined in Eq. [6.11], where we know that $\dot{\gamma}_{qtz-b} = \dot{\gamma}_B$. However, to maintain equal mean shear stresses in the clast body and overlap zones ($\tau_B = \tau_O$) and at the same time satisfy the relation $\dot{\gamma}_m = \dot{\gamma}_B + \dot{\gamma}_{O'}$ then $\dot{\gamma}_O = \dot{\gamma}_{qtz-o}$ needs to be expressed in terms of $\dot{\gamma}_{qtz-b}$ and the imposed total shear strain rate, $\dot{\gamma}_m$. For each increment of $\dot{\gamma}_m$ we can then thus calculate $\dot{\gamma}_{qtz-b}$ and $\tau_B = \tau_m$, yielding the desired description of the total shear strength as a function of the imposed shear strain rate. Alternatively, $\dot{\gamma}_{qtz-b}$ could be expressed in terms of $\dot{\gamma}_{qtz-o}$ and $\dot{\gamma}_m$, and τ_{qtz-o} could be obtained through Eq. [6.12], yielding $\tau_{O'}$ and hence τ_m , via Eq. [6.6].

6.6.1.2 Dilatant deformation

With reference to Fig. 6.4 (element 3), during dilatant deformation at high slip rates or low temperatures, $\tau_m = \tau_{dil}$ ($= \tau_B = \tau_O$). To calculate τ_{dil} as a function of $\dot{\gamma}_m$, we increment the porosity and calculate the corresponding values of $\tan\Psi_{dil}$, yielding τ_{dil} via Eq. [6.10]. At

steady state, the measured compaction strain rate $\dot{\epsilon}_m$, defined $\dot{\epsilon}_m = \dot{\epsilon}_{comp} + \dot{\epsilon}_{dil}$, is zero, since dilatation due to slip on the curved phyllosilicates and compaction of the quartz clasts by thermally activated creep (pressure solution) balance, i.e. $\dot{\epsilon}_{comp} = -\dot{\epsilon}_{dil}$. Combining this with $\dot{\gamma}_m = \dot{\gamma}_B + \dot{\gamma}_O + \dot{\gamma}_{dil}$, the known equalities $\dot{\gamma}_B = \dot{\gamma}_{qtz-b}$ and $\dot{\gamma}_O = \dot{\gamma}_{qtz-o}$ and Eq. [6.4] gives $\dot{\gamma}_m = \dot{\gamma}_{qtz-b} + \dot{\gamma}_{qtz-o} + (\dot{\epsilon}_{comp}/\tan \Psi_{dil})$ for a given τ_{dil} , hence τ_m . Note that the shear strain rates $\dot{\gamma}_{qtz-b}$ and $\dot{\gamma}_{qtz-o}$ in the last relation for $\dot{\gamma}_m$ follow from the flow laws Eq. [6.11] and [6.12], in which τ_{qtz-b} and τ_{qtz-o} are related to $\tau_{dil} = \tau_m$ via stress balances Eq. [6.5] and [6.6], respectively, where $\tau_{ph} = \tilde{\mu}\sigma_n^{eff}$. The compaction strain rate $\dot{\epsilon}_{comp}$ is obtained from Eq. [6.13].

6.6.2 Model input data

To obtain a clear picture of the model characteristics, i.e. the trends it predicts, while allowing for broad comparison with our previous experimental results for illite-quartz gouge (Fig 1; see also Den Hartog and Spiers, in press, Chapter 4), we applied the model to predict steady state frictional behaviour of illite-quartz gouge for a range of conditions typical of the experiments. Accordingly, we used an effective normal stress of 170 MPa, temperatures in the range 100-600°C and applied sliding velocities of 1-100 $\mu\text{m/s}$. Besides these variables, our model requires specification of the microstructural state variables D and f_{qtz} , the pore shape evolution parameter n , the phyllosilicate friction coefficient $\tilde{\mu}$ and the pressure solution rate coefficient I .

For the present calculations, a grain size D of $\sim 1 \mu\text{m}$ (specifically $0.93 \mu\text{m}$) was used, being the average grain size observed in the illite-quartz samples after deformation (Den Hartog et al., 2012a, Chapter 3). Sliding velocity (V) and macroscopic shear strain rate $\dot{\gamma}_m = V/w$ were connected using an average sample thickness (w) of 0.57 mm . This thickness was the average of the sample thicknesses of all experiments conducted at $\sigma_n^{eff} = 170 \text{ MPa}$, where each individual, average thickness was obtained from the final sample thickness and the axial displacement measured during the experiment. Here we assume that shear deformation was uniformly distributed throughout the thickness of the gouge samples. The corresponding average quartz fraction (f_{qtz}) during the experiments was estimated from the initial value of 35% assuming that the decrease in thickness during shear was caused by preferential loss of illite (cf. Den Hartog et al., 2012a, Chapter 3). This yielded an average quartz fraction of 56% for all experiments conducted at 170 MPa effective normal stress. A mean clast overlap at zero porosity of $0.15 \mu\text{m}$ was obtained from the grain size and f_{qtz} (Eq. [6.2]). This in turn yielded an average clast spacing L of $1.55 \mu\text{m}$ (Eq. [6.1]) and a critical state porosity ($\phi_c = x_\phi/D$) of 16%. Based on microstructural observations, we chose the exponent n to the porosity term in the equation for A_{pore} in Eq. [6.13] to be 0.3. This choice leads to a dependence of pore wall area on porosity consistent with a decrease in pore aspect ratio from $\sim 50:1$ upon initial formation (i.e. upon clast-matrix debonding) to $\sim 2.5:1$ at the critical state porosity.

To describe the kinetics of pressure solution, i.e. to obtain $I = k_+ \Omega$, we used the empirical equation for the dissolution rate coefficient (k_+) for quartz, based on geometric surface area provided by Tester et al. (1994). This relation represents a compilation of data on k_+ versus T . It is considered more suitable here than data on k_+ obtained with respect to quartz surface areas measured with BET methods (e.g. Rimstidt and Barnes, 1980), or obtained with respect to active site densities (e.g. Dove, 1999), because pressure solution rates in our

model are determined by the geometric area available for dissolution and precipitation on clast surfaces. Finally, given the similarity in composition, structure and interlayer bond strength between illite and muscovite (Moore and Lockner, 2004; Rieder et al., 1998), we used the temperature effect on friction coefficient observed by Den Hartog et al. (submitted, Chapter 5) for pure muscovite, plus the friction coefficient of 0.3 measured at room temperature by Tembe et al. (2010) for pure illite, to obtain $\tilde{\mu}$ for illite as a function of temperature. This yielded the relation $\tilde{\mu} = 0.303 + (T-20) \cdot 5.375 \cdot 10^{-4}$.

6.7 Model predictions and comparison with experimental results

In the following, we illustrate the principal trends predicted by our microphysical model for steady state shear of matrix-supported illite-quartz gouge, and we compare the results with the trends in strength and in the RSF parameter (*a-b*) previously observed in experiments on illite-quartz gouge by Den Hartog and Spiers (in press, Chapter 4; see also Fig. 6.1).

6.7.1 Dependence of shear strength (μ) on deformation conditions and microstructural variables

6.7.1.1 Predicted effect of sliding velocity V

The dependence of gouge friction coefficient μ on with sliding velocity V predicted by the model for the chosen reference conditions at steady state is shown in Fig. 6.5a. At low sliding velocities, non-dilatant deformation controls friction with slip on the horizontal foliation being accommodated by pressure solution of the quartz clasts. At the lowest velocities explored, μ approaches an asymptotic value, determined by the shear strength $\tilde{\mu}$ of the horizontal phyllosilicates (taking into account the relevant area fraction), since easy pressure solution of the clasts under these conditions contributes negligibly to the strength. With increasing velocity, pressure solution becomes more difficult, resulting in an increase in steady state friction coefficient μ (i.e. velocity-strengthening behaviour). This increase in μ continues until the shear resistance to activate slip on the anastomosing, curved foliation is reached (at the peak of the μ versus V curve). Activation of slip on the curved foliation leads to dilatant deformation, i.e. porosity development, which in turn activates compaction creep by pressure solution. Slip-induced porosity development and porosity reduction due to pressure solution compaction now compete with each other, balancing at steady state. The steady state porosity and dilation and Ψ_{dil} are higher at higher velocities, resulting in a lower shear stress (Eq. [6.7] and [6.10]) and hence velocity-weakening behaviour (Fig. 6.5a). This illustrates the fact that, in the present model, velocity-weakening is the result of compaction caused by thermally activated pressure solution of the quartz clasts, competing with dilatation.

Note that the present model predicts a similar μ versus V profile to that predicted by the Bos-Niemeijer-Spiers model (2001; 2005; 2007) for a clast-supported microstructure. There are two key differences, though. First, the extent of velocity-weakening is much lower and more realistic here. Second, the model itself predicts the transition from non-dilatant to dilatant deformation, whereas in the Bos-Niemeijer-Spiers model (2001; 2005; 2007) this was assumed to be achieved by an independent dilatation criterion resembling Byerlee's rule.

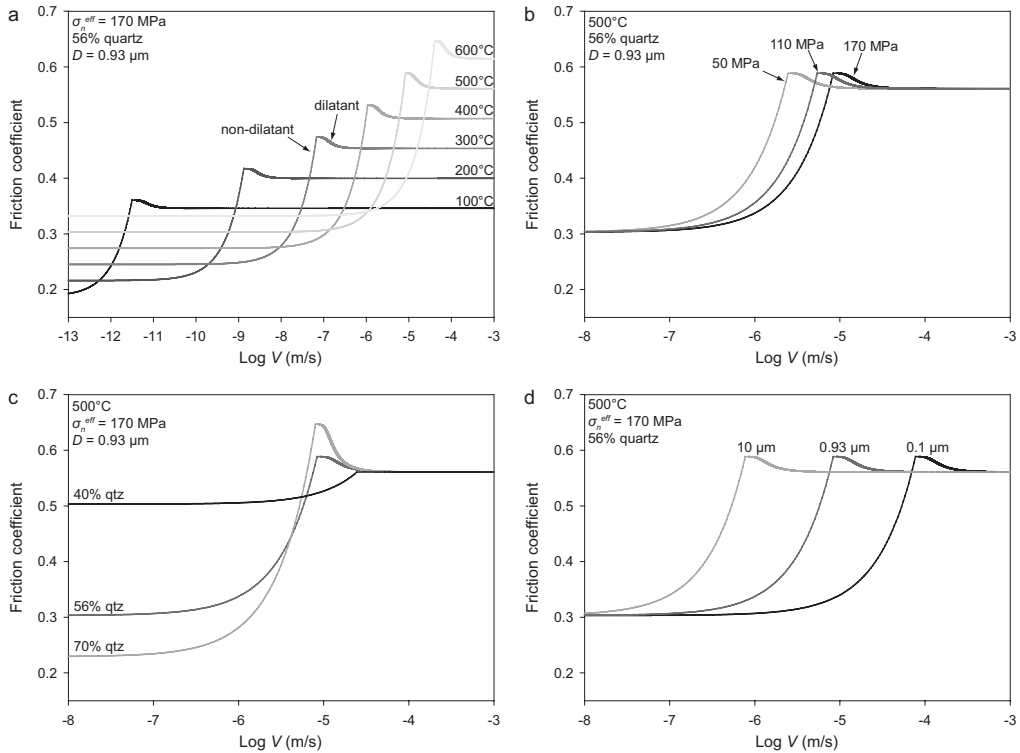


Figure 6.5 Evolution of the steady state friction coefficient μ with sliding velocity V predicted by the current model for different values of (a) temperature, (b) effective normal stress, (c) quartz fraction and (d) quartz clast grain size, at otherwise fixed conditions. The values of the quantities held constant are specified in the top left corner of each panel. The regions of non-dilatant versus dilatant behaviour are indicated for the curve at 300°C in (a).

6.7.1.2 Predicted effect of T

In keeping with the nature of all thermally activated deformation processes, the effect of increasing temperature on the stress to drive pressure solution of the quartz clasts is opposite in the model to the effect of slip velocity or strain rate, resulting in the displacement of the μ versus V curves towards higher velocities with increasing temperature, as shown in Fig. 6.5a. The temperature dependence of $\tilde{\mu}$ results in additional displacement of the μ versus V curves towards higher μ values with increasing T . The predicted effect of temperature on steady state friction coefficient is shown explicitly in Fig. 6.6a, at sliding velocities of 1, 10 and 100 $\mu\text{m/s}$. The main trend visible is an increase in μ with T . However, at 1 and 10 $\mu\text{m/s}$, μ sharply decreases at the highest temperatures. With reference to Fig. 6.5a, this is related to the transition from dilatant behaviour to non-dilatant behaviour, which occurs at progressively lower temperatures when the slip velocity is lower.

6.7.1.3 Predicted effect of σ_n^{eff}

The predicted effect of effective normal stress (σ_n^{eff}) on μ versus V at steady state is illustrated in Fig. 6.5b for $\sigma_n^{\text{eff}} = 50 \text{ MPa}$ and $\sigma_n^{\text{eff}} = 110 \text{ MPa}$ in addition to the reference curve at $\sigma_n^{\text{eff}} = 170 \text{ MPa}$. The curves are plotted for a temperature of 500°C, at which the model shows the

full range of non-dilatant to dilatant behaviour across the investigated velocity range of 1-100 $\mu\text{m/s}$ (Fig. 6.5a). With increasing effective normal stress, the μ versus V curve shifts towards higher slip rates. In the non-dilatant regime, this is the result of an increase in the shear strength (i.e. $\tau_{ph} = \tilde{\mu}\sigma_n^{eff}$) of the phyllosilicates with increasing normal stress, shifting the velocity at which pressure solution of quartz becomes more difficult than slip on the phyllosilicates to higher values. In the non-dilatant regime, compaction of quartz by pressure solution is enhanced at a higher σ_n^{eff} (cf. Eq. [6.13]), moving the velocity-weakening part of the μ versus V curve towards higher velocities. The curves for different effective normal stresses converge, at the lowest and highest velocities, towards the area-corrected friction coefficient related to slip on the horizontal phyllosilicates in the limiting cases of infinitely easy pressure solution and critical state deformation, respectively. The dependence of μ on σ_n^{eff} at a fixed sliding velocity of 10 $\mu\text{m/s}$ is shown in Fig. 6.6b at temperatures of 450, 500 and 550°C. This shows that σ_n^{eff} has little effect on μ at low temperatures (500°C, and below), but results in a decrease in μ with σ_n^{eff} at 550°C, because at this temperature, the effect of σ_n^{eff} on μ is evaluated at a fixed sliding velocity that falls near the maximum of the μ versus V curve (cf. Fig. 6.5a).

6.7.1.4 Predicted effect of f_{qtz}

The effect of changes in quartz fraction on the steady state μ versus V curve is shown in Fig. 6.5c, again at 500°C, for 40 and 70% quartz, as well as for the reference value of 56% quartz. An increase in quartz fraction results in a lower friction coefficient at the lowest sliding velocities investigated and a higher peak strength, but does not affect μ at the highest velocities. This is because friction at the lowest velocities is controlled by slip on the horizontal foliation, so that a larger quartz fraction reduces the area of horizontal foliation undergoing slip. At higher V , where shear deformation of quartz clasts by pressure solution becomes more difficult, an increase in quartz content leads to an increase in μ in the non-dilatant field. A larger quartz fraction also results in a larger initial vertical overlap x_0 of the quartz clasts (Fig. 6.3b), increasing the dilatation angle Ψ_{dil} and hence μ (cf. Eq. [6.10]), at the onset of dilatation, causing a more pronounced peak in μ and more pronounced velocity-weakening behaviour. At the highest velocities, μ is predicted to depend only on $\tilde{\mu}$ ($\tan \Psi_{dil} = 0$ in Eq. [6.10], clast overlap $x = 0$) and thus is the same for different quartz contents. The dependence of the friction coefficient on quartz fraction at 10 $\mu\text{m/s}$ and at 450, 500 or 550°C is shown explicitly in Fig. 6.6c. Depending on temperature, an increase in quartz fraction either results in a constant friction coefficient (450°C, and below), a decrease in μ with quartz fraction at low quartz contents followed by a slight increase (500°C) or an increase in μ with increasing quartz fraction (550°C, and above). These different responses are related to the position on the μ versus V curve, i.e. on the selected slip velocity in combination with the temperature (refer Fig. 6.5a and c).

6.7.1.5 Predicted effect of D

Although not addressed in our experiments on illite-quartz gouge, we also investigated the effect of quartz grain size on the steady state μ versus velocity curve predicted by the model - see Fig. 6.5d. Here, the reference μ versus V curve is plotted together with curves for grain sizes of 0.1 μm and 10 μm . An increase in grain size displaces the curve towards lower sliding velocities. At intermediate velocities, this leads to an increase in μ with D at low grain sizes, followed by a slight decrease towards a constant friction level at large

grain sizes, reflecting the transition from non-dilatant to dilatant behaviour (Fig. 6.6d). The predicted trend is due to a decrease in the rate of pressure solution with increasing grain size (see Eq. [6.11]-[6.13]).

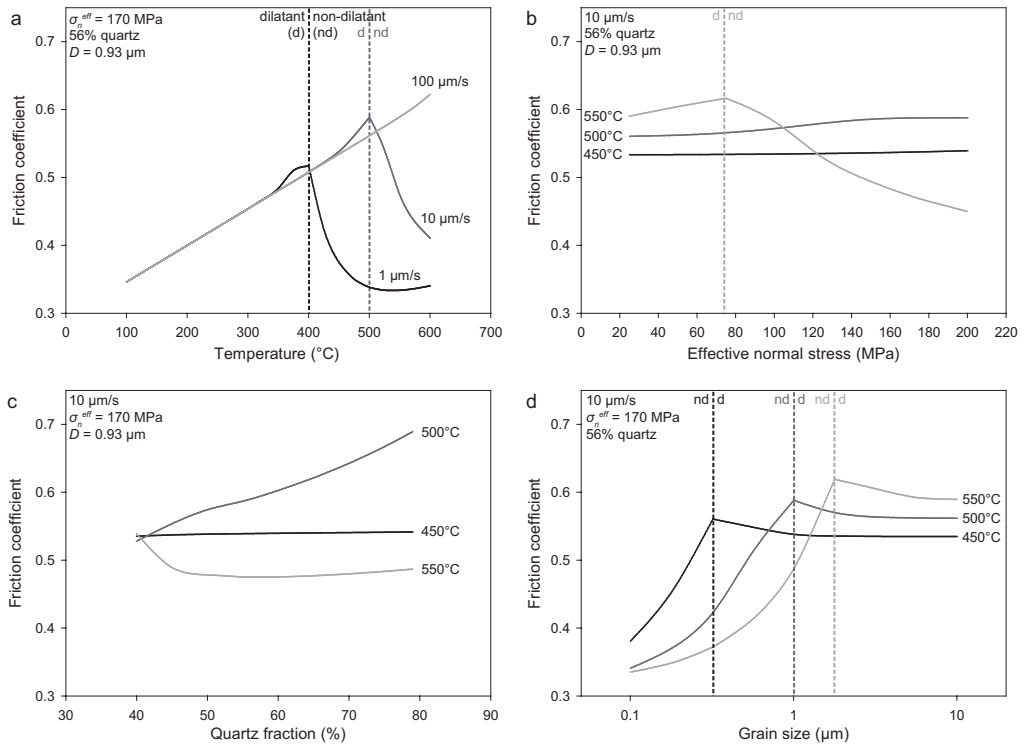


Figure 6.6 Trends predicted by the current model for the dependence of steady state friction coefficient μ on (a) temperature, (b) effective normal stress, (c) quartz fraction and (d) quartz grain size, under otherwise constant conditions. The values of the quantities held constant are specified in the top left corner of each panel. Discontinuities related to the switch from dilatant to non-dilatant behaviour with increasing temperature in the model, are indicated where relevant, with a dotted line in the same grey shade as the corresponding curve, with the regions corresponding to non-dilatant (nd) and dilatant (d) behaviour indicated.

6.7.1.6 Effect of P_f

In our previous experiments on illite-quartz gouge, we varied the pore fluid pressure, and found no significant effect on friction independently of σ_n^{eff} (Den Hartog and Spiers, in press, Chapter 4). Our current model does not allow testing of any effects of pore fluid pressure, independently of effective normal stress, as neither poro-elastic nor chemical effects of P_f are included (e.g. on the rate coefficient $I = k_+ \Omega$ for pressure solution). Note, however, that any effect of pore fluid pressure on the pressure solution rate is expected to be very minor, at least above 100 MPa, where quartz solubility and surface reaction rates in aqueous solution are insensitive to P_f (Walther and Helgeson, 1977). In the absence of an aqueous pore fluid, the pressure solution shear and compaction components of the present model are rendered inactive (infinite resistance to shear and compaction). This removes all dependence of μ on V , producing a constant steady state frictional strength determined by

dilatant granular flow and equal to μ at the corresponding critical state porosity. This in turn would be determined by $\tilde{\mu}$ for dry illite.

6.7.1.7 Comparison with experimental trends in μ

Since our previous experiments were conducted at only three velocities (1, 10 and 100 $\mu\text{m/s}$), and since the frictional strength data in the different velocity steps employed needed removal of background slip hardening (“detrending”) to obtain steady state values (Den Hartog et al., 2012a, Chapter 3), comparison of the measured μ versus V trends with our model predictions of Fig. 6.5a serves little purpose. Here we therefore compare the predicted versus measured effects of T , σ_n^{eff} , and quartz fraction on μ . Velocity effects on μ are considered in the following section making use of the RSF parameter ($a-b$).

The μ versus temperature trend observed in our previous experiments (Den Hartog et al., 2012a, Chapter 3; Den Hartog and Spiers, in press, Chapter 4) shows broad agreement with that predicted by our microphysical model, with μ increasing with T in both cases (compare Fig. 6.1b and 6.6a). Although the predicted sharp decrease in μ at high temperatures and low sliding velocities (Fig. 6.6a) was not observed in our experiments, the experimental data for a shear strain of 50 (Den Hartog et al., 2012a, Chapter 3; Fig. 6.1b) did show some flattening off in μ versus T above $\sim 350^\circ\text{C}$, which might reflect the onset of a smoothed out transition of the type seen in Fig. 6.6a. The present predictions of relatively little effect of σ_n^{eff} at low temperature on steady state friction (μ) also largely agree with the experimental observations (Fig. 6.6b vs. 6.1b). Note here that the decrease in μ with increasing σ_n^{eff} , observed at low σ_n^{eff} , in the experiments at low temperatures (Fig. 6.1b), was attributed by Den Hartog and Spiers (in press, Chapter 4) to sample cohesion at low effective normal stresses - an effect not incorporated in the model.

The main differences between our model predictions and experimental observations on the effects of T and σ_n^{eff} lie in (i) the very sharp decrease in μ predicted to occur with increasing temperature at 1 and 10 $\mu\text{m/s}$ (Fig. 6.6a) and (ii) the decrease in μ predicted to occur with increasing σ_n^{eff} at 550°C . Neither effect is seen in the experimental data (Fig. 6.1b). We believe that these anomalous predictions are the result of the discontinuous transition between the non-dilatant and dilatant regimes in our model (Fig. 6.5), which is expected to be smoothed out in real materials and in experiments performed at discrete intervals of T and σ_n^{eff} . In addition, the limited microstructural evidence for pressure solution (i.e. the absence of strongly elongated or tailed quartz clasts) suggests that a complete transition from dilatant to non-dilatant behaviour did not occur in the experiments.

No experimental data are available for comparison with the increase in μ with f_{qtz} predicted by the model at 500°C (Fig. 6.6c). The experimentally observed increase in μ with f_{qtz} seen by Den Hartog and Spiers (in press, Chapter 4) at 140°C (the only temperature tested – see Fig. 6.1b) and by others at room temperature (Brown et al., 2003; Tembe et al., 2010) is not reproduced by the model at these low temperatures. The absence of this trend at low temperatures in the predictions (i.e. in Regime 1 – Fig. 6.1b) is related to the approach to critical state behaviour in which the model predicts zero overlap of quartz clasts, hence no effect of f_{qtz} . The fact that experiments do show a positive effect of f_{qtz} on frictional strength suggests that in reality critical state behaviour may not require zero overlap of quartz clasts

($\chi = 0$) but involves a rate-independent balance between pore opening and closure due to slip on the anastomosing phyllosilicate foliation at a lower value of ϕ_c than used in the model.

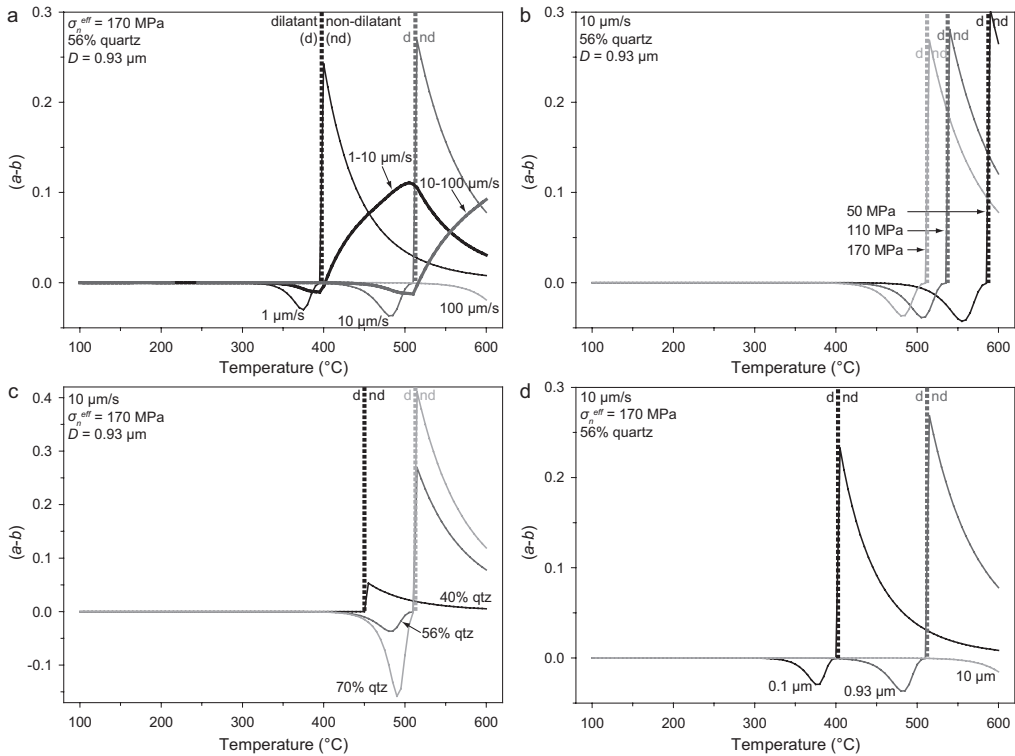


Figure 6.7 Plots of $(a-b)$ versus T predicted by the current model, showing dependence on (a) slip velocity, (b) effective normal stress, (c) quartz fraction and (d) grain size, under otherwise constant conditions. The values of the quantities held constant are specified in the top left corner of each panel. All curves are derivative-based, except the two bold curves in (a), which we obtained by taking the finite difference between the strengths predicted and 1 and 10 $\mu\text{m/s}$ or at 10 and 100 $\mu\text{m/s}$. The discontinuity related to the switch from dilatant to non-dilatant behaviour with increasing temperature in the model, visible in the derivative-based $(a-b)$ curves, is indicated with a dotted line for each curve, in the same grey shade as the corresponding curve, with the regions corresponding to non-dilatant (nd) and dilatant (d) behaviour indicated. In real materials, or in experiments where $(a-b)$ is determined from finite ($\times 10$) velocity-steps, such a discontinuity is expected to be smoothed out.

Lastly, it is important to note that the experimentally observed necessity of water for velocity-weakening behaviour in illite-quartz gouge reported by Den Hartog et al. (2012a, Chapter 3; cf. Den Hartog and Spiers, in press, Chapter 4) fits with our microphysical model. In the absence of water, thermally activated deformation of the quartz clasts will not take place in the model and thus no velocity-weakening behaviour can occur.

6.7.2 Trends in the RSF parameter $(a-b)$

The velocity dependence of friction observed in experiments is usually quantified in the

framework of the rate and state dependent friction model (RSF; Dieterich, 1978; 1979; Ruina, 1983), using the parameter:

$$(a-b) = \frac{\Delta\mu_{ss}}{\Delta \ln V} \quad (6.14)$$

$$= \frac{\partial\mu_{ss}}{\partial \ln V} \quad \text{in the limit } \Delta \ln V \rightarrow 0$$

(e.g. Marone, 1998; Scholz, 1998). Here a represents the absolute magnitude of the instantaneous change in apparent friction coefficient μ upon a step change in sliding velocity from a reference value V_0 , characterized by a steady state friction coefficient μ_{ss} , to a new velocity V , while b reflects the magnitude of the change in μ during evolution to a new steady state. The overall change in steady state friction coefficient is denoted $\Delta\mu_{ss}$. Positive $(a-b)$ values indicate an increase in friction coefficient with increasing velocity, i.e. velocity-strengthening, which ensures stable slip behaviour, while negative $(a-b)$ values signify velocity-weakening and potentially unstable behaviour (e.g. Scholz, 1998). Almost all previous experiments on illite-quartz gouge have made use of $(a-b)$ to investigate the velocity dependence of frictional behaviour (Ikari et al., 2009; Morrow et al., 1992; Saffer and Marone, 2003; Tembe et al., 2010), determining $(a-b)$ by stepping the sliding velocity, usually in order of magnitude jumps (e.g. 1, 10, 100 mm/s; Den Hartog et al., 2012a, Chapter 3), or else half-order jumps (Ikari et al., 2009).

6.7.2.1 Predicted effects of V and T

We determined $(a-b)$ from the predicted μ versus V curves (Fig. 6.5a) by direct application of Eq. [6.14], at fixed velocity and fixed temperatures in the range 100-600°C, to obtain a finite difference approximation of the continuous derivative of $\mu(V)$, i.e. of $\partial\mu/\partial V$, taking $\mu = \mu_{ss}$. The $(a-b)$ values thus calculated at velocities of 1, 10 and 100 $\mu\text{m/s}$ are shown versus temperature in Fig. 6.7a. Note the jump in $(a-b)$ at the discontinuous transition between dilatant and non-dilatant behaviour predicted by the model (Fig. 6.7a). In reality, such a discontinuity is expected to be smoothed out, by factors such as distributed grain size and distributed dilatation angle. Moreover, in experiments it will generally be smoothed out by the use of velocity steps to determine $(a-b)$. Three regions of behaviour can be distinguished in Fig. 6.7a: velocity-neutral behaviour at low temperatures, velocity weakening at intermediate temperatures and velocity-strengthening behaviour at high temperatures.

We also determined $(a-b)$ versus T as predicted by the model for finite jumps in V from either 1 to 10 $\mu\text{m/s}$ or 10 to 100 $\mu\text{m/s}$ (Fig. 6.7a), thus simulating the velocity stepping approach to determining $(a-b)$ used in our previous experiments on illite-quartz gouge (Den Hartog et al., 2012a, Chapter 3; Den Hartog and Spiers, in press, Chapter 4). These profiles show the same three regimes of $(a-b)$ versus temperature, but with reduced velocity-weakening, a shift in the velocity-weakening regime to slightly higher temperatures (+25°C) and a smoothing out of the discontinuity due to the switch from dilatant to non-dilatant behaviour. Note that all predicted $(a-b)$ curves shown in Fig. 6.7a show a clear dependence on slip velocity, shifting towards higher temperatures with an increase in slip velocity. In addition, velocity-

weakening is more pronounced at higher slip velocity, i.e. $(a-b)$ values are more negative.

6.7.2.2 Predicted effects of σ_n^{eff} , f_{qz} and D

The predicted effect of σ_n^{eff} on the $(a-b)$ versus temperature profile is shown in Fig. 6.7b, using the derivative of the corresponding μ versus V curve taken at 10 $\mu\text{m/s}$ for effective normal stresses of 50 and 110 MPa, in addition to the reference value of 170 MPa (cf. Fig. 6.5b). With increasing effective normal stress, the three temperature dependent $(a-b)$ regimes systematically shift towards lower temperatures.

The predicted dependence of the $(a-b)$ versus T curve on quartz content is shown in Fig. 6.7c, for quartz fractions of 0.56 (reference case), 0.4 and 0.7, again using the derivative of the relevant μ versus V curves determined at 10 $\mu\text{m/s}$. In line with the effects of increasing quartz content observed in Fig. 6.5c, $(a-b)$ values become more negative in the velocity-weakening regime upon an increase in the quartz fraction from 0.56 to 0.7, but span the same temperature range. A decrease in quartz content reduces the velocity-weakening response and, for a quartz fraction of 0.4, completely removes the velocity-weakening region (cf. Fig. 6.5c).

Profiles of $(a-b)$ versus temperature predicted for a quartz clast grain size of 0.1, 0.93 (reference grain size) and 10 μm are displayed in Fig. 6.7d. With increasing grain size, the velocity-weakening region shifts towards higher temperatures, in line with the displacement of the μ versus V curves towards lower velocities with increasing grain size, hence decreasing pressure solution rate, as predicted in Fig. 6.5d.

6.7.2.3 Comparison with experimental trends

The predicted existence of three regimes of $(a-b)$ with increasing temperature is in good agreement with our experimental observations on illite-quartz mixtures (Fig. 6.7a vs. Regimes 1, 2 and 3 in Fig. 6.1a; Den Hartog et al., 2012a, Chapter 3; Den Hartog and Spiers, in press, Chapter 4). The magnitude of $(a-b)$, i.e. $|a-b|$, shows reasonable agreement too, in the velocity-weakening regime (Regime 2). The predicted displacement of the $(a-b)$ versus T profile towards higher temperatures with increasing sliding velocity, and with decreasing effective normal stress, also agrees with the trends observed in the experiments (Fig. 6.1a, c and e). In the experiments at 140°C reported by Den Hartog and Spiers (in press, Chapter 4), an increase in quartz content was observed to lead to a decrease in $(a-b)$, which was interpreted to imply a shift of the $(a-b)$ profile versus T profile towards lower temperatures (Fig. 6.1e). However, our model predicts vertical exaggeration of the $(a-b)$ versus temperature profile with increasing quartz content, which is also in agreement with our experimental results (Den Hartog and Spiers, in press, Chapter 4).

The above demonstrates good qualitative agreement between experimental results for $(a-b)$ in illite-quartz gouge and the effects of T , V , σ_n^{eff} , and f_{qz} predicted by the model. However, the temperature range of velocity-weakening behaviour in our experiments was 250–400°C (Den Hartog et al., 2012a, Chapter 3; Den Hartog and Spiers, in press, Chapter 4; Fig. 6.1a). This range overlaps with those predicted in Fig. 6.7a for finite velocity steps involving 1 and 10 $\mu\text{m/s}$, but extends to lower temperatures. A possible explanation for this discrepancy lies in our assumption of homogeneous shear in the fault gouge model. If

in the experiments some degree of localization occurs, then the predicted μ versus V curves should be displaced to higher V for proper comparison (cf. Fig. 6.5), while the predicted $(a-b)$ versus T profiles should be shifted to lower temperatures. Note here that a factor 10x increase in strain rate produced by shear localization would shift the velocity-weakening regime down in temperature by $\sim 100^\circ\text{C}$ in the velocity range of 1-100 $\mu\text{m/s}$ (Fig. 6.7a).

A further discrepancy between model predictions and experiments concerns the velocity dependency of μ , i.e. $(a-b)$, at low temperatures. Although similar, three-regime, $(a-b)$ versus temperature behaviour is seen in our experimental data (Fig. 6.1) and in the model predictions (Fig. 6.1a and 6.7a), $(a-b)$ values at the lowest temperatures are positive in the experiments but zero in the predictions. This may be related to the velocity-strengthening behaviour typically reported for pure phyllosilicates sheared wet at low temperatures (e.g. Ikari et al., 2011) and recently also observed by Den Hartog et al. (submitted, Chapter 5) for pure muscovite notably at 200 and 600°C (at 400°C near neutral behaviour was observed). The present model assumes that $\tilde{\mu}$ for pure illite is velocity independent. Incorporating a velocity-strengthening $\tilde{\mu}$ would result in the observed velocity-strengthening behaviour at low temperatures. In addition, if pure illite shows a near neutral minimum in $(a-b)$ at intermediate temperatures, similar to pure muscovite, incorporation of such an effect into the model would tend to produce a broadening of the predicted temperature range of velocity-weakening, more closely approaching the experimental observations. However, as of yet, no microphysical model exists that can quantitatively predict the frictional behaviour of pure phyllosilicates. Rate and state friction descriptions of velocity-strengthening phyllosilicate friction cannot be used because they generally only hold for the experimental conditions addressed and usually cannot be successfully extrapolated even from one experimental temperature to another.

Regarding Regime 3 (velocity-strengthening, at high T), qualitative agreement between the model predictions and experimental observations is obtained, both showing positive values of $(a-b)$. The predicted magnitude of $(a-b)$ for the derivative-based curves (Fig. 6.7a), however, is much larger than that observed in the experiments (Fig. 6.1a). Comparison with the curves in which $(a-b)$ is obtained using finite jumps in velocity (Fig. 6.7a), i.e. similar to the experimental determination of $(a-b)$, is more relevant, but still shows predicted values $\sim 5\times$ larger than those observed experimentally (Fig. 6.7a vs. 6.1a). Once again, this could reflect the discontinuous nature of the transition from non-dilatant to dilatant deformation in the model, which in reality is expected to be smoothed out.

6.8 Implications for subduction megathrust seismogenesis

To predict the depth range of velocity-weakening behaviour, i.e. a negative $(a-b)$ under in-situ subduction megathrust conditions, depth profiles of all relevant quantities, notably temperature and effective normal stress, are needed. However, although the temperature is reasonably well constrained for various subduction zones (Peacock, 2009; Peacock and Wang, 1999; Spinelli and Wang, 2008), the pore fluid pressure versus depth profile, and thus the effective vertical and hence normal stress versus depth profile, is largely a matter of speculation at present (Den Hartog and Spiers, in press, Chapter 4; Saffer and Tobin, 2011). Though the effect of σ_n^{eff} on μ is probably relatively small, at least in the velocity-weakening regime (see Fig. 6.1b and 6.6b), this makes the construction of useful μ and $(a-b)$

versus depth profiles for natural subduction megathrusts problematic, beyond the simple assumption that σ_n^{eff} has no effect, or that P_f is hydrostatic ($P_f = \bar{\rho}_f g h$), or else that P_f is a fixed fraction of the lithostatic pressure (e.g. $P_f / P_{litho} = 0.9-0.98$; Seno, 2009).

Like the temperature, the slip rate associated with earthquake nucleation is somewhat better constrained, generally being assumed to be close to (within 1-2 orders of) plate velocities of $\sim 10^{-9}$ m/s (e.g. Segall and Rice, 2006), and thus three to five orders of magnitude lower than applied in our experiments and model predictions. In our previous work, we extrapolated our experimentally derived ($a-b$) versus temperature profile to these natural rates, using the observed trends in ($a-b$) versus V , assuming no influence of departures in σ_n^{eff} from the experimental value of 170 MPa (Den Hartog and Spiers, in press, Chapter 4). The extrapolated temperatures were respectively 155°C and 142°C, for the transitions from velocity-strengthening to velocity-weakening and back. Although the value of 155°C for the onset of velocity-weakening is in good agreement with the temperature usually connected to the upper seismogenic limit on subduction megathrusts (100-150°C; Hyndman et al., 1997), the value of 142°C for the reverse transition is obviously too low, presumably reflecting “over-extrapolation” of the observed ($a-b$) versus temperature and velocity trends due to insufficient constraints.

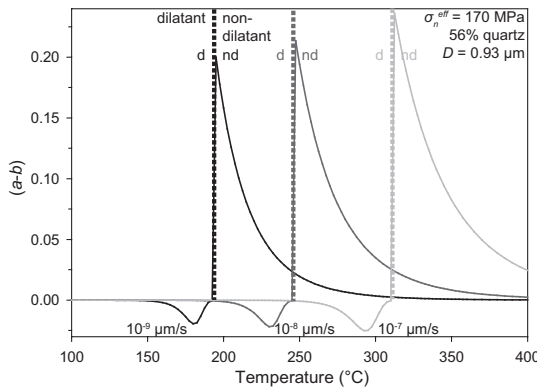


Figure 6.8 Model predictions for the dependence of ($a-b$) on temperature at slip rates of 10^{-9} , 10^{-8} and 10^{-7} m/s, expected to be relevant to earthquake nucleation (plate velocity V_{pl} , $10V_{pl}$ and $100V_{pl}$). The discontinuity at the boundary between dilatant and non-dilatant behaviour is marked with a dotted line, in the same grey shade as the corresponding ($a-b$) versus temperature curve (see also Fig. 6.7). The effective normal stress, quartz fraction and grain size were held constant, as indicated.

However, our current microphysical model provides an improved basis for extrapolation of the ($a-b$) versus temperature trend to sub-experimental slip velocities. The predicted dependence of ($a-b$) on temperature is shown in Fig. 6.8 for slip velocities of 10^{-9} , 10^{-8} and 10^{-7} m/s, using otherwise the same conditions as in our reference case defined above ($\sigma_n^{eff} = 170$ MPa, $f_{qtz} = 0.56$, $D = 0.93$ μm , sample thickness = 0.57 mm, $n = 0.3$). These predictions imply velocity-weakening behaviour at temperature of $\sim 140-193^\circ\text{C}$, $190-245^\circ\text{C}$ and $230-310^\circ\text{C}$, at 10^{-9} , 10^{-8} and 10^{-7} m/s, respectively. The temperature of 140°C for onset of velocity-weakening behaviour at 10^{-9} m/s again agrees well with the up-dip seismogenic limit on subduction megathrusts, but, with the transition back to velocity-strengthening occurring at 193°C , the temperature range of velocity-weakening is still narrower than that of $150-350^\circ\text{C}$ over which seismogenesis occurs on megathrusts (Hyndman et al., 1997). This may imply that velocities higher than 10^{-9} m/s should be taken into account, in relation to rupture nucleation (Fig. 6.8). However, as we emphasized previously (Den Hartog et al., submitted, Chapter 5), illite will

be replaced by muscovite at temperatures of ~200-300°C (Hunziker, 1986; Merriman and Frey, 1999; Van de Kamp, 2008), and thus it is the behaviour of muscovite-quartz gouge that should determine the temperature at which velocity weakening behaviour changes back to strengthening. Prediction of the temperature associated with this transition requires a microphysical model specifically developed for muscovite-quartz mixtures. This will form the subject of a future paper. Here, we note simply that experiments on muscovite-quartz gouge extend the range of velocity-weakening seen in illite-quartz gouge upwards in temperature by 100°C at similar conditions (Den Hartog et al., submitted, Chapter 5). A possible reason for the different behaviour of muscovite-quartz gouge as compared to illite-quartz gouge, in the experiments reported by Den Hartog et al. (2012a, Chapter 3; submitted, Chapter 5), may lie in different (*a-b*) versus *T* profiles for pure illite and pure muscovite gouges, which is at present only available for pure muscovite (Den Hartog et al., submitted, Chapter 5). Alternatively, the difference may reflect the observed differences in the quartz grain size or grain size distribution in the starting materials (<10 µm and ~15 µm in illite-quartz and muscovite-quartz, respectively) and during deformation (~1 µm quartz clasts in illite-quartz samples, versus polycrystalline quartz clasts of ~20-200 µm in the muscovite-quartz gouge samples).

Following the earlier approach of Den Hartog et al. (2012a, Chapter 3; 2012b, Chapter 2), based on experimental data only, the temperature range of velocity-weakening behaviour at 10^{-9} m/s predicted by the current model can be compared with that assumed in numerical studies, addressing seismogenesis on subduction megathrusts - such as those by Liu and Rice (2005) or Shibazaki and Shimamoto (2007). As explained above, the transition from illite to muscovite at ~200-300°C limits the comparison of the present model for illite-quartz to temperatures below this. In this range, the model predicts the onset of velocity-weakening behaviour at ~140°C. This is higher than the 100°C assumed by Liu and Rice (2005) and Shibazaki and Shimamoto (2007) for the southwest Japan subduction zone. In addition, the (*a-b*) values predicted in the current study have a significantly higher magnitude (i.e. 5x more negative) than those used by Liu and Rice (2005) and Shibazaki and Shimamoto (2007). The effects of these higher values should be explored in future modelling work. Further improvements in (*a-b*) versus depth profiles in future will require better insight into the pore fluid pressure distribution and hence effective normal stress that may be expected in-situ.

Finally, we note that the good agreement found between the predicted temperature-dependent three-regime behaviour and the sequence of aseismic-seismic-aseismic zones seen on natural megathrusts suggests that seismogenic behaviour is caused by the same mechanism that results in velocity-weakening behaviour in the model. This would mean that seismogenesis is in fact caused by gouge compaction through thermally activated deformation of quartz clasts, most likely by pressure solution. Without a thermally activated compaction process such as this to compete with rate-independent dilation due to slip on the anastomosing foliation (i.e. due to granular/cataclastic flow), our model implies that velocity-weakening would not occur. The implication is that velocity-weakening, as represented by our model, is a truly brittle-ductile transition process in that it occurs under conditions where pressure solution is too slow to accommodate shear without dilatation (velocity-strengthening ductile deformation) yet fast enough to influence frictional

behaviour by moderating the amount of dilatation that can occur at a given slip velocity to values below ϕ_c .

6.9 Conclusions

In this study, we aimed to derive a microphysical model to explain the steady state frictional behaviour of illite-quartz gouges, based on the approach of Bos and Spiers (2001) and Niemeijer and Spiers (2005; 2007), but accounting for the matrix supported nature of phyllosilicate-rich gouge. We assumed deformation to be controlled by frictional slip on the phyllosilicates and thermally activated deformation of the quartz clasts. Although the microstructures of deformed illite-quartz mixtures suggested an important role of SCC, reducing the grain size at least initially, the poorly constrained nature of SCC led us to implement pressure solution as the thermally activated deformation mechanism, in our model – with the objective of evaluating the potential role of this process in controlling gouge friction. We conclude the following:

1. Incorporating pressure solution plus rate independent phyllosilicate friction in the model explains many of the main experimental observations on illite-quartz gouges.
2. The trends in steady state friction coefficient μ predicted by the microphysical model, like the experiments reported by Den Hartog and Spiers (in press, Chapter 4), show an increase in μ with increasing T and little effect of σ_n^{eff} , across much of the range of conditions explored experimentally.
3. A predicted decrease in μ with increasing T at high temperatures and low slip rates does not agree with the experimental results, but is likely related to the discontinuous transition from non-dilatant to dilatant behaviour, which in reality is expected to be smoothed out, or was never attained in the experiments. The same may explain the predicted decrease in μ with increasing σ_n^{eff} at high temperature. In addition, the absence of an effect of quartz fraction on μ in the predictions at low temperatures, an effect which has been widely observed in experiments on phyllosilicate-quartz gouges, may point to a critical state in which a rate-independent balance between pore opening and closure leads to non-zero overlap of quartz clasts, as opposed to zero overlap assumed in the model.
4. Predicted $(a-b)$ versus T profiles shows three regimes of $(a-b)$, with velocity-weakening at intermediate temperatures. This is consistent with the experimental observations on illite-quartz mixtures. These regimes are predicted to shift towards higher temperatures with increasing slip rate and decreasing effective normal stress, as observed in the experiments. The velocity-weakening regime in the predicted $(a-b)$ versus T profile, shows similar $(a-b)$ magnitudes but is displaced towards higher temperatures compared with the experimental results. This may point to localised (inhomogeneous) shear deformation of the aggregate or to a velocity-dependence of $\tilde{\mu}$ for pure illite, as seen in pure muscovite.
5. The model predicts velocity-neutral behaviour at low temperatures, whereas the experiments showed velocity-strengthening behaviour. This difference can be explained by the fact that pure phyllosilicates show velocity-strengthening behaviour, as opposed to rate-independent phyllosilicate friction behaviour assumed in the model. Incorporation of such an effect into the model in future requires formulation of a separate model for thermally activated phyllosilicate friction.
6. The velocity-strengthening predicted at high temperature is in agreement with the

- experimental observations on illite-quartz gouge. The predicted magnitude of (*a-b*), however, is too high, possibly related to the discontinuous transition from non-dilatant to dilatant behaviour in the model, which in reality is expected to be smoothed out.
7. Application of the model to slip rates believed to be relevant for earthquake nucleation (10^{-9} - 10^{-7} m/s), but using otherwise equivalent conditions to the experiments on illite-quartz gouge, predicts velocity-weakening starting at 140°C, which is in good agreement with the temperature associated with the up-dip seismogenic limit on subduction megathrusts. Prediction of the temperature at which the behaviour changes from velocity-weakening, back to strengthening at higher temperature, i.e. the equivalent of the down-dip seismogenic limit, requires formulation of a microphysical model for muscovite-quartz friction, accounting for the rate dependence of friction in pure muscovite plus the characteristics of the microstructures observed in these materials.
 8. The similarity between the three regimes of (*a-b*) behaviour versus temperature predicted by the model, seen in experiments, and implied by the sequence of aseismic-seismic-aseismic behaviour on natural megathrusts, suggests that subduction zone seismogenesis is related to velocity-weakening caused by competition between gouge compaction involving pressure solution of quartz clasts and dilatant frictional slip on the intervening phyllosilicates. Any thermally activated creep process should in principle have similar effects, producing velocity-weakening and seismogenesis literally in the brittle-ductile transition, i.e. under conditions where the creep process is fast enough to moderate “brittle” dilatation to remain at subcritical porosity values but too slow to allow ductile shear of the clast phase.

Acknowledgements

SdH was supported by a Toptalent Ph.D. grant awarded by the Netherlands Organisation for Scientific Research (NWO) (Project 021.002.025).

Appendix 6.A: Shear strain rate of clast bodies

Here we derive a relation describing the shear strain rate of quartz clast bodies by pressure solution. In other words, we obtain a “flow law” for shear deformation of the clast bodies by pressure solution. In line with the main text (Fig. 6.3), the clasts are taken to be cylindrical with axial length equal to the diameter D (Fig. 6.A1). It is assumed that pressure solution is dissolution and/or precipitation controlled, as grain scale diffusion is relatively fast for quartz grains in the (micrometer) size range expected in a fault gouge (Niemeijer et al., 2002; Spiers et al., 2004). In addition, we assume that clast shear and pore filling (compaction) by pressure solution can be treated independently (see also Niemeijer and Spiers, 2007; Raj, 1982). The relations obtained for shear deformation of the quartz clasts by pressure solution are accordingly valid both in the non-dilatant and dilatant regimes. It is further assumed that the pressure solution “flow law” describing homogeneous simple shear of a clast body is the same as that for a complete (circular sectioned) clast.

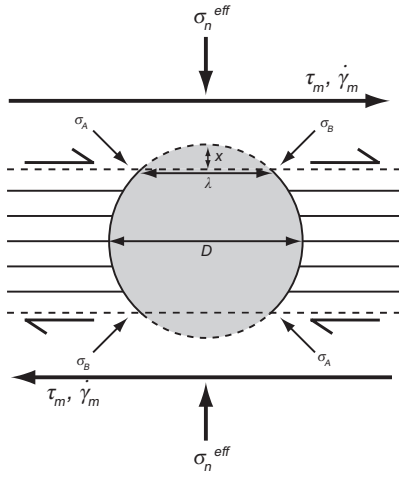


Figure 6.A1 Grain geometry used to derive the rate law describing clast shearing by pressure solution. The variables are defined in the text and/or in Table 6.1.

For a complete clast, homogeneous simple shear, imposed by shear on a horizontal phyllosilicate foliation, generates a uniform shear stress supported by the clast of $\tau_{q|c-b}$. If the shear strain rate of the clast is $\dot{\gamma}$, the mechanical work rate associated with shearing each clast is $\dot{w} = \tau_{q|c-b} \dot{\gamma} \pi D^3/4$. Assuming that all work is dissipated in driving pressure solution transfer (Lehner, 1990; Spiers and Schutjens, 1990), then we can write $\dot{w} = [(\Delta\mu_s V_s A_s)/\Omega] + [(\Delta\mu_p V_p A_p)/\Omega]$, where $\Delta\mu_s$ and $\Delta\mu_p$ are the mean chemical potential drops associated with dissolution and precipitation (Lehner, 1990; Raj, 1982; Rutter, 1983). Since the areas of dissolution (A_s) and precipitation (A_p) remain equal during simple shear of a cylinder by pressure solution, and assuming that mass is conserved (so that $V_s A_s = V_p A_p$), then the mean dissolution and precipitation velocities V_s and V_p are equal. Now, from crystal growth/dissolution theory (e.g. Raj, 1982) and from dissolution/precipitation rate measurements on quartz (Rimstidt and Barnes, 1980; Tester et al., 1994), the (mean) velocity of dissolution and precipitation can be written in the form

$$V_i = I \frac{\Delta\mu_i}{RT} \quad (6.A1)$$

for small $\Delta\mu_i$, where $i=s$ for dissolution or $i=p$ for precipitation, I is the product of the reaction rate coefficient k_s ($\text{mol}\cdot\text{m}^{-2}\text{s}^{-1}$) and the molar volume of quartz, Ω , R is the gas constant and T is the temperature in Kelvin. Since $V_s = V_p$, this kinetic relation in turn implies that $\Delta\mu_s = \Delta\mu_p$. Using the above relationship for \dot{w} , the mean chemical potential drop for both dissolution and precipitation are accordingly given

$$\Delta\mu_s = \Delta\mu_p = \frac{\dot{w}\Omega}{2V_s A_s} = \frac{\pi}{8} \frac{\tau_{qtz-b} \Omega \dot{\gamma} D^3}{V_s A_s} \quad (6.A2)$$

But $V_s A_s$ is the volume M_s of quartz dissolved (and precipitated) per second. From the clast geometry, this is given $M_s = \dot{\gamma} D^3/2$. Hence $\Delta\mu_s = \Delta\mu_p = \pi \tau_{qtz-b} \Omega/4$. Using Eq. [6.A1], we can therefore write

$$V_s = \frac{\pi}{4} \frac{I \tau_{qtz-b} \Omega}{RT} \quad (6.A3)$$

But again from the clast geometry, $\dot{\gamma} \approx (2V_s)/(D/2) = 4V_s/D$. Hence

$$\dot{\gamma} = \frac{\pi I \tau_{qtz-b} \Omega}{RTD} \quad (6.A4)$$

Applying this to the clast body only, which has vertical dimension $(D-2x)$, implies a horizontal velocity contribution to shear of the unit cell of $V_b = \dot{\gamma}(D-2x)$ - refer Fig. 6.3 in the main text. Since the thickness of the unit cell is $s = D-x$, the strain rate contribution to the unit cell by pressure solution of the clast bodies is $\dot{\gamma}_{qtz-b} = V_b/(D-x)$ or

$$\dot{\gamma}_{qtz-b} = \frac{\pi I \tau_{qtz-b} \Omega}{RT} \frac{D-2x}{D(D-x)} \quad (6.A5)$$

Appendix 6.B: Shear strain rate of clast overlaps

With reference to Fig. 6.A1 and to Fig. 6.3 and 6.4 of the main text, we assume that the overlapping portions (segments) of the quartz clasts retain their shape during horizontal “shearing off” by pressure solution (refer Fig. 6.4). The wholesale shear displacement of each overlap per unit time is associated with a mechanical work rate per overlap of $\dot{w} = \tau_{qtz-o} \lambda D V_{qtz-o'}$ where τ_{qtz-o} is the shear stress supported by the overlap at its base and $V_{qtz-o'}$ is the velocity of overlap displacement relative to the clast body due to pressure solution. Assuming, as in Appendix 6.A, that all of this work is dissipated in driving pressure solution (Lehner, 1990; Spiers and Schutjens, 1990), then we can again write $\dot{w} = [(\Delta\mu_s V_s A_s)/\Omega] + [(\Delta\mu_p V_p A_p)/\Omega]$, where $\Delta\mu_s$ and $\Delta\mu_p$ are now the mean potential drops associated with overlap dissolution and precipitation. Since the areas of dissolution (A_s) and precipitation (A_p) remain equal during overlap dissolution, and since mass is conserved ($V_s A_s = V_p A_p$), then once again $V_s = V_p$ and Eq. [6.A1] implies that $\Delta\mu_s = \Delta\mu_p$. Accordingly, the mean chemical potential drop for both dissolution and precipitation of clast overlaps is given by

$$\Delta\mu_s = \Delta\mu_p = \frac{\dot{\gamma}\Omega}{2V_s A_s} = \frac{\tau_{qtz-o} \Omega \lambda D V_{qtz-o}}{2V_s A_s} \quad (6.B1)$$

But, from the clast overlap geometry (Fig. 6.A1, 6.3 and 6.4), the volume of material dissolved per overlap per second is $V_s A_s = V_{qtz-o} x D$, hence $\Delta\mu_s = \Delta\mu_p = (\tau_{qtz-o} \Omega \lambda) / (2x)$. Applying Eq. [6.A1], and assuming that dissolution and precipitation occur in a horizontal direction consistent with horizontal clast overlap displacement so that $V_s \approx V_{qtz-o}$ yields:

$$V_{qtz-o} = \frac{I \tau_{qtz-o} \Omega}{2RT} \frac{\lambda}{x} \quad (6.B2)$$

Since there are two quartz clast overlaps per unit cell, since $\lambda = 2\sqrt{(Dx - x^2)}$ and since the thickness of the unit cell is $s = D - x$, the shear strain rate of the unit cell due to pressure solution of the quartz overlaps is given by:

$$\dot{\gamma}_{qtz-o} = \frac{2V_{qtz-o}}{s} = \frac{2I \tau_{qtz-o} \Omega}{RT} \frac{1}{\sqrt{(Dx - x^2)}} \quad (6.B3)$$

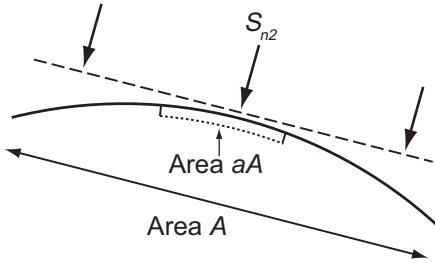


Figure 6.A2 Grain geometry used to derive the rate law describing compaction by pressure solution of quartz clasts. The variables are defined in the text.

Appendix 6.C: Compaction rate

The above mentioned assumption that the effects of shear stress and normal stress on clast deformation by pressure solution can be separated, means that compaction will be driven by normal stress only. A similar separation of the effect of shear and normal stress was employed by Niemeijer and Spiers (2007) for granular gouge with such thin films of phyllosilicate that the material was essentially clast-supported. With reference to Fig. 6.A2, and making the conventional assumption for pressure solution that gradients in chemical potential are linearly related to gradients in (effective) normal stress (Rutter, 1976), the difference in chemical potential μ_{ps} between the stress-supporting clasts-matrix contact region and the non-stress-bearing clast surface bounding the pore and exposed to fluid at pressure P_f only, is given by $\Delta\mu_{ps} = (S_{n2}\Omega)/(1-a)$. Here S_{n2} is the average effective normal stress component acting locally on the clast boundary segment (i.e. on ℓ_2) and a is the fraction of the grain boundary segment occupied by the pore. Now, since dissolution and precipitation are serial steps, characterized by potential drops $\Delta\mu_s$ and $\Delta\mu_p$, $\Delta\mu_{ps} = \Delta\mu_s + \Delta\mu_p$ (Raj, 1982; Spiers et al., 2004). Using Eq. [6.A1] and accounting for local mass balance written $V_s A(1-a) = V_p Aa$ (refer Fig. 6.A2) thus yields $\Delta\mu_p = S_{n2}\Omega$. Note that here V_s and V_p are the local velocities of dissolution and of precipitation on the pore wall (area $A_{pore} = Aa$).

Taking the above expression for $\Delta\mu_p$, Eq. [6.A1] implies that the quartz precipitation velocity on the clast wall within the pore is given

$$V_p = \frac{I\Delta\mu_p}{RT} = \frac{IS_{n2}\Omega}{RT} \quad (6.C1)$$

The compaction strain rate of the unit cell is then obtained from $\dot{\epsilon}_{comp} = (2V_p A_{pore})/V_u$, where $V_u = (D-x)DL$ is the unit cell volume. Using Eq. [6.A1], $\Delta\mu_p = S_{n2}\Omega$ and the geometry shown in Fig. 6.3b yields

$$\dot{\epsilon}_{comp} = \frac{2IS_{n2}\Omega}{RT} \frac{A_{pore}}{(D-x)DL} \quad (6.C2)$$

The effective normal stress S_{n2} can be obtained by considering the force balance in Fig. 6.3b (taking $L_1 \approx L_2$), yielding

$$S_{n2} = \frac{\sigma_n^{eff}}{\tan^2 \Psi_{fr} + 1} - \frac{\tau_m}{2} \frac{\tan \Psi_{fr}}{\tan^2 \Psi_{fr} + 1} \quad (6.C3)$$

This approaches σ_n^{eff} for small values of Ψ_{fr} . We will therefore use the approximation $S_{n2} \approx \sigma_n^{eff}$, yielding

$$\dot{\epsilon}_{comp} = \frac{2I\sigma_n^{eff}\Omega}{RT} \frac{A_{pore}}{(D-x)DL} \quad (6.C4)$$

Chapter 7

General conclusions and suggestions for future research

This thesis has reported an experimental study aimed at determining the frictional behaviour of compositionally realistic subduction megathrust fault gouges under near in-situ P - T conditions, addressing low sliding velocities relevant to earthquake nucleation. In addition, an attempt was made to explain the underlying microscale processes both qualitatively and in terms of a microphysical model. The experimental programme focused in particular on simulated illite-quartz and muscovite-quartz gouges, thus capturing the main effect of increasing metamorphic grade with depth/temperature on pelitic, megathrust fault rock composition. The work done has provided some of the first results on the frictional behaviour of realistic gouges under realistic P - T conditions. In the following, the principal conclusions will be integrated and summarized and the overall implications for subduction megathrust behaviour assessed. Finally, questions which remain unanswered are identified and suggestions are made for future research.

7.1 Main findings

7.1.1 Effect of temperature on the frictional properties of illite-quartz gouge

An extensive series of ring shear experiments was performed on simulated 65:35 illite-quartz gouge at temperatures (T) covering the range 150–500°C, at an effective normal stress (σ_n^{eff}) of 170 MPa, a pore fluid pressure (P_f) of 100 MPa and sliding velocities (V) of 1–100 $\mu\text{m/s}$. Velocity-stepping experiments (Chapter 3) showed three regimes of velocity-dependence, with velocity-strengthening behaviour occurring at ~150–250°C (Regime 1), velocity-weakening at ~250–400°C (Regime 2) and velocity-strengthening at ~400–500°C (Regime 3). Increasing the temperature was also found to lead to an increase in friction coefficient (μ), this being sharpest at ~350°C (i.e. in velocity-weakening Regime 2). The velocity-strengthening, velocity-weakening, velocity-strengthening behaviour observed with increasing temperature bears a striking parallel to the sequence of aseismic-seismic-aseismic behaviour seen on megathrusts at slightly (50–100°C) lower temperature.

7.1.2 Effects of other variables on frictional properties

The above ring shear experiments on 65:35 illite-quartz mixtures also showed an effect of slip rate on the frictional properties. Specifically, a decrease in slip rate was found to result in a shift of the three “slip stability” regimes towards lower temperatures (Chapters 3 and 4). Ring shear experiments were also performed on the illite-quartz gouge at effective normal stresses of 25–200 MPa, pore fluid pressures of 50–200 MPa, sliding velocities of 1–100 $\mu\text{m/s}$ and at 140–600°C to determine the effects of σ_n^{eff} and P_f on frictional behaviour of 65:35 illite-quartz gouge. The results (Chapter 4) showed a shift of the velocity-weakening regime (Regime 2) towards higher temperatures with a decrease in the effective normal stress, being located at ~350–600°C at $\sigma_n^{eff} = 50$ MPa. The pore fluid pressure slightly increased (a - b) at all temperatures explored, apparently narrowing Regime 2, although a shift of the entire (a - b) profile towards lower temperatures could not be excluded. These effects of T , V , σ_n^{eff} and P_f suggest that velocity-weakening can occur in illite-quartz gouge at a range of depths on subduction zone megathrusts, including the range where seismogenic behaviour is typically observed (seismogenic zone).

Alongside the ring shear experiments performed at elevated temperature, double direct shear (biaxial) experiments were performed at room temperature, using the same, wet, illite-quartz gouge, extending the dataset to connect with previous work (Chapter 2). These

experiments showed positive ($a-b$) values, consistent with velocity-strengthening, Regime 1 behaviour seen in the ring shear machine from 140-250°C. In contrast to the effect of σ_n^{eff} on ($a-b$) at these temperatures, ($a-b$) determined at room temperature increased with increasing normal stress over the investigated range of 5-30 MPa, as did the friction coefficient μ .

Nearly all experiments, whether ring or double direct shear, showed and increase in μ with displacement, i.e. slip hardening behaviour. In the direct shear tests, a trend of increasing slip hardening rate with increasing normal stress was found. Reduced strain hardening rates in ring shear control experiments, conducted dry, suggested this was caused by preferred phyllosilicate loss from wet samples.

7.1.3 Effect of quartz-phyllosilicate composition on frictional properties

The effect of varying quartz content on the frictional behaviour of illite-quartz gouge was investigated in experiments employing an illite:quartz ratio of 65:35 to zero, at an effective normal stress of 100 MPa, a pore fluid pressure of 200 MPa, sliding velocities of 1-100 $\mu\text{m/s}$ and a temperature of 140°C (Chapter 4). These conditions fall in the Regime 1 velocity-strengthening field for the 65:35 gouge mixture. The experiments showed an increase in the friction coefficient with increasing quartz content, in line with previous studies addressing the frictional properties of phyllosilicate-quartz gouges. In addition, values of ($a-b$) were found to decrease towards velocity-neutral values with increasing quartz content, pointing to either a horizontal or vertical shift of the ($a-b$) versus temperature profile, and suggesting that increased quartz content can lead to velocity-weakening slip at low temperatures (140°C) associated with the nucleation of events such as the Tohoku-Oki earthquake for example.

Friction experiments were also performed on phyllosilicate-quartz gouges with other phyllosilicates. The frictional properties of wet, smectite-rich Nankai ODP material were determined in biaxial (double direct shear) experiments, performed at room temperature, normal stresses of 10 and 15 MPa and sliding velocities of 0.18-18 $\mu\text{m/s}$ (Chapter 2). This material showed similar behaviour to the 65:35 illite-quartz mixtures deformed under the same conditions, being characterized by velocity-strengthening behaviour and an increase in slip hardening rate with increasing normal stress, but also with increasing sliding velocity. These results confirmed previous work on smectite-rich gouges at room temperature, pointing to positive ($a-b$) on megathrusts (at least) down to the smectite-illite transition.

Ring shear experiments on 65:35 muscovite-quartz mixtures performed at the same conditions as the 65:35 illite-quartz mixtures (i.e. $\sigma_n^{eff} = 170$ MPa, $P_f = 100$ MPa, $V = 1$ -100 $\mu\text{m/s}$) but at temperatures of 100-600°C, showed very similar behaviour to illite-quartz gouge (Chapter 5). In particular, three similar regimes of ($a-b$) versus temperature were observed, along with a similar increase in μ with temperature. However, the temperature range of velocity-weakening (Regime 2) was shifted towards higher temperatures for muscovite-quartz mixtures, being located at ~350-500°C compared with ~250-400°C for illite-quartz gouge (Chapter 5). The overlap in the velocity-weakening regimes exhibited by the two gouges suggests that the illite-muscovite transition extends the zone of velocity-weakening behaviour on megathrusts to a total width in temperature of 250-500°C, i.e. extending the

seismogenic zone beyond that expected for illite-quartz.

Finally, the effect of the presence versus the absence of quartz was addressed by experiments on 100% pure muscovite gouge, performed at the same P - T and velocity conditions as the muscovite-quartz mixtures and at temperatures of 200, 400 and 600°C (Chapter 5). This material showed mainly velocity-strengthening or neutral behaviour, with a minimum in the $(a-b)$ versus T curve, i.e. predominantly neutral $(a-b)$ values, occurring at 400°C, where velocity-weakening occurs in megathrusts. This implies a key role of quartz in causing velocity-weakening. The control ring shear experiments conducted on dry illite-quartz gouge also showed near-neutral $(a-b)$ values, suggesting that water is also necessary for velocity-weakening behaviour in phyllosilicate-quartz mixtures.

7.1.4 Microscale processes

The microstructures of the ODP material and illite-quartz gouge deformed at room temperature showed an anastomosing phyllosilicate network, defining a foliation in the P shear orientation, with embedded quartz clasts and discrete shears in the P , R_1 and Y orientations. The microstructure of the illite-quartz and muscovite-quartz gouges deformed at in-situ P - T was also characterised by quartz clasts surrounded by fine, aligned and often anastomosing phyllosilicates. The quartz clasts present in the illite-quartz samples were mostly monocrystalline, in contrast to the muscovite-quartz mixtures, in which small quartz grains were concentrated in polycrystalline clusters. No clear evidence for pressure solution of clasts was found, and the main deformation mechanism leading to clast size reduction was inferred to be cataclasis, probably involving Stress Corrosion Cracking (SCC). Any pressure solution of the clasts which did occur was insufficiently active to produce observable microstructures, such as tailed quartz clasts in the illite-quartz samples. In the muscovite-quartz mixtures, however, the fine quartz grain clusters, formed from originally larger quartz clasts, often displayed a sigmoidal shape, possibly deformed by pressure solution as a whole. The otherwise broadly similar microstructures seen in the illite-quartz and muscovite-quartz gouges were cross-cut by discrete shears, in the P , R_1 and Y orientations.

Based on the microstructural observations on illite-quartz gouge deformed under near in-situ megathrust conditions ($\sigma_n^{eff} = 170$ MPa, $T = 150$ -500°C, $P_f = 100$ MPa), a microphysical model for the frictional behaviour of illite-quartz gouge at steady state was developed (Chapter 6), accounting for the phyllosilicate matrix-supported nature of the material. The aim was to develop a model describing the deformation behaviour occurring in such materials under the experimental conditions, and to apply it to constrain behaviour in situ. Illite-quartz gouge was chosen because of its simpler microstructures (monocrystalline clasts embedded in phyllosilicate matrix). The model resembles the model of Niemeijer and Spiers (2007) in that it assumes deformation by rate-independent frictional sliding on the phyllosilicate foliation coupled with thermally activated deformation of the intervening quartz clasts. However, it differs in assuming a phyllosilicate-rich, matrix-supported microstructure as opposed to a clast-supported microstructure with subordinate phyllosilicates, supporting the clasts at grain boundaries. Velocity-strengthening in the present model is the result of non-dilatant slip on flat portions of the phyllosilicate foliation with serial accommodation by thermally activated shear deformation of the intervening

quartz grains. Velocity-weakening, on the other hand, results from a balance between (i) porosity generation, caused by activation of dilatant slip on anastomosing, curved portions of the phyllosilicate foliation, and (ii) compaction caused by deformation of the quartz clasts by the thermally activated mechanism. Assuming pressure solution as the thermally activated mechanism, the trends in friction coefficient and ($a-b$) versus T , V and σ_n^{eff} (and in ($a-b$) versus quartz content) predicted by this model were in good agreement with those observed in the experiments on illite-quartz gouge. This suggests that pressure solution played an important role in controlling frictional behaviour, though not evident in the microstructure. The main discrepancies between the predictions and observations were attributed to the discontinuous transition from non-dilatant to dilatant behaviour predicted by the model, which is expected to be smoothed out in reality.

7.2 Implications for subduction megathrust behaviour: a synthesis

The experimental results on smectite-rich ODP material, and on simulated illite-quartz and muscovite-quartz gouges, reported in this thesis, have been shown to have several important implications for the frictional behaviour of subduction zone megathrusts and their seismogenic potential. The results are applicable to subduction zones dominated by metapelitic input, in which the composition with increasing temperature is expected to be dominated by smectite-quartz (<~150°C), followed by illite-quartz (~150-200/300°C) and finally muscovite-quartz (>200/300°C). The observed effect of temperature on ($a-b$) values for the illite- and muscovite-quartz gouges implies velocity-weakening behaviour over the entire range of ~250 to 500°C, at least at $\sigma_n^{eff} = 170$ MPa, $P_f = 100$ MPa and $V = 1-100$ $\mu\text{m/s}$. Rough extrapolation of the experimental data on ($a-b$) versus sliding velocity to earthquake nucleation slip rates of $\sim 10^{-9}$ m/s (Chapter 4) suggests the onset of velocity-weakening at 155°C, in reasonable agreement with the upper limit of the seismogenic zone at ~150°C. Though data for muscovite-quartz mixtures were too limited to determine whether a systematic relationship with V also existed for this material, the similarity in frictional behaviour to illite-quartz gouge suggests it, potentially shifting the maximum temperature of velocity-weakening behaviour towards lower values as well (Chapter 5). This would improve correspondence with the down-dip limit of seismogenesis on subduction megathrusts at ~350°C.

The microphysical model developed for shear deformation of illite-quartz gouge provided an improved basis for extrapolation of the experimental results to earthquake nucleation slip rates. This yielded a temperature of ~140°C for the onset of velocity-weakening behaviour (Chapter 6), in very good agreement with the temperature usually associated with the up-dip seismogenic limit on subduction megathrusts. An improved prediction of the temperature at which velocity-weakening behaviour changes back to velocity-strengthening with continued increase in temperature, requires the formulation of a microphysical model for muscovite-quartz mixtures, taking into account possible differences in the microstructure of these materials (e.g. the presence of sigmoidal quartz clusters as seen in the present experiments on muscovite-quartz mixtures), as well as possible differences in the behaviour of illite versus muscovite. Viewed overall, the agreement obtained in the main trends of frictional behaviour versus T , V , σ_n^{eff} and quartz content, between model predictions, experimental data, and the location of the up-dip seismogenic limit on subduction megathrusts, implies that seismogenesis is caused by a key brittle-ductile

transitional process, namely competition between dilation, due to slip on an anastomosing phyllosilicate foliation, and thermally activated compaction, most likely involving pressure solution of quartz clasts.

Apart from the slip rate, the results presented in Chapter 4 have shown that the temperature range of velocity-weakening in illite-quartz and muscovite-quartz at in-situ P - T conditions also depends on effective normal stress, quartz content and to a lesser extent on the pore fluid pressure. This implies that prediction of the temperature and depth range of seismogenesis on subduction megathrusts should ideally incorporate these effects too. However, besides from a few constraints from sedimentary basins and from preliminary results of ODP drilling and NanTroSEIZE, accurate depth-profiles of the pore fluid pressure (and resulting effective normal stress profile) are not yet available for subduction zone megathrusts. In contrast, the quartz content of subduction megathrusts is often better constrained so that effects of local subducted sediment composition are easier to assess. For example, given the experimentally observed decrease in $(a-b)$ with increasing quartz content at low temperatures, the high chert content of the sediments present in the Tohoku-Oki region may explain the relatively low temperature of $\sim 140^{\circ}\text{C}$ at which nucleation of the Tohoku-Oki earthquake occurred.

Finally, the observed general increase in slip hardening rate with increasing normal stress and sliding velocity at room temperature implies that unstable slip behaviour is promoted at low effective normal stresses and at low sliding velocities, thus favouring the nucleation of earthquakes and SSEs when effective normal stresses are low.

7.3 Remaining problems and suggestions for further research

As already indicated, this research has provided some of the first results on the frictional behaviour of megathrust fault gouges under in-situ subduction zone conditions, at large shear displacements, and low sliding velocities relevant to earthquake nucleation. In addition, a first step towards understanding and quantifying the underlying microphysical mechanisms has been made. However, the work leaves behind a number of unsolved problems and has brought up a number of new issues that should be addressed as well. These are outlined below.

7.3.1 Unsolved issues and remaining data needs

A number of possible issues to address in future (experimental) work follow directly from the present research. In addition, the datasets are in not all cases complete and call for further work.

Cause of slip hardening

First, the cause of the ubiquitous slip/strain hardening, or occasionally softening, behaviour could not be unambiguously proven based on the current experiments. Reduced slip hardening in dry ring shear experiments compared to wet tests on illite-quartz gouge strongly suggested an important role of preferential loss of phyllosilicates. This was assumed to be the cause throughout much of this thesis and formed the basis for specifying the average quartz content in the illite-quartz samples in the comparison with the microphysical model (Chapter 6). An alternative process put forward in Chapter 2 to explain the slip hardening

behaviour was progressive refinement of quartz followed by mixing with phyllosilicates (see also Tembe et al., 2010). However, this hypothesis was not confirmed by the present experimental evidence because the relationship between grain size reduction, as visible in the microstructures after deformation, and shear displacement/strain was not systematically investigated. Given the slip neutral steady state or slip softening behaviour required for the nucleation of unstable, seismogenic slip or repetitive stick-slip behaviour, it is important to gain better insight into the cause of the slip hardening behaviour in the present experiments – and indeed in almost all friction experiments. Note here that hardening in the current experiments was not greater than in other experiments, but is more apparent because of large displacements. In particular, it is essential to know whether the underlying cause is an experimental artefact, or a material property of the gouge. Only in the second case will such behaviour affect slip zone stability in nature.

Effects of P_f on illite-quartz gouge

The data presented on illite-quartz gouge in Chapter 4 was too limited to draw firm conclusions regarding the effect of the pore fluid pressure on the temperature-dependent three-regime behaviour of illite-quartz gouge. The pore fluid pressure was cautiously interpreted to result in an increase in $(a-b)$ in all three regimes, but a shift of the three regimes towards lower temperatures with an increase in P_f could not be excluded. Clearly, more data are needed to firmly establish the effect of pore fluid pressure on the three-regime behaviour of illite-quartz gouge, whether mechanical, poroelastic or through a change of the total normal stress, or chemical by affecting the dissolution kinetics of quartz.

Model versus shear band microstructure

The mechanical behaviour of illite-quartz gouges could be reasonably well predicted by the microphysical model presented in Chapter 6, assuming pressure solution as the deformation mechanism affecting the quartz clasts and assuming deformation to be accommodated in foliated, P , R_1 and Y shear bands. It was further assumed that deformation dominated by slip on P , R_1 or Y shears would be similar, treating Y shears for simplicity. These are reasonable assumptions, but do not address why the shear bands form. While the general reasons have been discussed in the literature (e.g. Logan et al., 1992; Marone, 1998), a complete model should address this too – or a complimentary model should be added. Notably, macroscopic fractures in the R_1 orientation seemed to develop only at temperatures up to 350°C (Chapter 3), an observation that has not been explained in the current research, beyond noting here that this is the region where the porosity is greatest, as predicted by the model due to dilatation.

Behaviour of pure muscovite and pure illite gouges

In the present study, only a few experiments were performed on pure muscovite gouge, for comparison with the muscovite-quartz samples. This was adequate for identifying that velocity-weakening in the mixtures depends on the presence of quartz. However, more data are needed to gain insight into the behaviour of muscovite itself under (near) in-situ P - T conditions. Note here that the muscovite used in previous studies performed at elevated P - T conditions (Mariani et al., 2006; Van Diggelen et al., 2010), was not 100% pure muscovite. Since no experiments were conducted on pure illite gouge, and since previous data is at room temperature (Tembe et al., 2010), it is more important still to obtain data on

the frictional properties of this at in-situ P - T conditions. This would yield not only additional information on the effect of quartz, in the illite-quartz gouge, but would also serve as input to the microphysical model, in which the temperature-dependent illite friction coefficient is currently based on μ at room temperature plus the effect of temperature on the friction coefficient observed for pure muscovite. Furthermore, comparison of the data for pure illite with that for pure muscovite should yield insight into the cause of the observed shift of the temperature regime of velocity-weakening behaviour of muscovite-quartz compared to that for illite-quartz. Data on both pure phyllosilicates is important for future microphysical modelling of the frictional behaviour of these materials and of mixtures with quartz.

Dry versus wet behaviour

Only two dry control experiments on illite-quartz gouge were performed in the current study. These showed near-neutral behaviour at 200 and 350°C, i.e. in Regimes 1 (velocity-strengthening) and 2 (velocity-weakening) identified for the wet experiments, thus indicating a key role of water in causing velocity-weakening. Better insight into the effect of water on the frictional behaviour of megathrust fault gouges clearly requires additional control experiments on dry materials, including muscovite-quartz gouge, pure illite and pure muscovite gouge, at a wider range of P - T conditions, covering Regimes 1 through 3.

Extrapolation to natural slip rates

The slowest slip rates addressed in the current study (1.8×10^{-7} m/s) were still high compared to earthquake nucleation slip rates which are likely around 10^{-9} m/s or 10^{-8} m/s. Our microphysical model provides a basis for extrapolation to rates below lab rates – this was a strong motivation to develop it. However, to test the model predictions for slow slip rates, experiments should ideally be performed at the lowest slip rates that can reasonably be achieved – probably $\sim 3 \times 10^{-9}$ m/s. It should be noted, on the other hand, that strain rate rather than the sliding velocity is likely to be the controlling variable and thus it is this parameter that should be matched to nature in experiments. This, though, requires an accurate estimate of the width of the active slip zone. Input from field studies is needed on this.

Additional data needed for the materials investigated

The frictional properties of (natural) smectite-rich materials have not been determined under in-situ P - T conditions in this study, nor have the effects of normal stress and pore fluid pressure on the temperature-dependent behaviour of muscovite-quartz gouge. Such data would add to the depth/temperature profiles presented in Chapters 2 and 3 and would be valuable additional input for modelling studies. In addition, no tests were performed on any of the materials studied at very low effective normal stress (< 25 MPa) and a high temperature ($> 300^\circ\text{C}$), which are believed to prevail at depths where Slow Slip Events (SSEs) nucleate, especially just beyond the down-dip limit of the seismogenic zone. This is an important aim for the future.

7.3.2 Broader challenges for the future

In the current research, several issues have been identified that are outside the scope of a direct follow-up study, adding to the data obtained in this one, but deserve attention in parallel efforts in their own right.

Microphysical model developments

Given the absence of a realistic microphysical model for thermally activated (rate-dependent) clast deformation by SCC, predictions were made with the microphysical model developed in this thesis including pressure solution as the thermally activated process (Chapter 6). Although the agreement between the predicted trends and those observed in the experiments on illite-quartz gouge was surprisingly good, these predictions should ideally be compared with alternative predictions made using SCC as the thermally activated mechanism. This means developing a realistic microphysical model for clast deformation by SCC. Moreover, the governing parameter values need to be determined by testing such a model against specifically designed experiments. Besides extension of the microphysical model by inclusion of quartz deformation by SCC, it should also be improved by incorporating velocity-strengthening phyllosilicate friction. This requires the formulation of a separate model for phyllosilicate friction. In addition, extension of the model to the case of polycrystalline quartz clasts, of the type observed in our muscovite-quartz experiments, should be attempted.

Finally, the microphysical model developed in Chapter 6 applies to steady state behaviour, whereas a complete treatment of frictional behaviour should involve transient effects as well. The model can be generalized to account for such behaviour by avoiding the steady state assumption of zero net compaction rate, caused by a balance between dilatation and thermally activated compaction, and instead using the differential equation describing the net compaction rate as the difference between the dilatation and thermally activated compaction rate. This would allow for prediction of trends in μ , a , b , $(a-b)$ and d_c with V , T , σ_n^{eff} and quartz content. The microphysical model would also benefit from further refinement allowing for a more realistic description of critical state frictional behaviour and for a non-homogeneous microstructure (characterized by, for example, a distributed grain size).

In-situ pore and effective stress profiles

The attempt in this thesis to assess the implications of the measured and modelled frictional properties and trends, for subduction megathrust seismicity, clearly demonstrated that quantitative information on pore fluid pressure and effective normal stress versus depth profiles is needed to allow proper extrapolation of the experimental results to natural conditions. Since direct measurement of the pore fluid pressure at depths exceeding several kilometres is impossible, this demands an integrated approach, involving not only seismological observations, but also hydrological modelling or even coupled hydrological/fault-mechanics modelling.

Other gouge compositions: from metabasaltic to carbonate-bearing

The materials used in this study have been limited to either natural or synthetic mixtures of phyllosilicates and quartz, while other minerals could be present within the accreted and subducting sediments as well, such as carbonates. In addition, it cannot be excluded that the basaltic rocks forming the oceanic crust become incorporated in the base of the subduction megathrusts, accommodating slip as well, if they become weaker than metapelitic fault rocks present. Thus, a more complete understanding of megathrust frictional properties would involve the determination of the frictional behaviour of gouges derived from carbonate-

rich sediments (Ikari, pers. comm; cf. Verberne et al., 2010) and basalts (cf. gabbroic gouge investigated by He et al., 2007; 2006) under in-situ megathrust conditions. Such knowledge, combined with the available data on that of the weak, aseismically deforming serpentinite-rich mantle wedge, at depths beyond the seismogenic zone (e.g. Hirauchi et al., 2012; Moore and Lockner, 2011), will all contribute to the development of a more complete picture of subduction megathrust behaviour.

In addition, simulated phyllosilicate-quartz mixtures have been used here as a representation of the main phases present in metapelitic materials at deeper levels in the subduction megathrust. However, field studies (e.g. Moore et al., 2007; Rowe et al., 2009) of exhumed materials show that minerals such as albite, chlorite, pyrite and pumpellyite are also present depending on bulk chemistry and metamorphic grade. Although direct extraction of natural materials from depths >7 km is technically impossible, either exhumed fault rocks or perhaps even laboratory-reacted, natural, ODP materials recovered from shallow depths could be considered for future experimental studies, as these probably approach in-situ fault rock and gouge composition. As a related issue, the use of pore fluids that are similar in composition to those found at convergent margins (e.g. Kastner et al., 1991) could be considered. This may be of particular importance since fluid assisted processes such as pressure solution and SCC of quartz clasts, inferred to be active in the experiments presented in this thesis, can be strongly affected by the ionic species present in the pore fluid.

Advances in experimental methodology

This thesis has focused on active megathrust behaviour, i.e. on determining the mechanical behaviour during fault slip imposed as a velocity boundary condition. Almost all experiments done in other studies to date have also been performed by imposing a fixed sliding velocity. However, in reality, rupture nucleation and displacement along a megathrust represents the response to the ambient state of stress. Therefore, natural conditions are better simulated by performing constant stress and stress relaxation experiments, whereby the shear stress decays as elastic distortion of the loading environment is converted into fault zone slip. These rarely used testing methods are a future challenge and will give new insight into nucleation of unstable seismogenic slip and notably into SSE behaviour, as the resulting displacement rates are expected to approach those actually occurring during SSEs (1-100 nm/s).

To understand the seismic cycle at subduction megathrusts, the current results should also be complemented by data on post-seismic creep and the healing behaviour of realistic megathrust gouges under in-situ conditions. This too indicates a need for constant shear stress and slide-hold-slide experiments, in which the evolution of the decay of frictional strength (shear stress relaxation – Rutter and Mainprice, 1978) during the hold stage and the subsequent increase during re-initiation of shear are examined could yield useful insight into the thermally activated deformation mechanisms operative in the system, useful for understanding both slip nucleation (low velocity frictional behaviour) and post-seismic slip.

A further issue to consider in future experimental studies addressing the frictional

behaviour of subduction megathrusts is accurate measurement of sample thickness and sample porosity during shear. This will be especially important for testing microphysical models such as that developed in Chapter 6, in which the porosity is an important dynamic parameter governing frictional behaviour. The technical challenge, however, is a formidable one, since it ideally requires displacement measurements to be performed inside the high P - T environment, with zero sample loss.

Finally, a crucial aspect of understanding megathrust seismicity includes addressing rupture acceleration and propagation at high velocity besides the nucleation velocities addressed here. This requires data on the frictional properties of realistic megathrust gouges at in-situ P - T and P_f conditions, at coseismic slip rates. This means ongoing developments are needed in the field of high velocity friction and in linking low and high velocity behaviour, through development of appropriate machines and experimental methods.

References

- Ader, T.J., Ampuero, J.-P. and Avouac, J.-P., 2012. The role of velocity-neutral creep on the modulation of tectonic tremor activity by periodic loading. *Geophys. Res. Lett.* 39 (16), L16310, 10.1029/2012GL052326.
- Audet, P., Bostock, M.G., Christensen, N.I. and Peacock, S.M., 2009. Seismic evidence for overpressured subducted oceanic crust and megathrust fault sealing. *Nature* 457, 76-78.
- Baumberger, T., Berthoud, P. and Caroli, C., 1999. Physical analysis of the state- and rate-dependent friction law. II. Dynamic friction. *Phys. Rev. B* 60 (6), 3928-3939.
- Becker, K., Fisher, A.T. and Davis, E.E., 1997. The CORK experiment in hole 949C: long-term observations of pressures and temperature in the Barbados accretionary prism. *Proc. Ocean Drill. Program Sci. Results* 156, 247-252.
- Beeler, N.M., 2007. Laboratory-observed faulting in intrinsically and apparently weak materials, in: Dixon, T.H. and Moore, J.C. (Eds.), *The Seismogenic Zone of Subduction Thrust Faults*. Columbia University Press, New York, pp. 370-449.
- Beeler, N.M., Tullis, T.E., Blanpied, M.L. and Weeks, J.D., 1996. Frictional behavior of large displacement experimental faults. *J. Geophys. Res.* 101 (B4), 8697-8715.
- Behnsen, J. and Faulkner, D.R., 2012. The effect of mineralogy and effective normal stress on frictional strength of sheet silicates. *J. Struct. Geol.* 42, 49-61.
- Bekins, B. and Screatton, E.J., 2007. Pore pressure and fluid flow in the northern Barbados accretionary complex, in: Dixon, T.H. and Moore, J.C. (Eds.), *The Seismogenic Zone of Subduction Thrust Faults*. Columbia University Press, New York, pp. 148-170.
- Ben-Zion, Y. and Sammis, C.G., 2003. Characterisation of fault zones. *Pure Appl. Geophys.* 160 (3-4), 677-715.
- Beroza, G.C. and Ide, S., 2011. Slow earthquakes and nonvolcanic tremor. *Annu. Rev. Earth Planet. Sci.* 39, 271-296.
- Bilek, S.L., 2010. Invited review paper: Seismicity along the South American subduction zone: review of large earthquakes, tsunamis, and subduction zone complexity. *Tectonophysics* 495 (1-2), 2-14.
- Bilek, S.L. and Lay, T., 1999. Rigidity variations with depth along interplate megathrust faults in subduction zones. *Nature* 400, 443-446.
- Blanpied, M.L., Lockner, D.A. and Byerlee, J.D., 1991. Fault stability inferred from granite sliding experiments at hydrothermal conditions. *Geophys. Res. Lett.* 18 (4), 609-612.
- Blanpied, M.L., Lockner, D.A. and Byerlee, J.D., 1995. Frictional slip of granite at hydrothermal conditions. *J. Geophys. Res.* 100 (B7), 13045-13064.
- Blanpied, M.L., Marone, C.J., Lockner, D.A., Byerlee, J.D. and King, D.P., 1998. Quantitative measure of the variation in fault rheology due to fluid-rock interactions. *J. Geophys. Res.* 103 (B5), 9691-9712.
- Bolton, M.D., 1986. The strength and dilatancy of sands. *Geotechnique* 36 (1), 65-78.
- Bos, B., Peach, C.J. and Spiers, C.J., 2000. Frictional-viscous flow of simulated fault gouge caused by the combined effects of phyllosilicates and pressure solution. *Tectonophysics* 327, 173-194.
- Bos, B. and Spiers, C.J., 2001. Experimental investigation into the microstructural and mechanical evolution of phyllosilicate-bearing fault rock under conditions favouring pressure solution. *J. Struct. Geol.* 23 (8), 1187-1202.
- Bos, B. and Spiers, C.J., 2002. Frictional-viscous flow of phyllosilicate-bearing fault rock: microphysical model and implications for crustal strength profiles. *J. Geophys. Res.* 107, B2, 2028, DOI:10.1029/2001JB000301.
- Brown, K.M., Kopf, A., Underwood, M.B. and Weinberger, J.L., 2003. Compositional and fluid pressure controls on the state of stress on the Nankai subduction thrust: a weak plate boundary. *Earth Planet. Sci. Lett.* 214 (3-4), 589-603.
- Byerlee, J., 1978. Friction of rocks. *Pure Appl. Geophys.* 116 (4), 615-626.
- Byrne, D.E., Davis, D.M. and Sykes, L.R., 1988. Loci and maximum size of thrust earthquakes and the mechanics of the shallow region of subduction zones. *Tectonics* 7 (4), 833-857.
- Chester, F.M. and Higgs, N.G., 1992. Multimechanism friction constitutive model for ultrafine quartz gouge at hypocentral conditions. *J. Geophys. Res.* 97 (B2), 1859-1870.
- Colletini, C., Niemeijer, A., Viti, C. and Marone, C., 2009. Fault zone fabric and fault weakness. *Nature* 462 (7275), 907-910.
- Cowan, D.S., 1999. Do faults preserve a record of seismic slip? A field geologist's opinion. *J. Struct. Geol.* 21 (8-9), 995-1001.
- Dahl, P.S. and Dorais, M.J., 1996. Influence of F(OH)-1 substitution on the relative mechanical strength of rock-forming micas. *J. Geophys. Res.* 101 (B5), 11519-11524.

- Davis, E., Heesemann, M. and Wang, K., 2011. Evidence for episodic aseismic slip across the subduction seismogenic zone off Costa Rica: CORK borehole pressure observations at the subduction prism toe. *Earth Planet. Sci. Lett.* 306 (3-4), 299-305.
- Den Hartog, S.A.M., Niemeijer, A.R. and Spiers, C.J., 2012a. New constraints on megathrust slip stability under subduction zone P-T conditions. *Earth Planet. Sci. Lett.* 353-354, 240-252.
- Den Hartog, S.A.M., Niemeijer, A.R. and Spiers, C.J., submitted. Friction on subduction megathrust faults: beyond the illite-muscovite transition. Submitted to *Earth Planet. Sci. Lett.*
- Den Hartog, S.A.M., Peach, C.J., De Winter, D.A.M., Spiers, C.J. and Shimamoto, T., 2012b. Frictional properties of megathrust fault gouges at low sliding velocities: new data on effects of normal stress and temperature. *J. Struct. Geol.* 38, 156-171.
- Den Hartog, S.A.M. and Spiers, C.J., in press. Influence of subduction zone conditions and gouge composition on frictional slip stability of megathrust faults. *Tectonophysics* DOI:10.1016/j.tecto.2012.11.006.
- Di Toro, G., Hirose, T., Nielsen, S., Pennacchioni, G. and Shimamoto, T., 2006. Natural and experimental evidence of melt lubrication of faults during earthquakes. *Science* 311, 647-649.
- Di Toro, G. et al., 2010. From field geology to earthquake simulation: a new state-of-the-art tool to investigate rock friction during the seismic cycle (SHIVA). *Rend. Fis. Acc. Lincei* 21 (1), 95-114.
- Dieterich, J.H., 1978. Time-dependent friction and the mechanics of stick-slip. *Pure Appl. Geophys.* 116, 790-806.
- Dieterich, J.H., 1979. Modeling of rock friction 1. Experimental results and constitutive equations. *J. Geophys. Res.* 84 (B5), 2161-2168.
- Dieterich, J.H., 1992. Earthquake nucleation on faults with rate- and state-dependent strength. *Tectonophysics* 211 (1-4), 115-134.
- Douglas, A., Beavan, J., Wallace, L. and Townend, J., 2005. Slow slip on the northern Hikurangi subduction interface, New Zealand. *Geophys. Res. Lett.* 32, L16305, DOI:10.1029/2005GL023607.
- Dove, P.M., 1999. The dissolution kinetics of quartz in aqueous mixed cation solutions. *Geochim. et Cosmochim. Acta* 63 (22), 3715-3727.
- Dragert, H., Wang, K. and James, T.S., 2001. A silent slip event on the deeper Cascadia subduction interface. *Science* 292, 1525-1528.
- Faulkner, D.R., Mitchell, T.M., Behnsen, J., Hirose, T. and Shimamoto, T., 2011. Stuck in the mud? Earthquake nucleation and propagation through accretionary forearcs. *Geophys. Res. Lett.* 38 (18), L18303, DOI:10.1029/2011GL048552.
- Folk, R.L., 1962. Petrography and origin of the Silurian Rochester and McKenzie Shales, Morgan County, West Virginia. *J. Sediment Petrol.* 32 (3), 539-578.
- Foucher, J.-P., Henry, P. and Harmegnies, F., 1997. Long-term observations of pressure and temperature in hole 948D, Barbados accretionary prism. *Proc. Ocean Drill. Program Sci. Results* 156, 239-245.
- Frost, H.J. and Ashby, M.F., 1982. Deformation-mechanism maps: the plasticity and creep of metals and ceramics, Pergamon Press, Oxford.
- Gerogiannopoulos, N.G. and Brown, E.T., 1978. The critical state concept applied to rock. *Int. J. rock Mech. Min. Sci. & Geomech. Abstr.* Vol. 15 (1), 1-10.
- Guha-Sapir, D., Vos, F., Below, R. and Ponserre, S., 2012. Annual disaster statistical review 2011: the numbers and trends. Brussels: CRED.
- Harris, J.W. and Stocker, H., 1998. *Handbook of Mathematics and Computational Science*, Springer-Verlag, New York.
- Hart, B.S., Flemings, P.B. and Deshpande, A., 1995. Porosity and pressure: role of compaction disequilibrium in the development of geopressures in a Gulf Coast Pleistocene basin. *Geology* 23 (1), 45-48.
- He, C., Wang, Z. and Yao, W., 2007. Frictional sliding of gabbro gouge under hydrothermal conditions. *Tectonophysics* 445 (3-4), 353-362.
- He, C., Yao, W., Wang, Z. and Zhou, Y., 2006. Strength and stability of frictional sliding of gabbro gouge at elevated temperatures. *Tectonophysics* 427 (1-4), 217-229.
- Hirauchi, K.-I., Den Hartog, S.A.M. and Spiers, C.J., 2012. Weakening of the slab-mantle wedge interface induced by metasomatic growth of talc. *Geology* 41 (1), 75-78.
- Hirose, H., Hirahara, K., Kimata, F., Fujii, N. and Miyazaki, S., 1999. A slow thrust slip event following the two 1996 Hyuganada earthquakes beneath the Bungo Channel, southwest Japan. *Geophys. Res. Lett.* 26 (21), 3237-3240.
- Hirth, G. and Tullis, J., 1994. The brittle-plastic transition in experimentally deformed quartz aggregates. *J.*

- Geophys. Res. 99 (B6), 11731-11747.
- Hori, T., Kato, N., Hirahara, K., Baba, T. and Kaneda, Y., 2004. A numerical simulation of earthquake cycles along the Nankai Trough in southwest Japan: lateral variation in frictional property due to the slab geometry controls the nucleation position. *Earth Planet. Sci. Lett.* 228 (3-4), 215-226.
- Houston, H. and Vidale, J.E., 2007. Relationships in a slow slip. *Nature* 447, 49-50.
- Hower, J., Eslinger, E.V., Hower, M.E. and Perry, E.A., 1976. Mechanism of burial metamorphism of argillaceous sediment: 1. Mineralogical and chemical evidence. *Geol. Soc. Am. Bull.* 87 (5), 725-737.
- Hüpers, A. and Kopf, A.J., 2009. The thermal influence on the consolidation state of underthrust sediments from the Nankai margin and its implications for excess pore pressure. *Earth Planet. Sci. Lett.* 286 (1-2), 324-332.
- Hunziker, J.C., 1986. The evolution of illite to muscovite: an example of the behaviour of isotopes in low-grade metamorphic terrains. *Chem. Geol.* 57 (1-2), 31-40.
- Hyndman, R.D., 2007. The seismogenic zone of subduction thrust faults: what we know and don't know, in: Dixon, T.H. and Moore, J.C. (Eds.), *The Seismogenic Zone of Subduction Thrust Faults*. Columbia University Press, New York, pp. 15-40.
- Hyndman, R.D. and Peacock, S.M., 2003. Serpentinization of the forearc mantle. *Earth Planet. Sci. Lett.* 212 (3-4), 417-432.
- Hyndman, R.D. and Wang, K., 1993. Thermal constraints on the zone of major thrust earthquake failure: the Cascadia subduction zone. *J. Geophys. Res.* 98 (B2), 2039-2060.
- Hyndman, R.D., Yamano, M. and Oleskevich, D.A., 1997. The seismogenic zone of subduction thrust faults. *Isl. Arc* 6 (3), 244-260.
- Ide, S., Baltay, A. and Beroza, G.C., 2011. Shallow dynamic overshoot and energetic deep rupture in the 2011 Mw 9.0 Tohoku-Oki earthquake. *Science* 332, 1426-1429.
- Ide, S., Beroza, G.C., Shelly, D.R. and Uchide, T., 2007. A scaling law for slow earthquakes. *Nature* 447, 76-79.
- Iio, Y., Kobayashi, Y. and Tada, T., 2002. Large earthquakes initiate by the acceleration of slips on the downward extensions of seismogenic faults. *Earth Planet. Sci. Lett.* 202 (2), 337-343.
- Ikari, M.J., Marone, C. and Saffer, D.M., 2011. On the relation between fault strength and frictional stability. *Geology* 39 (1), 83-86.
- Ikari, M.J. and Saffer, D.M., 2011. Comparison of frictional strength and velocity dependence between fault zones in the Nankai accretionary complex. *Geochem. Geophys. Geosy.* 12, Q0AD11, DOI:10.1029/2010GC003442.
- Ikari, M.J., Saffer, D.M. and Marone, C., 2007. Effect of hydration state on the frictional properties of montmorillonite-based fault gouge. *J. Geophys. Res.* 112, B06423, DOI:10.1029/2006JB004748.
- Ikari, M.J., Saffer, D.M. and Marone, C., 2009a. Frictional and hydrologic properties of a major splay fault system, Nankai subduction zone. *Geophys. Res. Lett.* 36 (20), L20313, DOI:10.1029/2009GL040009.
- Ikari, M.J., Saffer, D.M. and Marone, C., 2009b. Frictional and hydrologic properties of clay-rich fault gouge. *J. Geophys. Res.* 114, B05409, DOI:10.1029/2008JB006089.
- Ikesawa, E. et al., 2005. Tectonic incorporation of the upper part of oceanic crust to overriding plate of a convergent margin: an example from the Cretaceous-early Tertiary Mugi Mélange, the Shimanto Belt, Japan. *Tectonophysics* 401, 217-230.
- Israelachvili, J.N., 1986. Measurement of the viscosity of liquids in very thin films. *J. Colloid Interf. Sci.* 110 (1), 263-271.
- Ito, Y. and Obara, K., 2006. Very low frequency earthquakes within accretionary prisms are very low stress-drop earthquakes. *Geophys. Res. Lett.* 33, L09302, DOI:10.1029/2006GL025883.
- Jennings, S. and Thompson, G.R., 1986. Diagenesis of Plio-Pleistocene sediments of the Colorado River delta, Southern California. *Jour. Sed. Petrology* 56 (1), 89-98.
- Kameda, J. et al., 2012. Silica diagenesis and its effect on interplate seismicity in cold subduction zones. *Earth Planet. Sci. Lett.* 317-318, 136-144.
- Kameda, J., Raimbourg, H., Kogure, T. and Kimura, G., 2011. Low-grade metamorphism around the down-dip limit of seismogenic subduction zones: example from an ancient accretionary complex in the Shimanto Belt, Japan. *Tectonophysics* 502 (3-4), 383-392.
- Kanagawa, K., Cox, S.F. and Zhang, S., 2000. Effects of dissolution-precipitation processes on the strength and mechanical behavior of quartz gouge at high-temperature hydrothermal conditions. *J. Geophys. Res.* 105 (B5), 11115-11126.

- Kanamori, H. and Cipar, J.J., 1974. Focal process of the great Chilean earthquake May 22, 1960. *Phys. Earth Plan. In.* 9 (2), 128-136.
- Kaneko, Y. and Lapusta, N., 2008. Variability of earthquake nucleation in continuum models of rate-and-state faults and implications for aftershock rates. *J. Geophys. Res.* 113, B12312, DOI:10.1029/2007JB005154.
- Kastner, M., Elderfield, H. and Martin, J.B., 1991. Fluids in Convergent Margins: What do We Know about their Composition, Origin, Role in Diagenesis and Importance for Oceanic Chemical Fluxes? *Philos. Trans. R. Soc. Lond. Ser. A* 335 (1638), 243-259.
- Kato, A. et al., 2010. Variations of fluid pressure within the subducting oceanic crust and slow earthquakes. *Geophys. Res. Lett.* 37, L14310, DOI:10.1029/2010GL043723.
- Kato, A. et al., 2012. Propagation of slow slip leading up to the 2011 Mw 9.0 Tohoku-Oki earthquake. *Science* 335, 705-708.
- Kato, N., 2003. A possible model for large preseismic slip on a deeper extension of a seismic rupture plane. *Earth Planet. Sci. Lett.* 216, 17-25.
- Kato, N. and Yoshida, S., 2011. A shallow strong patch model for the 2011 great Tohoku-oki earthquake: A numerical simulation. *Geophys. Res. Lett.* 38 (15), L15305, 10.1029/2011GL048565.
- Kawamoto, E. and Shimamoto, T., 1997. Mechanical behavior of halite and calcite shear zones from brittle to fully-plastic deformation and a revised fault model, in: Zheng, Y., Davis, G.A. and Yin, A. (Eds.), *Proceedings of the 30th International Geological Congress*, pp. 89-105.
- Kawamoto, E. and Shimamoto, T., 1998. The strength profile for biminerale shear zones: an insight from high-temperature shearing experiments on calcite-halite mixtures. *Tectonophysics* 295 (1-2), 1-14.
- Kimura, G. and Ludden, J., 1995. Peeling oceanic crust in subduction zones. *Geology* 23 (3), 217-220.
- Kimura, G., Sreaton, E.J. and Curewitz, D., 2007. NanTroSEIZE Stage 1: NanTroSEIZE shallow megasplay and frontal thrusts. *IODP Sci. Prosp.* 316, DOI: 10.2204/iodp.sp.316.2007.
- Kitajima, H. and Saffer, D.M., 2012. Elevated pore pressure and anomalously low stress in regions of low frequency earthquakes along the Nankai Trough subduction megathrust. *Geophys. Res. Lett.* 39 (23), L23301, DOI:10.1029/2012GL053793.
- Kitamura, Y. and Kimura, G., 2012. Dynamic role of tectonic mélange during interseismic process of plate boundary mega earthquakes. *Tectonophysics* 568-569, 39-52.
- Kodaira, S. et al., 2004. High pore fluid pressure may cause silent slip in the Nankai Trough. *Science* 304, 1295-1298.
- Koketsu, K. et al., 2011. A unified source model for the 2011 Tohoku earthquake. *Earth Planet. Sci. Lett.* 310 (3-4), 480-487.
- Kopf, A. and Brown, K.M., 2003. Friction experiments on saturated sediments and their implications for the stress state of the Nankai and Barbados subduction thrusts. *Mar. Geol.* 202 (3), 193-210.
- Kronenberg, A.K., Kirby, S.H. and Pinkston, J., 1990. Basal slip and mechanical anisotropy of biotite. *J. Geophys. Res.* 95 (B12), 19257-19278.
- Lay, T. et al., 2005. The great Sumatra-Andaman earthquake of 26 December 2004. *Science* 308, 1127-1133.
- Lehner, F.K., 1990. Thermodynamics of rock deformation by pressure solution, in: Barber, D. and Meredith, P. (Eds.), *Deformation Processes in Minerals, Ceramics and Rocks*. Unwin Hyman, London, pp. 296-333.
- Lemmon, E.W., Huber, M.L. and McLinden, M.O., 2010. NIST Standard Reference Database 23: Reference Fluid Thermodynamic and Transport Properties-REFPROP, Version 9.0, National Institute of Standards and Technology, standard reference data program, Gaithersburg.
- Linde, A.T. and Sacks, I.S., 2002. Slow earthquakes and great earthquakes along the Nankai trough. *Earth Planet. Sci. Lett.* 203, 265-275.
- Linde, A.T., Suyehiro, K., Miura, S., Sacks, I.S. and Takagi, A., 1988. Episodic aseismic earthquake precursors. *Nature* 334, 513-515.
- Liu, Y. and Rice, J.R., 2005. Aseismic slip transients emerge spontaneously in three-dimensional rate and state modeling of subduction earthquake sequences. *J. Geophys. Res.* 110, B08307, DOI:10.1029/2004JB003424.
- Liu, Y. and Rice, J.R., 2007. Spontaneous and triggered aseismic deformation transients in a subduction fault model. *J. Geophys. Res.* 112, B09404, DOI:10.1029/2007JB004930.
- Liu, Y. and Rice, J.R., 2009. Slow slip predictions based on granite and gabbro friction data compared to GPS measurements in northern Cascadia. *J. Geophys. Res.* 114, B09407, DOI:10.1029/2008JB006142.
- Logan, J.M., Dengo, C.A., Higgs, N.G. and Wang, Z.Z., 1992. Fabrics of experimental fault zones: their

- development and relationship to mechanical behavior, in: Evans, B., Wong, T.-F. and Brace, W.F. (Eds.), *Fault Mechanics and Transport Properties of Rocks*. Academic Press, London, pp. 33-67.
- Logan, J.M. and Rauenzahn, K.A., 1987. Frictional dependence of gouge mixtures of quartz and montmorillonite on velocity, composition and fabric. *Tectonophysics* 144 (1-3), 87-108.
- Lowry, A.R., Larson, K.M., Kostoglodov, V. and Bilham, R., 2001. Transient fault slip in Guerrero, southern Mexico. *Geophys. Res. Lett.* 28 (19), 3753-3756.
- Lupini, J.F., Skinner, A.E. and Vaughan, P.R., 1981. The drained residual strength of cohesive soils. *Geotechnique* 31 (2), 181-213.
- Mackenzie, R.C. (Editor), 1957. *The differential thermal analysis of clays*. Mineralogical Society (Clay Minerals Group), London.
- Mares, V.M. and Kronenberg, A.K., 1993. Experimental deformation of muscovite. *J. Struct. Geol.* 15 (9-10), 1061-1075.
- Mariani, E., Brodie, K.H. and Rutter, E.H., 2006. Experimental deformation of muscovite shear zones at high temperatures under hydrothermal conditions and the strength of phyllosilicate-bearing faults in nature. *J. Struct. Geol.* 28 (9), 1569-1587.
- Marone, C., 1998. Laboratory-derived friction laws and their application to seismic faulting. *Annu. Rev. Earth Planet. Sci.* 26, 643-696.
- Marone, C. and Saffer, D.M., 2007. Fault friction and the upper transition from seismic to aseismic faulting, in: Dixon, T.H. and Moore, J.C. (Eds.), *The Seismogenic Zone of Subduction Thrust Faults*. Columbia University Press, New York, pp. 346-369.
- Marone, C. and Scholz, C.H., 1988. The depth of seismic faulting and the upper transition from stable to unstable slip regimes. *Geophys. Res. Lett.* 15 (6), 621-624.
- Masel, R.L., 1996. *Principles of adsorption and reaction on solid surfaces*, John Wiley & Sons Inc., New York.
- Matsuzawa, T., Hirose, H., Shibazaki, B. and Obara, K., 2010. Modeling short- and long-term slow slip events in the seismic cycles of large subduction earthquakes. *J. Geophys. Res.* 115, B12301, DOI:10.1029/2010JB007566.
- Mazzotti, S. and Adams, J., 2004. Variability of near-term probability for the next great earthquake on the Cascadia subduction zone. *B. Seismol. Soc. Am.* 94 (5), 1954-1959.
- McCaffrey, R., Wallace, L.M. and Beavan, J., 2008. Slow slip and frictional transition at low temperature at the Hikurangi subduction zone. *Nat. Geosci.* 1 (5), 316-320.
- Meneghini, F. and Moore, J.C., 2007. Deformation and hydrofracture in a subduction thrust at seismogenic depths: the Rodeo Cove thrust zone, Marin Headlands, California. *Geol. Soc. America Bull.* 119 (1), 174-183.
- Merriman, R.J., 2002. Contrasting clay mineral assemblages in British Lower Palaeozoic slate belts: the influence of geotectonic setting. *Clay Miner.* 37, 207-219.
- Merriman, R.J. and Frey, M., 1999. Patterns of very low-grade metamorphism in metapelitic rocks, in: Frey, M. and Robinson, D. (Eds.), *Low-Grade Metamorphism*. Blackwell Science, Oxford, pp. 61-107.
- Merriman, R.J. and Peacor, D.R., 1999. Very low-grade metapelites: mineralogy, microfabrics and measuring reaction progress, in: Frey, M. and Robinson, D. (Eds.), *Low-Grade Metamorphism*. Blackwell Science, Oxford, pp. 10-60.
- Meunier, A., 2005. *Clays*, Springer, Berlin.
- Meunier, A. and Velde, B., 2004. *Illite*, Springer-Verlag, Berlin.
- Miller, M.M., Melbourne, T., Johnson, D.J. and Sumner, W.Q., 2002. Periodic slow earthquakes from the Cascadia subduction zone. *Science* 295, 2423.
- Mitsui, N. and Hirahara, K., 2006. Slow slip events controlled by the slab dip and its lateral change along a trench. *Earth Planet. Sci. Lett.* 245 (1-2), 344-358.
- Mogi, K., 1984. Temporal variation of crustal deformation during the days preceding a thrust-type great earthquake — The 1944 Tonankai earthquake of magnitude 8.1, Japan. *Pure Appl. Geophys.* 122 (6), 765-780.
- Moore, D.E. and Lockner, D.A., 2004. Crystallographic controls on the frictional behavior of dry and water-saturated sheet structure minerals. *J. Geophys. Res.* 109, B03401, DOI:10.1029/2003JB002582.
- Moore, D.E. and Lockner, D.A., 2008. Talc friction in the temperature range 25°-400 °C: relevance for fault-zone weakening. *Tectonophysics* 449 (1-4), 120-132.
- Moore, D.E. and Lockner, D.A., 2011. Frictional strengths of talc-serpentine and talc-quartz mixtures. *J.*

- Geophys. Res. 116, B01403, DOI:10.1029/2010JB007881
- Moore, D.E., Summers, R. and Byerlee, J.D., 1986a. The effects of sliding velocity on the frictional and physical properties of heated fault gouge. *Pure Appl. Geophys.* 124 (1), 31-52.
- Moore, D.E., Summers, R. and Byerlee, J.D., 1986b. Strength measurements of heated illite gouge at low and high pore pressures. U.S. Geological Survey Open File Report 86-578.
- Moore, D.E., Summers, R. and Byerlee, J.D., 1989. Sliding behavior and deformation textures of heated illite gouge. *J. Struct. Geol.* 11 (3), 329-342.
- Moore, J.C., 1989. Tectonics and hydrogeology of accretionary prisms: role of the décollement zone. *J. Struct. Geol.* 11 (1-2), 95-106.
- Moore, J.C., Rowe, C.D. and Meneghini, F., 2007. How accretionary prisms elucidate seismogenesis in subduction zones, in: Dixon, T.H. and Moore, J.C. (Eds.), *The Seismogenic Zone of Subduction Thrust Faults*. Columbia University Press, New York, pp. 288-315.
- Moore, J.C. and Saffer, D.M., 2001. Updip limit of the seismogenic zone beneath the accretionary prism of southwest Japan: an effect of diagenetic to low-grade metamorphic processes and increasing effective stress. *Geology* 29 (2), 183-186.
- Moore, J.C. and Vrolijk, P., 1992. Fluids in accretionary prisms. *Rev. Geophys.* 30 (2), 113-135.
- Morrow, C.A., Moore, D.E. and Lockner, D.A., 2000. The effect of mineral bond strength and adsorbed water on fault gouge frictional strength. *Geophys. Res. Lett.* 27 (6), 815-818.
- Morrow, C.A., Radney, B. and Byerlee, J., 1992. Frictional strength and the effective pressure law of montmorillonite and illite clays, in: Evans, B., Wong, T.-F. and Brace, W.F. (Eds.), *Fault Mechanics and Transport Properties of Rocks*. Academic Press, London, pp. 69-88.
- Morrow, C.A., Shi, L.Q. and Byerlee, J.D., 1982. Strain hardening and strength of clay-rich fault gouges. *J. Geophys. Res.* 87 (B8), 6771-6780.
- Nakatani, M., 2001. Conceptual and physical clarification of rate and state friction: Frictional sliding as a thermally activated rheology. *J. Geophys. Res.* 106 (B7), 13347-13380.
- National Geophysical Data Center, 2012.
- Niemeijer, A., Marone, C. and Elsworth, D., 2010. Fabric induced weakness of tectonic faults. *Geophys. Res. Lett.* 37 (3), L03304, DOI:10.1029/2009GL041689.
- Niemeijer, A.R. and Spiers, C.J., 2005. Influence of phyllosilicates on fault strength in the brittle-ductile transition: insights from rock analogue experiments. *Geol. Soc. Spec. Publ.* 245, 303-327.
- Niemeijer, A.R. and Spiers, C.J., 2006. Velocity dependence of strength and healing behaviour in simulated phyllosilicate-bearing fault gouge. *Tectonophysics* 427 (1-4), 231-253.
- Niemeijer, A.R. and Spiers, C.J., 2007. A microphysical model for strong velocity weakening in phyllosilicate-bearing fault gouges. *J. Geophys. Res.* 112, B10405, DOI:10.1029/2007JB005008.
- Niemeijer, A.R., Spiers, C.J. and Bos, B., 2002. Compaction creep of quartz sand at 400-600°C: experimental evidence for dissolution-controlled pressure solution. *Earth Planet. Sci. Lett.* 195, 261-275.
- Niemeijer, A.R., Spiers, C.J. and Peach, C.J., 2008. Frictional behaviour of simulated quartz fault gouges under hydrothermal conditions: results from ultra-high strain rotary shear experiments. *Tectonophysics* 460, 288-303.
- Noda, H. and Shimamoto, T., 2009. Constitutive properties of clayey fault gouge from the Hanaore fault zone, southwest Japan. *J. Geophys. Res.* 114, B04409, DOI:10.1029/2008JB005683.
- Obana, K. and Kodaira, S., 2009. Low-frequency tremors associated with reverse faults in a shallow accretionary prism. *Earth Planet. Sci. Lett.* 287 (1-2), 168-174.
- Obara, K., Hirose, H., Yamamizu, F. and Kasahara, K., 2004. Episodic slow slip events accompanied by non-volcanic tremors in southwest Japan subduction zone. *Geophys. Res. Lett.* 31, L23602, DOI:10.1029/2004GL020848.
- Ohta, Y., Freymueller, J.T., Hreinsdóttir, S. and Suito, H., 2006. A large slow slip event and the depth of the seismogenic zone in the south central Alaska subduction zone. *Earth Planet. Sci. Lett.* 247 (1-2), 108-116.
- Oleskevich, D.A., Hyndman, R.D. and Wang, K., 1999. The updip and downdip limits to great subduction earthquakes: thermal and structural models of Cascadia, south Alaska, SW Japan, and Chile. *J. Geophys. Res.* 104 (B7), 14965-14992.
- Outerbridge, K.C. et al., 2010. A tremor and slip event on the Cocos-Caribbean subduction zone as measured by a global positioning system (GPS) and seismic network on the Nicoya Peninsula, Costa Rica. *J. Geophys. Res.* 115, B10408, DOI:10.1029/2009JB006845.

- Ozawa, S. et al., 2011. Coseismic and postseismic slip of the 2011 magnitude-9 Tohoku-Oki earthquake. *Nature* 475, 373-376.
- Passchier, C.W. and Trouw, R.A.J., 2005. *Microtectonics*, 2nd ed. Springer, Berlin.
- Paterson, M.S., 1995. A theory for granular flow accommodated by material transfer via an intergranular fluid. *Tectonophysics* 245 (3-4), 135-151.
- Paterson, M.S. and Wong, T.-F., 2005. *Experimental Rock Deformation - the Brittle Field*, 2nd ed. Springer, Berlin.
- Peacock, S.M., 2009. Thermal and metamorphic environment of subduction zone episodic tremor and slip. *J. Geophys. Res.* 114, B00A07, DOI:10.1029/2008JB005978.
- Peacock, S.M. and Hyndman, R.D., 1999. Hydrous minerals in the mantle wedge and the maximum depth of subduction thrust earthquakes. *Geophys. Res. Lett.* 26 (16), 2517-2520.
- Peacock, S.M. and Wang, K., 1999. Seismic consequences of warm versus cool subduction metamorphism: examples from southwest and northeast Japan. *Science* 286, 937-939.
- Peng, Z. and Gombert, J., 2010. An integrated perspective of the continuum between earthquakes and slow-slip phenomena. *Nat. Geosci.* 3 (9), 599-607.
- Perfettini, H. and Ampuero, J.-P., 2008. Dynamics of a velocity strengthening fault region: implications for slow earthquakes and postseismic slip. *J. Geophys. Res.* 113, B09411, DOI:10.1029/2007JB005398.
- Plafker, G., 1965. Tectonic deformation associated with the 1964 Alaska earthquake. *Science* 148, 1675-1687.
- Plafker, G. and Savage, J.C., 1970. Mechanism of the Chilean Earthquakes of May 21 and 22, 1960. *Geol. Soc. America Bull.* 81 (4), 1001-1030.
- Pritchard, M.E. and Simons, M., 2006. An aseismic pulse in northern Chile and along-strike variations in seismogenic behavior. *J. Geophys. Res.* 111, B08405, DOI:10.1029/2006JB004258.
- Pytte, A.M. and Reynolds, R.C., 1988. The thermal transformation of smectite to illite, in: McCulloh, T.H. and Naeser, N.D. (Eds.), *Thermal histories of sedimentary basins*. Springer, New York, pp. 133-140.
- Raj, R., 1982. Creep in Polycrystalline Aggregates by Matter Transport Through a Liquid Phase. *J. Geophys. Res.* 87 (B6), 4731-4739.
- Ramsay, J.G. and Huber, M.I., 1983. *The techniques of modern structural geology, Volume 1: Strain analysis*, Academic Press, London.
- Rice, J.R., 1983. Constitutive relations for fault slip and earthquake instabilities. *Pure Appl. Geophys.* 121 (3), 443-475.
- Rice, J.R., Lapusta, N. and Ranjith, K., 2001. Rate and state dependent friction and the stability of sliding between elastically deformable solids. *J. Mech. Phys. Solids* 49 (9), 1865-1898.
- Rieder, M. et al., 1998. Nomenclature of the micas. *Can. Mineral.* 36, 41-48.
- Rimstidt, J.D. and Barnes, H.L., 1980. The kinetics of silica-water reactions. *Geochim. Cosmochim. Ac.* 44 (11), 1683-1699.
- Rogers, G. and Dragert, H., 2003. Episodic tremor and slip on the Cascadia subduction zone: the chatter of silent slip. *Science* 300, 1942-1943.
- Rowe, C.D., Meneghini, F. and Moore, J.C., 2009. Fluid-rich damage zone of an ancient out-of-sequence thrust, Kodiak Islands, Alaska. *Tectonics* 28, TC1006, DOI:10.1029/2007TC002126.
- Rubin, A.M. and Ampuero, J.P., 2005. Earthquake nucleation on (aging) rate and state faults. *J. Geophys. Res.* 110, B11312, DOI:10.1029/2005JB003686.
- Ruina, A., 1983. Slip instability and state variable friction laws. *J. Geophys. Res.* 88 (B12), 10359-10370.
- Rutter, E.H., 1976. The kinetics of rock deformation by pressure solution. *Phil. Trans. R. Soc. Lond.* 283, 203-219.
- Rutter, E.H., 1983. Pressure solution in nature, theory and experiment. *J. Geol. Soc. London* 140 (5), 725-740.
- Rutter, E.H. and Brodie, K.H., 2004. Experimental intracrystalline plastic flow in hot-pressed synthetic quartzite prepared from Brazilian quartz crystals. *J. Struct. Geol.* 26 (2), 259-270.
- Rutter, E.H. and Glover, C.T., 2012. The deformation of porous sandstones; are Byerlee friction and the critical state line equivalent? *J. Struct. Geol.* 44, 129-140.
- Rutter, E.H. and Mainprice, D.H., 1978. The effect of water on stress relaxation of faulted and unfaulted sandstone. *Pure Appl. Geophys.* 116 (4-5), 634-654.
- Saffer, D.M., Frye, K.M., Marone, C. and Mair, K., 2001. Laboratory Results Indicating Complex and Potentially Unstable Frictional Behavior of Smectite Clay. *Geophys. Res. Lett.* 28 (12), 2297-2300.
- Saffer, D.M., Lockner, D.A. and McKiernan, A., 2012. Effects of smectite to illite transformation on the

- frictional strength and sliding stability of intact marine mudstones. *Geophys. Res. Lett.* 39 (11), L11304, DOI:10.1029/2012GL051761.
- Saffer, D.M. and Marone, C., 2003. Comparison of smectite- and illite-rich gouge frictional properties: application to the updip limit of the seismogenic zone along subduction megathrusts. *Earth Planet. Sci. Lett.* 215 (1-2), 219-235.
- Saffer, D.M. and Tobin, H.J., 2011. Hydrogeology and mechanics of subduction zone forearcs: fluid flow and pore pressure. *Annu. Rev. Earth Planet. Sci.* 39, 157-186.
- Sagiya, T., 2004. Interplate coupling in the Kanto district, central Japan, and the Boso peninsula silent earthquake in May 1996. *Pure Appl. Geophys.* 161 (11-12), 2327-2342.
- Scholz, C., 1988. The brittle-plastic transition and the depth of seismic faulting. *Geol. Rundsch.* 77 (1), 319-328.
- Scholz, C.H., 1998. Earthquakes and friction laws. *Nature* 391, 37-42.
- Scholz, C.H., 2002. The mechanics of earthquakes and faulting, second ed. Cambridge University Press, Cambridge.
- Schutjens, P.M.T.M., 1991. Experimental compaction of quartz sand at low effective stress and temperature conditions. *J. Geol. Soc. London* 148, 527-539.
- Schwartz, S.Y. and Rokosky, J.M., 2007. Slow slip events and seismic tremor at circum-Pacific subduction zones. *Rev. Geophys.* 45, RG3004, DOI:10.1029/2006RG000208.
- Scruggs, V.J. and Tullis, T.E., 1998. Correlation between velocity dependence of friction and strain localization in large displacement experiments on feldspar, muscovite and biotite gouge. *Tectonophysics* 295 (1-2), 15-40.
- Segall, P. and Rice, J.R., 2006. Does shear heating of pore fluid contribute to earthquake nucleation? *J. Geophys. Res.* 111, B09316, DOI:10.1029/2005JB004129.
- Segall, P., Rubin, A.M., Bradley, A.M. and Rice, J.R., 2010. Dilatant strengthening as a mechanism for slow slip events. *J. Geophys. Res.* 115, B12305, DOI:10.1029/2010JB007449.
- Seno, T., 2009. Determination of the pore fluid pressure ratio at seismogenic megathrusts in subduction zones: Implications for strength of asperities and Andean-type mountain building. *J. Geophys. Res.* 114, B05405, DOI:10.1029/2008JB005889.
- Shelly, D.R., Beroza, G.C., Ide, S. and Nakamura, S., 2006. Low-frequency earthquakes in Shikoku, Japan, and their relationship to episodic tremor and slip. *Nature* 442, 188-191.
- Shibazaki, B., Bu, S., Matsuzawa, T. and Hirose, H., 2010. Modeling the activity of short-term slow slip events along deep subduction interfaces beneath Shikoku, southwest Japan. *J. Geophys. Res.* 115, B00A19, DOI:10.1029/2008JB006057.
- Shibazaki, B. and Iio, Y., 2003. On the physical mechanism of silent slip events along the deeper part of the seismogenic zone. *Geophys. Res. Lett.* 30 (9), 1489, DOI:10.1029/2003GL017047.
- Shibazaki, B. et al., 2011. 3D modeling of the cycle of a great Tohoku-oki earthquake, considering frictional behavior at low to high slip velocities. *Geophys. Res. Lett.* 38 (21), L21305, DOI:10.1029/2011GL049308.
- Shibazaki, B. and Shimamoto, T., 2007. Modelling of short-interval silent slip events in deeper subduction interfaces considering the frictional properties at the unstable-stable transition regime. *Geophys. J. Int.* 171, 191-205.
- Shimamoto, T., 1986. Transition between frictional slip and ductile flow for halite shear zones at room temperature. *Science* 231, 711-714.
- Shipboard Scientific Party, 2000. Leg 190 Preliminary Report: deformation and fluid flow processes in the Nankai Trough and accretionary prism. ODP Prelim. Rpt 190.
- Shipboard Scientific Party, 2001a. Leg 190 Summary, in: Moore, G.F., Taira, A. and Klaus, A. (Eds.), *Proceedings of the Ocean Drilling Program, Initial Reports*. College Station, TX (Ocean Drilling Program), pp. 1-87.
- Shipboard Scientific Party, 2001b. Site 1174, in: Moore, G.F., Taira, A. and Klaus, A. (Eds.), *Proceedings of the Ocean Drilling Program, Initial Reports*. College Station, TX (Ocean Drilling Program), pp. 1-149.
- Shipboard Scientific Party, 2003. Leg 205 Summary, in: Morris, J.D., Villinger, H.W. and Klaus, A. (Eds.), *Proceedings of the Ocean Drilling Program, Initial Reports*. College Station, TX (Ocean Drilling Program), pp. 1-75.
- Sibson, R.H., 1981. Fluid flow accompanying faulting: field evidence and models, *Earthquake Prediction: An International Review*, 4. AGU, Washington, DC, pp. 593-603.
- Simons, M. et al., 2011. The 2011 magnitude 9.0 Tohoku-Oki earthquake: mosaicking the megathrust from seconds to centuries. *Science* 332, 1421-1425.

- Song, T.-R.A. et al., 2009. Subducting slab ultra-slow velocity layer coincident with silent earthquakes in southern Mexico. *Science* 324, 502-506.
- Spiers, C.J., De Meer, S., Niemeijer, A.R. and Zhang, X., 2004. Kinetics of rock deformation by pressure solution and the role of thin aqueous films, in: Nakashima, S., Spiers, C.J., Mercury, L., Fenter, P.A. and Hochella, M.F., Jr. (Eds.), *Physicochemistry of water in geological and biological systems - structures and properties of thin aqueous films*. Universal Academy Press, Tokyo, pp. 129-158.
- Spiers, C.J. and Schutjens, P.M.T.M., 1990. Densification of crystalline aggregates by fluid-phase diffusional creep, in: Barber, D. and Meredith, P. (Eds.), *Deformation Processes in Minerals, Ceramics and Rocks*. Unwin Hyman, London, pp. 334-353.
- Spinelli, G.A. and Underwood, M.B., 2004. Character of sediments entering the Costa Rica subduction zone: Implications for partitioning of water along the plate interface. *The Island Arc* 13 (3), 432-451.
- Spinelli, G.A. and Wang, K., 2008. Effects of fluid circulation in subducting crust on Nankai margin seismogenic zone temperatures. *Geology* 36 (11), 887-890.
- Steurer, J.F. and Underwood, M.B., 2003. Clay mineralogy of mudstones from the Nankai Trough reference sites 1173 and 1177 and frontal accretionary prism site 1174, in: Mikada, H. et al. (Eds.), *Proceedings of the Ocean Drilling Program, Scientific Results*, pp. 1-37.
- Suito, H. and Freymueller, J.T., 2009. A viscoelastic and afterslip postseismic deformation model for the 1964 Alaska earthquake. *J. Geophys. Res.* 114, B11404, DOI:10.1029/2008JB005954.
- Tanikawa, W. et al., 2012. Velocity dependence of shear-induced permeability associated with frictional behavior in fault zones of the Nankai subduction zone. *J. Geophys. Res.* 117, B05405, DOI:10.1029/2011JB008956.
- Tembe, S., Lockner, D. and Wong, T.-F., 2009. Constraints on the stress state of the San Andreas Fault with analysis based on core and cuttings from San Andreas Fault Observatory at Depth (SAFOD) drilling phases 1 and 2. *J. Geophys. Res.* 114, B11401, DOI:10.1029/2008JB005883.
- Tembe, S., Lockner, D.A. and Wong, T.-F., 2010. Effect of clay content and mineralogy on frictional sliding behavior of simulated gouges: binary and ternary mixtures of quartz, illite and montmorillonite. *J. Geophys. Res.* 115, B03416, DOI:10.1029/2009JB006383.
- Tester, J.W., Worley, W.G., Robinson, B.A., Grigsby, C.O. and Feerer, J.L., 1994. Correlating quartz dissolution kinetics in pure water from 25 to 625°C. *Geochim. Cosmochim. Ac.* 58 (11), 2407-2420.
- Thomas, A.M., Bürgmann, R., Shelly, D.R., Beeler, N.M. and Rudolph, M.L., 2012. Tidal triggering of low frequency earthquakes near Parkfield, California: Implications for fault mechanics within the brittle-ductile transition. *J. Geophys. Res.* 117, B05301, DOI:10.1029/2011JB009036.
- Tichelaar, B.W. and Ruff, L.J., 1993. Depth of Seismic Coupling Along Subduction Zones. *J. Geophys. Res.* 98 (B2), 2017-2037.
- Tsutsumi, A., Fabbri, O., Karpoff, A.M., Ujiie, K. and Tsujimoto, A., 2011. Friction velocity dependence of clay-rich fault material along a megasplay fault in the Nankai subduction zone at intermediate to high velocities. *Geophys. Res. Lett.* 38 (19), L19301, DOI:10.1029/2011GL049314.
- Tullis, T.E., 1988. Rock friction constitutive behavior from laboratory experiments and its implications for an earthquake prediction field monitoring program. *Pure Appl. Geophys.* 126 (2), 555-588.
- Ujiie, K. and Tsutsumi, A., 2010. High-velocity frictional properties of clay-rich fault gouge in a megasplay fault zone, Nankai subduction zone. *Geophys. Res. Lett.* 37 (24), L24310, DOI:10.1029/2010GL046002.
- Underwood, M.B., 2007. Sediment inputs to subduction zones, in: Dixon, T.H. and Moore, J.C. (Eds.), *The Seismogenic Zone of Subduction Thrust Faults*. Columbia University Press, New York, pp. 42-85.
- Underwood, M.B. and Deng, X., 1997. Clay mineralogy and clay geochemistry in the vicinity of the décollement zone, northern Barbados Ridge. *Proc. Ocean Drill. Program Sci. Results* 156, 3-30.
- Underwood, M.B., Pickering, K.T., Gieskes, J.M., Kastner, M. and Orr, R., 1993. Sediments geochemistry, clay mineralogy, and diagenesis: a synthesis of data from Leg 131, Nankai Trough, in: Hill, I.A., Taira, A. and Firth, J.V. (Eds.), *Proceedings of the Ocean Drilling Program, Scientific Results*, pp. 343-363.
- Van de Kamp, P.C., 2008. Smectite-illite-muscovite transformations, quartz dissolution, and silica release in shales. *Clay Clay Miner.* 56, 66-81.
- Van Diggelen, E.W.E., De Bresser, J.H.P., Peach, C.J. and Spiers, C.J., 2010. High shear strain behaviour of synthetic muscovite fault gouges under hydrothermal conditions. *J. Struct. Geol.* 32, 1685-1700.
- Verberne, B.A., He, C. and Spiers, C.J., 2010. Frictional properties of sedimentary rocks and natural fault gouge from the Longmenshan Fault Zone, Sichuan, China. *B. Seismol. Soc. Am.* 100 (5B), 2767-2790.
- Vrolijk, P., 1990. On the mechanical role of smectite in subduction zones. *Geology* 18 (8), 703-707.

-
- Wagner, W. and Pruss, A., 2002. The IAPWS formulation 1995 for the thermodynamic properties of ordinary water substance for general and scientific use. *J. Phys. Chem. Ref. Data* 31, 387-535.
- Walther, J.V. and Helgeson, H.C., 1977. Calculation of the thermodynamic properties of aqueous silica and the solubility of quartz and its polymorphs at high pressures and temperatures. *Am. J. Sci.* 277 (10), 1315-1351.

Samenvatting

De grootste en meest destructieve aardbevingen op Aarde ontstaan op plaatsen waar de ene tektonische plaat of aardschol onder de andere beweegt in een zogenaamde subductiezone (zie Figuur 1.1). Dit gebeurt langs een mega-breuk of, preciezer, een mega-opschuiving. Een mega-aardbeving, zeker wanneer deze leidt tot een tsunami, is desastreus, zowel wat betreft het menselijk leed als de gevolgen voor het milieu en de economie. Recente voorbeelden van aardbevingen met gerelateerde tsunami's zijn die in Sumatra in december 2004 en de Tohoku-Okai aardbeving in Japan in maart 2011. De impact van deze natuurrampen heeft het besef doen toenemen dat het cruciaal is om het risico op aardbevingen langs mega-opschuivingen en daaraan gerelateerde tsunami's goed in te kunnen schatten. Om dit te kunnen doen is het noodzakelijk om te weten welke processen er ten grondslag liggen aan het ontstaan van aardbevingen.

Eén manier om inzicht te krijgen in de processen die leiden tot mega-aardbevingen is het doen van laboratoriumexperimenten. Het doel van zulke experimenten is het bepalen van het wrijvingsgedrag van breukgesteenten onder de verplaatsingssnelheden waarbij aardbevingen ontstaan. Het is bekend dat het wrijvingsgedrag afhangt van verschillende factoren, zoals de samenstelling van het gesteente en de druk en temperatuur condities waaronder de experimenten uitgevoerd worden. Het is daarom belangrijk dat experimenten die tot doel hebben om inzicht te krijgen in het ontstaan van mega-aardbevingen gedaan worden op de juiste materialen en onder de juiste condities. Dit was tot nu toe veelal niet het geval, met name omdat het technisch een uitdaging is om de hoge temperatuur en druk condities die heersen op de dieptes waar aardbevingen ontstaan – de *in situ* *P-T* condities – in het laboratorium na te bootsen. In het onderzoek omschreven in dit proefschrift wordt gebruik gemaakt van een unieke machine, de *ring shear machine* (ringwrijvingsmachine) in het hoge druk en temperatuur laboratorium van Universiteit Utrecht, waarmee de *in situ* *P-T* condities wel kunnen worden nagebootst. De resultaten beschreven in dit proefschrift leveren zodoende een belangrijke bijdrage aan de kennis van de wrijvingseigenschappen van breuken waarlangs mega-aardbevingen plaats kunnen vinden.

Beweging langs het breukvlak leidt tot vermaling van het breukgesteente zodat er fijn verpoederd materiaal ontstaat, zogenaamd breukmeel. Experimenten worden dan ook vaak gedaan op zulk breukmeel. Dit materiaal wordt in een wrijvingsexperiment tussen twee (stalen of stenen) cylinders (of blokken) aangebracht en die cylinders worden vervolgens op elkaar geperst, oftewel, onder druk gezet. Deze druk bootst de druk als gevolg van het bovenliggende gesteente in de Aarde na. Vervolgens worden één van de cylinders langs de andere geroteerd en de kracht die hier voor nodig is, in combinatie met de uitgeoefende druk, is een maat voor de wrijvingsweerstand van het breukmeel. Van cruciaal belang voor het ontstaan van een aardbeving is het effect dat een verandering in de rotatiesnelheid van de cylinder heeft op de wrijvingsweerstand. Een aardbeving, oftewel onstabiel gedrag, kan alleen ontstaan als de wrijvingsweerstand afneemt met een toename in de snelheid. Dit gedrag noemen we snelheidsverzwakking. Het tegenovergestelde gedrag, snelheidsversterking, geeft stabiel gedrag en kan dus niet tot een aardbeving leiden.

De wrijvingsexperimenten uitgevoerd onder *in situ* *P-T* condities in dit promotieonderzoek worden beschreven in Hoofdstukken 2-5, direct na de algemene Introductie (Hoofdstuk 1). In Hoofdstukken 2-4 wordt hoofdzakelijk gekeken naar het effect van de experimentele

condities op het wrijvingsgedrag van breukmeel bestaande uit illiet (klei) en kwarts. In Hoofdstuk 5 wordt vervolgens het effect van de samenstelling van het breukmeel onderzocht door een mengsel van muscoviet (een klei-achtig mineraal karakteristiek voor hogere temperaturen) en kwarts te gebruiken. Het belangrijkste resultaat van deze experimenten samen is dat de snelheidsafhankelijkheid van de wrijvingsweerstand sterk afhangt van de temperatuur, zowel voor illiet-kwarts als voor muscoviet-kwarts. Op lage en hoge temperaturen domineert snelheidsversterkend gedrag, terwijl op tussenliggende temperaturen het gedrag snelheidsverzwakkend is. Deze opeenvolging van stabiel-onstabiel-stabiel gedrag met toenemende temperatuur is vergelijkbaar met wat er in subductiezones met toenemende diepte (en dus toenemende temperatuur) gevonden wordt: aardbevingen ontstaan alleen op ~10-40 km diepte, waar de temperatuur tussen ~150°C en 350°C ligt.

De mate van snelheidsverzwakking en snelheidsversterking wordt in Hoofdstukken 2-5 op de gebruikelijke manier gekwantificeerd met standaard parameters (zogenaamde *rate and state friction* parameters). Dit zijn beschrijvende parameters, die geen verband leggen met de onderliggende, microschaal processen en daarom alleen iets zeggen over de wrijvingseigenschappen van een materiaal onder de condities waarbij de experimenten gedaan zijn. Extrapolatie van de experimentele resultaten naar andere condities kan alleen gedaan worden als we de onderliggende processen begrijpen en in een fysisch/mathematisch model kunnen vangen. In Hoofdstuk 6 wordt een dergelijk model ontwikkeld om het wrijvingsgedrag, en de snelheidsafhankelijkheid daarvan, beschreven in Hoofdstuk 2-5, te verklaren. De ontwikkeling van dit model wordt grotendeels gebaseerd op de structuren zoals onder de (elektronen) microscoop zichtbaar zijn. In dit nieuwe model speelt vervorming van het mineraal kwarts door temperatuursafhankelijke processen die water nodig hebben een grote rol. Dit model vormt een verbeterd uitgangspunt voor studies die met behulp van computersimulaties proberen om mega-aardbevingen te reproduceren, en op termijn ook te voorspellen. Als laatste worden de belangrijkste conclusies die volgen uit dit promotieonderzoek beschreven in Hoofdstuk 7, gevolgd door suggesties voor vervolgonderzoeken.

Acknowledgements

A number of people have helped me to make this thesis into what it is now, and I would like to thank them for that.

First of all, I would like to thank my promotor, Chris Spiers. Chris, I have learned a tremendous amount from you and feel privileged to have had that opportunity. You have always encouraged and supported me, which made working together with you very enjoyable.

I want to thank my co-promotor, André Niemeijer, for being a to-the-point discussion-partner concerning the ring shear machine and for being a critical co-author on some of my papers. I have learned much from André on the use of software to control machine operation and subsequently log and interpret data. Colin Peach taught me how to use the ring shear machine, as well as being a mine of information on numerous other aspects of doing experiments, which I highly appreciate. Hans de Bresser has always been helpful and encouraging.

Magda Mathot-Martens has taken care of all administration concerned with my work, in the most efficient and pleasant way imaginable; Magda, thank you for that! My experimental work would have been impossible without the support of our lab technicians, Gert Kastelein, Eimert de Graaff, Peter van Krieken and Thony van der Gon Netscher. I feel lucky to have had the opportunity to use the ring shear machine, constructed and maintained by contributions from you all.

I would like to thank Toshi Shimamoto for giving me the opportunity to spend 2 months at Hiroshima University. Toshi, it has been a pleasure to learn from you and be supported by you. Takehiro Hirose supervised me during my subsequent 1-month stay at Kochi Core Centre, which I highly appreciate.

In Hiroshima, Tetsuhiro Togo and Keishi Okazaki taught me how to use the biaxial machine. It was fun working with you! At the Kochi Core Centre, Hideki Mukoyoshi and Wataru Tanikawa helped me with the high velocity experiments, which I did not include in this thesis, but hope to publish in the future. Osamu Tadaï performed the XRD analysis at Kochi Core Centre for me.

My microstructural work has greatly benefited from the help of Matthijs de Winter, also co-author of one of my papers, as well as Martyn Drury, Gill Pennock, Hans Meeldijk and Tilly Bouten.

I am happy to have received the illite gouge material from Chris Marone and Brett Carpenter and to have been able to use their XLook program for data analysis. In addition, Chris Marone provided a constructive review of Chapter 3 during its review as a paper, as did an anonymous reviewer. Editor Peter Shearer allowed for fast publication of this chapter. I want to thank Giulio di Toro for his help in the publication of Chapters 2 and 4. In addition, Fabio Ferri and an anonymous reviewer are thanked for their helpful reviews of Chapter 2. I am especially grateful for Kyu Kanagawa's encouragement to contribute to the Kochi conference in February-March 2012, which resulted in the publication of Chapter 4. Kyu

Kanagawa also provided a helpful review of Chapter 5 during the paper review process, as did Demian Saffer, for which I am thankful. The revisions to the paper incorporated as Chapter 5 are only taken into account partially here. Matt Ikari and Hiro Noda provided helpful reviews to Chapter 4 during the paper review process.

The daily routine at the HPT lab has been made more pleasant by my colleagues: Saskia, Suzanne, Reinier, Emilia, Esther, Sabrina, Sander Hol, Sander de Jong, Anne, Elisenda (my paranimf), Tim (my paranimf), Bart, Jon, Nawaz, Ken, Ross, Chen, Amir and Miao. In Japan, it was fun to have Loes, Oohashi san, Michiyo and Han san around.

Als laatste wil ik mijn familie bedanken, pap en mam, Brigit, Kees-Jan en kleine Julian en Ilona en Rachid. Bedankt voor jullie onvoorwaardelijke steun.

Curriculum vitae

08-10-1984	Born in Woerden, The Netherlands
1997-2003	Atheneum, Kalsbeek College, Woerden, The Netherlands (<i>cum laude</i> / distinction)
2003-2006	B.Sc. Earth Sciences, Utrecht University, The Netherlands (<i>cum laude</i> / distinction)
2006-2008	M.Sc. Geology, Utrecht University, The Netherlands (<i>cum laude</i> / distinction)
2008-2013	Ph.D. Experimental Rock Deformation, Utrecht University, The Netherlands